(NASA-CR-4180) SIMULATION OF 2-DIMENSIONAL VISCOUS FLOW THROUGH CASCADES USING A SEMI-ELLIPTIC ANALYSIS AND HYBRID C-H GRIDS Final Report (Cincinnati Univ.) 194 p CSCL 01A H1/02

N89-12553

Unclas 0174644

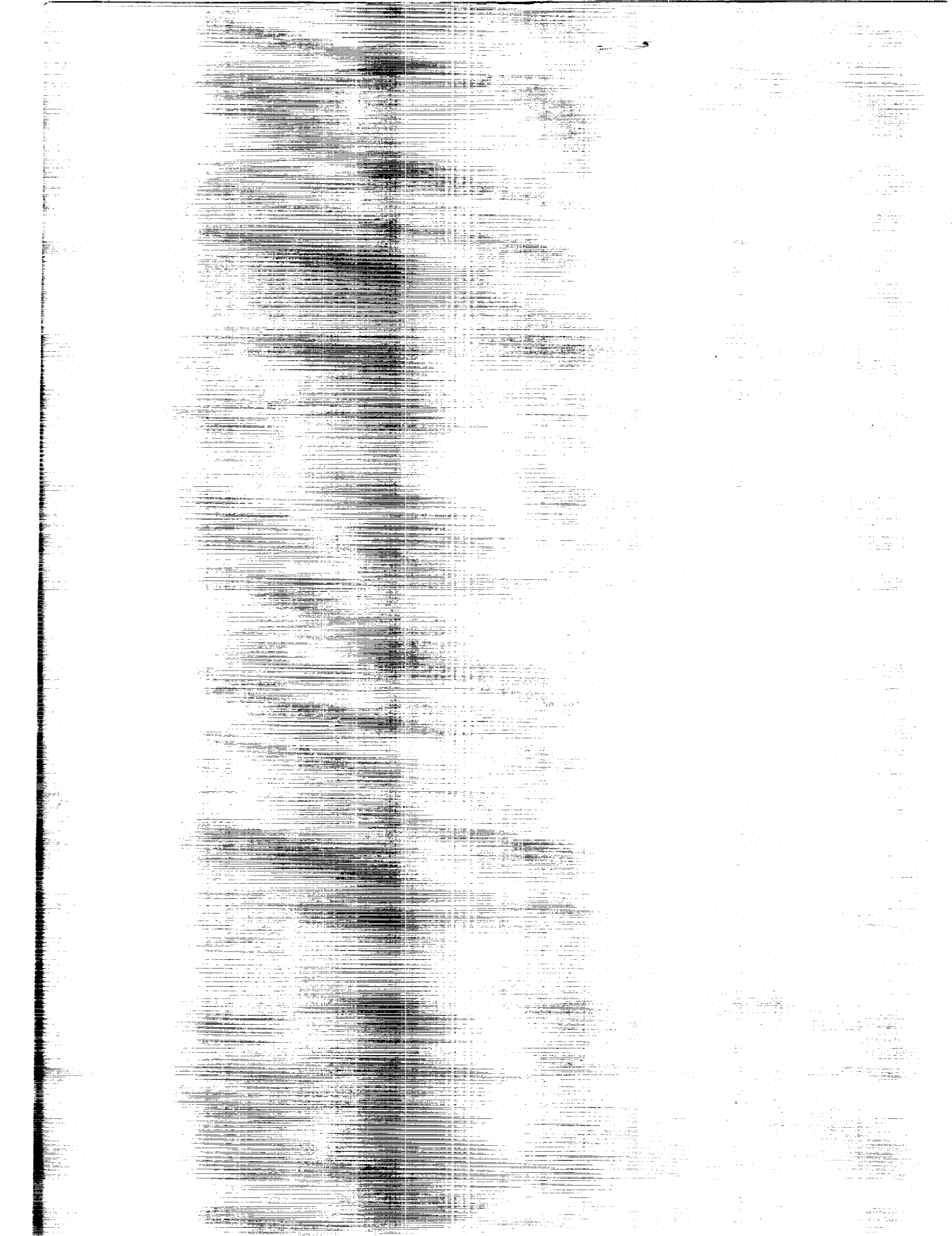

NASA Contractor Report 4180

Simulation of Two-Dimensional Viscous Flow Through Cascades Using a Semi-Elliptic Analysis and Hybrid C-H Grids

R. Ramamurti, U. Ghia,
and K. N. Ghia
University of Cincinnati
Cincinnati, Ohio

Prepared for
Lewis Research Center
under Grant NAG3-194

National Aeronautics
and Space Administration

**Scientific and Technical
Information Division**

1988

SUMMARY

A semi-elliptic formulation, termed the interacting parabolized Navier-Stokes (IPNS) formulation, is developed for the analysis of a class of subsonic viscous flows for which streamwise diffusion is negligible but which are significantly influenced by upstream interactions. The IPNS equations are obtained from the Navier-Stokes equations by dropping the streamwise viscous-diffusion terms but retaining upstream influence via the streamwise pressure-gradient. A two-step alternating-direction-explicit numerical scheme is developed to solve these equations. The quasi-linearization and discretization of the equations are carefully examined so that no artificial viscosity is added externally to the scheme. Also, solutions to compressible as well as nearly incompressible flows are obtained without any modification either in the analysis or in the solution procedure.

The procedure is applied to constricted channels and cascade passages formed by airfoils of various shapes. These geometries are represented using numerically generated general curvilinear boundary-oriented coordinates forming an H-grid. Stagnation pressure, stagnation temperature and streamline slope are prescribed at inflow, while static pressure is prescribed at the outflow boundary. Results are obtained for various values of Reynolds number, thickness ratio and Mach number. The regular behavior of the solutions demonstrates that the technique is viable for flows with strong interactions, arising due to either boundary-layer separation or the presence of sharp leading/trailing edges. Mesh refinement studies are conducted to verify the accuracy of the results obtained.

PRECEDING PAGE BLANK NOT FILMED

PAGE 11 INTENTIONALLY BLANK

A new hybrid C-H grid, more appropriate for cascades of airfoils with rounded leading edges, is also developed. Appropriate decomposition of the physical domain leads to a multi-block computational domain bounded only by the physical-problem boundaries. This permits development of a composite solution procedure which, unlike most found in literature, is not a patching procedure. Satisfactory results are obtained for flows through cascades of Joukowski airfoils. The implementation of the IPNS formulation on the C-H grid exposes two small portions of the grid interfaces and these require special treatment. However, with a hybrid grid, the use of complete Navier-Stokes equations is recommended, so as also to avoid inconsistencies in the parabolization approximation due to changing orientation of the coordinates at a given location.

TABLE OF CONTENTS

NOMENCLATURE

Symbol	Description
a, b, c	Constants in coordinate transformation
$\bar{A}, \bar{B}$	Jacobian matrices of inviscid flux vectoes
A_j, B_j, C_j	Block matrices of the coefficient matrix
B_v	Jacobian matrix of the viscous term
D_j	Right-hand side of the discretized Eq. (3.33)
e, e_t	Specific internal and specific total energies, respectively
E, F	Inviscid flux vectors
E_v, F_v	Viscous terms
h	Nondimensional channel height or cascade spacing
i,j	Streamwise and normal mesh indices
IMAX, JMAX	Indices corresponding to the maximum (ξ,η) locations
J	Jacobian of the coordinate transformation
L	Reference length
M, M_x, M_∞	Mach number
p	Static pressure
Pr	Prandtl number
p_0	Total pressure
q	Heat transfer rate
$\bar{Q}$	Vector of flow variables
P, Q	Forcing functions in the grid equation
R	Gas constant
Re	Reynolds number

t	Time, maximum thickness of airfoils
T	Temperature
T_0	Total temperature
u,v	Cartesian components of velocity
U,V	Contravariant velocity components
U_{avg}	Mass-averaged velocity at the inflow boundary
x,y	Cartesian coordinates
z	Airfoil plane in the Joukowski transformation

Greek Symbols	Description
∇^2	Two-dimensional Laplacian operator
γ	Ratio of specific heats
Δ	Forward difference operator
$\Delta x, \Delta y$	Incremental mesh spacings in the Cartesian coordinates
Δt	Time step
$\Delta\xi, \Delta\eta$	Incremental mesh spacings in the transformed coordinate system
ϵ_{abs}, ϵ_{rel}	Absolute and relative errors
ζ	Circle plane in the Joukowski transformation
θ	Flow direction at the inflow boundary
μ	Coefficient of viscosity
ξ,η	Transformed coordinates
ξ_x, ξ_y, η_x, η_y	Metric derivatives
ρ	Density
τ	Stress component, transformed time

τ_w	Wall shear parameter
ω	Parameter for splitting the pressure gradient term

Subscripts	Description
b	Body, backward difference
f	Forward difference
ref	Reference quantity
v	Viscous term
w	Wall
x,y	Partial derivatives wth respect to Cartesian coordinates
ξ,η	Partial derivatives with respect to the transformed coordinates

Superscripts	Description
i	Streamwise mesh index
j	Normal mesh index
n	Temporal index
*	Dimensional quantity

CHAPTER 1

INTRODUCTION

The flow through compressors and turbines of gas-turbine engines is fairly complex. The complexities arise due to unsteadiness, separation, periodic transition from laminar to turbulent flows and complex geometries. A clear understanding of these flow phenomena is needed in order to improve the performance of these components of the engine. It is well known that the complete Navier-Stokes (NS) equations accurately describe the important physical aspects of fluid flow occurring in these components. However, in spite of all the advances made to date in numerical algorithms and computer firmware, numerical solution of the complete NS equations can still require large amounts of computer resources in terms of time and storage. Hence, an approximate form of the NS equations which accurately depicts the physics is preferred. The simplest of the approximate forms of the NS equations is provided by the boundary-layer equations. The classical boundary layer (CBL) equations with specified pressure gradient are parabolic in nature. Therefore, a spatial-marching procedure can be employed to numerically solve these equations very efficiently. However, this formulation does not contain any mechanism for transmitting downstream disturbances upstream and, hence, cannot be employed for problems where there is a strong pressure interaction or when the flow is separated. Goldstein [1] showed that the solutions to the classical boundary-layer equations exhibit a square root singularity in the wall shear at the separation point. This singularity leads to the failure of the weak interaction method wherein

the outer inviscid flow and the inner boundary-layer region are analyzed sequentially, with the interaction between the two regions being modelled through the pressure gradient term. These limitations were overcome by the development of interacting-boundary layer [2] and triple deck [3] theories. In interacting boundary-layer (IBL) theory the pressure gradient is treated as unknown. In subsonic flows, the pressure gradient is related to the derivative of the displacement thickness through Cauchy's integral. Detailed discussion on interacting boundary-layer theory has been given by Veldman [2]. An interacting boundary-layer model has been used by Rothmayer [4] for analyzing high Reynolds number flows with large regions of separation. However, the interacting boundary-layer model also has its drawbacks. For complex flows, relating the pressure gradient to the displacement thickness is not sufficient. Also, for flow past bodies with large curvature, the normal pressure gradient is no longer negligible and should be included.

To account for these effects, Briley [5] and Ghia et al. [6] developed a non-iterative parabolic procedure for calculating flow through curved ducts. Their procedure employed parabolized Navier-Stokes (PNS) equations obtained by neglecting the viscous diffusion terms in the streamwise direction, with the streamwise pressure gradient term being represented by a backward difference. Hence, this procedure is applicable for flows with little upstream influence and no streamwise separation.

The thin-layer Navier-Stokes (TLNS) equations of Steger [7] include the upstream influence. These equations are obtained from the

unsteady NS equations by dropping the streamwise diffusion terms. The procedure employed to solve these equations is a 'time-marching' technique and has proved to be costly in terms of computer time, in order to obtain steady-state solutions of flows around isolated airfoils. Steger, Pulliam and Chima [8] have employed the two-dimensional TLNS equations and a C-type of grid for solving viscous flows through cascades. They experienced difficulties in obtaining steady-state solutions when the pressure is not prescribed at the upstream boundary. Buggeln, Briley and McDonald [9] have computed laminar and turbulent flows through ducts using the Navier-Stokes equations. Chima and Johnson [10] employed an explicit multiple-grid algorithm to solve the NS equations in order to improve convergence. Shamroth, McDonald and Briley [11] and Hah [12] have computed cascade flows using the complete NS equations. Rhie [13] has employed the partially-parabolic NS equations to analyze three-dimensional viscous flows through curved ducts of arbitrary cross-section. Recently, Chima [14], Davis et al. [15] and Rhie [16] have developed methods for predicting cascade flows using NS equations. References [14] and [16] have also employed a multigrid algorithm to enhance convergence. Most of the works mentioned above have incorporated second- and fourth-order dissipation terms, in order to suppress oscillations in the flow field. The difference in computational effort involved in obtaining the solution to TLNS and complete NS equations is not significant. The numerical solution of both the TLNS and the complete NS equations require large amounts of computer resources.

In the present study, a single system of equations which can include the upstream influence is obtained from the full NS equations. It is termed the interacting parabolized Navier-Stokes (IPNS) formulation and belongs to the class of semi-elliptic models, one form of which was developed earlier by U. Ghia et al. [17]. Only steady flows are discussed here and, hence, the time-derivative term in the NS equations is dropped. It should be mentioned, however, that the analysis can be extended readily to unsteady flows by the inclusion of this term. The semi-elliptic form of the equations is obtained by dropping the viscous diffusion terms in the streamwise direction. This approximation is supported by the fact that the streamwise diffusion is negligible compared to the normal diffusion, for the flows under consideration. Clearly, the approximation is appropriate if the coordinate system employed is a body-oriented, near-orthogonal system. The semi-elliptic or IPNS formulation is tested via application to 2-D flows through channels with varying cross section in the streamwise direction and flows through cascades of airfoils of various shapes. These configurations are chosen as they are akin to the geometries of a turbomachinery compressor or turbine.

In all of the works mentioned above, either an H- or a C-type of grid is employed. In order to analyze flow around airfoils with rounded leading edges, it is often desired to employ a combination of these types of grids. Near the leading edge, the channel or the H-type of grid becomes excessively skewed and non-orthogonal and a C-grid is more suitable in this region. But, in the latter, the grid density decreases

rapidly with distance away from the leading edge. In this region, an H-grid can be employed. Norton, Thompkins and Haimes [18] have employed a mixed sheared and O-type grid for computing flows through turbine cascades. Rai [19] has employed a patched and overlaid grid system in order to compute flow through a rotor-stator combination of a turbomachine. Bush [20] developed a zonal methodology and a time-dependent procedure to obtain solution of the NS equations for flow through an external compression inlet. When the zonal or overlaid grid systems are employed to solve the governing equations of motion, it is important to transfer information from one grid system to the other appropriately. Hence, in the present study, the hybrid C-H grid generation procedure developed by U. Ghia, K. Ghia and Ramamurti [21] for turbomachinery cascades is employed. When this hybrid C-H grid is employed to solve the complete NS equations in a composite manner, the explicit transfer of information across the zonal boundaries is not required.

Details of the derivation of the governing equations are given in Chapter 2. Also, the appropriate boundary conditions to be specified for solving the governing equations, for both channel and cascade configurations, are discussed. In Chapter 3, the numerical procedure employed is discussed. The appropriate form of the pressure gradient term and the metric terms associated with it and the implementation of the boundary conditions and modeling for reversed flow, are also included in that chapter. Results for flows through constricted channels and cascades of airfoils of different shapes, obtained

employing the channel or H-type of grid, are discussed in Chapter 4. A composite procedure for generating a hybrid C-H grid for cascades with rounded leading edges is given in Chapter 5. In Chapter 6, the implementation of the solution procedure for flow through a cascade of Joukowski airfolis using a hybrid C-H grid is discussed. Some results obtained are presented in this chapter. Details of the implicit solution of a system of equations subjected to a periodicity boundary condition arising in cascade flows, the discretized representation of the metric coefficients and the treatment of the five-sided cell occurring in the hybrid C-H grid are included in the appendices.

CHAPTER 2

FORMULATION OF THE PROBLEM

2.1 Basic Equations

The governing equations for the mathematical model of fluid flow can be derived from the Navier-Stokes equations. The nondimensional, conservation form of the equations for two-dimensional laminar flow of a compressible fluid can be written in Cartesian coordinates as follows:

Continuity

$$\frac{\partial \rho}{\partial t} + \frac{\partial}{\partial x}(\rho u) + \frac{\partial}{\partial y}(\rho v) = 0 \qquad (2.1\ a)$$

x-Momentum

$$\frac{\partial}{\partial t}(\rho u) + \frac{\partial}{\partial x}(\rho u^2+p) + \frac{\partial}{\partial y}(\rho uv) = \frac{\partial}{\partial x}(\tau_{xx}) + \frac{\partial}{\partial y}(\tau_{xy}) \qquad (2.1\ b)$$

y-Momentum

$$\frac{\partial}{\partial t}(\rho v) + \frac{\partial}{\partial x}(\rho uv) + \frac{\partial}{\partial y}(\rho v^2+p) = \frac{\partial}{\partial x}(\tau_{xy}) + \frac{\partial}{\partial y}(\tau_{yy}) \qquad (2.1\ c)$$

Energy

$$\frac{\partial}{\partial t}(\rho e_t) + \frac{\partial}{\partial x}\{(\rho e_t+p)u\} + \frac{\partial}{\partial y}\{(\rho e_t+p)v\}$$

$$= \frac{\partial}{\partial x}(u\tau_{xx}+v\tau_{xy}-q_x) + \frac{\partial}{\partial y}(u\tau_{xy}+v\tau_{yy}-q_y) \qquad (2.1\ d)$$

where ρ is the density, u and v are the Cartesian components of velocity and e_t is the specific total energy given in terms of specific internal energy e by

$$e_t = e + \frac{u^2+v^2}{2} \quad . \qquad (2.2\ a)$$

The stress components and the heat flux terms can be written as

$$\tau_{xx} = \frac{1}{Re} \{(\lambda+2\mu)u_x + \lambda v_y\} \quad ,$$

$$\tau_{yy} = \frac{1}{Re} \{(\lambda+2\mu)v_y + \lambda u_x\} \quad ,$$

$$\tau_{xy} = \frac{1}{Re} \{\mu(u_y + v_x)\} \quad ,$$

$$q_x = \frac{-\mu}{Re\ Pr\ (\gamma-1)M_\infty^2} T_x$$

and

$$q_y = \frac{-\mu}{Re\ Pr\ (\gamma-1)M_\infty^2} T_y \quad . \qquad (2.2\ b\text{-}f)$$

According to Stokes' hypothesis, λ is taken as $(-\frac{2}{3}\mu)$.

The equation of state is given by

$$p = (\gamma-1)\ \rho e \quad . \qquad (2.3)$$

The constitutive equation for viscosity is given by Sutherland's viscosity law

$$\mu = \frac{(1+\bar{T})}{(T+\bar{T})} T^{3/2} \quad , \qquad (2.4)$$

where

$$\bar{T} = \frac{110°K}{T_{ref}} \quad .$$

The Reynolds number and the Mach number are based on the conditions at the inlet boundary and are given as

$$Re = (\rho_{ref}\ U_{avg}\ L)/\ \mu_{ref} \qquad (2.5\ a)$$

and

$$M_\infty = U_{avg} / (\gamma R\ T_{ref})^{1/2} \qquad (2.5\ b)$$

where U_{avg} is the mass-averaged inflow velocity at the inlet given by

$$U_{avg} = \frac{\int_0^h \rho V \, ds}{\int_0^h \rho \, ds} \quad , \tag{2.6}$$

with h as the cascade blade spacing or the channel height, V the velocity normal to the inlet boundary and s the distance measured along the inlet boundary.

The reference length L is the chord length of the airfoils for cascade flows and the channel height for channel flows.

Equation (2.1) has been obtained by the following nondimensionalization:

$$x = \frac{x^*}{L} \quad , \quad y = \frac{y^*}{L} \quad , \quad t = \frac{t^*}{(L / U_{avg})} \quad , \quad u = \frac{u^*}{U_{avg}} \quad ,$$

$$v = \frac{v^*}{U_{avg}} \quad , \quad \rho = \frac{\rho^*}{\rho_{ref}} \quad , \quad p = \frac{p^*}{\rho_{ref} U^2_{avg}} \quad , \quad e = \frac{e^*}{U^2_{avg}}$$

and

$$T = \frac{T^*}{T_{ref}} \quad . \tag{2.7}$$

All the dimensional quantities are denoted with a superscript asterisk.

Equation (2.1) can be written in a vector form as

$$\frac{\partial \bar{Q}}{\partial t} + \frac{\partial \bar{E}}{\partial x} + \frac{\partial \bar{F}}{\partial y} = \frac{\partial}{\partial x} (\bar{E}_v) + \frac{\partial}{\partial y} (\bar{F}_v) \tag{2.8}$$

where

$$\bar{Q} = [\, \rho, \rho u, \rho v, \rho e_t \,]^T \quad ,$$

$$\bar{E} = [\ \rho u,\ \rho u^2+p,\ \rho uv,\ (\rho e_t+p)u\ ]^T \quad ,$$

$$\bar{F} = [\ \rho v,\ \rho uv,\ \rho v^2+p,\ (\rho e_t+p)v\ ]^T \quad ,$$

$$\bar{E}_v = [\ 0,\ \tau_{xx},\ \tau_{xy},\ (u\tau_{xx}+v\tau_{xy}-q_x)\ ]^T \quad ,$$

and

$$\bar{F}_v = [\ 0,\ \tau_{xy},\ \tau_{yy},\ (u\tau_{xy}+v\tau_{yy}-q_y)\ ]^T \quad . \qquad (2.9\ a\text{-}e)$$

2.2 Coordinate Transformation

The success of a numerical solution procedure for the governing equations of motion depends heavily on the proper choice of coordinates. One of the first requirements placed on a coordinate system is that the coordinates be aligned with the problem boundaries. The use of boundary-fitted coordinates reduces the complexities otherwise encountered in the treatment of boundaries of arbitrary shape. Hence, the Navier-Stokes equations in the physical (x,y) coordinates are transformed to a system of computational (ξ,η) coordinates through the following general transformation:

$$\xi = \xi(x,y) \quad ,$$

$$\eta = \eta(x,y)$$

and $$\tau = t \quad . \qquad (2.10)$$

According to Viviand [22], the transformed governing equations in the (ξ,η,τ) coordinates can be written in the strong-conservation-law (SCL) form as follows:

$$\frac{\partial}{\partial\tau}\left(\frac{\bar{Q}}{J}\right)+\frac{\partial}{\partial\xi}\left(\frac{\xi_x}{J}\bar{E}+\frac{\xi_y}{J}\bar{F}\right)+\frac{\partial}{\partial\eta}\left(\frac{\eta_x}{J}\bar{E}+\frac{\eta_y}{J}\bar{F}\right)$$

$$=\frac{\partial}{\partial\xi}\left(\frac{\xi_x}{J}\bar{E}_v+\frac{\xi_y}{J}\bar{F}_v\right)+\frac{\partial}{\partial\eta}\left(\frac{\eta_x}{J}\bar{E}_v+\frac{\eta_y}{J}\bar{F}_v\right) \qquad (2.11)$$

where J is the Jacobian of the transformation and is defined as

$$J=\det\left|\frac{\partial(\xi,\eta)}{\partial(x,y)}\right|=\frac{1}{x_\xi\,y_\eta-y_\xi\,x_\eta}=\xi_x\,\eta_y-\xi_y\,\eta_x \quad . \qquad (2.12)$$

The metrics ξ_x, ξ_y, η_x and η_y are determined after the mapping, given by Eq. (2.10), has been defined. The metrics are related to the derivatives x_ξ, y_ξ, etc., by the following relations.

$$\xi_x=J\,y_\eta \quad , \quad \xi_y=-J\,x_\eta \quad ,$$

$$\eta_x=-J\,y_\xi \quad , \quad \eta_y=J\,x_\xi \quad . \qquad (2.13)$$

It is convenient to write Eq. (2.11) in the following form.

$$\frac{\partial Q}{\partial\tau}+\frac{\partial E}{\partial\xi}+\frac{\partial F}{\partial\eta}=\frac{\partial}{\partial\xi}(E_v)+\frac{\partial}{\partial\eta}(F_v) \quad , \qquad (2.14)$$

where

$$Q=\frac{\bar{Q}}{J} \quad ,$$

$$E=\frac{\xi_x}{J}\bar{E}+\frac{\xi_y}{J}\bar{F} \quad ,$$

$$F=\frac{\eta_x}{J}\bar{E}\quad\frac{\eta_y}{J}\bar{F} \quad ,$$

$$E_v=\frac{\xi_x}{J}\bar{E}_v+\frac{\xi_y}{J}\bar{F}_v$$

and

$$F_v=\frac{\eta_x}{J}\bar{E}_v+\frac{\eta_y}{J}\bar{F}_v \quad . \qquad (2.15\ a\text{-}e)$$

An alternative compact representation of the inviscid flux vectors E and F is also possible and is obtained by using Eqs. (2.9 b,c) in Eqs. (2.15 b,c) to yield

$$E = \frac{1}{J}\begin{bmatrix} \rho U \\ \rho u U + \xi_x p \\ \rho v U + \xi_y p \\ (\rho e_t + p)U \end{bmatrix} \quad \text{and} \quad F = \frac{1}{J}\begin{bmatrix} \rho V \\ \rho u V + \eta_x p \\ \rho v V + \eta_y p \\ (\rho e_t + p)V \end{bmatrix} \qquad (2.16\ a,b)$$

where U and V are the contravariant velocities along the ξ and η coordinates, respectively, and are related to the Cartesian components u and v by

$$U = \xi_x u + \xi_y v$$

and

$$V = \eta_x u + \eta_y v \quad . \qquad (2.17)$$

Equations (2.14) are the complete Navier-Stokes equations in SCL form in the general boundary-oriented (ξ,η) coordinates. As discussed in Chapter 1, certain approximations will be introduced in these equations so as to optimize the efficiency of their numerical solution and their ability to represent important physical flow phenomena accurately.

2.3 Derivation of the Semi-Elliptic Form of the Governing Equations

The time-derivative term is dropped from Eq. (2.14) because only steady flows are considered in the present study. The parabolized Navier-Stokes equations are obtained by neglecting all the streamwise

diffusion terms. This involves dropping the second-order derivatives ($\partial^2/\partial\xi^2$) and the cross derivatives ($\partial^2/\partial\xi\,\partial\eta$) in the viscous terms. This approximation is supported by the fact that the streamwise diffusion is negligible compared to the normal diffusion in most of the regions of the flows under consideration. This approximation is appropriate only if the (ξ,η) coordinate system is a body-oriented, near-orthogonal coordinate system, that is, the ξ coordinate is nearly aligned with the streamwise direction and the η coordinate is nearly orthogonal to it. The reduced set of equations can be written as follows.

$$\frac{\partial E}{\partial \xi} + \frac{\partial F}{\partial \eta} = \frac{\partial}{\partial \eta}\,(F_v) \tag{2.18}$$

where E, F and F_v are as given in Eq. (2.15).

It should be emphasized that the above set of equations is 'parabolized' and not parabolic. The mathematical character of the system of equations (2.18) depends on the manner in which the streamwise pressure gradient term p_ξ is treated. If p_ξ is prescribed, as in the case of classical boundary-layer theory, the system is parabolic. In this case, a marching method can be employed to obtain the solution for this system. This method of solution is very efficient, but it does not have any mechanism for including upstream influence and is, therefore, not suitable for flows with separation and sudden streamwise changes in boundary conditions. When the p_ξ term is treated as unknown and forward

differenced, the system of equations is no longer parabolic but has an elliptic character.

When the parabolized Navier-Stokes equations are solved as an inital-value problem, as in the case of single-sweep marching solutions, the ill-posedness of the equations leads to 'departure solutions' similar to the eigensolutions of the viscous sublayer equations proposed by Lighthill [23]. Vigneron, Rakich and Tannehill [24] have described a method for suppressing the departure solutions in their study of supersonic flow over delta-wings. They introduced a parameter, ω, to split the pressure gradient term p_x into '$\omega\, p_x$ ', which was backward differenced and treated implicitly, and $(1-\omega)p_x$. The latter term, even when represented using a backward difference, led to instabilities and, hence, was dropped entirely. This is appropriate if the flow is predominantly supersonic, as in the case these authors considered, but not in general. These authors performed a characteristics analysis for the inviscid as well as the viscous limits of the equations. From the viscous analysis, they found that the equations are well posed for space marching when

$$\omega \leq \frac{\gamma M_x^2}{1+(\gamma-1) M_x^2} = f(M_x) \text{ if } f(M_x) \leq 1 \qquad (2.19\ a)$$

$$\text{and } \omega = 1 \text{ if } f(M_x) > 1 \ , \qquad (2.19\ b)$$

$$\text{where } M_x = \frac{u}{a} \ . \qquad (2.19\ c)$$

In the present study, the pressure-gradient term is split in the manner described above, but is discretized so as to include upstream

influence in flows with strong interaction by forward differencing the '$(1-\omega)\ \partial p/\partial \xi$ ' term, i.e., by using the representation

$$\frac{\partial p}{\partial \xi} = \omega \left.\frac{\partial p}{\partial \xi}\right|_b + (1-\omega) \left.\frac{\partial p}{\partial \xi}\right|_f \quad . \tag{2.20}$$

Here, the subscripts b and f denote backward and forward differences, respectively.

2.4 Boundary Conditions

The appropriate boundary conditions to be specified for solving the governing equations, described in the prevoius section, for flows through cascade and channel configurations are described in this section. These conditions are specified along the inflow and outflow boundaries, and lower and upper wall boundaries for channels and airfoil portions of the cascade passages. These boundaries are shown in Fig. 1. Also, for cascade flows, the periodicity of the flow variables along the wake boundaries is considered. A set of wall-wall boundary conditions is one that is imposed at the ends of a ξ = constant grid-line which starts at a body surface and ends at the facing body surface. A set of wake-wake boundary conditions is one which is imposed at the ends of a ξ = constant line which starts at a point in the wake region and ends at a point in the facing wake region. In the case of staggered cascades, a set of wall-wake boundary conditions may be needed in regions where a ξ = constant line starts from a point along a wall and ends at a point in the facing wake region.

2.4.1 Inflow and Outflow Boundary Conditions

For the problems considered in the present study, the flow near the inflow and outflow boundaries behaves in an almost inviscid manner. von Mises [25] has carried out a characteristics analysis for inviscid systems and found that for subsonic flows, all the characteristics are real, with two of them being positive and one negative. Using the counting principle of Courant and Hilbert [26] that one boundary condition is to be specified per entering characteristic, this requires that two conditions are to be specified at the inflow boundary, and one at the outflow boundary.

In Ref. [27], McDonald and Briley have described a specific set of boundary conditions. They considered a typical duct flow proceeding from a large reservoir and exhausting into a plenum. The reservoir conditions and the plenum static pressure were known. This duct flow model leads to prescribing the reservoir total conditions and the plenum static pressure. The specified stagnation temperature and pressure constitute the two required inflow boundary conditions and the specified static pressure constitutes the one outflow boundary condition.

In the present study, at the **inflow boundary**, the total pressure prescribed for cascade flows is that corresponding to a uniform velocity profile, while the stagnation temperature is taken to be constant. For channel flows, the conditions prescribed at the inflow boundary are the velocity and static temperature profiles corresponding to a fully developed flow in the channel.

In the problems considered, the **outflow boundary** is situated far downstream of the cascade of airfoils or the channel constriction, so that uniform static pressure is an appropriate condition.

As the static pressure at the inlet is not specified, the mass flow in the configuration is not set a priori and pressure waves can escape upstream, avoiding the problem of reflecting waves discussed by Rudy and Strikwerda [28]. To facilitate a marching procedure, the conditions at the inflow boundary are obtained by assuming the velocity-profile shape, guessing a representative magnitude characterizing this profile, and obtaining the static pressure using the prescribed total pressure. The guessed representative velocity magnitude, U_{avg}, is then updated as the overall solution evolves. For channel flows, McDonald and Briley [27] have suggested updating the total pressure distribution within the boundary layer, in order to maintain the required velocity- and temperature-profile shapes prescribed at the inflow boundary. This implies that for fully developed flow conditions at the inlet, as used in the present channel-flow studies, the total pressure distribution has to be updated over the entire channel width.

The procedure for updating the velocity profile for cascade flows will be described in the next chapter.

2.4.2 Wall-Wall Boundary Conditions

The governing equations given by Eq. (2.18) consist of one first-order equation, namely, the continuity equation, and three second-order equations, namely, the x- and y-momentum and the energy equations.

Here, the order refers to the highest-order derivative in the η direction. These comprise a system of seventh order with respect to η, so that a total of seven boundary conditions need to be specified along the two η = constant boundaries. At the wall, the no-slip boundary condition is imposed; also, the walls are assumed to be impermeable and, hence, there is no injection or suction at the surface. In addition, the temperature, T_w, at the surface is specified. These constitute a total of six boundary conditions at the two surfaces. Therefore, one additional condition has yet to be specified. A valid flow approximation such as $(\partial p/\partial \eta) = 0$ can be imposed as an additional boundary condition. The resulting solution will reflect the approximations inherent in the boundary condition. Another method to obtain the additional condition is to write the governing equations in one-sided difference form at the wall, as has been done by Rubin and Lin [29] and Briley and McDonald [30].

In the present study, an approximate form of the normal momentum equation, obtained by dropping the viscous terms in that equation and written at the first cell center near the wall surface, is used as the additional condition. The viscous terms in the normal momentum equation can be shown to be negligible near the wall surface for most of the flows considered in this research.

In order to ascertain that enough independent equations are available at a particular streamwise location, a typical grid line along the η direction, consisting of five computational points as shown in Fig. 2a, is considered. Counting four unknowns, namely,

$\bar{Q} = (\rho, \rho u, \rho v, \rho e_t)^T$, per point, this line involves a total of 20 unknowns. The independent equations that can be written are the continuity equation written at the 4 points denoted by c in Fig. 2a, and the momentum equations and the energy equation written at the 3 points denoted by x, y and e, respectively. This constitutes a total of 13 independent equations. When combined with the six specified wall-boundary conditions, these equations leave one additional condition to be specified. This additional condition is taken to be the reduced y-momentum equation as discussed in this section, and may be imposed near either wall surface.

These boundary conditions can be stated mathematically as follows. At the walls,

$$u = u_w = 0 \quad ,$$

$$v = v_w = 0$$

$$\text{and} \quad T = T_w \quad . \tag{2.21}$$

The reduced normal momentum equation near one of the walls can be written as

$$\frac{\partial}{\partial \xi} \left\{ \frac{1}{J} (\rho v U + \xi_y p) \right\} + \frac{\partial}{\partial \eta} \left\{ \frac{1}{J} (\rho v V + \eta_y p) \right\} = 0 \quad . \tag{2.22}$$

2.4.3 Wake-wake Boundary Conditions

For cascade flows, specification of boundary conditions along the wake boundary needs to be considered. For symmetric configurations, the wake boundary, is in addition to being the wake centerline, also a line

of symmetry. For unstaggered cascades, a 'line-periodic' grid is employed. In this type of grid, the same η-coordinate line connects the corresponding periodic points, such as points 1 and 5 or 0 and 4 in Fig. 2b. In this case, the periodic-boundary conditions can be enforced implicitly. The periodicity condition is that the corresponding values of all the flow variables, $\bar{Q} = (\rho, \rho u, \rho v, \rho e_t)^T$, and the normal derivatives, u_η, v_η and T_η, of the velocities and temperature which are governed by second-order equations, namely, the momentum and energy equations, must be the same at corresponding periodic points along the wake boundaries. It should be mentioned that, in terms of the conserved variables, $\bar{Q} = (\rho, \rho u, \rho v, \rho e_t)^T$, the repeating condition on the η-derivatives must be satisfied for all four elements of $\bar{Q}_\eta$. This condition can be written as

$$\bar{Q}_1 = \bar{Q}_5 \quad \text{or} \quad \bar{Q}_0 = \bar{Q}_4 \tag{2.23}$$

for a typical computational line consisting of points 1 through 5 as shown in Fig. 2b. Imposing the periodicity boundary condition described above between points 1 and 5, leaves a total of 16 unknowns counting four unknown variables per computational point. The system of equations that can be written along this computational line consists of the continuity equation at 5 points, and the momentum and energy equations at 4 points, denoted by c, x, y and e, respectively, in Fig. 2b. As periodicity has already been imposed, the continuity equation, which is of the first order, written employing points 4 and 5, becomes identical

to that employing points 0 and 1. Hence, there are only 16 independent equations and the system is closed. Also, in the case where symmetry exists along the wake boundary, the viscous terms in the y-momentum equation can be dropped, and this reduced first-order equation can be written employing points 1 and 2.

2.4.4 Wall-Wake Boundary Conditions

This type of boundary condition is needed for cascades with stagger when a 'region-periodic' grid is employed. A 'region-periodic' grid is one in which the corresponding periodic points in the flow are not connected by the same η-coordinate line. This type of grid has to be employed for cascades with large stagger in order to avoid excessive skewness of the coordinates. The use of this type of coordinates, in conjunction with a marching procedure, forces the periodicity condition to be imposed in an explicit manner.

Figure 2c shows a typical grid consisting of six points along an η-coordinate line in the wall-wake region. The 18 independent equations along this line consist of the continuity equation written at 5 points and the momentum and energy equations written at 4 points, in addition to the reduced momentum equation written at the wall surface. The six boundary conditions consist of the zero slip, zero injection/suction and the specified temperature at the wall surface and the specified velocity and temperature conditions at the wake boundary. The conditions at the wake boundary are obtained from the corresponding periodic point along

the upper wake boundary in the flow. These conditions can be stated mathematically as follows.

At the wall, the conditions are

$$u = u_w = 0 \quad ,$$

$$v = v_w = 0$$

and $$T = T_w \quad . \tag{2.24}$$

Along the wake, for example, at point 0 in Fig. 2c, the conditions are

$$u_0 = u_a \quad ,$$

$$v_0 = v_a$$

and $$T_0 = T_a \quad . \tag{2.25}$$

Here, '0' and 'a' are the corresponding periodic points.

2.4.5 Wake-wake Boundary Conditions (Region-Periodic Grid)

Along this type of boundary for staggered cascades employing a region-periodic grid, the periodicity condition is imposed in an explicit manner. The independent equations to be considered along a typical computational line consisting of six grid points 0 through 5 are the continuity equation written at 5 points and the (x,y) momentum and energy equations written at 4 points. The boundary conditions consist of the specified values of $\bar{Q} = (\rho, \rho u, \rho v, \rho e_t)^T$ at point 5, obtained from the values at the corresponding periodic point in the flow, such as point b in Fig. 2d. For this purpose, the most recent values of $\bar{Q}$ are used. This implies that only three more boundary conditions can be

supplied for the seventh-order system. Hence, the velocities u and v and the temperature, which are lagged in time, are specified at point 0. These conditions can be stated as follows.

Along the wake, at point 5,

$$\rho_s = \rho_b \quad , \quad u_s = u_b \quad , \quad v_s = v_b \quad \text{and} \quad T_s = T_b \tag{2.26}$$

and at point 0,

$$u_o = u_a \quad , \quad v_o = v_a \quad \text{and} \quad T_o = T_a \quad . \tag{2.27}$$

CHAPTER 3

NUMERICAL PROCEDURE

The interacting parabolized Navier-Stokes equations (2.18), described in the preceding chapter, are a set of nonlinear coupled partial differential equations. Analytical solution of this system of equations exists only for a small, special class of problems. Hence, for the general problems of present interest, a numerical solution of these equations is sought.

The linearization and discretization of the governing equations, the solution procedure for the discretized set of equations, the implementation of the boundary conditions, including the periodicity boundary condition for cascade flows, as well as the treatment of problems with flow separation are detailed in the following sections of this chapter.

3.1 Quasi-linearization and Discretization

The system of governing equations (2.18) is first re-written here for easy reference.

$$\frac{\partial E}{\partial \xi} + \frac{\partial F}{\partial \eta} = \frac{\partial}{\partial \eta} (F_v) \tag{3.1}$$

where

$$E = \frac{\xi_x}{J} \bar{E} + \frac{\xi_y}{J} \bar{F} \quad ,$$

and $$F = \frac{\eta_x}{J} \bar{E} + \frac{\eta_y}{J} \bar{F} \quad . \tag{3.2}$$

As mentioned above, this system of equations is nonlinear. Therefore, these equations must be linearized or quasi-linearized in order to obtain a system of algebraic equations amenable to numerical solution. In the present study, employing forward marching for the solution vector $\bar{Q}$, a quasi-linearization of the nonlinear terms at a given streamwise station is carried out about the solution at the preceding streamwise location. From Eq. (3.2), it is seen that the quasi-linearization of the **inviscid flux vectors** E and F requires that the flux vectors $\bar{E}$ and $\bar{F}$ be quasi-linearized. This is achieved by using Taylor's series expansions. The results can be expressed as follows.

$$\bar{E}^{i+1} = \bar{E}^{i} + \bar{A}^{i}\,\Delta^{i}\bar{Q} \quad , \tag{3.3}$$

$$\bar{F}^{i+1} = \bar{F}^{i} + \bar{B}^{i}\,\Delta^{i}\bar{Q} \quad , \tag{3.4}$$

where

$$\Delta^{i}\bar{Q} = \bar{Q}^{i+1} - \bar{Q}^{i} \quad ,$$

$$\bar{A}^{i} = \frac{\partial \bar{E}^{i}}{\partial \bar{Q}} \quad \text{and} \quad \bar{B}^{i} = \frac{\partial \bar{F}^{i}}{\partial \bar{Q}} \quad . \tag{3.5 a-c}$$

Here, the superscripts i and (i+1) denote two successive streamwise locations as shown in Fig. 3. The quantities with superscript (i+1) are the unknown terms, which contribute to the nonlinearities in the equations.

Recognizing the fact that the inviscid flux vectors, $\bar{E}\ (\bar{Q})$ and $\bar{F}\ (\bar{Q})$ are homogeneous functions of degree 1 in $\bar{Q}$, and using the property of homogeneous functions (see Ref. [31]), one can write

$$\frac{\partial \bar{E}}{\partial \bar{Q}}\,\bar{Q} = \bar{E} \quad \text{and} \quad \frac{\partial \bar{F}}{\partial \bar{Q}}\,\bar{Q} = \bar{F} \quad . \tag{3.6}$$

This property allows some conceptual simplifications of the equations and leads to computational efficiency. Using this property of homogeneous functions, Eqs. (3.3) and (3.4) can be written as follows.

$$\bar{E}^{i+1} = \bar{A}^{i}\,\bar{Q}^{i+1} \quad ,$$

$$\text{and} \quad \bar{F}^{i+1} = \bar{B}^{i}\,\bar{Q}^{i+1} \quad . \tag{3.7 a,b}$$

The Jacobian matrices $\bar{A}$ and $\bar{B}$, defined in Eqs. (3.5 b,c), are given as follows.

$$\bar{A} = (\partial \bar{E}/\partial \bar{Q}) = \begin{bmatrix} 0 & 1 & 0 & 0 \\ \phi^2 - u^2 & (3-\gamma)u & -(\gamma-1)v & (\gamma-1) \\ -uv & v & u & 0 \\ u\,(2\phi^2-\gamma e_t) & \{\gamma e_t-\phi^2 -(\gamma-1)u^2\} & -(\gamma-1)uv & \gamma u \end{bmatrix}$$

and

$$\bar{B} = (\partial \bar{F}/\partial \bar{Q}) = \begin{bmatrix} 0 & 0 & 1 & 0 \\ -uv & v & u & 0 \\ \phi^2 - u^2 & -(\gamma-1)u & (3-\gamma)v & (\gamma-1) \\ v\,(2\phi^2-\gamma e_t) & -(\gamma-1)uv & \{\gamma e_t-\phi^2 -(\gamma-1)u^2\} & \gamma u \end{bmatrix} ,$$

where $\phi^2 \triangleq \frac{(\gamma-1)}{2}(u^2+v^2)$. (3.8 a-c)

Using Eqs. (3.7) and (3.2), the flux vectors E and F can be written as

$$E^{i+1} = \tilde{A}^i \bar{Q}^{i+1}$$

where $\tilde{A}^i = (\frac{\xi_x}{J})^{i+1} \bar{A}^i + (\frac{\xi_y}{J})^{i+1} \bar{B}^i$. (3.9 a,b)

Similarly,

$$F^{i+1} = \tilde{B}^i \bar{Q}^{i+1}$$

where $\tilde{B}^i = (\frac{\eta_x}{J})^{i+1} \bar{A}^i + (\frac{\eta_y}{J})^{i+1} \bar{B}^i$. (3.9 c,d)

As the metric terms at (i+1) station are known quantities, the metric terms involved in Eqs. (3.9 a-d) are evaluated at station (i+1). This type of quasi-linearization has been employed by Schiff and Steger [32]. It is different from that employed by Steger [7], who used

$$E^{i+1} = E^i + A^i \Delta^i \bar{Q} \quad (3.10\ a)$$

with

$$A^i = \frac{\partial E^i}{\partial \bar{Q}} \quad . \quad (3.10\ b)$$

The Jacobian matrix A^i contains metric quantities evaluated at station i. The ~ on the Jacobian matrices A and B in Eq. (3.9) is used to denote that the metrics in these matrices are evaluated at station (i+1), and distinguishes these matrices from the Jacobian matrix in Eq. (3.10).

The **viscous term** F_v is quasi-linearized as follows. A typical term of F_v is of the form $(\alpha \frac{\partial \beta}{\partial \eta})$. Starting with the Taylor's series expansion for $(\alpha \frac{\partial \beta}{\partial \eta})^{i+1}$ and re-arranging leads to the expression

$$(\alpha \frac{\partial \beta}{\partial \eta})^{i+1} = \alpha^{i+1} (\frac{\partial \beta}{\partial \eta})^{i} + \alpha^{i+1} (\partial \beta / \partial \bar{Q}\ \Delta^{i} \bar{Q}) \qquad (3.11\ a)$$

Further, it is observed that the term β is homogeneous of degree zero, in $\bar{Q}$. Hence,

$$(\partial \beta / \partial \bar{Q})\ \bar{Q} = 0. \qquad (3.11\ b)$$

Therefore, Eq. (3.11 a) becomes

$$(\alpha \frac{\partial \beta}{\partial \eta})^{i+1} = \alpha^{i+1} (\frac{\partial \beta}{\partial \eta})^{i} + \alpha^{i+1} (\partial \beta / \partial \bar{Q})^{i}\ \bar{Q}^{i+1} \qquad (3.11\ c)$$

Using Eq. (3.11 c), the viscous term F_v^{i+1} can be written as

$$F_v^{i+1} = \tilde{F}_v^{i} + \tilde{B}_v^{i}\ \bar{Q}^{i+1}$$

where a typical term of $\tilde{F}_v^{i}$ is of the form $\alpha^{i+1} (\frac{\partial \beta}{\partial \eta})^{i}$, and of $\tilde{B}_v^{i}\ \bar{Q}^{i+1}$ is $\alpha^{i+1} (\partial \beta / \partial \bar{Q})^{i}\ \bar{Q}^{i+1}$. Again, the $\tilde{}$ denotes that the metrics involved are evaluated at station (i+1).

The **discretization** of the derivative terms is discussed next. The ξ-derivative term $(\frac{\partial E}{\partial \xi})^{i+1}$ is considered first. This term can be written as

$$(\frac{\partial E}{\partial \xi})^{i+1} = \theta_1 (\frac{\partial E}{\partial \xi})^{i+1} + (1-\theta_1) (\frac{\partial E}{\partial \xi})^{i} . \qquad (3.12)$$

The values of θ_1 are chosen depending on whether an implicit, explicit or the Crank-Nicolson scheme is to be employed. The various values of θ_1 commonly employed, and the corresponding schemes, are

$$\theta_1 = \begin{cases} 1 & \text{for an implicit scheme ,} \\ 0 & \text{for an explicit scheme ,} \\ 1/2 & \text{for Crank-Nicolson scheme .} \end{cases} \tag{3.13}$$

Also, depending on the type of differencing and the desired accuracy, one can write

$$\left(\frac{\partial E}{\partial \xi}\right)^{i+1} = (1+\theta_2)\,\frac{\Delta^i E}{\Delta \xi} - \theta_2\,\frac{\Delta^{i-1} E}{\Delta \xi} \tag{3.14}$$

where Δ^i is the forward difference operator defined by Eq. (3.5 a). The type of differencing, and the corresponding order of accuracy, for various values of θ_2 are given as

$$\theta_2 = \begin{cases} -1/2, & \text{central,} & O(\Delta\xi^2) \\ 0\ , & \text{two-point backward,} & O(\Delta\xi) \\ 1/2\ , & \text{three-point backward,} & O(\Delta\xi^2) \end{cases} \tag{3.15}$$

Combining Eqs. (3.12) and (3.14) leads to,

$$\theta_1 \left(\frac{\partial E}{\partial \xi}\right)^{i+1} + (1-\theta_1) \left(\frac{\partial E}{\partial \xi}\right)^{i} = (1+\theta_2)\,\frac{\Delta^i E}{\Delta \xi} - \theta_2\,\frac{\Delta^{i-1} E}{\Delta \xi} \quad . \tag{3.16}$$

An explicit scheme usually has some stability condition such as the Courant-Friedrichs-Lewy (CFL) condition associated with it. Hence, an implicit scheme, corresponding to $\theta_1 = 1$, is employed in the present work, to enhance the numerical stability of the resulting method. To facilitate a marching type of procedure, either two-point backward

differencing or three-point backward differencing has to be employed. In the present work, the two-point backward differencing, with $\theta_2 = 0$, has been employed.

Substituting for $\left(\frac{\partial E}{\partial \xi}\right)$ from the governing differential equation (3.1) into Eq. (3.16) gives

$$-\theta_1 \frac{\partial}{\partial \eta} (F-F_v)^{i+1} + (1-\theta_1) \left(\frac{\partial E}{\partial \xi}\right)^i = (1+\theta_2) \frac{\Delta^i E}{\Delta \xi} - \theta_2 \frac{\Delta^{i-1} E}{\Delta \xi} \quad . \tag{3.17 a}$$

Equation (3.17 a) can be rearranged as follows:

$$\Delta^i E = \frac{\theta_2}{1+\theta_2} \Delta^{i-1} E - \frac{\theta_1}{1+\theta_2} \Delta \xi \frac{\partial}{\partial \eta} (F-F_v)^{i+1} - \frac{1-\theta_1}{1+\theta_2} \Delta \xi \frac{\partial}{\partial \eta} (F-F_v)^i \tag{3.17 b}$$

Substituting for the quantities at station (i+1) using the quasi-linearization given by Eqs. (3.9) and (3.11), Eq. (3.17 b) can be rewritten as

$$\tilde{A}^i \bar{Q}^{i+1} - E^i = \frac{\theta_2}{1+\theta_2} \Delta^{i-1} E - \frac{\theta_1}{1+\theta_2} \Delta \xi \frac{\partial}{\partial \eta} \{(\tilde{B}^i - \tilde{B}_v{}^i) \bar{Q}^{i+1} - \tilde{F}_v{}^i\} - \Delta \xi \frac{1-\theta_1}{1+\theta_2} \frac{\partial}{\partial \eta} (F-F_v)^i \quad . \tag{3.18}$$

Equation (3.18) can be re-arranged to contain the unknowns at station (i+1) in the incremental or delta form, by subtracting

$$\tilde{A}^i \bar{Q}^i + \Delta \xi \frac{\theta_1}{1+\theta_2} \frac{\partial}{\partial \eta} \{(\tilde{B}^i - \tilde{B}_v^i) \bar{Q}^i\}$$

from both sides of Eq. (3.18) and is given as

$$\tilde{A}^i \Delta^i\bar{Q} + \Delta\xi \frac{\theta_1}{1+\theta_2} \frac{\partial}{\partial\eta} \{(\tilde{B}^i - \tilde{B}_v^i) \Delta^i\bar{Q}\}$$

$$= E^i - \tilde{A}^i \bar{Q}^i + \frac{\theta_2}{1+\theta_2} \Delta^{i-1} E - \Delta\xi \frac{1-\theta_1}{1+\theta_2} \frac{\partial}{\partial\eta} (F-F_v)^i$$

$$- \Delta\xi \frac{\theta_1}{1+\theta_2} \frac{\partial}{\partial\eta} \{(\tilde{B}^i - \tilde{B}_v^i) \bar{Q}^i - \tilde{F}_v^i\} \quad . \qquad (3.19\ a)$$

Here,

$$\tilde{A}^i \bar{Q}^i = \left(\frac{\xi_x}{J}\right)^{i+1} \bar{E}^i + \left(\frac{\xi_y}{J}\right)^{i+1} \bar{F}^i \quad ,$$

$$\tilde{B}^i \bar{Q}^i = \left(\frac{\eta_x}{J}\right)^{i+1} \bar{E}^i + \left(\frac{\eta_y}{J}\right)^{i+1} \bar{F}^i$$

and $\tilde{B}_v^i \bar{Q}^i = 0.$ (3.19 b-d)

It may be important to recall that Eqs. (3.19 b,c) are obtained from the definitions of the Jacobian matrices $\tilde{A}$ and $\tilde{B}$, given by Eqs. (3.9 b,d), and by using the homogeneous property [Eqs. (3.6)] of the flux vectors $\bar{E}$ and $\bar{F}$.

For an implicit scheme employing a two-point backward difference, $\theta_1 = 1$ and $\theta_2 = 0$. Hence, Eq. (3.19 a) reduces to the following.

$$\tilde{A}^i \Delta^i\bar{Q} + \Delta\xi \frac{\partial}{\partial\eta} \{(\tilde{B}^i - \tilde{B}_v^i) \Delta^i\bar{Q}\}$$

$$= E^i - \tilde{A}^i \bar{Q}^i - \Delta\xi \frac{\partial}{\partial\eta} (\tilde{B}^i \bar{Q}^i - F_v^i) \qquad (3.20)$$

The next step in the numerical procedure is the **introduction of upstream influence.** For flows with strong viscous-inviscid interaction, as mentioned in Section 2.3, the streamwise pressure gradient term is split according to Eq. (2.20) and upstream influence is introduced by

forward differencing the '$(1-\omega)\ \partial p/\partial \xi$ ' term. With this 'ω - split', the governing equation (3.1) can be written as

$$\frac{\partial E^*}{\partial \xi} + \frac{\partial F}{\partial \eta} - \frac{\partial}{\partial \eta}(F_v) = - a \frac{\partial p}{\partial \xi_f} \qquad (3.21\ a)$$

where

$$a = \frac{1}{J} \begin{bmatrix} 0 \\ (1-\omega)\ \xi_{x,f} \\ (1-\omega)\ \xi_{y,f} \\ 0 \end{bmatrix} . \qquad (3.21\ b)$$

The subscript f on the pressure gradient term denotes that this term is forward differenced and those on the metrics ξ_x and ξ_y denote that these are obtained using coordinate values at station (i+2). This representation of the metric terms was arrived at by applying the procedure for a test case in which a fully developed flow was reproduced in a straight channel using a coordinate system with metrics varying along the streamwise direction.

The flux vector E^* is different from E given in Eq. (2.16), in that the pressure terms in it are multiplied by the factor ω. It is given as

$$E^* = \frac{1}{J} \begin{bmatrix} \rho U \\ \rho u U + \xi_x\ \omega p \\ \rho v U + \xi_y\ \omega p \\ (\rho e_t + p)\ U \end{bmatrix} , \qquad (3.22)$$

where U is the contravariant velocity given by Eq. (2.17 a).

For low subsonic flows considered in the present study, according to Eq. (2.19), $\omega = 0$. This implies that the total streamwise pressure-gradient term is forward differenced. Also, it is clear from Eq. (3.21 a) that the streamwise pressure gradient term is no longer in the SCL form. This necessitates that the pressure gradient term p_η should no longer be in the SCL form, as the starting governing equations were written in the conservation form in Cartesian coordinates. Accordingly, Eq. (3.21 a) must be written in the following form.

$$\frac{\partial E^*}{\partial \xi} + \frac{\partial F^*}{\partial \eta} + b \frac{\partial p}{\partial \eta} - \frac{\partial}{\partial \eta}(F_v) = - a \frac{\partial p}{\partial \xi_f} \qquad (3.23\ a)$$

where

$$b = \frac{1}{J} \begin{bmatrix} 0 \\ (1-\omega)\ \eta_x \\ (1-\omega)\ \eta_y \\ 0 \end{bmatrix} \qquad (3.23\ b)$$

and $F^* = F - b\ p$. (3.23 c)

The procedure for quasi-linearization of Eq. (3.23 a) is similar to that used to obtain Eq. (3.20). The resulting equation has an extra source term on the right hand side, arising out of the pressure gradient $(\partial p/\partial \xi)_f$ term. The quasi-linearized form of Eq. (3.23 a) becomes

$$\tilde{A}^{*i}\ \Delta^i \bar{Q} + \Delta\xi \left[\frac{\partial}{\partial \eta} \{(\tilde{B}^{*i} - \tilde{B}_v^i)\ \Delta^i \bar{Q}\} + b^{i+1} \frac{\partial}{\partial \eta} \{(\frac{\partial p}{\partial \bar{Q}})^i\ \Delta^i \bar{Q}\right]$$

$$= E^{*i} - \tilde{A}^{*i}\ \bar{Q}^i - \Delta\xi \{\frac{\partial}{\partial \eta}(\tilde{B}^{*i}\ \bar{Q}^i) + b^{i+1} (\frac{\partial p}{\partial \eta})^i - \frac{\partial}{\partial \eta}(\tilde{F}_v^i)\}$$

$$- a^{i+1}\ \Delta^{i+1}\ p \quad . \qquad (3.24)$$

The asterisk on the Jacobian matrices $\tilde{A}^*$ and $\tilde{B}^*$ denotes that these are obtained from the corresponding flux vectors E^* and F^*, respectively.

A possible method of solution of Eq. (3.24) is to employ an alternating-direction explicit (ADE) method. In the first step of this method, $\Delta^{i}\bar{Q}$ is computed starting at the inflow boundary and proceeding towards the outflow boundary and in the second step, $\Delta^{i+1}p$ is computed starting from the outflow boundary and proceeding towards the inflow boundary. Such a method requires the inclusion of a time-derivative term, p_t, in the momentum equations containing $(\partial p/\partial \xi)_f$ term, in order to unlock the solution from its initial conditions. This method, like the pressure updating procedure used previously by K. Ghia and U. Ghia [33], is capable of transmitting the downstream disturbances upstream efficiently. It is, however, algebraically much simpler and has been successfully used by Barnett and Davis [34], for solving supersonic external flow problems.

With the inclusion of the time-derivative term, the governing equation (3.23 a) assumes the following form.

$$\frac{\partial E^*}{\partial \xi} + \frac{\partial F^*}{\partial \eta} + b\,\frac{\partial p}{\partial \eta} - \frac{\partial}{\partial \eta}\,(F_v) = -\,a\,\frac{\partial p}{\partial \xi_f} + a\,\frac{\partial p}{\partial t} \quad . \tag{3.25}$$

The quasilinearized form of Eq. (3.25) is obtained by utilizing Eq. (3.24), in addition to discretizing the $(\partial p/\partial t)$ term as

$$\left(\frac{\partial p}{\partial t}\right)^{i+1} = \frac{1}{\Delta t}\,(p^{i+1,n+1/2} - p^{i+1,n}) \tag{3.26}$$

and quasilinearizing $p^{i+1,n+1/2}$ about $p^{i,n+1/2}$. The resulting equation is

$$\tilde{A}^{*i}\,\Delta^i\bar{Q} + \Delta\xi\left[\frac{\partial}{\partial\eta}\{(\tilde{B}^{*i} - \tilde{B}_v^i)\,\Delta^i\bar{Q}\} + b^{i+1}\frac{\partial}{\partial\eta}\{(\frac{\partial p}{\partial\bar{Q}})^i\,\Delta^i\bar{Q}\}\right.$$

$$\left. - \frac{a^{i+1}}{\Delta t}\{(\frac{\partial p}{\partial\bar{Q}})^i\,\Delta^i\bar{Q}\}\right]$$

$$= E^{*i} - \tilde{A}^{*i}\,\bar{Q}^i - \Delta\xi\{\frac{\partial}{\partial\eta}(\tilde{B}^{*i}\,\bar{Q}^i) + b^{i+1}\frac{\partial p^i}{\partial\eta} - \frac{\partial}{\partial\eta}(\tilde{F}_v^i)\}$$

$$+ a^{i+1}\{\frac{\Delta\xi}{\Delta t}(p^{i,n+1/2} - p^{i+1,n}) - \Delta^{i+1}\,p^n\} \quad . \tag{3.27}$$

The discretization of the above equation in the η direction is considered next. The discretization is performed such that the discretized form of the inviscid portion of the equations constitute a consistent set of equations by themselves; the viscous portion of the equation is also discretized in a self-consistent manner. The inviscid part of Eq. (3.27) is given by

$$\tilde{A}^{*i}\,\Delta^i\bar{Q} + \Delta\xi\left[\frac{\partial}{\partial\eta}\{(\tilde{B}^{*i}\,\Delta^i\bar{Q}\} + b^{i+1}\frac{\partial}{\partial\eta}\{(\frac{\partial p}{\partial\bar{Q}})^i\,\Delta^i\bar{Q}\}\right.$$

$$\left. - \frac{a^{i+1}}{\Delta t}\{(\frac{\partial p}{\partial\bar{Q}})^i\,\Delta^i\bar{Q}\}\right]$$

$$= E^{*i} - \tilde{A}^{*i}\,\bar{Q}^i - \Delta\xi\{\frac{\partial}{\partial\eta}(\tilde{B}^{*i}\,\bar{Q}^i) + b^{i+1}\frac{\partial p^i}{\partial\eta}\}$$

$$+ a^{i+1}\{\frac{\Delta\xi}{\Delta t}(p^{i,n+1/2} - p^{i+1,n}) - \Delta^{i+1}\,p\} \quad . \tag{3.28}$$

All normal derivatives are represented by central differences, with the first-order derivative representation involving points across one normal mesh interval only. The discretized equations are second-order

accurate in the η direction. Equation (3.28) is written at a normal mesh midpoint, $j+1/2$, as

$$\frac{1}{2}\{(\tilde{A}^{*i}\,\Delta^{i}\bar{Q})_j + (\tilde{A}^{*i}\,\Delta^{i}\bar{Q})_{j+1}\} + \frac{\Delta\xi}{\Delta\eta}\left[(\tilde{B}^{*i}\,\Delta^{i}\bar{Q})_{j+1} - (\tilde{B}^{*i}\,\Delta^{i}\bar{Q})_j\right.$$

$$\left. + b^{i+1}_{j+1/2}\ \{(\frac{\partial p^{i}}{\partial\bar{Q}}\,\Delta^{i}\bar{Q})_{j+1} - (\frac{\partial p^{i}}{\partial\bar{Q}}\,\Delta^{i}\bar{Q})_j\}\right]$$

$$- \frac{\Delta\xi}{2\,\Delta t}\ a^{i+1}_{j+1/2}\ \{(\frac{\partial p^{i}}{\partial\bar{Q}}\,\Delta^{i}\bar{Q})_{j+1} + (\frac{\partial p^{i}}{\partial\bar{Q}}\,\Delta^{i}\bar{Q})_j\}$$

$$= \frac{1}{2}\{E^{*i}_j + E^{*i}_{j+1} - (\tilde{A}^{*i}\,\bar{Q}^{i})_j - (\tilde{A}^{*i}\,\bar{Q}^{i})_{j+1}\}$$

$$- \frac{\Delta\xi}{\Delta\eta}\{(\tilde{B}^{*i}\,\bar{Q}^{i})_{j+1} - (\tilde{B}^{*\,i}\,\bar{Q}^{i})_j + b^{i+1}_{j+1/2}\,(p^{i,n}_{j+1} - p^{i,n}_j)\}$$

$$+ \frac{1}{2}\,a^{i+1}_{j+1/2}\left[\frac{\Delta\xi}{\Delta t}\{(p^{i,n+1/2} - p^{i+1,n})_{j+1}\right.$$

$$\left. + (p^{i,n+1/2} - p^{i+1,n})_j\} - \Delta^{i+1}\,p^{n}_{j+1} - \Delta^{i+1}\,p^{n}_j\right] \qquad (3.29\ a)$$

where

$$a^{i+1}_{j+1/2} = \frac{1}{2}\,(a^{i+1}_j + a^{i+1}_{j+1})$$

and

$$b^{i+1}_{j+1/2} = \frac{1}{2}\,(b^{i+1}_j + b^{i+1}_{j+1}) \quad . \qquad (3.29\ b,c)$$

In order to include the viscous terms at mesh point j, the inviscid part of the equation should also be written at j. This is obtained by writing a discretized equation similar to Eq. (3.29) at location (j-1/2) and forming the arithmetic mean of this equation and Eq. (3.29). The resulting equation is

$$\frac{1}{4}\,(\tilde{A}^{*i}\,\Delta^{i}\bar{Q}\,)_{j+1} + \frac{1}{4}\,(\tilde{A}^{*i}\,\Delta^{i}\bar{Q}\,)_{j} + \frac{1}{4}\,(\,\tilde{A}^{*i}\,\Delta^{i}\bar{Q})_{j-1}$$

$$+ \frac{\Delta\xi}{2\,\Delta\eta}\,\Big[(\tilde{B}^{*i}\,\Delta^{i}\bar{Q}\,)_{j+1} - (\tilde{B}^{*i}\,\Delta^{i}\bar{Q})_{j-1}$$

$$+ b^{i+1}_{j+1/2}\,\{(\frac{\partial p^{i}}{\partial\bar{Q}}\,\Delta^{i}\bar{Q}\,)_{j+1} - (\frac{\partial p^{i}}{\partial\bar{Q}}\,\Delta^{i}\bar{Q}\,)_{j}\}$$

$$+ b^{i+1}_{j-1/2}\,\{(\frac{\partial p^{i}}{\partial\bar{Q}}\,\Delta^{i}\,\bar{Q})_{j} - (\frac{\partial p^{i}}{\partial\bar{Q}}\,\Delta^{i}\,\bar{Q})_{j-1}\}\Big]$$

$$- \frac{\Delta\xi}{4\,\Delta t}\,\Big[a^{i+1}_{j+1/2}\,\{(\frac{\partial p^{i}}{\partial\bar{Q}}\,\Delta^{i}\bar{Q}\,)_{j+1} + (\frac{\partial p^{i}}{\partial\bar{Q}}\,\Delta^{i}\bar{Q}\,)_{j}\}$$

$$+ a^{i+1}_{j-1/2}\,\{(\frac{\partial p^{i}}{\partial\bar{Q}}\,\Delta^{i}\bar{Q})_{j} + (\frac{\partial p^{i}}{\partial\bar{Q}}\,\Delta^{i}\bar{Q})_{j-1}\}\Big]$$

$$= \frac{1}{4}\,\{\,E^{*i}_{j+1}\,-(\tilde{A}^{*i}\,\bar{Q}^{i})_{j+1} + E^{*i}_{j-1}\,-(\tilde{A}^{*i}\,\bar{Q}^{i})_{j-1}\} + \frac{1}{2}\,\{E^{*\,i}_{j}\,-(\tilde{A}^{*i}\,\bar{Q}^{i})_{j}\}$$

$$- \frac{\Delta\xi}{2\,\Delta\eta}\,\{(\,\tilde{B}^{*i}\,\bar{Q}^{i})_{j+1} - (\tilde{B}^{*i}\,\bar{Q}^{i})_{j-1}$$

$$+ b^{i+1}_{j+1/2}\,(p^{i,n}_{j+1} - p^{i,n}_{j}) + b^{i+1}_{j-1/2}\,(p^{i,n}_{j} - p^{i,n}_{j-1})\}$$

$$+ \frac{1}{4}\,a^{i+1}_{j+1/2}\;\frac{\Delta\xi}{\Delta t}\,\{(p^{i,n+1/2} - p^{i+1,n})_{j+1} + (p^{i,n+1/2} - p^{i+1,n})_{j}\}$$

$$+ \frac{1}{4}\,a^{i+1}_{j-1/2}\;\frac{\Delta\xi}{\Delta t}\,\{(p^{i,n+1/2} - p^{i+1,n})_{j} + (p^{i,n+1/2} - p^{i+1,n})_{j-1}\}$$

$$- \frac{1}{4}\,[a^{i+1}_{j+1/2}\,(\Delta^{i+1}\,p^{n}_{j+1} + \Delta^{i+1}\,p^{n}_{j}) + a^{i+1}_{j-1/2}\,(\Delta^{i+1}\,p^{n}_{j} + \Delta^{i+1}\,p^{n}_{j-1})]$$

(3.30)

The discretization of the viscous terms in Eq. (3.27), for example, $\partial(\tilde{B}_v^i \Delta^i \bar{Q})/\partial\eta$, is considered next. The viscous flux vector F_v and the Jacobian matrix $\tilde{B}_v$ can be given as follows:

$$F_v = \frac{\mu}{J\,Re} \begin{bmatrix} 0 \\ \ell_1 u_\eta + \ell_3 v_\eta \\ \ell_3 u_\eta + \ell_2 v_\eta \\ \ell_1 uu_\eta + \ell_2 vv_\eta + \ell_3 (uv)_\eta \\ + \ell_4 \left(e_t - \frac{u^2+v^2}{2}\right)_\eta \end{bmatrix} \qquad (3.31\ a)$$

$$\tilde{B}_v = \frac{\mu}{J\,Re} \left[\begin{array}{c|c|c|c} 0 & 0 & 0 & 0 \\ \hline -\ell_1 \left(\frac{u}{\rho}\right)_\eta - \ell_3 \left(\frac{v}{\rho}\right)_\eta & \ell_1 \left(\frac{1}{\rho}\right)_\eta & \ell_3 \left(\frac{1}{\rho}\right)_\eta & 0 \\ \hline -\ell_3 \left(\frac{u}{\rho}\right)_\eta - \ell_2 \left(\frac{v}{\rho}\right)_\eta & \ell_3 \left(\frac{1}{\rho}\right)_\eta & \ell_2 \left(\frac{1}{\rho}\right)_\eta & 0 \\ \hline \begin{array}{l} -\ell_1 \left(\frac{u^2}{\rho}\right)_\eta \\ -\ell_2 \left(\frac{v^2}{\rho}\right)_\eta \\ -2\ell_3 \left(\frac{uv}{\rho}\right)_\eta \\ -\ell_4 \left(\frac{\bar{e}}{\rho}\right)_\eta \end{array} & \begin{array}{l} (\ell_1-\ell_4) \left(\frac{u}{\rho}\right)_\eta \\ +\ell_3 \left(\frac{v}{\rho}\right)_\eta \end{array} & \begin{array}{l} \ell_3 \left(\frac{u}{\rho}\right)_\eta \\ +(\ell_2-\ell_4) \left(\frac{v}{\rho}\right)_\eta \end{array} & \ell_4 \left(\frac{1}{\rho}\right)_\eta \end{array}\right]$$

where

$$\bar{e} = e_t - (u^2+v^2),$$

$$\ell_1 = \frac{4}{3}\eta_x^2 + \eta_y^2 \quad ,$$

$$\ell_2 = \eta_x^2 + \frac{4}{3}\eta_y^2 \quad ,$$

$$\ell_3 = (\eta_x\ \eta_y)/3 \quad ,$$

and

$$\ell_4 = \frac{\gamma}{Pr}\ (\eta_x^2 + \eta_y^2) \quad . \qquad (3.31\ b\text{-}g)$$

It should be mentioned that when the term $(\tilde{B}_v\ \Delta\bar{Q})$ is formed, the $\Delta\bar{Q}$ term should be contained in the η-derivatives appearing in Eq. (3.31 b). A typical term of this product can be expressed as $[\alpha\ \frac{\partial(\beta\ \delta)}{\partial\eta}\ ]$. For example, for the element corresponding to the (2,2) location of $(\tilde{B}_v\ \Delta\bar{Q})$, $\alpha = \ell_1$, $\beta = \frac{1}{\rho}$ and $\delta = \Delta(\rho v)$. The discretization of a typical term $\frac{\partial}{\partial\eta}\ \{\alpha\ \frac{\partial}{\partial\eta}\ (\beta\ \delta)\}$ is performed by evaluating the quantity in brackets at two successive mesh mid-points, such as (j+1/2) and (j-1/2), and forming a difference expression at the mesh point j to obtain a second-order accurate representation for this term. This is outlined below.

$$\frac{\partial}{\partial\eta}\ \{\alpha\ \frac{\partial}{\partial\eta}\ (\beta\ \delta)\}_j = \frac{1}{\Delta\eta}\ \{(\alpha\ \frac{\partial}{\partial\eta}\ (\beta\ \delta))_{j+1/2} - (\alpha\ \frac{\partial}{\partial\eta}\ (\beta\ \delta))_{j-1/2}\}$$

where

$$(\alpha\ \frac{\partial}{\partial\eta}\ (\beta\ \delta))_{j+1/2} = \frac{1}{\Delta\eta}\ \{\alpha_{j+1/2}(\beta_{j+1}\ \delta_{j+1} - \beta_j\ \delta_j)\}$$

and

$$(\alpha\ \frac{\partial}{\partial\eta}\ (\beta\ \delta))_{j-1/2} = \frac{1}{\Delta\eta}\ \{\alpha_{j-1/2}(\beta_j\ \delta_j - \beta_{j-1}\ \delta_{j-1})\} \quad .$$

(3.32 a-c)

Using the discretization described by Eqs. (3.30) and (3.32), Eq. (3.27) can be written in a compact form as

$$A_j \, \Delta^i\bar{Q}_{j-1} + B_j \, \Delta^i\bar{Q}_j + C_j \, \Delta^i\bar{Q}_{j+1} = D_j \quad . \tag{3.33}$$

The discretization described above applies at a general interior point; the treatment of boundary points will be discussed in the next section.

Equation (3.33), written at all the mesh locations j along a line (i+1), results in a block-tridiagonal system of equations, with A_j, B_j and C_j being (4x4) matrices. This system of equations, can then be solved using L-U decomposition of the coefficient matrix of the system. The implicit solution procedure for such a system can be found in Ref. [35], by Anderson, Tannehill and Pletcher.

3.2 Details of the Solution Procedure

The solution procedure consists of two time steps. In the first step, the solution proceeds from the inflow boundary towards the outflow boundary, employing Eq. (3.25) to update $\bar{Q}$. The pressure field is updated in the second step of the procedure. This step proceeds from the outflow boundary towards the inflow boundary. The outflow boundary condition on pressure is directly employed during this step. These two steps can be expressed as follows.

Step 1: $$R^{n+1/2} = - a \left(\frac{\partial p}{\partial \xi}\right)^n_f + a \left(\frac{\partial p}{\partial t}\right)^{n+1/2} \tag{3.34 a}$$

Step 2: $$R^{n+1/2} = - a \left(\frac{\partial p}{\partial \xi}\right)_f^{n+1} + a \left(\frac{\partial p}{\partial t}\right)^{n+1} \qquad (3.34\ b)$$

where R contains all terms in Eq. (3.25) except the pressure terms which appear explicitly in the above equation. In Eq. (3.34), superscripts denote time levels. Thus, for example, the superscript (n+1/2) denotes that the time derivative is evaluated at time level (n+1/2). Backward-difference approximations are used for the time derivatives, so that the time derivative at (n+1/2) employs the pressure at time levels n and (n+1/2).

A simpler equation for the second step can be obtained by eliminating $R^{n+1/2}$ between equations (3.34 a) and (3.34 b). The resulting equation is

$$- \left(\frac{\partial p}{\partial \xi}\right)_f^n + \left(\frac{\partial p}{\partial t}\right)^{n+1/2} = - \left(\frac{\partial p}{\partial \xi}\right)_f^{n+1} + \left(\frac{\partial p}{\partial t}\right)^{n+1} \quad . \qquad (3.35)$$

The discretized form of Eq. (3.35) at station (i+1) is

$$- (p^{i+2,n} - p^{i+1,n}) + \frac{\Delta\xi}{\Delta t} (p^{i+1,n+1/2} - p^{i+1,n})$$

$$= - (p^{i+2,n+1} - p^{i+1,n+1}) + \frac{\Delta\xi}{\Delta t} (p^{i+1,n+1} - p^{i+1,n+1/2}) \quad . \qquad (3.36)$$

From this equation, $p^{i+1,n+1}$ can be solved for in an explicit manner as

$$p^{i+1,n+1} = [p^{i+1,n} - p^{i+2,n} + p^{i+2,n+1} + \frac{\Delta\xi}{\Delta t} (2p^{i+1,n+1/2} - p^{i+1,n})] \Big/ \left(1 + \frac{\Delta\xi}{\Delta t}\right) \qquad (3.37)$$

Equation (3.37) is applied along lines of constant n and the pressure field is updated by marching upstream. The prescribed condition on the pressure at the outflow boundary is imposed via the

$p^{i+2,n+1}$ term in Eq. (3.37). The two steps described above constitute one global iteration, during which the flow solution is advanced from the time level n to time level (n+1).

If the pressure terms are retained in the SCL form, then the equation for the upstream marching step, corresponding to Eq. (3.35), will be a set of two equations in the single variable p. This system can be reduced to an equation similar to Eq. (3.35) by combining the two equations after multiplying each of them by the appropriate metrics. This is equivalent to taking a projection of the two equations along a line of constant η.

3.3 Updating of Velocity Profile at the Inflow Boundary

The reference velocity, U_{avg}, characterizing the velocity profile at the inlet, needs to be updated before the next global iteration is performed. This is necessary because at the inflow boundary the total pressure and temperature are prescribed as boundary conditions, so that U_{avg} has to be guessed to initiate the solution procedure. The updating of U_{avg} is as follows. At the inflow boundary, knowing the dimensional total pressure p_0^* and the dimensional static pressure p^* (which is evaluated through the upstream marching step), the local Mach number M can be obtained using the isentropic relation

$$\frac{p_0^*}{p^*} = \left(1 + \frac{\gamma-1}{2} M^2\right)^{\gamma/\gamma-1} \quad . \qquad (3.38\ a)$$

Then, using the dimensional total temperature T_0^* prescribed at the inflow boundary, the static temperature T^* can be obtained from the following relation

$$\frac{T_0^*}{T^*} = \left(1 + \frac{\gamma-1}{2} M^2\right) \quad . \tag{3.38 b}$$

The dimensional density ρ^* can then be found, using the equation of state, as

$$\rho^* = p^* / R\, T^* \quad . \tag{3.38 c}$$

Knowing M^2 and T^*, together with the definition of the local sonic velocity, the local dimensional speed V^* $(= \{u^{*2} + v^{*2}\}^{1/2})$, can be determined from the relation

$$V^{*2} = M^2\, \gamma R T^* \quad . \tag{3.38 d}$$

The Cartesian components of the velocity u^* and v^* can be determined from the given flow direction, θ, at the inlet so that

$$u^* = \{V^2 / (1+\tan^2\theta)\}^{1/2} \tag{3.38 e}$$

and

$$v^* = u^* \tan\theta \quad . \tag{3.38 f}$$

The reference velocity U_{avg} is then obtained using Eq. (2.6) and all the variables are then re-nondimensionalized.

3.4 Convergence Criteria

The two steps of the solution procedure described in Section 3.2 are repeated until convergence is achieved. To test for convergence, the maximum absolute value of the error (L_∞-norm) and the root-mean square of the relative error (L_2-norm) in the pressure field are monitored. These are defined, respectively, as

$$\varepsilon_{abs} = \max_{\substack{i=1,IMAX \\ j=1,JMAX}} \left| p_j^{i,n+1} - p_j^{i,n} \right|$$

and $$\varepsilon_{rel} = \left\{ \sum_{j=1}^{JMAX} \sum_{i=1}^{IMAX} \left(1 - \frac{p_j^{i,n}}{p_j^{i,n+1}}\right)^2 \right\}^{1/2} / (\Delta t \; IMAX \; JMAX) \qquad (3.39\ a,b)$$

Convergence is said to have been achieved when $\varepsilon_{abs} \leq 10^{-4}$ and $\varepsilon_{rel} \leq 10^{-6}$.

3.5 Implementation of the Boundary Conditions along η = Constant Boundaries

In the present study, the boundary conditions at the walls and, in the case of cascade flows, along the wake boundaries are implemented in an implicit manner, consistent with the numerical procedure employed in the interior of the computational domain. The implicit treatment of these boundary conditions in an otherwise already implicit solution procedure removes the mesh spacing constraints encountered in an explicit scheme and also aids in enhancing the convergence process.

3.5.1 Wall Boundary Condition

As mentioned in Section 2.4.2, the zero-slip and zero suction/injection conditions at the wall, together with the wall temperature, are specified. These are written as

$$u = u_w = 0,$$

$$v = v_w = 0$$

and $$T = T_w \quad . \qquad (3.40\ a\text{-}c)$$

Expressed in terms of the increments in the variable $\bar{Q} = (\rho, \rho u, \rho v, \rho e_t)^T$, Eq. (3.40) yields

$$- u^{i+1}\ \Delta^i\rho + \Delta^i(\rho u) = \rho^i\ \Delta^i u \quad ,$$

$$- v^{i+1}\ \Delta^i\rho + \Delta^i(\rho v) = \rho^i\ \Delta^i v$$

and $$- e_t^{i+1}\ \Delta^i\rho + \Delta^i(\rho e_t) = \rho^i\ \Delta^i e_t \quad . \qquad (3.41\ a\text{-}c)$$

In the above equation, all quantities with superscript (i+1) are known from the conditions given by Eq. (3.40) and the right-hand side of Eq. (3.41) can be evaluated using the known solution vector $\bar{Q}^i$ at station i. The three equations given by Eq. (3.41), together with either the continuity equation or the reduced y-momentum equation, constitute the four equations at the wall boundaries.

3.5.2 Periodicity Boundary Condition for Cascades

For flows through cascades employing a 'line-periodic' grid, the periodicity boundary condition can be imposed in an implicit manner. The periodicity condition, as described in Section 2.4.3, requires that

the flow variables have the same values at corresponding periodic points along the wake boundaries. When this condition is imposed, the discretized equation (3.33) assumes the following form.

At j=1,

$$A_1 \, \Delta^i\bar{Q}_{JMAX-1} + B_1 \, \Delta^i\bar{Q}_1 + C_1 \, \Delta^i\bar{Q}_2 = D_1 \tag{3.42}$$

and, at j=JMAX-1,

$$A_{JMAX-1} \, \Delta^i\bar{Q}_{JMAX-2} + B_{JMAX-1} \, \Delta^i\bar{Q}_{JMAX-1} + C_{JMAX-1} \, \Delta^i\bar{Q}_1 = D_{JMAX-1} \tag{3.43}$$

Here, JMAX is the index corresponding to the maximum value of η. Equations (3.42) and (3.43), together with Eq. (3.33) written at each interior normal mesh point j=2 through JMAX-2, form a system of equations which is basically a tridiagonal system, except for non-zero corner elements. The corresponding coefficient matrix is shown below.

$$\begin{bmatrix} B_1 & C_1 & 0 & & 0 & A_1 \\ A_2 & B_2 & C_2 & & 0 & 0 \\ \cdot & \cdot & \cdot & & \cdot & \cdot \\ \cdot & \cdot & \cdot & & \cdot & \cdot \\ 0 & 0 & 0 & A_{JMAX-2} & B_{JMAX-2} & C_{JMAX-2} \\ C_{JMAX-1} & 0 & & & A_{JMAX-1} & B_{JMAX-1} \end{bmatrix} \begin{bmatrix} \Delta\bar{Q}_1 \\ \Delta\bar{Q}_2 \\ \cdot \\ \cdot \\ \Delta\bar{Q}_{JMAX-2} \\ \Delta\bar{Q}_{JMAX-1} \end{bmatrix} = \begin{bmatrix} D_1 \\ D_2 \\ \cdot \\ \cdot \\ D_{JMAX-2} \\ D_{JMAX-1} \end{bmatrix} \tag{3.44}$$

Here, A, B and C are (4x4) blocks, while $\Delta\bar{Q}$ annd D are (4x1) blocks. The procedure for solving the above periodic block tridiagonal system in an implicit (non-iterative) manner is detailed in Appendix A.

3.6 Separated Flow Modeling

In this section, the approximations involved in obtaining the governing equations in separated flow regions are described. It is known that forward marching in space with the parabolized Navier-Stokes equations in regions of reversed flow, that is, where the tangential contravariant velocity component U is negative, is unstable. This instability can be overcome if all the equations are forward differenced in the regions of reverse flow. This requires that, in addition to the pressure, the preceding iterate of the solution vector $\bar{Q}$ be stored in these regions .

Reyhner and Flügge-Lotz [36] have suggested a simple alternative to this situation. They suggested that, in the reverse-flow region, the convective term $u\,\partial u/\partial x$ in the momentum equation be represented by $C\,|u|\,\partial u/\partial x$, where C is zero or a small positive constant. This representation, known as the FLARE approximation, assumes that the convective terms are small in regions of reverse flow and is valid when the reverse flow velocities are small. This approximation is employed in the present study also, by neglecting all the convective terms in the momentum and energy equations in the reverse-flow region. Hence, in

regions of reverse flow, the governing equations take the following form.

When $U = (\xi_x\, u + \xi_y\, v) < 0$,

$$\frac{\partial E}{\partial \xi} + \frac{\partial F}{\partial \eta} = \frac{\partial}{\partial \eta}\,(F_v) \tag{3.45}$$

where

$$E = \frac{1}{J}\begin{bmatrix} \rho U \\ \xi_x\, p \\ \xi_y\, p \\ 0 \end{bmatrix}, \qquad F = \frac{1}{J}\begin{bmatrix} \rho V \\ \eta_x\, p \\ \eta_y\, p \\ 0 \end{bmatrix}$$

and F_v is as described earlier in Eq. (2.15).

3.7 Discretization of Metric Terms

The numerical representation of the metric coefficients arising due to a general coordinate transformation from the physical domain to a computational domain, given by Eq. (2.10), is described in this section. The metric coefficients, such as ξ_x, ξ_y etc., are obtained from the derivatives x_η, y_η, etc., using the relation given by Eq. (2.13).

The discretization of the metric derivatives should be done in a manner consistent with the discretization of the governing equations. Hindman [37] has shown the appropriate representation of the metrics for solving a 1-dimensional wave equation, using MacCormack's scheme and various forms of the governing equation, such as the strong-conservation-law (SCL) form, the weak-conservation-law (WCL) form, etc.

In his work, he employed a simple test of reproducing uniform flow, starting with the entire computational mesh initialized with a uniform flow and advancing in time, employing a selected numerical integration algorithm. In the present study a similar test is performed to determine the appropriate representation of the metric derivatives and is detailed in Appendix B. As shown in the Appendix B, representation of the transformed equations in the SCL form requires the following relation

$$\frac{\partial}{\partial \xi}\left(\frac{\xi_x}{J}\right) + \frac{\partial}{\partial \eta}\left(\frac{\eta_x}{J}\right) = 0$$

and

$$\frac{\partial}{\partial \xi}\left(\frac{\xi_y}{J}\right) + \frac{\partial}{\partial \eta}\left(\frac{\eta_y}{J}\right) = 0 \quad .$$

be satisfied in the discretized form. This implies that the discretized representation of the η derivative in y_η $\left(= \frac{\xi_x}{J}\right)$ should be the same as that employed for the η-derivative in $\frac{\partial}{\partial \eta}(y_\xi)$; also, the ξ-derivatives are to be discretized in a similar manner. The results are summarized here.

At an interior point (i,j), the coordinate derivatives take the following form.

$$x_\eta\big|_{i,j} = (x_{i,j+1} - x_{i,j-1})/2\Delta\eta \quad ,$$

$$y_\eta\big|_{i,j} = (y_{i,j+1} - y_{i,j-1})/2\Delta\eta \quad ,$$

$$x_\xi\big|_{i,j} = \frac{1}{4\Delta\xi}\left[(x_{i,j+1} - x_{i-1,j+1}) + (x_{i,j-1} - x_{i-1,j-1})\right] + \frac{1}{2\Delta\xi}(x_{i,j} - x_{i-1,j})$$

and

$$y_\xi\big|_{i,j} = \frac{1}{4\Delta\xi}\left[(y_{i,j+1} - y_{i-1,j+1}) + (y_{i,j-1} - y_{i-1,j-1})\right] + \frac{1}{2\Delta\xi}(y_{i,j} - y_{i-1,j}) \quad . \qquad (3.46\ a\text{-}d)$$

From Eq. (3.46), it is clear that the η-derivatives are represented by second-order accurate central differences and the ξ-derivatives are represented as averages of first-order accurate backward differences.

At a boundary point j=JMIN or JMAX, the ξ-derivatives are represented by

$$x_\xi\big|_{i,j} = (x_{i,j} - x_{i-1,j})/\Delta\xi$$

and

$$y_\xi\big|_{i,j} = (y_{i,j} - y_{i-1,j})/\Delta\xi \quad . \qquad (3.47\ a,b)$$

The η-derivatives at these boundary points are represented as follows. At j = JMIN,

$$x_\eta\big|_{i,j} = (x_{i,j+1} - x_{i,j})/\Delta\eta \quad ,$$

$$y_\eta\big|_{i,j} = (y_{i,j+1} - y_{i,j})/\Delta\eta \quad ,$$

and at j = JMAX,

$$x_\eta\big|_{i,j} = (x_{i,j} - x_{i,j-1})/\Delta\eta \quad ,$$

$$y_\eta\big|_{i,j} = (y_{i,j} - y_{i,j-1})/\Delta\eta \quad . \qquad (3.47\ c\text{-}f)$$

CHAPTER 4

RESULTS AND DISCUSSION

The analysis developed in the present study and described in the preceding two chapters is employed to solve the flow in constricted channels and several cascade configurations. The channel configurations considered here are the straight channel, which is employed primarily to verify the analysis developed, and a channel with an exponential constriction. The latter configuration is shown in Fig. 4a; its lower boundary is represented by the relation

$$y_{b,lower} = C_1 \exp\left[-\left(\frac{x - x_m}{C_2}\right)^2\right] \qquad (4.1)$$

where the subscript b denotes the boundary, x_m is the x location where the maximum constriction is situated and C_1 and C_2 are constants controlling the maximum height and the extent of the constriction, respectively. The equation for the upper wall of the channel is written as

$$y_{b,upper} = 1 - y_{b,lower} \quad . \qquad (4.2)$$

The cascade configurations considered in the present study are the flat-plate cascade and cascades with exponential, parabolic and Joukowski airfoils. These configurations are shown in Figs. 4b-e. The exponential airfoils are obtained using Eq. (4.1) for $x_{LE} \leq x \leq x_{TE}$, where x_{LE} and x_{TE} correspond to the x locations of the leading and trailing edges, respectively.

The parabolic arc airfoil is generated by the following equation:

$$y = C_1 + C_2 (x - x_m)^2 \quad , \quad x_{TE} \leq x \leq x_{LE} \quad . \tag{4.3}$$

The Joukowski airfoil is generated by the following transformation.

$$z = \zeta + \frac{C_3^2}{\zeta}$$

where

$$z = x + iy$$

and $$\zeta = C_4 e^{i\theta} + C_5 \quad . \tag{4.3 a-c}$$

Here, C_3 and C_4 are real constants and C_5 is a complex constant. The parameters C_3 and C_5 control the maximum thickness and the camber of the airfoil. As only symmetric airfoils are considered in the present study, C_5 is real.

The results presented in this chapter have been obtained employing a H-grid or a channel-type of grid. A simple H-grid is the sheared Cartesian grid in which $\xi = \xi(x)$ and $\eta = \eta(x,y)$.

4.1 Resolution of Spatial Length Scales

In viscous flows, the flow variables vary rapidly near the walls. To resolve these high gradients, a fine computational mesh is required near these boundaries. A non-uniform mesh is most suitable as it can provide a fine mesh in regions of high gradients without unduly increasing the total number of mesh points.

The scalings obtained from the asymptotic analysis of Stewartson [38] indicate the order of resolution required for strong-interaction problems. Accordingly, streamwise mesh spacings should be of the order

of magnitude of $Re^{-3/8}$ and normal mesh spacings should be of the order of magnitude of $Re^{-5/8}$. In the grids employed in the present calculations, at least five computational points are maintained within these length scales in regions of separation and near the trailing edges for cascade flows. The coordinate transformations employed to meet these mesh requirements are discussed next.

In the streamwise direction, variable mesh spacing Δx_i is obtained using a geometric series for Δx_i and the resulting transformation can be written in a parametric form as follows:

$$x_i = \Delta x_1 \frac{(r^{i-1} - 1)}{(r - 1)} \quad ,$$

$$\xi_i = (i-1)\,\Delta\xi \quad , \quad i = 1, \ldots, \mathrm{ILE} \quad . \tag{4.5}$$

Here, r is the stretching ratio, Δx_1 the mesh spacing at the inflow boundary, $\Delta\xi$ the uniform computational mesh spacing and ILE is the streamwise index corresponding to the leading edge location. Equation (4.5) is used with different values of r in various regions such as the airfoil surface and the wake, in order to obtain the required physical mesh spacings.

In the η-direction, the following analytical transformation is employed:

$$\eta = b + a \tan \frac{(y-b)}{c} \quad . \tag{4.6}$$

The parameters a and c in Eq. (4.6) provide control over the grid-point distribution. The constants a, b and c are obtained from the following conditions.

At $y = y_{b,\ lower}$: $\eta = \eta_{min}$ and $\eta_y = S$, a prescribed value.

At $y = y_{b,\ upper}$: $\eta = \eta_{max}$. (4.7)

The slope S controls the spacing near the boundaries. The transformation given by Eq. (4.6) is used to provide identical clustering near both boundaries, given by $y = y_{b,\ lower}$ and $y = y_{b,\ upper}$. Hence, b = 0.5.

A typical grid is shown in Fig. 5. Here, the grid clustering in both the streamwise and normal directions has been reduced to improve clarity of the presentation of the coordinate lines in the figure.

4.2 Results for Flow in a Straight Channel - Validation Study

The analysis and the numerical procedure developed in the present research are first tested via a model problem of flow in a straight channel. For this purpose, a fully developed flow profile was prescribed at the inlet boundary and the pressure field was initialized so as to yield the known streamwise pressure gradient for a fully developed incompressible channel flow. This streamwise pressure gradient is given as

$$p_x = \frac{12}{Re} \quad . \tag{4.8}$$

The velocity and the temperature profiles at the inlet were obtained not from their known analytical expressions but by numerical solution of the governing equations for fully developed flow. This ensures that, if the algorithm is formulated in a consistent manner, the application of the procedure should recover the a fully developed flow throughout the entire channel.

This testing procedure was applied to the straight-channel configuration with metrics varying in the streamwise direction. From this study, it was found that the metric terms ξ_x and ξ_y, which are associated with the streamwise pressure-gradient term $p_{\xi,f}$, should be forward differenced. Also, it was found necessary that the streamwise pressure-gradient term should no longer be in the SCL form. The proper form of the pressure-gradient terms should be as given in Eq. (3.21) in Chapter 3.

4.3 Results for Channels with Exponential Constriction

The geometry of this channel is represented by Eq. (4.1) and is shown in Fig 4a. Results are obtained for three values of the ratio t/h of the maximum constriction to the channel width, viz., 0.1, 0.16 and 0.2, for Re = 1500. The Reynolds number is based on the average velocity and channel height at the inlet station. As mentioned in Section 2.4.1, the inflow boundary conditions correspond to a fully developed flow in a straight channel.

Figure 6a shows the distributions of the wall-pressure variable p_b and the wall shear parameter τ_w for the case of t/h = 0.1. The wall-pressure variable p_b is defined as the difference between the pressure at the wall at a streamwise location i and that at the inlet boundary and can be written as

$$p_b = p_{w,\ inlet} - p_{w,\ i} \quad . \tag{4.9 a}$$

The wall shear parameter is defined as

$$\tau_w = \left.\frac{\partial U_{tgt}}{\partial n}\right|_{wall} \qquad (4.9\ b)$$

where U_{tgt} is the velocity tangential to the body surface and n is the direction normal to the body. From Fig. 6a(i and ii), it is clear that p_b varies linearly in the straight portion of the channel and behaves approximately similar to the body surface shape in the region of the constriction. From Fig. 6a(i), the pressure loss Δp across the constriction can be obtained to be 0.00875. From figures 6a(iii and iv), it can be seen that, far upstream and downstream of the constriction, τ_w is asymptotic to the value of 6, corresponding to a fully developed flow. The tendency of the flow to separate downstream of the constriction is indicated by the wall shear parameter approaching the value of zero. The grid employed for this case consists of (141 x 61) points. The value of Δx_{min} is 0.008 which occurs at locations upstream and downstream of the maximum constriction where the flow is anticipated to separate. The minimum mesh step Δy_{min} employed in the y direction in the straight portion of the channel is 5.7×10^{-3}.

Figures 6b and 6c show the wall pressure and the shear-parameter distribution for t/h of 0.16 and 0.2. From Fig. 6b(i), the pressure loss across the constriction can be obtained as 0.02, approximately. It is clear that the flow has separated downstream of the constriction, as indicated by the negative values of τ_w in Fig. 6b(iv). The results corresponding to the case of t/h = 0.2 are shown in Fig. 6c. Comparison

of Figs. 6b and 6c shows that the extent of separated region increases as t/h is increased from 0.16 to 0.2.

The pressure loss across the constriction, some information about the grid and the location of the inflow and outflow boundaries with respect to the constriction are shown in Table 1 for the three cases discussed above. One of the important factors in obtaining the above results is the appropriate location of the inflow and outflow boundaries with respect to the maximum-constriction location. These locations are obtained by numerical experimentation, so as to ensure that the flow near these boundaries is nearly fully-developed. Accordingly, as shown in Table 1, for the case of t/h = 0.1, the inflow boundary should be located at least 5 channel heights upstream of the maximum constriction and the outflow boundary at least 18 channel heights downstream of the position of the maxiimum constriction. Moreover, these boundaries must be moved further away from the position of the maximum constriction as the ratio t/h increases. It is also observed that the pressure loss across the constriction increases with increase in t/h.

Figure 7 shows the streamwise velocity profiles across the channel at various streamwise locations for the case with t/h = 0.2. From the enlarged-scale profiles shown in Fig. 7b, a small region of reverse flow can be observed.

Through this study of the flow in constricted channels, the analysis has been tested for a variable cross-section channel and for separated flows. The regular behaviour of the flow solution in the

presence of separation establishes that the IPNs formulation includes the appropriate strong upstream interactions occurring in this flow.

4.4 Results for Flat-Plate Cascades

The configuration for this cascade geometry is shown in Fig. 4b. The primary purpose of examining these flows was to test the implicit implementation of the periodicity boundary condition for cascade flows and to test the validity of the IPNS formulation in the strong-interaction flows around sharp (cusped) leading and trailing edges. Results are obtained for various values of Re ranging from 1500 to 16,000 and are shown in Fig. 8a-e. All of these results are obtained employing a grid containing (186 x 71) points. The point distribution is such that Δx_{LE} is 0.01 and Δx_{TE} is approximately 0.005. The step size in the y-direction at the wall is 1.225×10^{-3}. As mentioned in Section 2.4.1, the inflow boundary conditions for this configuration, consist of the specified values of total pressure and total temperature, while static pressure is prescribed at the outflow boundary.

Figure 8a(i) shows the distribution of the pressure p_b and the wake-centerline velocity. The corresponding behaviour of p_w is inferred easily through Eq. (4.9 a). As the leading edge is approached, the pressure p_w rises to its maximum value and drops rapidly immediately downstream thereof. There is a gradual pressure drop in the flat-plate region, until the trailing edge, where a sharp drop occurs. Thereafter, the pressure rises smoothly to approach the prescribed value at the

outflow boundary. The wake-centerline velocity shows a smooth streamwise variation and is asymptotic to a value of unity near the outflow boundary. The wall shear, shown in Fig. 8a(iv), attains a maximum at the leading edge in an almost singular manner while exhibiting a small peak near the trailing edge of the cascade. The behaviour near the trailing edge is due to the sudden change in the boundary condition. Along the wall, the velocity component u was prescribed to be zero and along the wake centerline, u_y is zero. Hence, there is a discontinuity in u_y, which is the primary contributor to the wall shear parameter. Through all this nonlinear behaviour, including that due to the sudden changes in boundary conditions at the leading and trailing edges, the solution is quite regular, confirming again that upstream influence is appropriately included in the IPNS model. Qualitatively, similar behaviour is observed for Re = 3100 to 16,000, as shown in Figs. 8b-e.

Figures 9a and b show the distribution of p_b and τ_w for various Reynolds numbers. With increase in Re, the peak in p_b at the trailing edge decreases, whereas that in τ_w increases.

4.5 Results for Cascades of Exponential Airfoils

The exponential airfoil cascade geometry is as shown in Fig. 4c. The computational grid, the point distribution and, hence, the mesh sizes employed are the same as for the flat-plate cascade configuration discussed in the previous section.

4.5.1 Effect of Thickness

Figure 10a-c shows the distributions of p_b and τ_w for an exponential airfoil cascade for Re = 1500 and thickness ratios (t/c) of 0.05, 0.075 and 0.1. Near the leading and trailing edges, the behaviour of pressure is similar to that for the cascade of finite flat plates. In the region of the airfoils, as the overall flow accelerates up to the maximum thickness location, the pressure falls to a minimum, while the shear parameter increases to a local maximum. The pressure and wall-shear parameter distributions for various values of t/c are shown in Figs. 11a and b, respectively. Superimposed on these figures are the corresponding flat-plate cascade results, i.e., the case of t/c =0. From Fig. 11a, it is clear that the maximum p_b increases with increase in t/c, while the peak at the trailing edge diminishes. The value of τ_w at the maximum-thickness location also increases with increase in t/c. The tendency for the flow to separate downstream of the maximum-thickness increases with increase in t/c. This can also be inferred from the pressure gradient, which becomes increasingly adverse in this region as t/c is increased. Also, the extent and intensity of the separated region are reduced, in comparison with the corresponding channel flow. This is because of the upstream influence of the higher velocity of the fluid downstream of the TE as compared to that of the fluid downstream of the constriction in the channel with zero slip at the walls.

4.5.2 Effect of Reynolds Number

Results for various values of Re between 3100 and 15,000 are shown in Fig. 12a-d. The qualitative behaviour of the flow properties examined for this range of Re is similar to that for Re = 1500, discussed in the previous section. Figure 13 shows the effect of Re on the pressure and wall-shear distribution. From Fig. 13a, it can be seen that the magnitude of p_b at the maximum-thickness location decreases with increase in Re. The pressure peak near the trailing edge also diminishes with increase in Re. It can also be seen that the pressure gradient downstream of the maximum thickness becomes increasingly adverse with increase in Re. A similar behavior in pressure can be seen, to a smaller degree, upstream of the maximum thickness. The possibility of flow separation in these adverse pressure-gradient regions is evident from the distribution of τ_w shown in Fig. 13b. In fact, for the case of Re = 15,000, a small separated region is present, as indicated by the negative values of τ_w. It is also evident that the separation region is centered around a point situated downstream of the maximum-thickess position and upstream of the trailing edge, i.e., as Re is increased, the separated region extends in both directions about this point. The analyses of H.K. Cheng and F.T. Smith [39] and Smith, Stewartson and Kaups [40] show similar results around a cusped trailing edge.

4.5.3 Effect of Grid Refinement

The effect of grid refinement is important in order to establish the reliability of the solutions obtained, especially when there are no experimental results with which to compare. Therefore, in the present study, the streamwise grid is refined in the region downstream of the maximum-thickness location, in order to study its effect on the separated region. For all the cases discussed in the previous section, the streamwise step Δx_t (i.e., Δx near the maximum-thickness location) was approximately 0.045 and the streamwise step size decreased gradually to a value of 0.005 near the trailing edge. In the grid-refinement study, a finer streamwise grid in this region was obtained by ensuring that $\Delta x_t = 0.025$ and $\Delta x_{TE} = 0.005$, and employing a computational grid consisting of (191 x 71) points.

A comparison of the results obtained employing the two grids, for Re = 1500 and 15,000, are shown in Figs. 14a and 14b, respectively. The wall-shear distribution agrees well and, in the case of Re = 15,000, the extent of the separated region remains almost the same, as seen from Fig. 14b(ii). Grid refinement has a slightly more significant effect on the pressure distribution, particularly for the case of Re = 15,000. In that case, the peak near the trailing edge diminished with grid refinement.

4.6 Results for Cascades of Parabolic-Arc Airfoils

A schematic of this cascade configuration is shown in Fig. 4d. All the results discussed in this section are obtained employing a grid

consisting of (186 x 71) points, with the streamwise mesh sizes near the leading and trailing edges being 0.01 and 0.005, respectively.

4.6.1 Effect of Thickness

Results in the form of the distribution of p_b and τ_w are shown in Figs. 15a-c, for t/c of 0.05, 0.075 and 0.1. Figure 15a(ii) shows the pressure distribution and the development of the wake-centerline velocity for the case of t/c = 0.05. An important difference between the pressure distribution for an airfoil with a wedge-shaped trailing edge such as the parabolic-arc airfoil and that for an airfoil with a cusped trailing edge such as the exponential airfoil, is that at the trailing edge the peak in the p_b distribution for the exponential airfoil cascade is replaced by a slope discontinuity for the parabolic-arc airfoil cascade. Also, from Fig. 15a(iv), it can be seen that the peak in the τ_w distribution at the trailing edge has diminished compared to that at a cusped trailing edge. From Fig. 16a, it is seen that p_b at the maximum-thickness location increases with increase in thickness ratio and the pressure gradient on the downstream side of maximum-thickness location becomes increasingly adverse. The wall-shear distribution exhibits a cross-over, with a small separated region near the trailing edge for the case of t/c = 0.1.

4.6.2 Effect of Reynolds Number

Figures 17a-d show the results for various Re ranging from 3100 to 15,000. From the velocity distribution in Fig. 17c(ii) and the wall-shear distribution in Fig. 17c(iv), corresponding to Re = 11000, it can be seen that a separated region exists, starting at a point upstream of the trailing edge, with the flow reattaching at a point in the wake. Further increase in Re results in the movement of both the separation and reattachment points away from the trailing edge. Therefore, for flows about wedge-shaped trailing edges, the separated region is centered at the trailing edge. This is due to the continued deceleration of the fluid up to the wedged TE whereas, for cusped trailing edges, the deceleration decreases as the fluid approaches the cusped TE. This result is also supported by the analysis of Cheng and Smith [39]. Comparison of the pressure and wall-shear distributions for the various values of Re discussed above is shown in Fig. 18.

4.6.3 Effect of Mach Number

In all of the results discussed so far, M_∞ was approximately 0.008. Results have also been obtained for Mach number ranging from 0.035 to 0.49 and are shown in Figs. 19a-c. All of these results are obtained for Re = 15,000. Figure 20a shows that the effect of compressibility, resulting from the increase in M_∞, becomes apparent on the wall-pressure distribution only for the case with $M_\infty = 0.49$. But the wall-shear distribution as well as the extent of separation remain almost unchanged

for all Mach number values considered. This result is due to the fact that the strong trailing-edge singularity overwhelms the effects due to the Mach number change, in the range considered. Figure 21 shows the contours of the static pressure p, for M = 0.49 and Re = 15,000.

4.6.4 Effect of Grid Refinement

In order to ensure the accuracy of the behaviour of the flow near the wedge-shaped trailing edges discussed above, it was considered necessary to refine the grid in this region. Hence, results were obtained employing a grid consisting of 231 points in the streamwise direction, so that the $\Delta x_{TE} \approx 0.001$. Results obtained using this grid are compared with those obtained with the grid of (186 x 71) points as discussed above, for Re = 3100 and 11,000, and are shown in Figs. 22a and 22b, respectively. The shear parameter τ_w remains unaffected by this grid refinement for the two values of Re considered here. Although there is a slight shift in the level of the pressure as a result of refining the grid, the behaviour near the trailing edge remains unchanged.

4.7 Results for Cascades of Joukowski Airfoils (Modified Leading Edge)

The cascade configurations considered in the previous sections were made up of airfoils with either cusped or wedge-shaped leading edges. The procedure developed in the present study was applied next to cascade passages with rounded leading edge blades such as the Joukowski airfoil, for which a typical configuration is shown in Fig. 1. This

configuration presented some difficulties to the numerical solution in the leading-edge region. These difficulties were traced back to the use of the sheared Cartesian grid for these cascades. It was observed that this type of grid exhibits a large discontinuity in the coordinate-transformation metrics at the leading edge. Hence, the leading-edge region was modified by replacing it with a wedge, as shown in Fig. 4e. Results have been obtained successfully for the modified configuration, even with the sheared Cartesian grid, for Re = 150 and 310, and are shown in Figs. 23a and 23b. The computational grid employed consists of (121 x 61) points and the value of the ratio t/c for the airfoil is 0.068.

Figures 23a(i) and 23b(i) show the p_b distribution and the development of streamwise velocity along the wake, for Re =150 and 310, respectively. It is evident that, as Re is increased, the peak in the p_b distribution near the trailing edge diminishes, as would be expected for flows over cusped trailing edges and as observed for the exponential-airfoil cascade. The wall-shear distribution, shown in Figs. 23a(ii) and 23b(ii), has a slope discontinuity near the maximum-thickness location. This is primarily a reflection of the discontinuity of the slope of the body surface where it changes from the wedge to the Joukowski-airfoil profile.

The difficulty in resolving the flow near the rounded trailing edges with an H-type grid arises mainly due to the orientation of the grid in this region. To circumvent this problem, a body-oriented grid such as a C-grid is more appropriate for rounded leading-edge blades and

should be employed. Therefore, a major effort was directed, in the present study, to develop a hybrid C-H grid which judiciously employs both C- and H-grids, thereby benefiting from the advantages of both of these types of grids. The generation and implementation of the C-H grid for a cascade of airfoils with rounded leading edges is discussed in the next two chapters.

4.8 Convergence Study

A typical convergence history of the solution is shown in Fig. 24 in terms of the maximum absolute error and the relative r.m.s. error in pressure, for the case of the parabolic-arc airfoil of thickness ratio 0.05 and Re = 6300. From this figure, it can be seen that convergence is achieved in approximately 160 iterations. All the other cases discussed in the previous sections also required a similar number of iterations. The definition of the errors and the tolerances used in the present study are described in Section 3.4. In all the results presented thus far, 3 local iterations were performed at each streamwise location in order to update the non-linear terms. It was found that quasi-linearization about a previous streamwise location was insufficient, especially in regions of large streamwise pressure gradients, such as the leading- and trailing-edge regions. Finer streamwise steps alone cannot resolve these high gradients due to their near-singular behaviour.

In order to study the effect of the time step Δt associated with the pressure gradient term (Eq. 3.25), a simple case of the flat-plate

cascade was considered. A constant step size of $\Delta x = 0.05$ was employed for this case. The decay of the maximum absolute error and the relative r.m.s. error in pressure was studied for various values of Δt in the range between 0.03 and 0.1. The corresponding convergence histories are shown in Fig. 25. For all values of Δt used, the convergence behaviour is identical for approximately the first 20 iterations. Beyond this stage, the convergence rate increases as Δt is increased from 0.03 to 0.06 and decreases with further increase to a value of 0.1. For the value of $\Delta t = 0.06$, a total error-reduction of approximately 6 decades is achieved in 200 iterations. Hence, it is observed that the procedure is rather sensitive to the value of the time step Δt used.

The convergence behaviour for a flat-plate cascade with variable streamwise mesh size was also studied. For this case, the mesh width was varied according to Eq. (4.5). Also, Δt was varied in the streamwise direction, according to the following relation:

$$\Delta t_i = C\,(x_{i+1} - x_i) \quad . \tag{4.10}$$

Here, C is a constant and subscript i denotes the streamwise location.

Figure 26 shows the convergence history for various values of the parameter C. It is clear that for the first 40 iterations, the parameter C does not affect the convergence rate. Thereafter, an increase in C results in faster convergence rates, for the range of C considered in the present study.

Finally, a convergence study was performed for the cascade with exponential airfoils with t/c = 0.05 and Re = 1500. The grid employed for this study consisted of (191 x 71) points. Figure 27 shows the

convergence history for values of C ranging from 2 to 5. As C is increased from 2 to 4, the convergence rate improves, but further increase in C results in a slower convergence rate. It can be seen that the slope of error curve for C = 3 is steeper than that for 4 so that C = 3 may be considered as a near-optimum value. Then, with $\Delta t_i/\Delta x_i$ = 3, results were also obtained for Re = 25,000 for a cascade of exponential airfoils and are shown in Fig. 28.

CHAPTER 5

GENERATION OF HYBRID C-H GRID

5.1 Introduction

The success of a numerical method for analyzing viscous flows in complex configurations depends on the proper choice of a coordinate system. It is usually desired that these coordinates be aligned with the problem boundaries. Also, as the governing equations of motion in the present study (see Chapter 2) involve a parabolizing approximation in the streamwise direction, it is important that the coordinate system employed be body-oriented and near-orthogonal.

For the study of subsonic viscous flows around isolated airfoils, two types of grids are often used. These are the O-grids and the C-grids. For analysis of flow through cascade passages formed by airfoils, the H-grid or the channel type of grid and the C-grid configurations are commonly used. Sockol [41] and Dulikravich [42] have generated C-type of grids for cascades. A typical C-grid is shown in Fig. 29a. Steger et al. [8] have also employed C-grids for calculations of viscous and inviscid flows through turbomachinery cascades. The C-type of grids are especially suited for subsonic viscous flow calculations, as they provide good resolution near the rounded leading-edge regions of the blades. From the results described in the previous chapter for flow through a cascade of Joukowski airfoils, it is clear that the channel type or H-grid is inappropriate, particularly near the rounded leading edges. A C-type of grid is satisfactory in most regions of the cascade flows, except further upstream of the stagnation point on

the blades. In this region, the grid density decreases rapidly with increasing distance upstream of the stagnation point. A possible means of minimizing this difficulty is to employ a channel or H-grid in the upstream region. Eiseman [43] has employed Cartesian extensions to an O-type of grid for cascades, in the regions upstream of the leading edges as well as downstream of the trailing edges.

Channel grids have been widely used for cascade-flow analyses. Chima and Johnson [10] have employed the H-type of grid for solving the Euler and NS equations through a cascade of bicircular-arc airfoils. Channel grids are easy to generate and can be conveniently aligned with the inflow. Also, implementation of the periodicity boundary condition is easy for cascades with low stagger angle. In this case, a grid line emanating from a particular point on the lower boundary ends at the corresponding periodic point on the upper boundary. With this grid distribution it is also possible to impose the periodicity condition in an implicit manner (Ref. [44]). This H-grid distribution is termed 'line-periodic' and is shown in Fig. 29b. For cascade configurations with large stagger or when the blades have rounded leading edges, the line-periodic H-grid becomes highly skewed and non-orthogonal. If this H-grid is modified to minimize the non-orthogonality, the implicit imposition of periodicity has to be sacrificed. A typical modified H-grid is shown in Fig. 29c and is called a 'region-periodic' grid. In this type of grid, the point distribution along the upper and lower boundaries is periodic, but corresponding periodic points are not connected by the same coordinate line.

Therefore, a suitable grid for cascade flows is one that combines the advantages of both the C- and H-grids while minimizing their disadvantages. This results in a multi-rectangular computational domain in terms of the transformed coordinates. The multi-block structure and the generation of such a grid are described in the following sections of this chapter.

5.2 Multi-Block Structured Grids

The flow region in the physical domain can be subdivided into several sub-regions, depending on either the geometrical complexity of the configuration or the need for different types of grids in various regions, as mentioned in the previous section. These sub-regions are termed 'blocks'. Lee et al. [45] have generated a 3-D body-fitted coordinate system around a wing-body-nacelle configuration by dividing the computational domain into multiple rectangular blocks. A single rectangular block in the computational domain would be insufficient to resolve the various physical corners of this complex configuration. Multi-block structured grids have also been employed for the complex geometries of the tri-element augmentor wing by Sorenson [46] and the breaking surface wave by U. Ghia et al. [47]. Also, Coleman [48] has employed multiple segments for generating alternate grids for flow over single airfoils. The O-type of grid with Cartesian patches for a cascade generated by Eiseman [43] can also be viewed as a multi-block structured grid.

Multi-block structured grids can be broadly classified into two types. The first type consists of 'patched' or 'zonal' grids where the various blocks share a common boundary called the interface. The other type of grids consist of 'overlaid' or 'overset' grids. In this case, the various blocks do not have a common boundary. The idea of overset grids has been pursued by Steger [49] in his development of the Chimera grid, which has also been extended to three dimensions by Benek et al. [50]. A typical overset grid is shown in Fig. 30a. The solution of the flow equations employing this type of grid requires additional transfer of information across the boundaries of various grids.

Patched grids can be further classified into joint and disjoint types of grids. The disjoint patched grid is one where the family of the coordinate lines crossing the patch interface are discontinuous across the interface, as shown in Fig. 30b. In the joint type of grid, shown in Fig. 30c, the coordinate lines are continuous across the interface, although their slope may be discontinuous across the interface. These gradient discontinuities are present when the coordinates in each of the sub-regions are generated separately and patched together. Some of these discontinuities can be relieved by suitable modification of the boundary-point distribution along the interface, followed by regeneration of the coordinates in the regions affected by this redistribution. These slope discontinuities can be eliminated by generating the coordinates in all the sub-regions simultaneously, without specifying the boundary-point distributions

along the interface. The disadvantage associated with a such a procedure is that the computer program can become quite complicated, depending on the number and orientation of the blocks employed to define the complex physical configuration. The latter direct multi-block grid generation concept has been employed by U. Ghia et al. [21] and Coleman [48]. The composite grid-generation procedure developed by U. Ghia et al. [21] is employed in the present study and the details are discussed in the next two sections.

5.3 Computational Domain for Hybrid Cascade Grids

For a general staggered cascade, the physical domain can be divided into sub-regions as shown in Fig. 31. The region BCD'B' is the portion of the C-grid adjacent to the upper surface of the lower blade. The regions BIHG and E'D'EM are the channel or H-regions. The computational regions corresponding to these sub-regions are shown in Fig. 32. Points E''_c and B''_c are 'special-points' at which 5 sub-regions come together. 'Special-points' commonly occur on the domain boundary or on the interfaces between sub-regions in a multi-block grid system. These points either have a non-standard number of immediate neighbours when they are the vertices of a computational cell or have a non-standard number of faces when they are the cell-centers, as illustrated in Fig. 33.

For the ease of visualization, the multi-block structured grid in the 2-D physical plane is best represented by a 3-D surface in the

computational domain. This 3-D surface is obtained by bringing the sub-regions in Fig. 32 together, along the arrows. The subregions $BCG'B''_c$ and IBB''_cL are bent out of the plane of the paper at the special-point B". Similarly, the sub-regions HKG"G, $GG''E''_cB_1$ and $C_1B_1E''_cE'$ are bent at E". The resulting computational domain is shown in Fig. 34. For a cascade with zero stagger, the sub-regions $B_1E''_cG''G$, $G''E''_cB'B''_c$ and $B''_cB'D'G'$ are not needed. The sub-region boundaries in the physical domain for the unstaggered grid are shown in Fig. 35. The solution procedure for generating the coordinate system is discussed in the next section.

5.4 Solution Procedure

The numerical transformation procedure consists of determining the boundary-oriented coordinates as the solutions of the following Poisson equations:

$$\nabla^2 \xi = P \tag{5.1 a}$$

and

$$\nabla^2 \eta = Q \tag{5.1 b}$$

where ∇^2 is the Laplacian operator in Cartesian coordinates, (ξ, η) are the transformed surface-oriented coordinates and P and Q are the forcing functions used to provide control on the coordinate clustering and orthogonality.

The boundary conditions used for the governing equations (5.1) are of the Dirichlet type. These consist of the prescribed values of x and

y along the boundaries $\xi = \xi_{min}$ and ξ_{max} and $\eta = \eta_{min}$ and η_{max}. In order to implement these boundary conditions, the roles of the independent (x,y) and dependent (ξ,η) variables have to be interchanged. Detailed analysis of this inversion is given by U. Ghia and K. Ghia [51] and the resulting 'inverted' equations can be written as follows:

$$a\, x_{\xi\xi} + 2b\, x_{\xi\eta} + c\, x_{\eta\eta} + J^2 (P\, x_{\xi} + Q\, x_{\eta}) = 0$$

and

$$a\, y_{\xi\xi} + 2b\, y_{\xi\eta} + c\, y_{\eta\eta} + J^2 (P\, y_{\xi} + Q\, y_{\eta}) = 0$$

where $a = x_{\eta}^2 + y_{\eta}^2$,

$b = -(x_{\xi}\, x_{\eta} + y_{\xi}\, y_{\eta})$,

$c = x_{\xi}^2 + y_{\xi}^2$,

and $J = x_{\xi}\, y_{\eta} - x_{\eta}\, y_{\xi}$. (5.2)

In the present study, the alternating-direction implicit (ADI) method is employed to solve the governing equations (5.2). The computational domain for the η- and the ξ-implicit sweeps of this procedure can be obtained from Fig. 34 and are shown in Figs. 36a and 36b, respectively. In Fig. 36, points denoted by alphabets with superscript + or -, refer to the neighbouring points. It should be noted that the subregions $IL^-B_1''B^-$, HK^+G^-G'' and $G^+G''E_1''B_1^-$ are encountered twice in the η-implicit sweep and, hence, the solution in these regions at the end of this sweep is already at the (n+1) level of the ADI

procedure. Therefore, these sub-regions must be excluded from the computational domain in the ξ-implicit sweep.

The treatment of various derivative terms that appear in Eqs. (5.2) needs special considerations around the points B''_C and E''_C. In the present study, these special points are considered to be the center of a non-standard, 5-sided cell. The selection of the appropriate neighbouring points involved in the discretized form of the governing equations at the vertices of the 5-sided cells is detailed in Appendix C.

5.5 Typical Grids

Figure 37a shows the hybrid C-H grid generated for a staggered cascade using the composite procedure just described. This grid is region-periodic and consists of 1620 points. The coordinates are uniformly spaced at the inflow boundary and are clustered along the wake. Figure 37b shows a hybrid grid for an unstaggered cascade of Joukowski airfoils. This grid is line-periodic and consists of 7103 points and is employed for obtaining a flow solution also using a composite solution procedure. This procedure for calculating the flow through a cascade employing a hybrid C-H grid is discussed in the next chapter.

CHAPTER 6

DETERMINATION OF FLOW THROUGH JOUKOWSKI CASCADE USING HYBRID C-H GRID

In the preceding two chapters, the inadequacy of the H-grid or the channel type of grid to resolve the flow around rounded leading edges, was pointed out. Also, the difficulties of using C-grids for cascade flows were discussed simultaneously. The disadvantages of using these grids in certain regions of cascade flows were observed. Hence, a viable alternative grid is the hybrid C-H grid. This hybrid grid, with its associated multiple rectangular computational domain, was developed in the preceding chapter, for use with cascade-flow studies. Analysis of flow over complex geometries, using multi-block structured grids, has been performed by many researchers. Benek, Steger and Dougherty [52] have employed overset grids to obtain the solution of the Euler equations about a supercritical flapped airfoil. They observed that the solution in the transonic regime exhibited an ill-defined shock at the grid boundaries. Eberhardt and Baganoff [53] developed characterestic boundary conditions, which alleviated the above mentioned difficulty. Norton, Thompkins and Haimes [18] have employed a patched grid of the joint type, consisting of sheared grids and O-grids, and a cell-centered implicit scheme to solve the complete Navier-Stokes equations for flow in turbine cascades. Rai [19] has used a system of patched and overlaid grids and obtained the solution of the thin-layer Navier-Stokes equations for a rotor-stator combination. When such a grid is employed, the solution on one grid system at the patch boundary has to be

interpolated and the boundary condition for the other grid system should be obtained in a manner that conserves all fluxes crossing the interface boundaries. In the present study, the semi-elliptic analysis developed in Chapter 2 is employed to determine the flow through a cascade of Joukowski airfoils, using the hybrid C-H grid described in the preceding chapter. The solution procedure for the governing equations of motion on the hybrid grid is described next.

6.1 Computational Procedure

The solution procedure used with the hybrid grid is, in principle, similar to that for the H-grid and consists of two steps, as described in Section 3.2. For a hybrid C-H grid, these two steps are represented schematically in Fig. 38. The regions denoted by H1 and H2 correspond to the H-grid regions of the hybrid grid and the regions C1 and C2 correspond to the two C-regions. The first step of the solution procedure, during which the flow variables $\bar{Q}$ are updated from time level n to (n + 1/2), is denoted by a thin arrow; the second step, in which the pressure field is updated from time level (n+1/2) to (n+1), is denoted by a thick arrow. The computation proceeds from the inflow boundary of region H1, with $\bar{Q}$ being updated first in this region. The boundary conditions used at the upper and lower boundaries in this region are the periodicity conditions, described in Section 2.4.3. Next, the first step of the solution procedure is applied to region C1. In order to employ a marching type of procedure, conditions should be prescribed along a line such as AB, in Fig. 38b. The flow conditions

along AB are obtained from the solution along the corresponding periodic line E_1F_1 at the time level n. When the first step of the solution procedure is applied to region C2, the flow conditions along A_1B_1 could be obtained from the latest available solution along the line EF. But, in the present study, in order to retain symmetry, even in the transient stages of the solution procedure, the flow conditions along A_1B_1 are obtained from the solution along EF at time level n. The boundary conditions in the C regions are the no-slip condition and the prescribed temperature at the airfoil surfaces, while boundary conditions at the interface are obtained from the solution in region H1. These interface boundary conditions are discussed in a later section of this chapter. Next, the solution in region H2 is obtained by marching, knowing the solution along the outflow boundaries of region H1 and the two C regions.

The second step of the solution procedure, during which the pressure field is updated, proceeds from the outflow boundary. The outflow boundary condition on pressure is applied directly during this step. Using Eq. (3.37), the pressure field is updated from a time level (n+1/2) to (n+1) in region H2 and then in the two C regions. This step of the procedure is then continued into region H1, knowing the values of p^{n+1} along the boundaries of the C region at the C-H1 interface and the first computational line in the region H2. The flow variables at the inflow boundary are updated as discussed in Section 3.3. The two steps are repeated until convergence is achieved.

6.2 Verification via a Mathematical Model Problem

The correctness of the formulation and programming of the solution procedure on the hybrid C-H grid was checked through application to a model problem. The verification of the scheme by recovering the known solution for fully developed flow in a straight channel cannot be employed here, as the C-H hybrid grid is not appropriate for this configuration. Hence, a mathematical model problem is employed. In order to check the first step of the solution procedure, the system of governing equations, given by Eq. (3.23) is considered and can be written as

$$\frac{\partial E^*}{\partial \xi} + \frac{\partial F^*}{\partial \eta} + b\,\frac{\partial p}{\partial \eta} - \frac{\partial}{\partial \eta}\,(F_v) = -\,a\,\frac{\partial p}{\partial \xi_f} \quad . \tag{6.1}$$

The quasi-linearized form of this equation is obtained from Eq. (3.24) and is

$$\tilde{A}^{*i}\,\Delta^i\bar{Q} + \Delta\xi\left[\frac{\partial}{\partial \eta}\left\{(\tilde{B}^{*i} - \tilde{B}_v^{i})\,\Delta^i\bar{Q}\right\} + b^{i+1}\,\frac{\partial}{\partial \eta}\left\{\left(\frac{\partial p}{\partial \bar{Q}}\right)^i\,\Delta^i\bar{Q}\right]\right.$$

$$= E^{*i} - \tilde{A}^{*i}\,\bar{Q}^i - \Delta\xi\left\{\frac{\partial}{\partial \eta}\,(\tilde{B}^{*i}\,\bar{Q}^i) + b^{i+1}\,\left(\frac{\partial p}{\partial \eta}\right)^i - \frac{\partial}{\partial \eta}\,(\tilde{F}_v^{i})\right\}$$

$$- a^{i+1}\,\Delta^{i+1}\,p \quad . \tag{6.2}$$

Next, $\bar{Q}$ is taken to be an analytical function as follows.

In regions H1 and H2,

$$\bar{Q} = \bar{Q}_1 \sin(\bar{\alpha}_1\,\xi)\cos(2\pi\,\bar{\beta}_1\,\eta) + \bar{Q}_2 \quad ,$$

and, in regions C1 and C2,

$$\bar{Q} = \bar{Q}_3 \cos(\bar{\alpha}_2\,\eta + \bar{\beta}_2) \tag{6.3 a,b}$$

where

$\bar{Q}_1$, $\bar{Q}_2$, $\bar{Q}_3$, $\bar{\alpha}$ and $\bar{\beta}$ are specified vectors.

In general, $\bar{Q}$ chosen as in Eq. (6.3) will not satisfy the governing equations (6.1). Therfore, the governing equation (6.1) is modified by including in it an extra source term, $R(\xi,\eta)$, such that $\bar{Q}$ is a solution of the modified equation. This modified equation is written as

$$\frac{\partial E^*}{\partial \xi} + \frac{\partial F^*}{\partial \eta} + b\,\frac{\partial p}{\partial \eta} - \frac{\partial}{\partial \eta}(F_v) + a\,\frac{\partial p}{\partial \xi_f} = R(\xi,\eta) \qquad (6.4)$$

The term $R(\xi,\eta)$ could be evaluated analytically using Eqs. (6.3) and (6.1). In this case, the solution that would be obtained by solving Eq. (6.4) numerically will not exactly equal the chosen analytical function $\bar{\bar{Q}}(\xi,\eta)$ and, hence, the correctness of the formulation may not be established accurately. It is, therefore, important that the source term $R(\xi,\eta)$ be evaluated using the discretized form given by Eq. (6.2).

This model problem was studied for various $\bar{\bar{\alpha}}_1$, $\bar{\alpha}_2$, $\bar{\beta}_1$ and $\bar{\beta}_2$. The model problem of uniform flow when all the boundary and initial conditions correspond to uniform flow is a degenerate case of the model problem discussed above and corresponds to $\bar{Q}$ = constant. In all the cases considered, the exact solution was reproduced. It was found that when $\bar{Q}$ was allowed to vary rapidly in the ξ direction, large errors were observed between the prescribed and computed values of the solution. This was due to the rather large truncation errors involved due to large

gradients in $\bar{Q}$ in the ξ direction. This implies that finer grids in the ξ direction have to be employed to resolve these high gradients.

6.3 Interface Boundary Conditions

The implementation of the semi-elliptic formulation on a hybrid grid exposes two small portions of the interfaces of the grid. Hence, the boundary conditions on these interfaces have to be considered.

The boundary conditions in the C-regions consist of the no-slip condition and the specified temperature at the walls, together with the conditions specified along the interface of the C and H1 regions. These interface conditions are obtained from the flow solution in the H1 region. As the governing equations are of order seven with respect to the η direction, 4 conditions are yet to be specified. These conditions could be obtained from the solution, $\bar{Q} = (\rho, \rho u, \rho v, \rho e_t)^T$, computed in region H1. But the physics of the flow dictates how disturbances travel in the flow and this must be incorporated in the numerical scheme used. A characteristics analysis for the quasi-one-dimensional Euler equations suggests that for subsonic flows only three conditions can be specified along the upstream boundary and that one condition is to be specified at the downstream boundary. This idea has also been employed by Eberhardt et al. [53] and Bush [20]. The former reference deals with the solution of the Euler equations while, in the latter, the complete Navier-Stokes equations are solved. In regions of flow where viscous effects dominate, the characteristic conditions obtained from the Euler

equations are not appropriate. However, these conditions should provide a reasonable approximation. In the present study, the three conditions used at the interface consist of specified values of the density ρ, the x-component of the velocity u, and the static pressure p. The additional condition needed to close the system is the reduced normal momentum equation (2.22) written at the half-mesh point off the wall.

6.4 Application to Joukowski Airfoil Cascade

The procedure described in the previous sections is applied to determine flow at Re = 150 through a cascade passage formed by Joukowski airfoils. The hybrid grid that was employed is shown in Fig. 37b. The extent of the C-region, measured in terms of the physical length of BC in Fig. 35, is approximately 10% of the airfoil chord. This value was arrived at from the results obtained previously employing an H-grid and corresponds to the nearest streamwise location upstream of the leading edge of the cascade where $p_{\xi\xi}$ and $u_{\xi\xi}$ are approximately zero. The streamwise distributions of the surface pressure p_b, the wake-centerline velocity and the wall-shear parameter τ_w are shown in Figs. 39a and 39b. The surface-pressure distribution is similar to that obtained for an exponential airfoil cascade, except that the behaviour near the leading edge is confined to approximately 1/4 of the chord. The τ_w distribution near the trailing edge exhibits a rise, as should be expected for low Re flows around cusped trailing edges. The velocity distribution along the stagnation line exhibits an overshoot in the C-region. This is probably

due to the fact that that the stagnation line represents a singularity in terms of $\bar{Q}$ and needs special treatment, paticularly for the y-momentum equation. Figure 39d shows the pressure contours superimposed on the hybrid grid. It is clear from this figure that there is an oscillation present along the first line of H2 region and this anomalous behaviour starts at the 5-sided cell. This oscillatory nature is due to the discontinuity in the y-component of velocity v, between C and H1 regions. This discontinuity leads to a sudden jump in $v_{\eta\eta}$ which appears in the viscous terms. This is supported by the fact that with increase in Re, the oscillatory behavior in p vanished. The results for Re = 600 are shown in Fig. 40. The pressure contours shown in Fig. 40c do not exhibit any oscillation, but the anomaly near the special cell persists. Figure 40e shows the development of velocity profile for Re = 600. The velocity profiles are well behaved, in spite of the anomaly in pressure, because these anomalies are of the order 0.01. Figure 41 shows the convergence history for this Reynolds number. The ε_{abs} and ε_{rel}, defined in section 3.3, are reduced by approximately 4 orders of magnitude in 100 iterations. The anomalous behaviour in pressure is due to the discontinuity in the metric derivatives along the coordinate line containing the downstream face of the five-sided cell. Along this line, the chain rule conservation law (CRCL) form, instead of the SCL form, is employed. The results are shown in Fig. 42. The pressure contours shown in Fig. 42c no longer exhibit the unrealistic behaviour near the

five-sided cell. Effort is being made to resolve this problem near the stagnation line in order to obtain solutions at higher Re.

CHAPTER 7

CONCLUSION

A semi-elliptic formulation has been developed for the analysis of subsonic viscous flows. The governing equations were obtained from the NS equations by neglecting streamwise viscous diffusion terms, but retaining upstream interaction via appropriate treatment of the streamwise pressure-gradient term.

A numerical procedure has been developed to solve the semi-elliptic equations. The discretization of the governing equations was performed such that the terms representing the inviscid contributions form a consistent set of equations by themselves. Appropriate discretized forms of the metric terms associated with the SCL form of the equations were obtained by requiring that a uniform flow solution be recovered in the interior when all boundary and initial conditions correspond to uniform flow. The discretized representation of the streamwise pressure-gradient term, as well as the metrics associated with it, was obtained by application of the procedure to the fully developed flow in a straight channel. Through this study, it was found necessary that the streamwise pressure-gradient term not be in SCL form and that the metrics associated with this term be discretized using forward differences.

The procedure developed was applied to several flow configurations such as channels with exponential constrictions and cascades of airfoils of various shapes. The technique was demonstrated to be adequate for strong-interaction flows, where boundary-layer separation and/or sudden

changes in boundary conditions due to the presence of sharp leading/trailing edges are present. A parametric study was carried out by varying Re for flows through cascades of exponential and parabolic-arc airfoils. This revealed a considerable difference between the flow behaviour near cusped and wedge-shaped trailing edges. The effect of Mach number was studied for a cascade of parabolic-arc airfoils in the range of M_∞ between 0.008 and 0.49, and was found to be minimal on the shear parameter, but to be evident in the pressure distribution for the highest M_∞ considered. The effect of grid refinement was also studied in order to establish the accuracy of the results obtained. In all of the calculations, the grids employed were reasonably fine and the step sizes near the TE and near the point of separation were chosen to be within the scalings of the triple-deck theory. The grids employed were considered to be adequate because the minimum step sizes were well within the triple-deck scalings. The grid independence of the results was also supported by the fact that the results remained unchanged with further refinement of the grid. As regards the convergence rate, for most of the flow solutions considered here, the maximum error was reduced by four to five orders of magnitude, within 150 iterations. However, the procedure remained sensitive to the magnitude and the spatial variation of the time step Δt.

The application of the procedure to cascades with rounded leading edge regions revealed some difficulties. These difficulties are attributed to the use of an H-grid for such configurations. To resolve these difficulties, a hybrid C-H grid, which is more appropriate for

such cascades, was generated using a composite solution procedure. The basic solution procedure was then extended for use with the multi-block structured computational domain corresponding to the C-H hybrid grid. Results were obtained for a cascade of Joukowski airfoils and are quite satisfactory, except near the stagnation line and the special, five-sided cell of the C-H hybrid grid. The unrealistic behaviour of the pressure near the five-sided cell was tracked down to the use of the SCL form of the equations. Use of the CRCL form along a single coordinate line containing a downstream face of the five-sided cell alleviated this difficulty.

In concluding, two important observations are made regarding the analysis and solution procedure developed in the present study. The implementation of the boundary conditions in an implicit manner, that is compatible with the finite difference equations employed in the interior of the computational domain, made it possible for the present procedure to provide satisfactory solutions, without requiring any externally added artificial viscosity. Also, the procedure is capable of producing satisfactory solutions for compressible flows, with no modifications being needed for analyzing nearly incompressible flow as well. This is generally not true for most other available density-based formulations.

As mentioned earlier, the solution procedure was sensitive to the time step Δt. In future work, an alternating-direction implicit (ADI) method, rather than the present ADE type of procedure, could be employed to solve the semi-elliptic equations. Also, the use of a strongly-implicit (SI) procedure, which is known to be less sensitive to the

problem parameters, should be explored, in conjunction with the IPNS model. The present analysis can also be extended to consider unsteady flow problems; important practical applications, such as rotor-stator interactions, could then be considered. Also, turbulent flows can be analyzed by the inclusion of a turbulence model such as the Baldwin-Lomax model [54]. Turbulent flow solutions could then be compared with experimental results.

The usage of the hybrid C-H grid with the semi-elliptic model has exposed a few other areas for further research. Firstly, for low subsonic flows, use of the CRCL form is quite satisfactory. It does not place any requirements on the representation of the metric terms, especially near special points and cells, where the metrics could be discontinuous along a particular coordinate direction. Secondly, decomposition of the conservation form of the governing equations of motion along the transformed-coordinate directions, using the contravariant components of velocity instead of the Cartesian components, may be more appropriate. This form of the equations is more natural for analyzing flows in general geometries, as they are the fundamental conservation equations written directly in the body-fitted coordinate system, rather than being transformed from the Cartesian coordinates to this system. This interface in the hybrid grid became exposed as a boundary only because of the semi-elliptic formulation employed. It would remain as an interior computational line if the complete NS equations were employed. Hence, an NS analysis on hybrid grids is highly desired. The use of complete NS equations would also

resolve some of the difficulties arising due to the change in the orientation of the coordinate directions and the use of a coordinate-related approximation in the vicinity of the five-sided cells.

REFERENCES

1. Goldstein, S., "On Laminar Boundary Layer Flow Near a Position of Separation," Quart. J. Mech. Applied Mathematics, Vol. 1, pp. 43-69, 1948.

2. Veldman, A.E.P., "New Quasi-Simulataneous Method to Calculate Interacting Boundary Layers," AIAA Journal, Vol. 19, No. 1, pp. 79-85, 1981.

3. Stewartson, K., "Multistructured Boundary Layers on Flat Plates and Related Bodies," Advances in Applied Mathematics, Vol. 14, Academic Press, 1974.

4. Rothmayer, A.P., "A study of High Reynolds Number Laminar Separation," Ph.D Dissertation, University of Cincinnati, 1985.

5. Briley, W.R., "Numerical Method for Predicting Three Dimensional Flows in Ducts," Journal of Computational Physics, Vol. 14, No. 1, pp. 8-28, 1974.

6. Ghia, U., Ghia, K.N. and Goyal, R.K., "Three Dimensional Viscous Incompressible Flow in Curved Polar Ducts," AIAA Paper No. 79-1536, 1979.

7. Steger, J.L., "Implicit Finite-Difference Simulation of Flow about Arbitrary Two-Dimensional Geometries," AIAA Journal, Vol. 16, No. 7, 1978.

8. Steger, J.L., Pulliam, T.H. and Chima, R.V., "An Implicit Finite Difference Code for Inviscid and Viscous Cascades Flow," AIAA Paper No. 80-1427, 1980.

9. Buggeln, R.C., Briley, W.R. and McDonald, H., "Computation of Laminar and Turbulent Flow in Curved Ducts, Channels and Pipes Using the Navier-Stokes Equations," Final Report, Contract No. 00014-79-C-0713, 1980.

10. Chima, R.V. and Johnson, G.M., "Efficient Solution of the Euler and Navier-Stokes Equations with a Vectorized Multiple-Grid Algorithm," Proceedings of the AIAA 6th CFD Conference, Danvers, MA, pp. 72-89, 1983.

11. Shamroth, S.J., McDonald, H. and Briley, W.R., "Prediction of Cascade Flow Fields Using the Averaged Navier-Stokes Equations," Journal of Engg. for Gas Turbine and Power, Vol. 106, pp. 383-390, 1984.

12. Hah, C., "A Navier-Stokes Analysis of Three-Dimensional Turbulent Flows inside Turbine Blade Rows at Design and Off-Design

Conditions," Journal of Engg. for Gas Turbines and Power, Vol. 106, pp. 421-429, 1984.

13. Rhie, C.M., "A Three-Dimensional Passage Flow Analysis Aimed at Centrifugal Impellers," Computers and Fluids, Vol. 13, No. 4, pp. 443-460, 1985.

14. Chima, R.V., "Development of an Explicit Multigrid Algorithm for Quasi-Three-Dimensional Flows in Turbomachinery," AIAA Paper No. 86-0032, 1986.

15. Davis, R.L., Ni, R.H. and Carter, J.E., "Cascade Viscous Flow Analysis Using the Navier-Stokes Equations," AIAA Paper No. 86-0033, 1986.

16. Rhie, C.M., "A Pressure Based Navier-Stokes Solver Using the Multigrid Method," AIAA Paper No. 86-0207, 1986.

17. Ghia,U., Ghia, K.N., Rubin, S.G. and Khosla, P.K., "Study of Incompressible Flow Separation Using Primitive Variables," International Journal of Computers and Fluids, Vol. 9, pp. 127-142, 1981.

18. Norton, R.J.G., Thompkins, W.T. and Haimes, R., "Implicit Finite Difference Schemes with Non-Simply Connected Grids - A Novel Approach," AIAA Paper No. 84-0003, 1983.

19. Rai, M.M., "Navier-Stokes Simulations of Rotor-Stator Interaction Using Patched and Overlaid Grids," Proceedings of the AIAA 7th CFD Conference, Cincinnati, Ohio, pp. 282-298, 1985.

20. Bush, R.H., "External Compression Inlet Predictions Using an Implicit, Upwind, Multiple Zone Approach," Proceedings of the AIAA 7th CFD Conference, Cincinnati, Ohio, pp. 438-447, 1985.

21. Ghia, U., Ghia, K.N. and Ramamurti, R., "Hybrid C-H Grids for Turbomachinery Cascades," Advances in Grid Generation, ASME Publication, K.N. Ghia and U. Ghia, Editors, pp. 143-149, 1983.

22. Viviand, H., "Conservation Forms of the Gas Dynamic Equations," La Recherche Aerospatiale, No. 1, pp. 65-68, 1974.

23. Lighthill, M.J., "On Boundary Layers and Upstream Influence - I. A Comparison Between Subsonic and Supersonic Flows," Proceedings of the Royal Society of London, 217, 1953.

24. Vigneron, Y.C., Rakich, J.V. and Tannehill, J.C., "Calculation of Supersonic Viscous Flow over Delta Wings with Sharp Subsonic Leading Edges," AIAA Paper No. 78-1137, 1978.

25. von Mises, R., Mathematical Theory of Compressible Flow, Academic Press, 1958.

26. Courant, R. and Hilbert, D., Methods of Mathematical Physics - Partial Differential Equations, Vol. II, Interscience Publishers, 1953.

27. McDonald, H. and Briley, W.R., "Some Observations on Numerical Solutions of the Three-Dimensional Navier-Stokes Equations," Numerical and Physical Aspects of Aerodynamic Flows, T. Cebeci, Editor, Springer-Verlag, 1982.

28. Rudy, D.H. and Strikwerda, J.C., " A Nonreflecting Outflow Boundary Condition for Subsonic Navier-Stokes Calculations," Journal of Computainal Physics, Vol. 36, No. 1, pp. 55-70, 1980.

29. Rubin, S.G. and Lin, T.C., "Numerical Methods for Two- and Three-Dimensional Viscous Flow Problems: Application to Hypersonic Leading Edge Equations," PIBAL Report No. 71-8, 1971.

30. Briley, W.R. and McDonald, H., "Solution of the Three-Dimensional Compressible Navier-Stokes Equations by an Implicit Technique," Proc. of the 4th International Conference on Numerical Methods in Fluid Dynamics, Boulder, CO., 1974.

31. Courant, R., Differential and Integral Calculus, Vol. II, Interscience Publishers, New York, 1936.

32. Schiff, L.B. and Steger, J.L., "Numerical Simulation of Steady Supersonic Viscous Flows," presented at the AIAA 17th Aerospace Sciences Meeting, New Orleans, 1979.

33. Ghia, K.N. and Ghia, U., "Semi-Elliptic Globally Iterative Analysis for Two-Dimensional Subsonic Internal Viscous Flows," presented at NASA-Lewis Research Review on Computational Fluid Mechanics, Cleveland, Ohio, 1983.

34. Barnett, M. and Davis, R.T., "A Procedure for the Calculation of Supersonic Flows with Strong Viscous-Inviscid Interaction," AIAA Paper No. 85-0166, presented at AIAA 23rd Aerospace Sciences Meeting, Reno, Nevada, 1985.

35. Anderson, D.A., Tannehill, J.C. and Pletcher, R.H., Computational Fluid Mechanics and Heat Transfer, Hemisphere Publishing Corporation, 1984.

36. Reyhner, T.A. and Flügge-Lotz, I., "The Interaction of a Shock Wave with a Laminar Boundary Layer," International J. of Non-Linear Mechanics, Vol. 3, pp. 173-199, 1968.

37. Hindman, R.G., "Generalized Coordinate Forms of Governing Fluid Motions and Associated Geometrically Induced Errors," AIAA Journal, Vol. 20, No. 10, pp. 1359-1367, 1982.

38. Stewartson, K., "Multistructured Boundary Layer of Flat Plates and Related Bodies," Advances in Applied Mathematics, Vol. 14, pp. 145-239, Academic Press, 1974.

39. Cheng, H.K. and Smith, F.T., "The Influence of Airfoil Thickness and Reynolds Number on Separation," Journal of Applied Mathematics and Physics, Vol. 33, pp. 151-180, 1982.

40. Smith, F.T., Stewartson, K. and Kaups, K., "Marginal Separation," Studies in Applied Mathematics, Vol. 67, pp. 45-61, August 1982.

41. Sockol, P.M., "Generation of C-type Cascade Grids for Viscous Flow Computation," Numerical Grid Generation Techniques, R.E. Smith, Editor, NASA CP-2166, 1980.

42. Dulikravich, D.S., "Fast Generation of Three-Dimensional Computational Boundary-Conforming Periodic Grids of C-Type," Numerical Grid Generation, J.F. Thompson, Editor, Elsevier Publishing Co., 1982.

43. Eiseman, P.R., "Automatic Algebraic Coordinate Generation," Numerical Grid Generation, J.F. Thompson, Editor, Elsevier Publishing Co., 1982.

44. Ghia, U. and Ghia, K.N., "Boundary-Fitted Coordinates for Regions with Highly Curved Boundaries and Reentrant Boundaries," Numerical Grid Generation Techniques, R.E. Smith, Editor, NASA CP-2166, 1980.

45. Lee, K.D., Hwang, M., Yu, N.J. and Ruppert, P.E., "Grid Generation for General Three-Dimensional configurations," Numerical Grid Generation Techniques, R.E. Smith, Editor, NASA CP-2166, 1980.

46. Sorenson, R.L., "Grid Generation by Elliptic Partial Differential Equations for a Tri-Element Augmentor-Wing Airfoil," Numerical Grid Generation, J.F. Thompson, Editor, Elsevier Publishing Co., 1982.

47. Ghia, U., Ghia, K.N. and Shin, C.T., "Analysis of a Breaking Free-Surface Wave Using Boundary-Fitted Coordinates for Regions Including Reentrant Boundaries," Proceedings of Third International Conf. on Ship Hydrodynamics, Paris, France, 1981.

48. Coleman, R.M., "Generation of Boundary Fitted Coordinate Systems Using Segmented Computational Regions," Numerical Grid Generation, J.F. Thompson, Editor, Elsevier Publishing Co., 1982.

49. Steger, J.L., "On Application of Body-Conforming Curvilinear grids for Finite Difference Solution of External flows," Numerical Grid Generation, J.F. Thompson, Editor, Elsevier Publishing Co., 1982.

50. Benek, J.A., Buning, P.G. and Steger, J.L., "A 3-D Chimera Grid Embedding Technique," Proceedings of the AIAA 7th CFD Conference, Cincinnati, Ohio, 1985.

51. Ghia, U. and Ghia, K.N., "Numerical Generation of a System of Curvilinear Coordinates for Turbine Cascade Flow Analysis," University of Cincinnati Report No. AFL 75-4-17, 1975.

52. Benek, J.A., Steger, J.L. and Dougherty, F.C., "A Flexible Grid Embedding Technique with Application to Euler Equations," Proc. of the AIAA 6th CFD Conference, Danvers, Massachusetts, 1983.

53. Eberhardt, S. and Baganoff, D., "Overset Grids in Compressible Flow," Proc. of the AIAA 7th CFD Conference, Cincinnati, Ohio, 1985.

54. Baldwin, B.S. and Lomax, H., "Thin-Layer Approximation and Algebraic Model for Separated Turbulent Flows," AIAA Paper No. 78-257, presented at the AIAA 16th Aerospace Sciences Meeting, Huntsville, Alabama, 1978.

APPENDIX A

INVERSION OF COEFFICIENT MATRIX OF BLOCK-TRIDIAGONAL SYSTEM WITH PERIODIC BOUNDARY CONDITIONS

The system of equations resulting from the discretization of the governing equations along a periodic boundary, where the peridicity condition is imposed in an implicit manner, is of the following form.

$$[P]\,\Delta\bar{Q} = D \qquad \text{(A.1 a)}$$

In expanded form, Eq. (A.1 a) is written as follows.

$$\begin{bmatrix} B_1 & C_1 & 0 & \cdots & 0 & 0 & A_1 \\ A_2 & B_2 & C_2 & \cdots & 0 & 0 & 0 \\ \cdot & \cdot & \cdot & & \cdot & \cdot & \\ \cdot & \cdot & \cdot & & \cdot & \cdot & \\ 0 & 0 & 0 & \cdots & A_{N-1} & B_{N-1} & C_{N-1} \\ C_N & 0 & 0 & \cdots & 0 & A_N & B_N \end{bmatrix} \begin{bmatrix} \Delta\bar{Q}_1 \\ \Delta\bar{Q}_2 \\ \cdot \\ \cdot \\ \Delta\bar{Q}_{N-1} \\ \Delta\bar{Q}_N \end{bmatrix} = \begin{bmatrix} D_1 \\ D_2 \\ \cdot \\ \cdot \\ D_{N-1} \\ D_N \end{bmatrix} \qquad \text{(A.1 b)}$$

Here, the subscript N corresponds to the index (JMAX-1) in Eq. (3.44). Also, the individual entries A_j, B_j, C_j are (4x4) blocks, while $\Delta\bar{Q}_j$ and D_j are (4x1) blocks.

The inversion of the coefficient matrix [P] is performed using a L-U decomposition, i.e., by factoring P into upper and lower triangular matrices U and L, respectively, such that

$$P = L\,U \qquad \text{(A.2 a)}$$

where

$$L = \begin{bmatrix} L_{1,1} & 0 & . & . & 0 \\ L_{2,1} & L_{2,2} & 0 & . & . \\ L_{3,1} & L_{3,2} & L_{3,3} & 0 & . \\ . & . & . & . & . \\ . & . & . & . & . \\ . & . & . & . & . \\ L_{N,1} & . & . & . & L_{N,N} \end{bmatrix}$$

and

$$U = \begin{bmatrix} I & U_{1,2} & . & . & U_{1,N} \\ 0 & I & U_{2,3} & . & U_{2,N} \\ . & . & I & U_{3,4} & U_{3,N} \\ . & . & . & . & . \\ . & . & . & . & . \\ . & . & . & . & . \\ 0 & . & . & . & I \end{bmatrix}$$

(A.2 b,c)

Here, I is the (4X4) identity matrix, and $L_{j,k}$ and $U_{j,k}$ are (4x4) blocks.

By forming the product LU and equating it, element by element, to the coefficient matrix P, the expression for the elemental blocks of L and U can be obtained and are given as follows.

$$L_{1,1} = B_1 \quad ,$$

$$L_{2,1} = A_2 \quad ,$$

$$L_{3,1} = L_{4,1} = \ldots = L_{N-1,1} = 0 \quad ,$$

$$L_{N,1} = C_N \quad ,$$

$$U_{1,2} = B_1^{-1} C_1 \quad ,$$

$$U_{1,3} = U_{1,4} = \ldots = U_{1,N-1} = 0 \quad ,$$

$$U_{1,N} = B_1^{-1} A_1 \quad ,$$

$$L_{2,2} = B_2 - A_2 B_1^{-1} C_1 \quad ,$$

$$L_{3,2} = A_3 \quad ,$$

$$L_{4,2} = L_{5,2} = \ldots = L_{N-1,2} = 0 \quad .$$

$$L_{N,2} = - C_N B_1^{-1} C_1 \quad ,$$

$$U_{2,3} = (B_2 - A_2 B_1^{-1} C_1)^{-1} C_2 \quad ,$$

$$U_{2,4} = U_{2,5} = \ldots = U_{2,N-1} = 0 \quad ,$$

$$U_{2,N} = - (B_2 - A_2 B_1^{-1} C_1)^{-1} A_2 B_1^{-1} A_1 \quad , \qquad \text{(A.3)}$$

etc.

Hence, the inversion of P is carried out in two steps. The first step is a forward elimination step in which the equation

$$L\ q = D \qquad \text{(A.4)}$$

is solved for q.

This is done in the following manner.

For m=1,

$$L_{1,1} = B_1 \quad ,$$

$$L_{N,1} = C_N \quad ,$$

$$U_{1,N} = B_1^{-1} A_1 \quad ,$$

$$q_1 = B_1^{-1} D_1 \quad .$$

For m equal 2 through N-1,

$$L_{m,m} = B_m - A_m U_{m-1,m} \quad ,$$

$$q_m = L_{m,m}^{-1} (D_m - A_m D_{m-1}) \quad ,$$

$$U_{m,m+1} = L_{m,m}^{-1} C_m \quad ,$$

$$U_{m,N} = - L_{m,m}^{-1} A_m U_{m-1,N} \quad ,$$

$$D_N = D_N - L_{N,m-1} q_{m-1} \quad ,$$

$$L_{N,m} = - L_{N,m-1} U_{m-1,m} \quad .$$

The last unknown vector q_N is obtained as follows.

$$L_{N,N-1} = A_N + L_{N,N-1} \quad ,$$

$$D_N = D_N - L_{N,N-1} q_{N-1} \quad ,$$

$$L_{N,N} = B_N - L_{N,N-1} (C_{N-1} + U_{N-1,N}) \quad ,$$

so that, finally,

$$q_N = L_{N,N}^{-1} D_N$$

The second step is the backward elimination step, during which the equation

$$U\,\Delta\bar{Q} = q \tag{A.5}$$

is solved to yield the solution vector $\Delta\bar{Q}$. From the structure of upper triangular matrix U, which has identity block matrices along the diagonal, and non-zero block matrices along the superdiagonal and the last column, it is seen that the following recursive relation should be employed to obtain $\Delta\bar{Q}$.

$$\Delta\bar{Q}_m + U_{m,m+1}\,\Delta\bar{Q}_{m+1} + U_{m,N}\,\Delta\bar{Q}_N = q_m \text{ for, } m = N-1, N-2, \ldots, 1\ , \tag{A.6}$$

with $\Delta\bar{Q}_N = q_N$

being used to initiate the determination of the solution vector $\Delta\bar{Q}$.

APPENDIX B

REPRESENTATION OF THE METRIC COEFFICIENTS

The metric coefficients, arising due to the transformation of the governing equations from the physical (x,y) coordinates to the computational (ξ,η) coordinates, should be evaluated in a manner consistent with the discretization of the governing equations.

The metric coefficients for a general mapping are given in Eq. (2.13) and are

$$\xi_x = J\, y_\eta \quad , \quad \xi_y = -J\, x_\eta \quad ,$$

$$\eta_x = -J\, y_\xi \quad \text{and} \quad \eta_y = J\, x_\xi \quad . \qquad \text{(B.1 a-d)}$$

The metric derivatives x_η and y_η are evaluated using central differences at a general interior computational point (i+1,j). Hence,

$$x_\eta\big|_{i+1,j} = (x_{i+1,j+1} - x_{i+1,j-1})/2\Delta\eta$$

$$\text{and} \quad y_\eta\big|_{i+1,j} = (y_{i+1,j+1} - y_{i+1,j-1})/2\Delta\eta \quad . \qquad \text{(B.2 a,b)}$$

At a boundary point, these terms are evaluated using a first-order accurate representation. Accordingly,

At j = JMIN,

$$x_\eta\big|_{i+1,j} = (x_{i+1,j+1} - x_{i+1,j})/\Delta\eta \quad ,$$

$$y_\eta\big|_{i+1,j} = (y_{i+1,j+1} - y_{i+1,j})/\Delta\eta \quad ,$$

and, at j = JMAX,

$$x_\eta\big|_{i+1,j} = (x_{i+1,j} - x_{i+1,j-1})/\Delta\eta \quad ,$$

$$y_\eta\big|_{i+1,j} = (y_{i+1,j} - y_{i+1,j-1})/\Delta\eta \quad . \qquad \text{(B.3 a-d)}$$

In order to determine the appropriate representation of x_ξ and y_ξ, a simple test of uniform-flow computation is employed. This test involves assuming a uniform flow at a streamwise location i and applying the numerical integration algorithm, along with uniform-flow boundary conditions, to obtain the solution at station (i+1). If the algorithm is formulated consistently, a uniform flow should result at station (i+1). To this end, it is sufficient to consider the inviscid part of the governing equations, i.e.,

$$\frac{\partial E^*}{\partial \xi} + \frac{\partial F^*}{\partial \eta} = 0 \tag{B.4}$$

since ξ-derivatives appear only in the streamwise convective and pressure-gradient terms. The quasi-linearized form of the above equation can be obtained from Eqn. (3.27) and is

$$\tilde{A}^i \, \Delta^i \bar{Q} + \Delta\xi \, \frac{\partial}{\partial \eta} \left(\tilde{B}^i \, \Delta^i \bar{Q} \right) = S$$

where

$$S = E^{*i} - \tilde{A}^{*i} \, \bar{Q}^i - \Delta\xi \, \frac{\partial}{\partial \eta} \left(\tilde{B}^{*i} \, \bar{Q}^i \right) \quad . \tag{B.5 a,b}$$

Here,

$$E^{*i} = \left(\frac{\xi_x}{J}\right)^i \bar{E}^{*i} + \left(\frac{\xi_y}{J}\right)^i \bar{F}^{*i} \quad ,$$

$$\tilde{A}^{*i} \, \bar{Q}^i = \left(\frac{\xi_x}{J}\right)^{i+1} \bar{E}^{*i} + \left(\frac{\xi_y}{J}\right)^{i+1} \bar{F}^{*i}$$

and $\tilde{B}^{*i} \, \tilde{Q}^i = \left(\frac{\eta_x}{J}\right)^{i+1} \bar{E}^{*i} + \left(\frac{\eta_y}{J}\right)^{i+1} \bar{F}^{*i} \quad .$ (B.6)

Following the discretization procedure, as discussed in Chapter 3, for the inviscid terms, the discretized form of the right-hand side of Eqn. (B.5 b) at location (i+1,j) can be written as

$$
\begin{aligned}
S = \frac{1}{2} \{ & [(\frac{\xi_x}{J})^i_j - (\frac{\xi_x}{J})^{i+1}_j] \bar{E}^{*i}_j + [(\frac{\xi_y}{J})^i_j - (\frac{\xi_y}{J})^{i+1}_j] \bar{F}^{*i}_j \} \\
& + \frac{1}{4} [\{ [(\frac{\xi_x}{J})^i_{j+1} - (\frac{\xi_x}{J})^{i+1}_{j+1}] \bar{E}^{*i}_{j+1} + [(\frac{\xi_y}{J})^i_{j+1} - (\frac{\xi_y}{J})^{i+1}_{j+1}] \bar{F}^{*i}_{j+1} \} \\
& + \{ [(\frac{\xi_x}{J})^i_{j-1} - (\frac{\xi_x}{J})^{i+1}_{j-1}] \bar{E}^{*i}_{j-1} + [(\frac{\xi_y}{J})^i_{j-1} - (\frac{\xi_y}{J})^{i+1}_{j-1}] \bar{F}^{*i}_{j-1} \}] \\
& + \frac{\Delta\xi}{2\,\Delta\eta} \{ (\frac{\eta_x}{J})^{i+1}_{j-1} \bar{E}^{*i}_{j-1} - (\frac{\eta_x}{J})^{i+1}_{j-1} \bar{E}^{*i}_{j-1} \\
& + (\frac{\eta_y}{J})^{i+1}_{j-1} \bar{F}^{*i}_{j-1} - (\frac{\eta_y}{J})^{i+1}_{j-1} \bar{F}^{*i}_{j-1} \} \quad . \qquad \text{(B.7)}
\end{aligned}
$$

In order to recover a uniform-flow solution, it will be sufficient to show that the source term S is zero, starting from uniform-flow conditions at station i, and using uniform-flow boundary conditions. To show this, it is recognized that, for the case with constant density, velocity and temperature,

$$\rho = \rho_1 \quad ,$$

$$u = u_1 \quad ,$$

$$v = 0$$

and $T = T_1$,

where ρ_1, u_1 and T_1 are constants. Hence, the flux vectors are constant with respect to the η direction, i.e.,

$$\bar{E}^{*i}_{j-1} = \bar{E}^{*i}_j = \bar{E}^{*i}_{j+1} \quad , \quad \text{for} \quad j = \text{JMIN+1, ... , JMAX-1}$$

and $\bar{F}^{*i}_j = 0$, for $j = \text{JMIN, ... , JMAX}$. (B.9)

With these conditions, the source term S can be written in the following mannner.

$$S = \{ \frac{1}{2} [(\frac{\xi_x}{J})^i_j - (\frac{\xi_x}{J})^{i+1}_j]$$

$$+ \frac{1}{4} [(\frac{\xi_x}{J})^i_{j+1} - (\frac{\xi_x}{J})^{i+1}_{j+1} + (\frac{\xi_x}{J})^i_{j-1} - (\frac{\xi_x}{J})^{i+1}_{j-1}]$$

$$- \frac{\Delta\xi}{2\,\Delta\eta} [(\frac{\eta_x}{J})^{i+1}_{j-1} - (\frac{\eta_x}{J})^{i+1}_{j-1}]\} \bar{E}^{*i}_j \qquad \text{(B.10)}$$

Substituting for (ξ_x/J) and (η_x/J) from Eq. (B.1) and employing the discretization given by Eq. (B.2), Eq. (B.10) can be written as

$$S = \{ \frac{1}{4\,\Delta\eta} [- (y_{i+1,j+1} - y_{i+1,j-1}) + (y_{i,j+1} - y_{i,j-1})]$$

$$+ \frac{1}{8\,\Delta\eta} [- (y_{i+1,j+2} - y_{i+1,j}) + (y_{i,j+2} - y_{i,j})$$

$$- (y_{i+1,j} - y_{i+1,j-2}) + (y_{i,j} - y_{i,j-2})]$$

$$+ \frac{\Delta\xi}{2\,\Delta\eta} [(y_\xi)_{i+1,j+1} - (y_\xi)_{i+1,j-1}]\} \bar{E}^{*i}_j \quad . \qquad \text{(B.11)}$$

For S to be equal to zero, it is clear, from the above equation, that y_ξ is to be evaluated, as an average of its neighbours, as follows.

$$y_\xi\big|_{i+1,j+1} = \frac{1}{4\,\Delta\xi} [y_{i+1,j+2} - y_{i,j+2} + y_{i+1,j} - y_{i,j}]$$

$$+ \frac{1}{2\,\Delta\xi} [y_{i+1,j+1} - y_{i,j+1}] \qquad \text{(B.12)}$$

Similarly, by assuming v = constant and u = 0, we can arrive at the following representation for the term x_ξ.

$$x_\xi\Big|_{i+1,j+1} = \frac{1}{4\,\Delta\xi}\left[x_{i+1,j+2} - x_{i,j+2} + x_{i+1,j} - x_{i,j}\right] + \frac{1}{2\,\Delta\xi}\left[x_{i+1,j+1} - x_{i,j+1}\right] \quad . \tag{B.13}$$

The representation of x_ξ and y_ξ at η = constant boundaries, for example, at j = JMAX can be obtained by forming the discretized form of Eq. (B.5 b) at j = JMAX-1.

At the location [i+1,j (= JMAX-1)], the source term is written as follows.

$$\begin{aligned} S = \{ & \frac{1}{4\,\Delta\eta}\left[- (y_{i+1,j+1} - y_{i+1,j-1}) + (y_{i,j+1} - y_{i,j-1})\right] \\ & + \frac{1}{8\,\Delta\eta}\left[- (y_{i+1,j+2} - y_{i+1,j}) + (y_{i,j+2} - y_{i,j}) \right. \\ & \qquad \left. - (y_{i+1,j} - y_{i+1,j-2}) + (y_{i,j} - y_{i,j-2})\right] \\ & + \frac{\Delta\xi}{2\,\Delta\eta}\left[(y_\xi)_{i+1,j+1} - \frac{1}{2\,\Delta\xi}(y_{i+1,j-1} - y_{i,j-1}) \right. \\ & \qquad \left. - \frac{1}{4\,\Delta\xi}(y_{i+1,j} - y_{i,j} + y_{i+1,j-2} - y_{i,j-2})\right] \end{aligned} \tag{B.14}$$

In order to produce a zero source term S, from Eq. (B.14), y_ξ term should be represented in the following manner:

$$y_\xi\Big|_{i+1,j = \text{JMAX}} = (y_{i+1,j} - y_{i,j}) \,/\, \Delta\xi \quad . \tag{B.15}$$

Similarly, the discretization for the term x_ξ is performed as follows.

$$x_\xi\Big|_{i+1,j = \text{JMAX}} = (x_{i+1,j} - x_{i,j}) \,/\, \Delta\xi \quad . \tag{B.16}$$

ORIGINAL PAGE IS
OF POOR QUALITY

APPENDIX C

DISCRETIZATION OF DERIVATIVES AT CORNERS OF FIVE-SIDED CELLS

In a hybrid grid, 'special-points' commonly occur at the congruence of more than two different types of sub-regions. As stated in Chapter 5, these 'special-points', B''_c and E''_c in Fig. 31, are presently considered to be the centers of non-standard 5-sided cells. In the discretization of the various derivative terms in Eq. (5.1), special consideration is required in arriving at the appropriate neighbours for the vertices of these 5-sided cells, i.e., in defining the computational molecule at the vertices of these cells. The vertices of these non-standard cells are B''_1 , B''_2 , ... , B''_5 and E''_1 , E''_2 , ... , E''_5 , as shown in Fig. 31. The eight immediate neighbours for each of these points are shown as the encircled points in the sketches below.

At vertex B''_1 ,

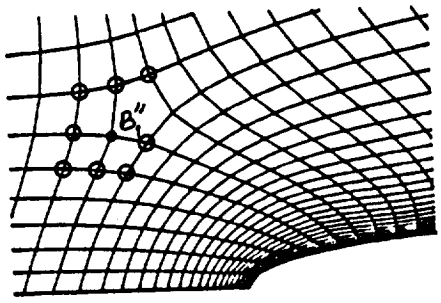

At vertex B''_2 ,

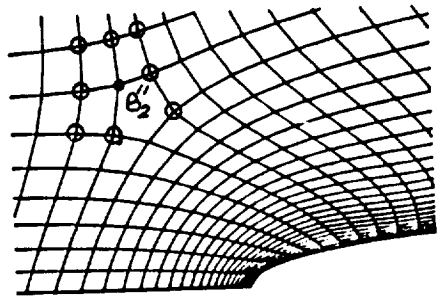

At vertex B''_3 ,

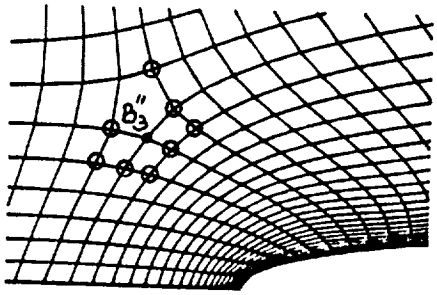

At vertex B''_4 ,

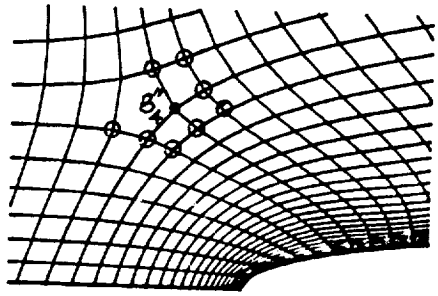

At vertex B''_5 ,

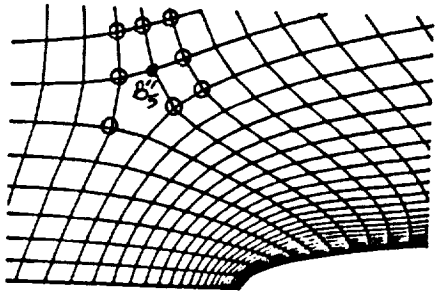

⊙ immediate neighbours

The computational moleclues shown were arrived at by examining the multi-block structured computational region and seeking the natural neighbours of a given computational point. The neighbours at the corners of the cell around E''_c are assigned in a similar manner. At a given vertex, the computational molecule employed during one step of the two-step solution procedure, for the grid-generation equations as well as the flow equations, is the same as that for the second step of the procedure. This is essential for consistency of the discretized equations used during the two steps.

TABLE. 1. PRESSURE LOSS AND GRID DATA FOR CHANNEL WITH EXPONENTIAL CONSTRICTION, RE = 1500.

t/h	Grid	Distance from Maximum-Constriction Location (in Channel Heights)		Δp
		Inflow Boundary	Outflow Boundary	
0.10	(141x61)	5.0	20.0	0.00875
0.16	(176x61)	15.0	29.0	0.02083
0.20	(201x61)	28.5	60.0	0.02500

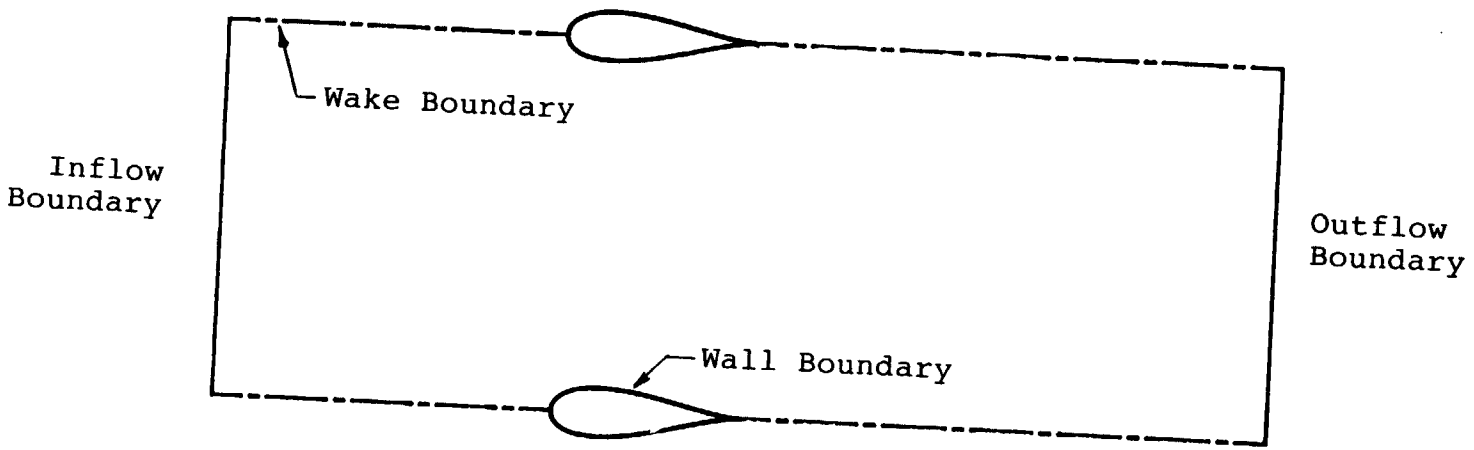

FIG. 1. SCHEMATIC OF A CASCADE CONFIGURATION.

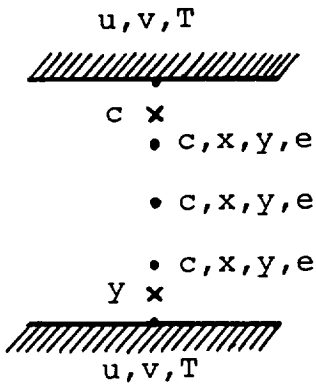

NO. OF UNKNOWNS	NO. OF EQUATIONS	
	4	CONTINUITY
20	3	x-MOMENTUM
	(3+1)	y-MOMENTUM
	3	ENERGY
	6	BOUNDARY CONDITIONS
TOTAL	20	

WALL-WALL BOUNDARY CONDITIONS

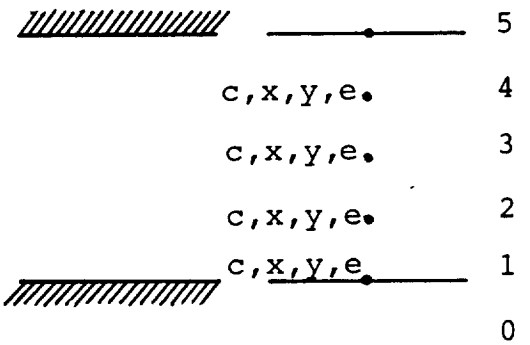

NO. OF UNKNOWNS	NO. OF EQUATIONS	
	4	CONTINUITY
16	4	x-MOMENTUM
	4	y-MOMENTUM
	4	ENERGY
TOTAL	16	

b. WAKE-WAKE BOUNDARY CONDITIONS

FIG. 2. TYPES OF BOUNDARY CONDITIONS FOR CASCADE FLOWS.

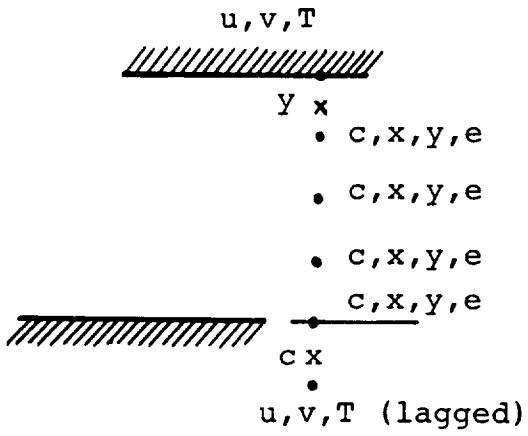

NO. OF UNKNOWNS	NO. OF EQUATIONS	
	5	CONTINUITY
	4	x-MOMENTUM
24	(4+1)	y-MOMENTUM
	4	ENERGY
	6	BOUNDARY CONDITIONS
TOTAL	24	

c. WALL-WAKE BOUNDARY CONDITIONS

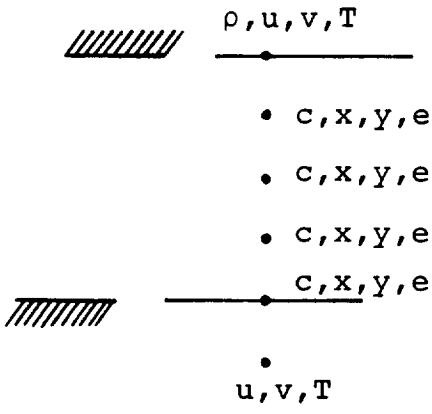

NO. OF UNKNOWNS	NO. OF EQUATIONS	
	5	CONTINUITY
	4	x-MOMENTUM
24	4	y-MOMENTUM
	4	ENERGY
	7	BOUNDARY CONDITIONS
TOTAL	24	

d. WAKE-WAKE BOUNDARY CONDITIONS (REGION-PERIODIC GRID)

FIG. 2 (CONCLUDED). TYPES OF BOUNDARY CONDITIONS FOR CASCADE FLOWS.

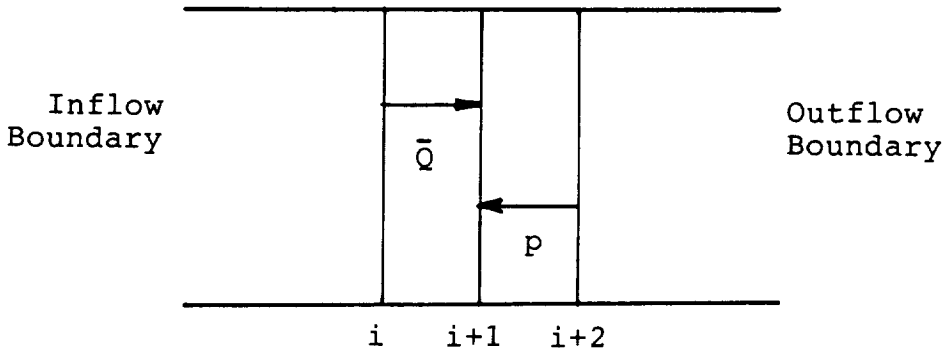

FIG. 3. TWO STEPS OF THE SOLUTION PROCEDURE.

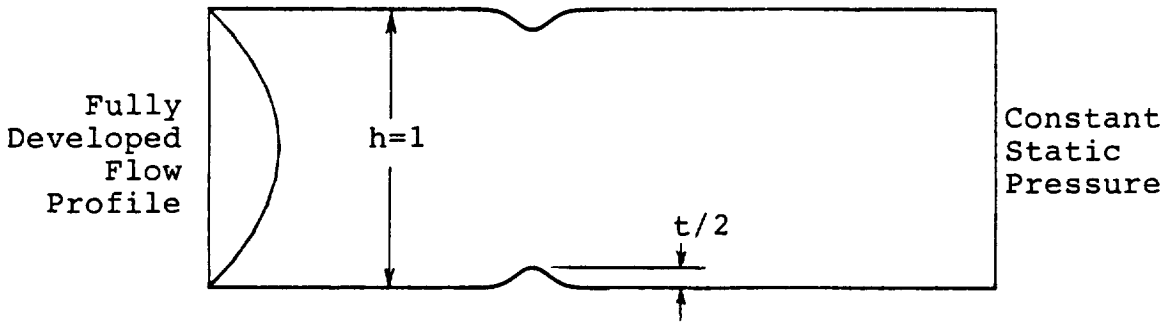

a. EXPONENTIAL CHANNEL

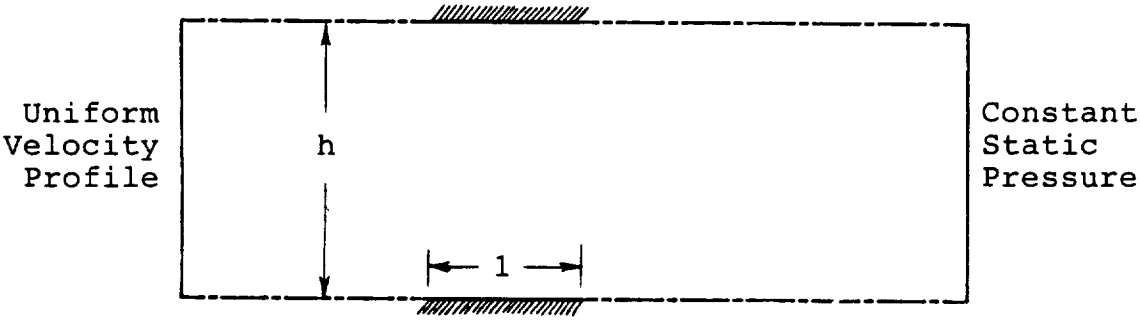

b. FLAT-PLATE CASCADE

FIG. 4. CONSTRICTED CHANNEL AND VARIOUS CASCADE CONFIGURATIONS, AND INFLOW-OUTFLOW BOUNDARY CONDITIONS.

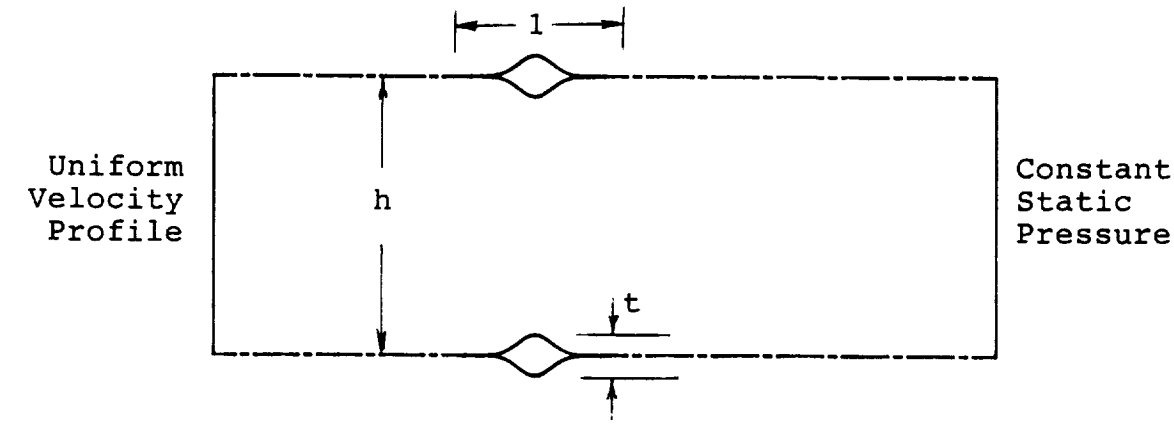

c. CASCADE OF EXPONENTIAL AIRFOILS

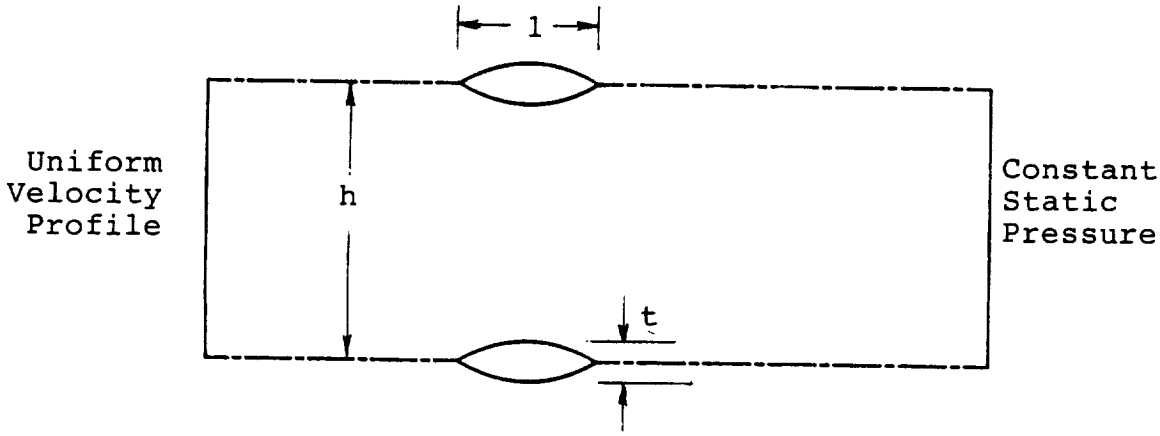

d. CASCADE OF PARABOLIC-ARC AIRFOILS

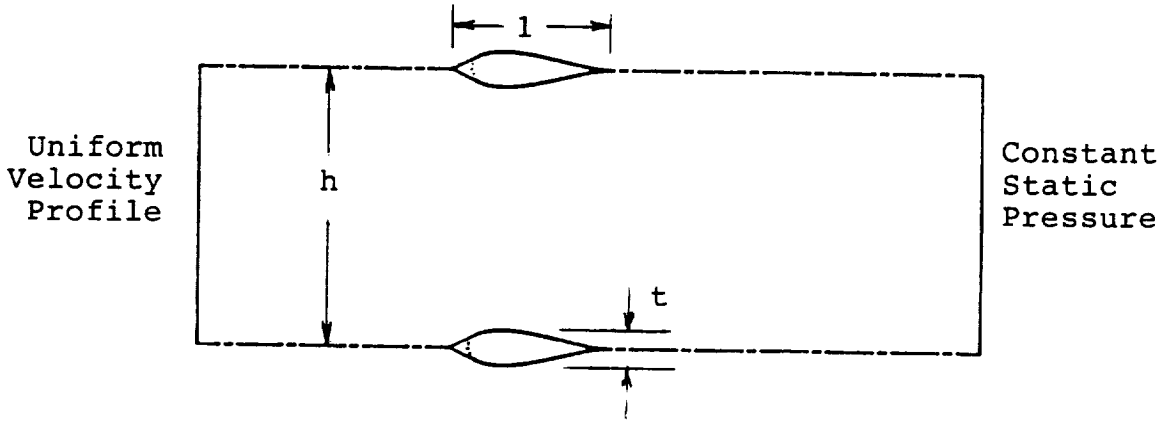

e. CASCADE OF JOUKOWSKI AIRFOILS WITH MODIFIED LEADING EDGES

FIG. 4 (CONCLUDED). CONSTRICTED CHANNEL AND VARIOUS CASCADE CONFIGURATIONS, AND INFLOW-OUTFLOW BOUNDARY CONDITIONS.

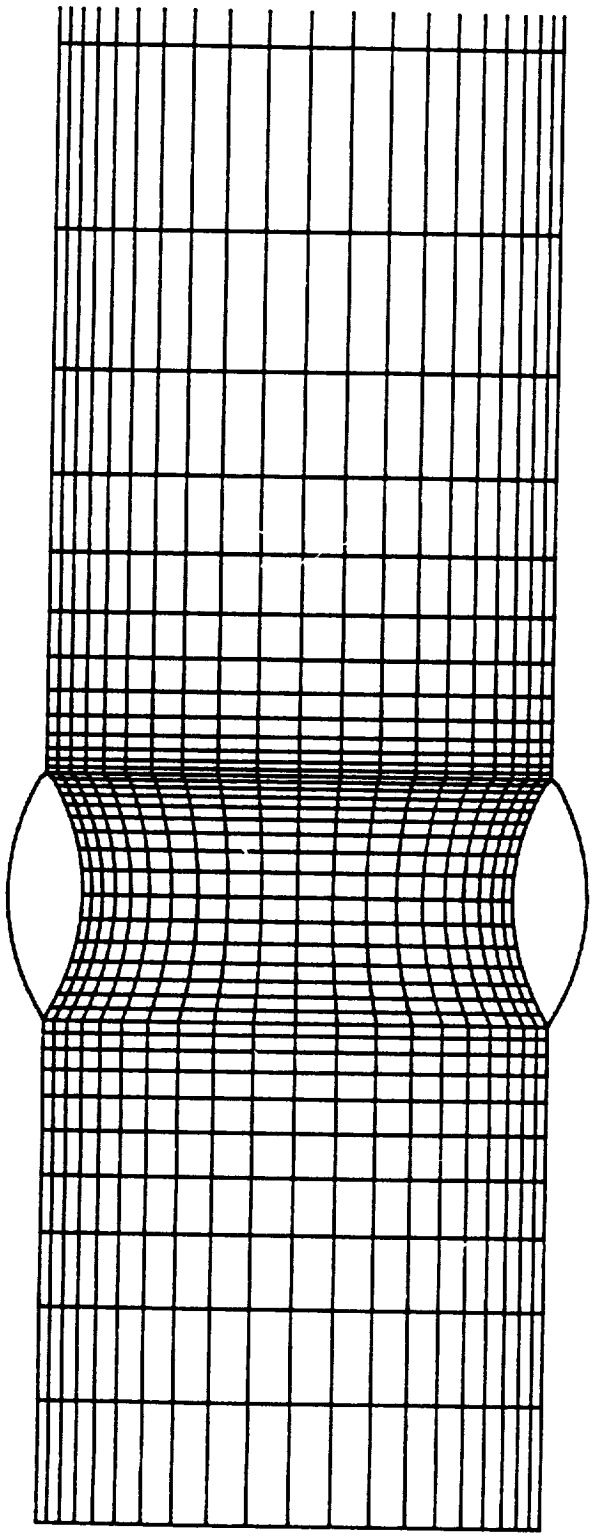

FIG. 5. TYPICAL GRID, WITH REDUCED CLUSTERING.

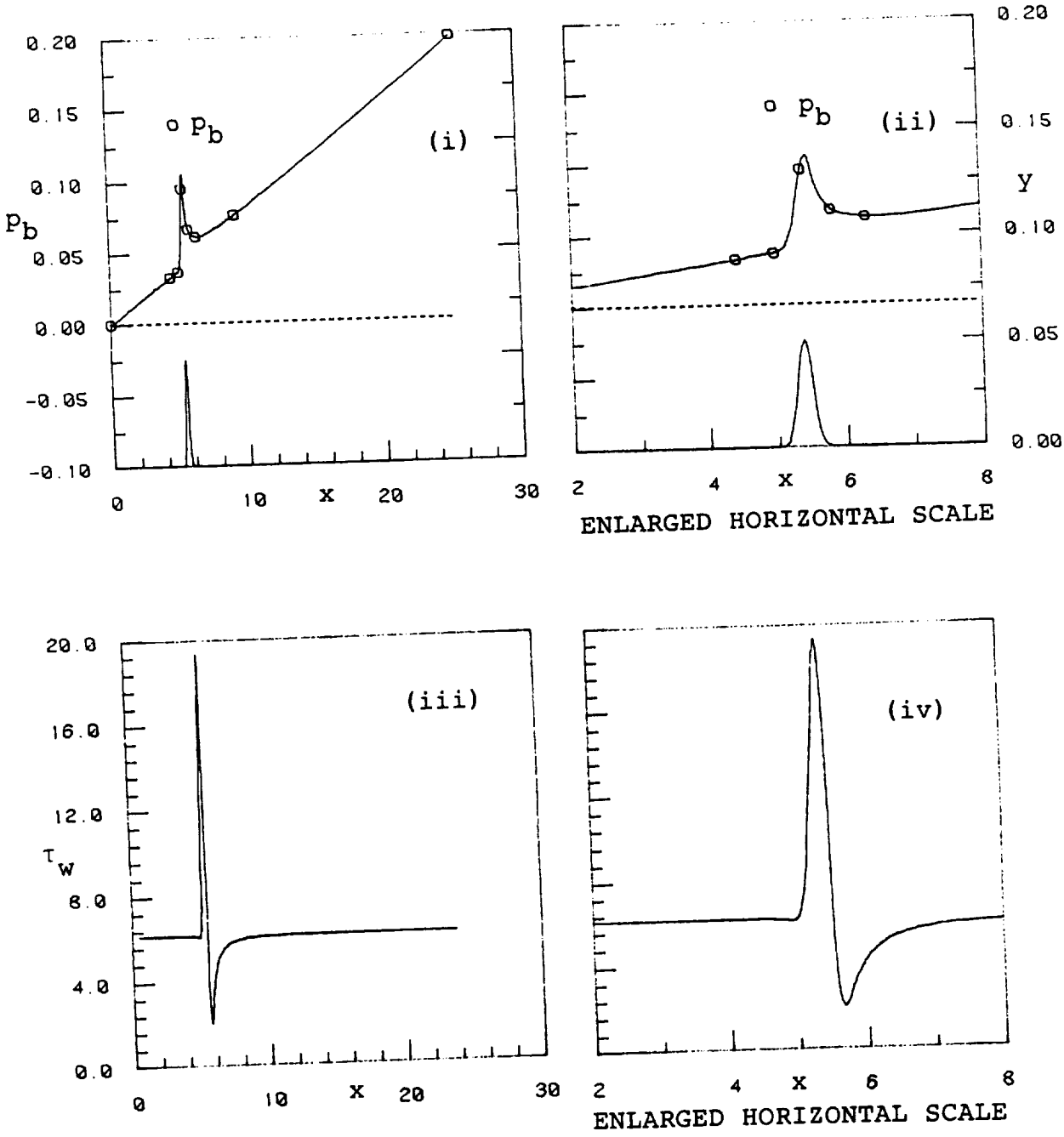

a. t/h = 0.1

FIG. 6. WALL-PRESSURE AND WALL-SHEAR PARAMETER DISTRIBUTIONS FOR EXPONENTIAL CHANNEL CONFIGURATION, Re = 1500.

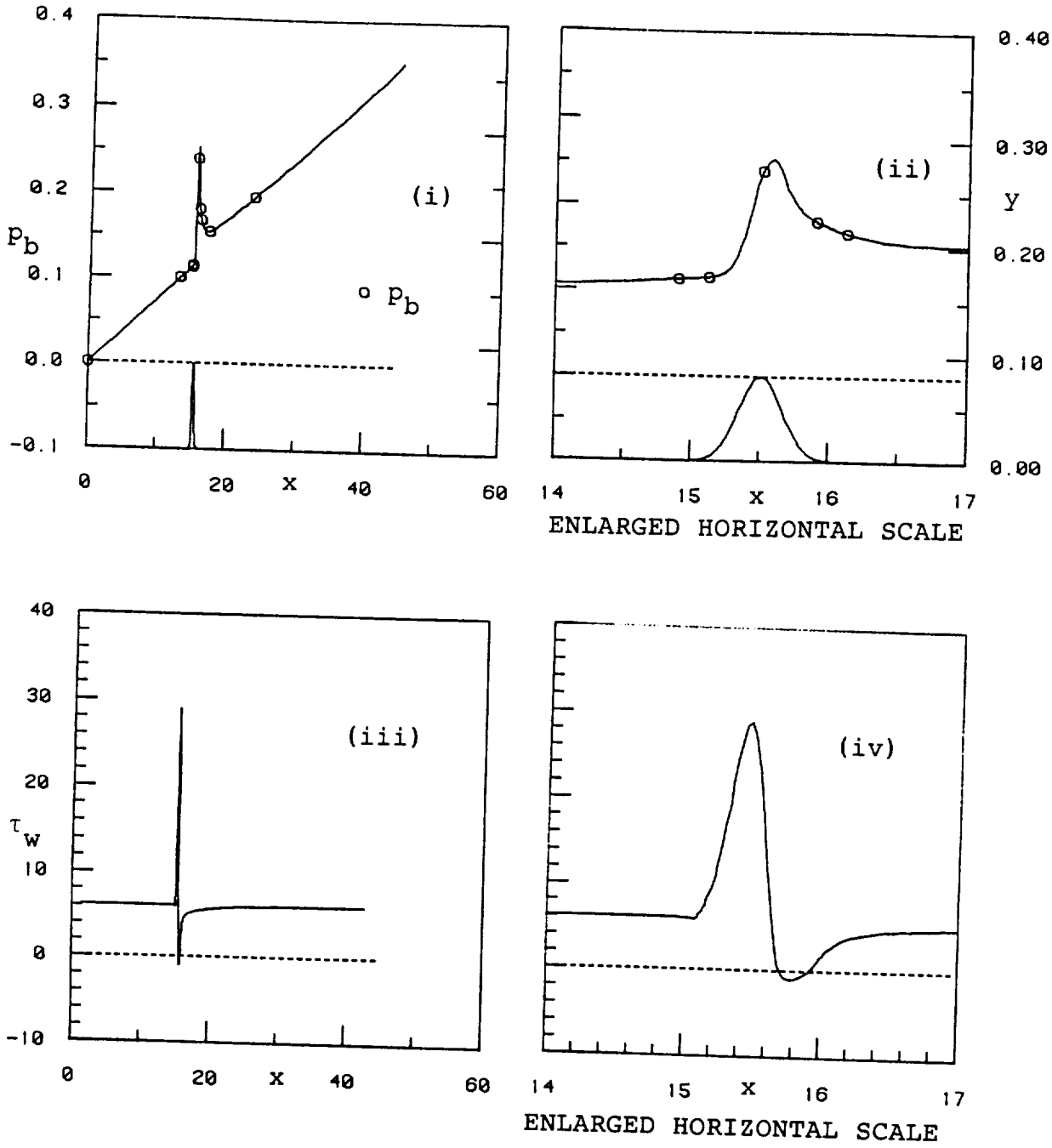

b. t/h = 0.16

FIG. 6 (CONT'D). WALL-PRESSURE AND WALL-SHEAR PARAMETER DISTRIBUTIONS FOR EXPONENTIAL CHANNEL CONFIGURATION, Re = 1500.

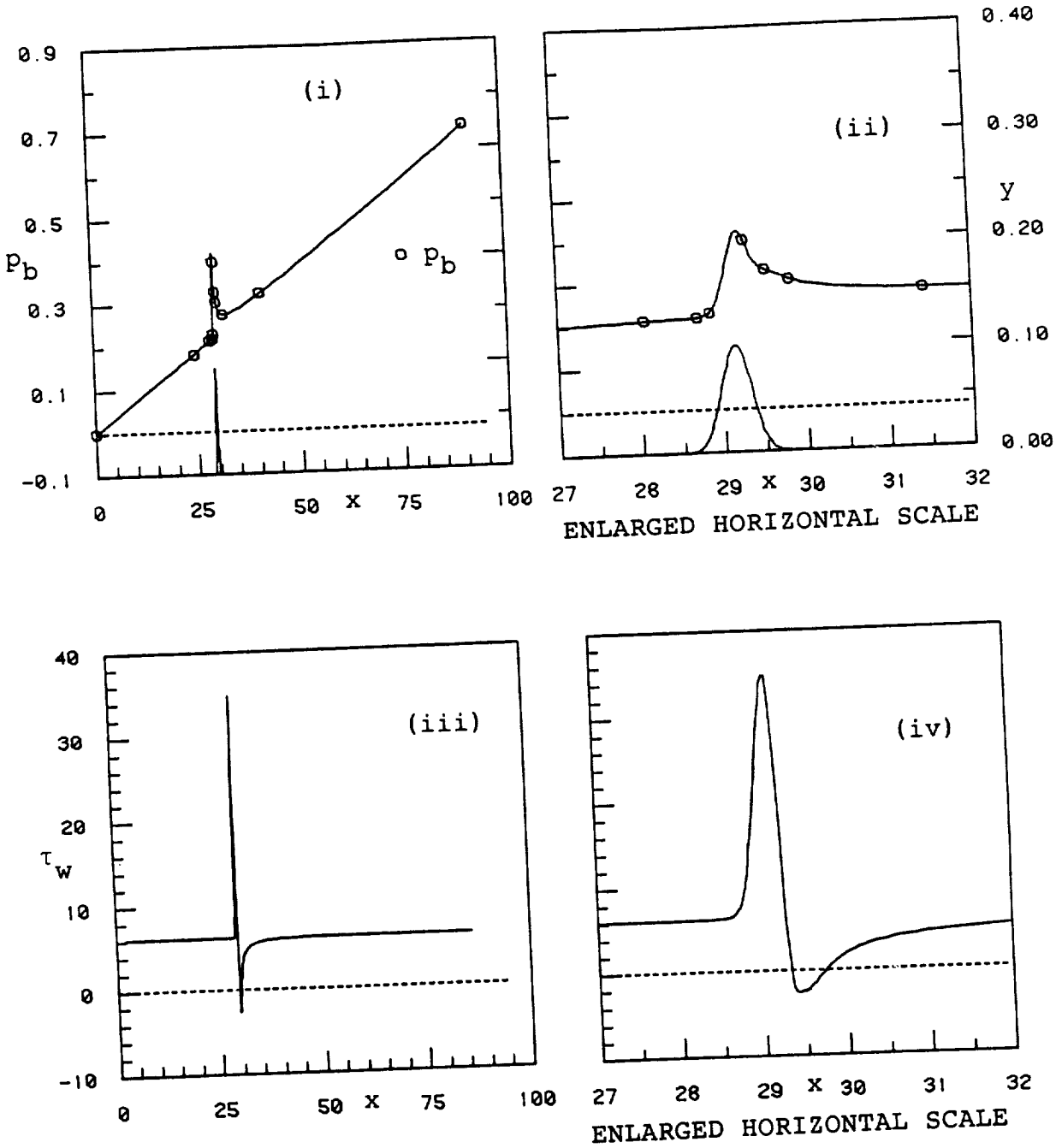

c. t/h = 0.2

FIG. 6 (CONCLUDED). WALL-PRESSURE AND WALL-SHEAR PARAMETER DISTRIBUTIONS FOR EXPONENTIAL CHANNEL CONFIGURATION, Re = 1500.

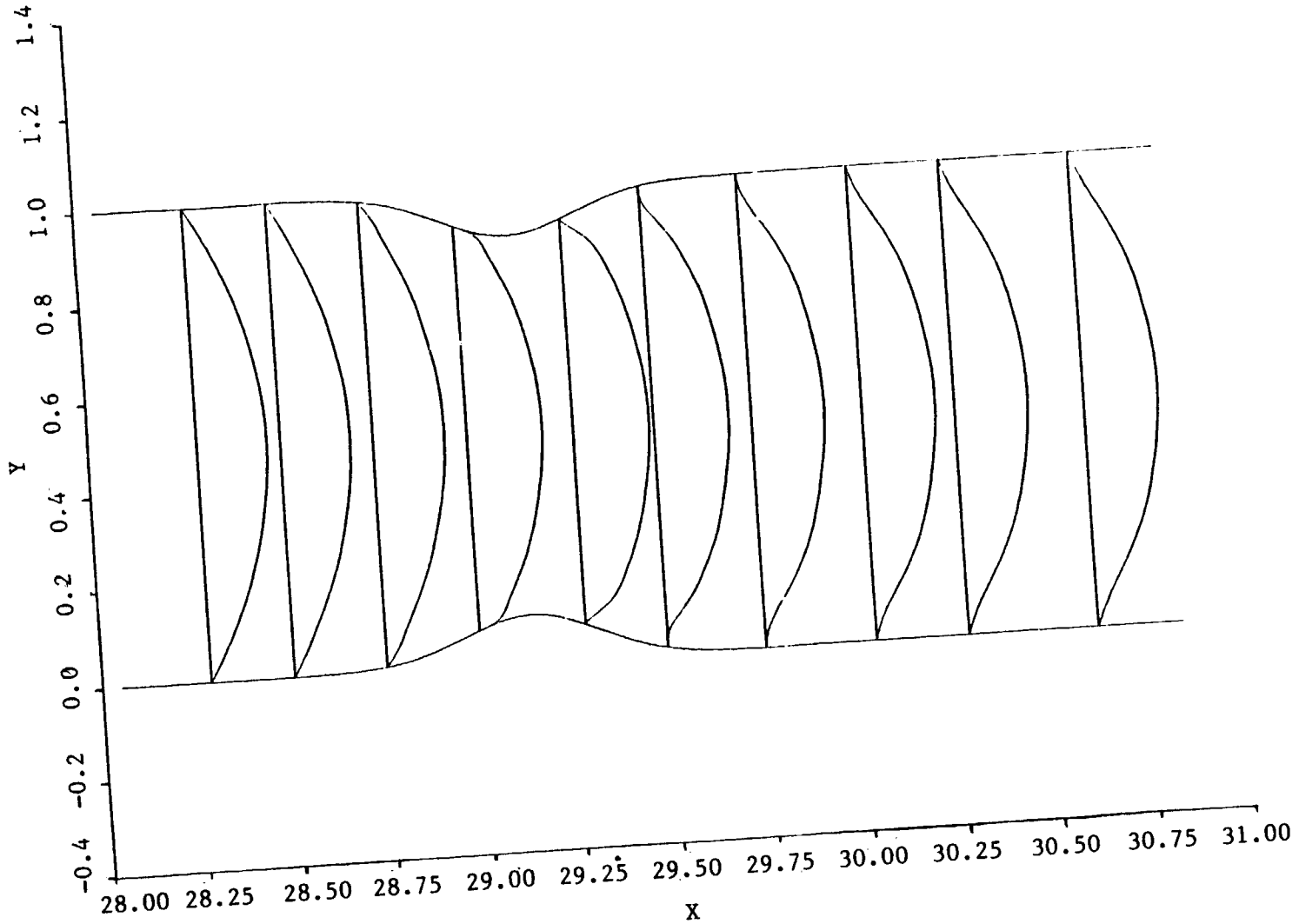

FIG. 7. STREAMWISE VELOCITY PROFILES FOR AN EXPONENTIAL CHANNEL, Re = 1500, t/h = 0.2.

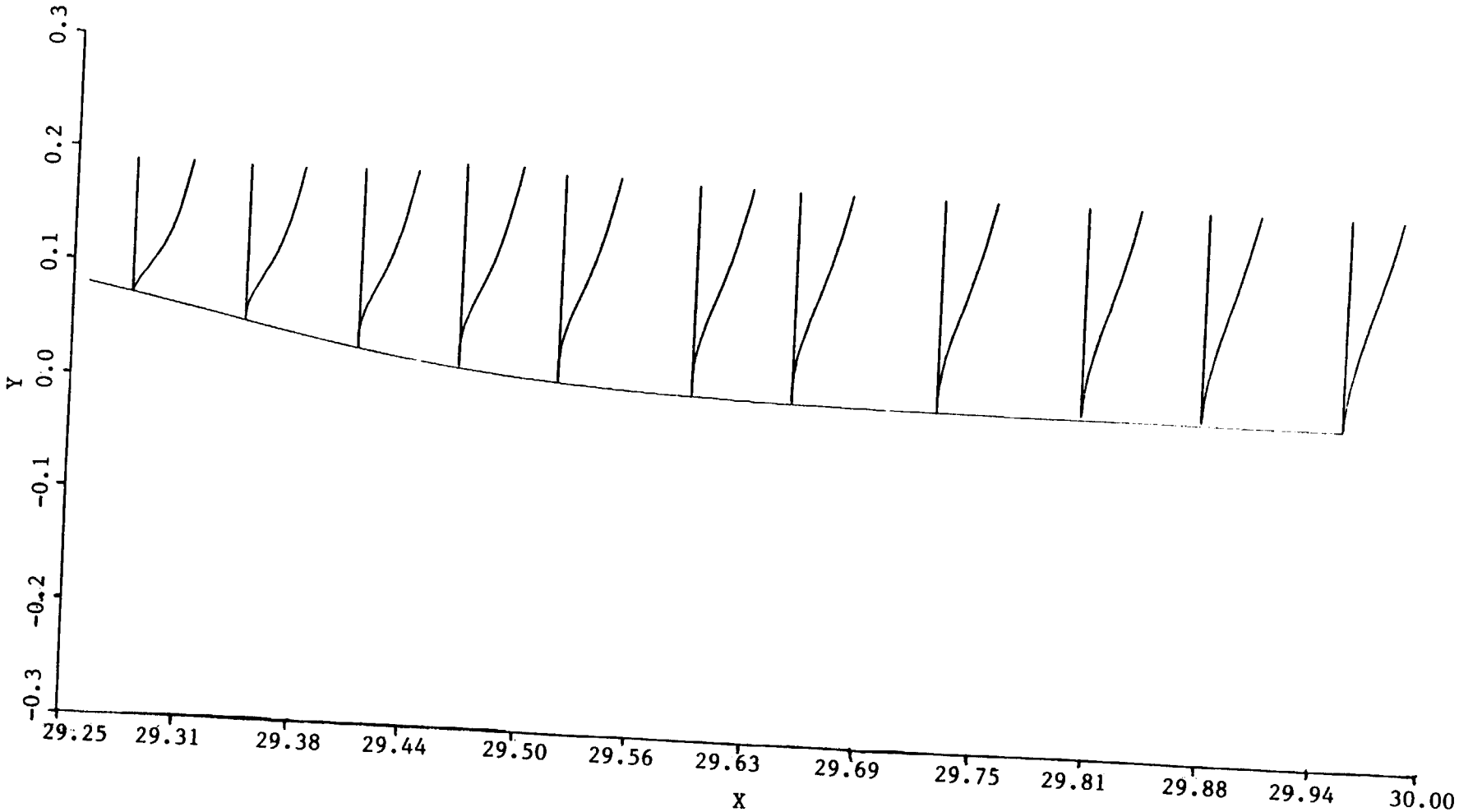

FIG. 7b. ENLARGED VIEW OF WALL REGION NEAR SEPARATION

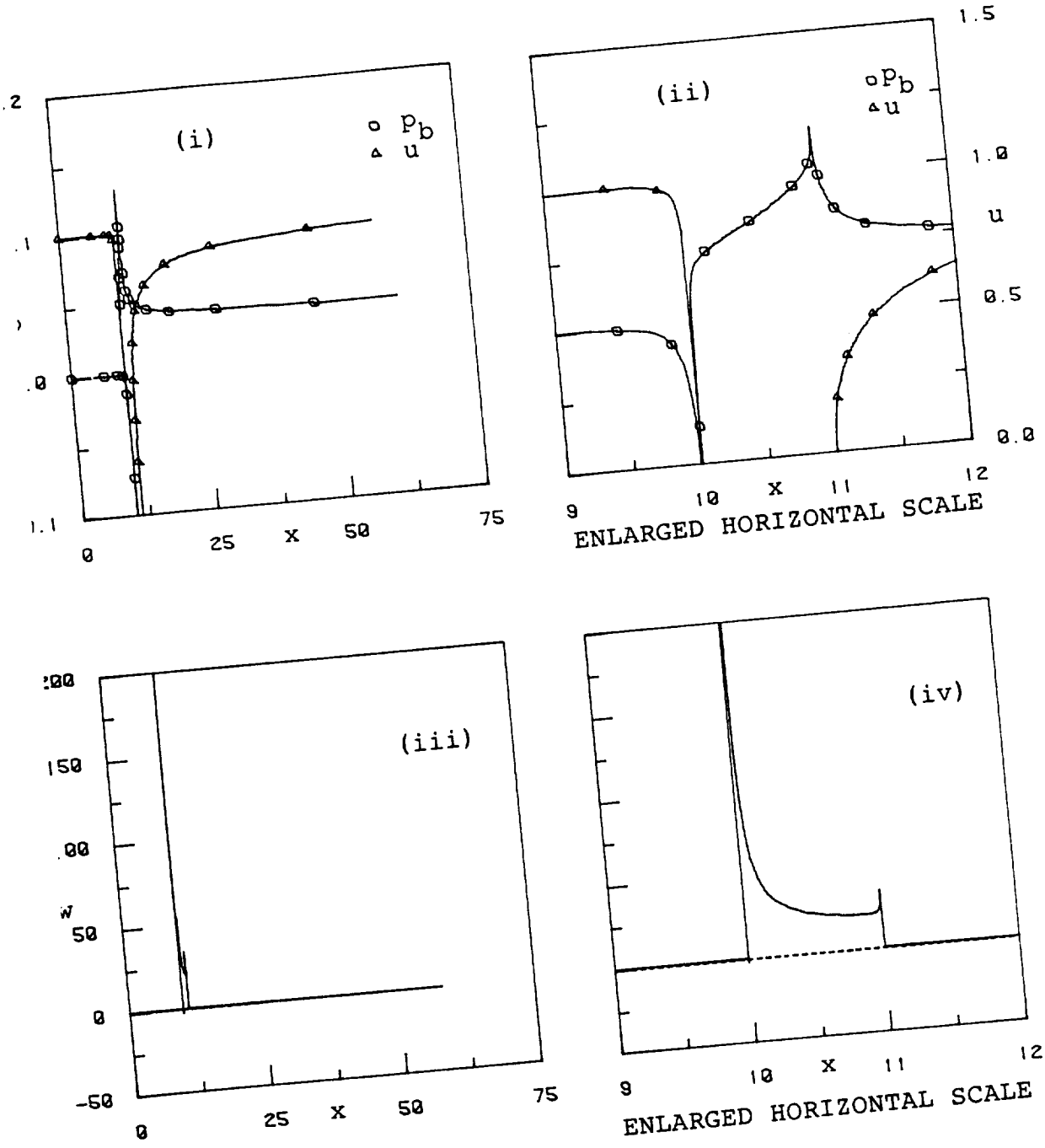

a. Re = 1500

FIG. 8. WALL-PRESSURE, WAKE-CENTERLINE VELOCITY AND WALL-SHEAR PARAMETER DISTRIBUTIONS FOR A CASCADE OF FINITE FLAT PLATES.

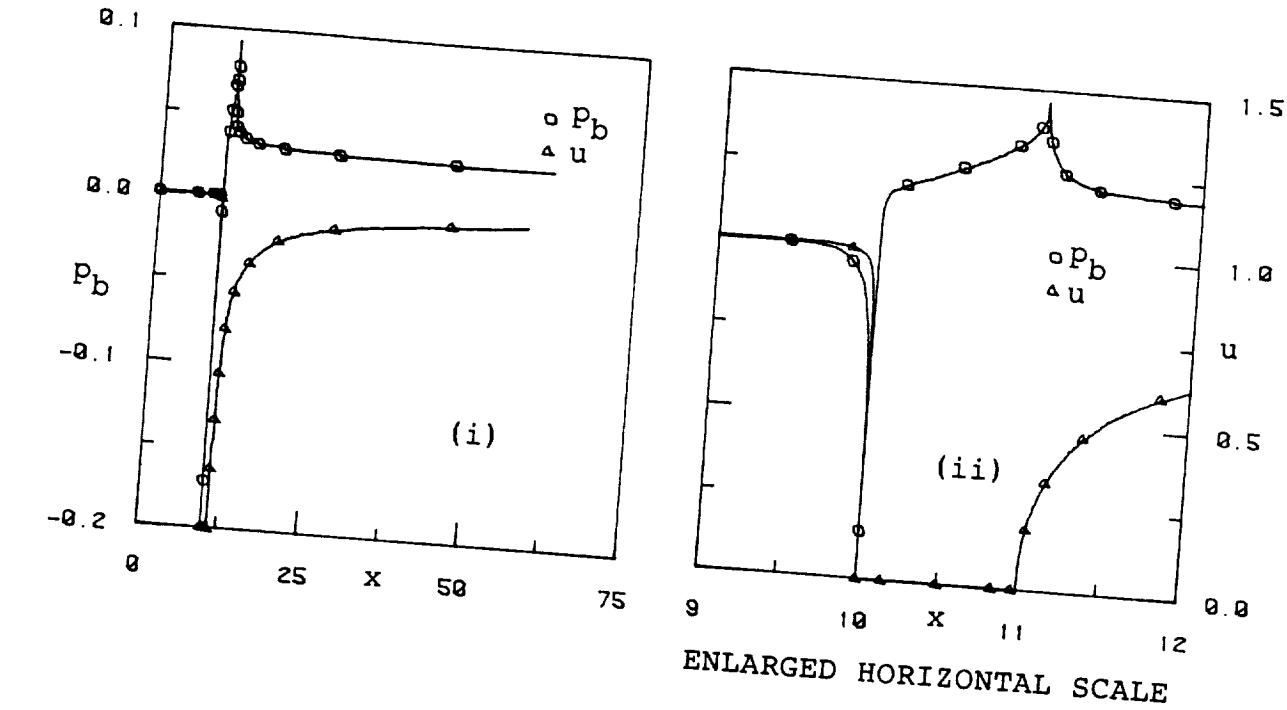

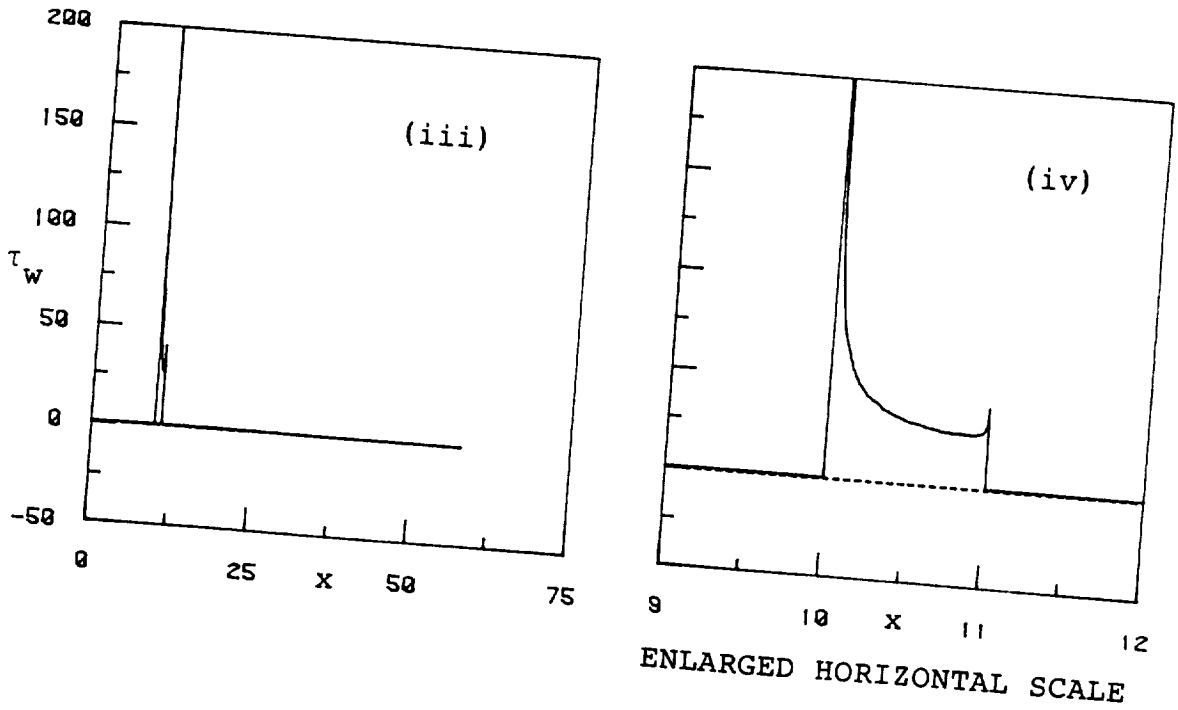

b. Re = 3100

FIG. 8 (CONT'D). WALL-PRESSURE, WAKE-CENTERLINE VELOCITY AND WALL-SHEAR PARAMETER DISTRIBUTIONS FOR A CASCADE OF FINITE FLAT PLATES.

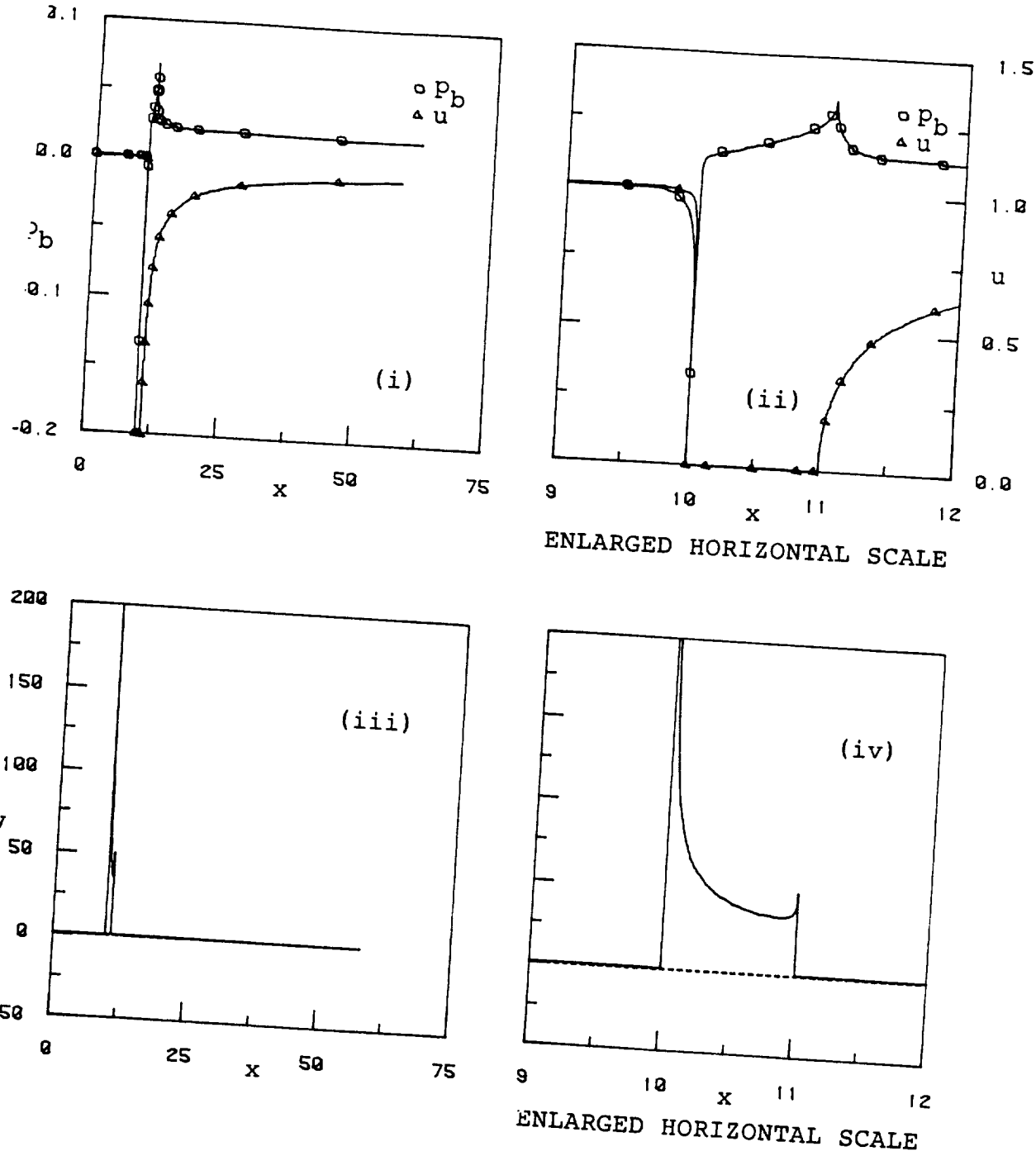

c. Re = 6200

FIG. 8 (CONT'D). WALL-PRESSURE, WAKE-CENTERLINE VELOCITY AND WALL-SHEAR PARAMETER DISTRIBUTIONS FOR A CASCADE OF FINITE FLAT PLATES.

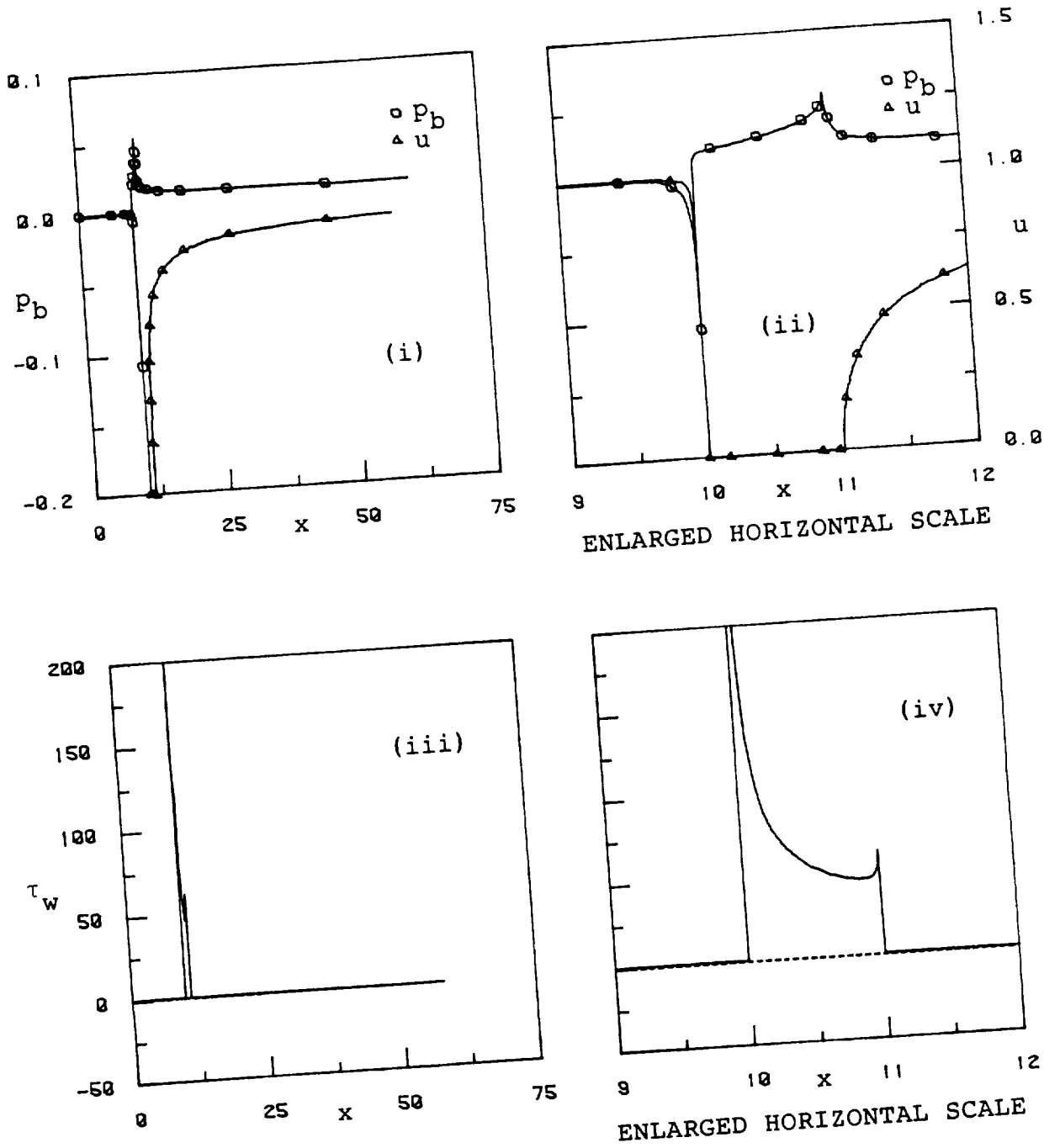

d. Re = 11000

FIG. 8 (CONT'D). WALL-PRESSURE, WAKE-CENTERLINE VELOCITY AND WALL-SHEAR PARAMETER DISTRIBUTIONS FOR A CASCADE OF FINITE FLAT PLATES.

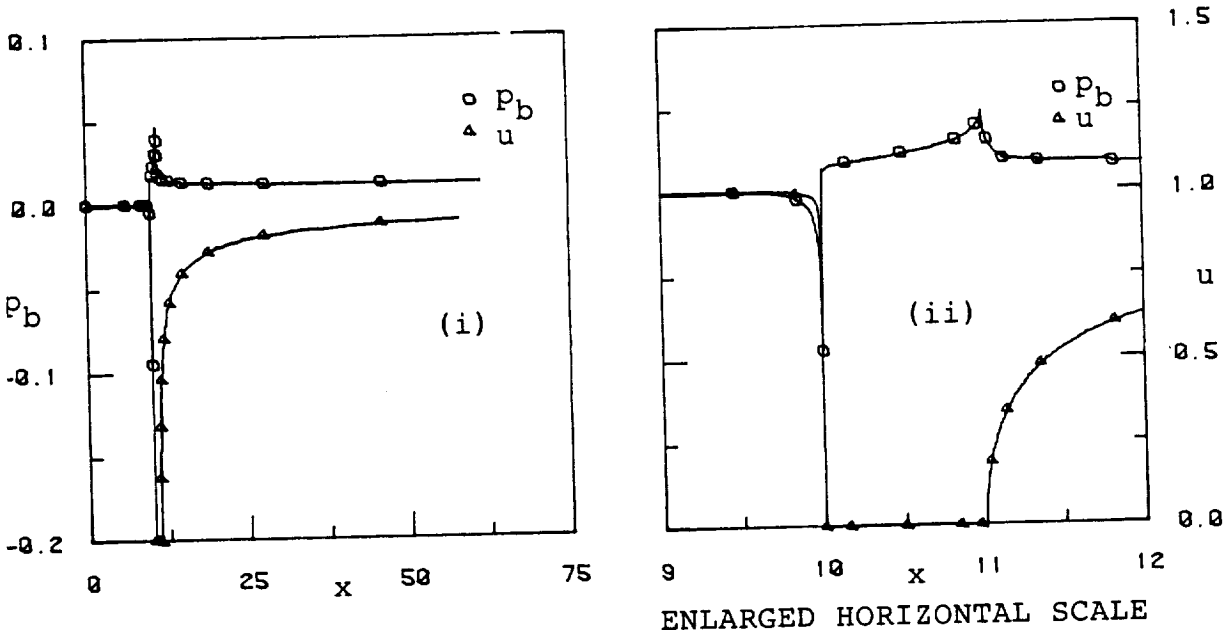

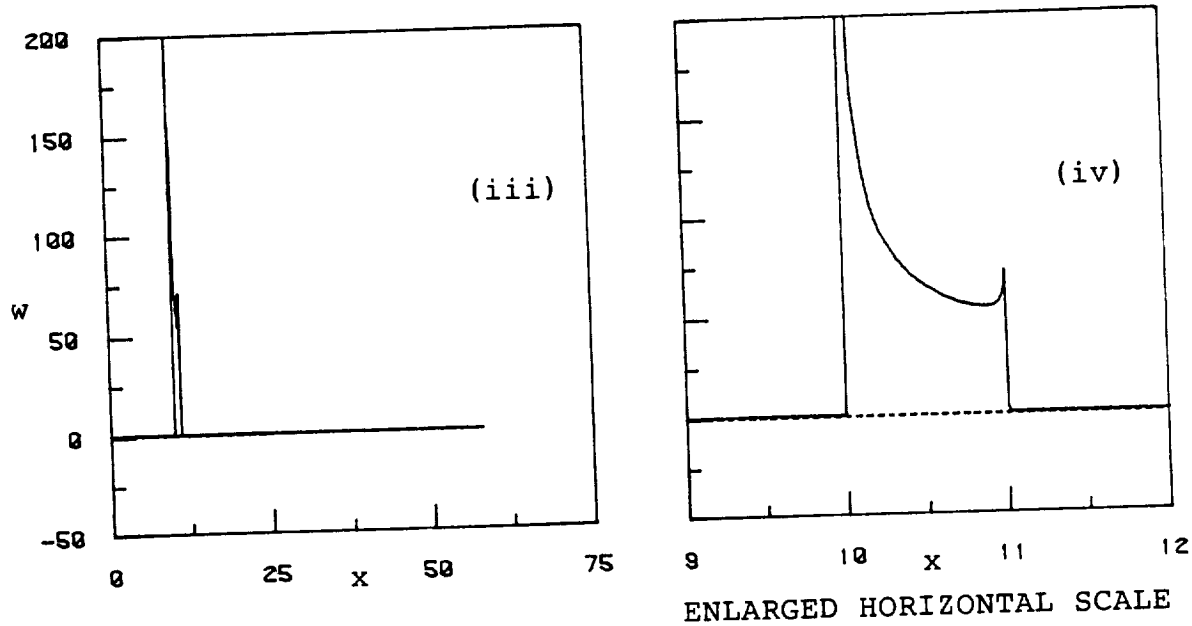

e. Re = 16000

FIG. 8 (CONCLUDED). WALL-PRESSURE, WAKE-CENTERLINE VELOCITY AND WALL-SHEAR PARAMETER DISTRIBUTIONS FOR A CASCADE OF FINITE FLAT PLATES.

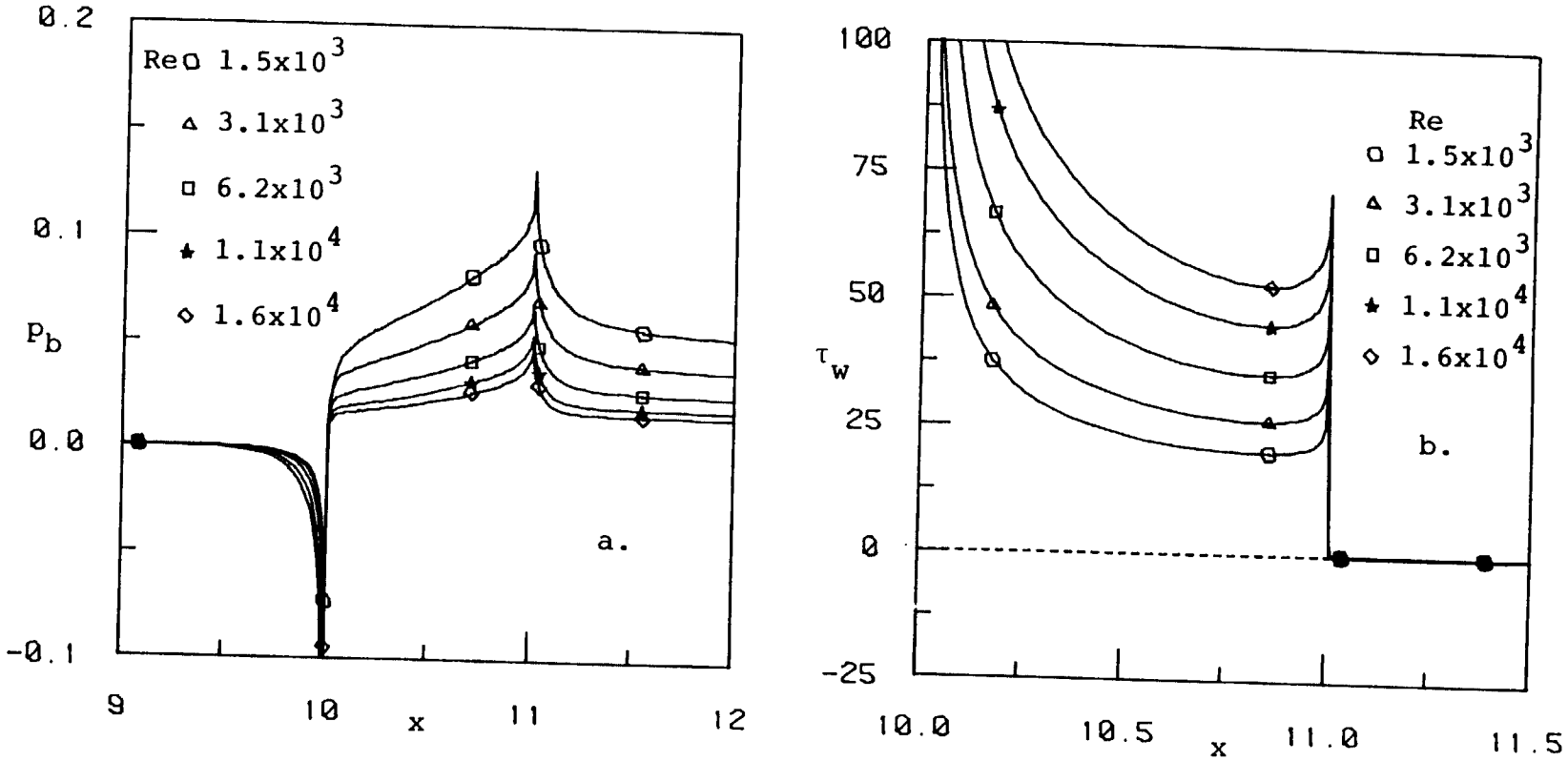

FIG. 9. COMPARISON OF WALL-PRESSURE AND WALL-SHEAR PARAMETER DISTRIBUTIONS FOR VARIOUS Re FOR A CASCADE OF FINITE FLAT PLATES.

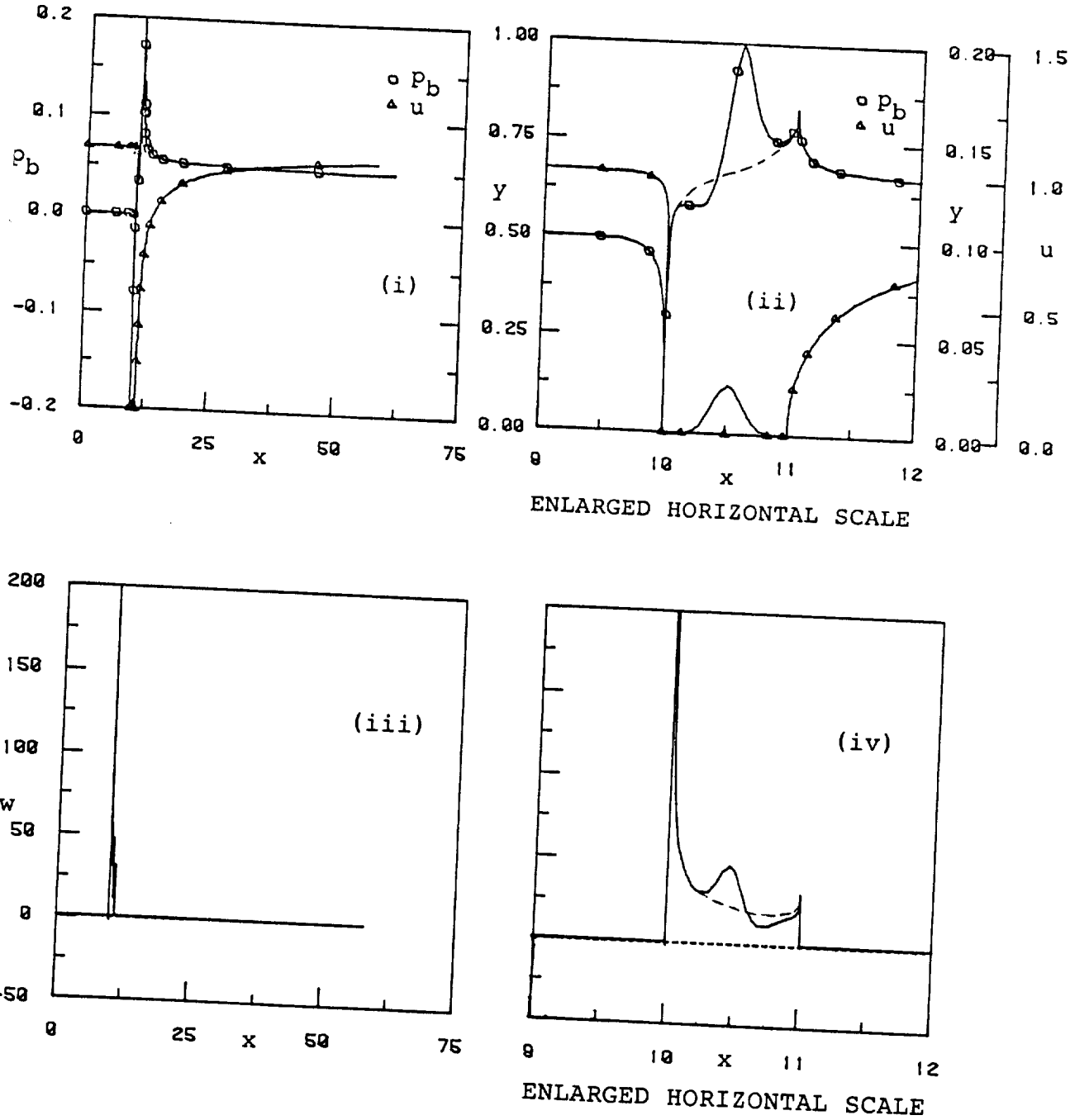

a. t/c = 0.05

FIG. 10. WALL-PRESSURE, WAKE-CENTERLINE VELOCITY AND WALL-SHEAR PARAMETER DISTRIBUTIONS FOR A CASCADE OF EXPONENTIAL AIRFOILS, Re = 1500.

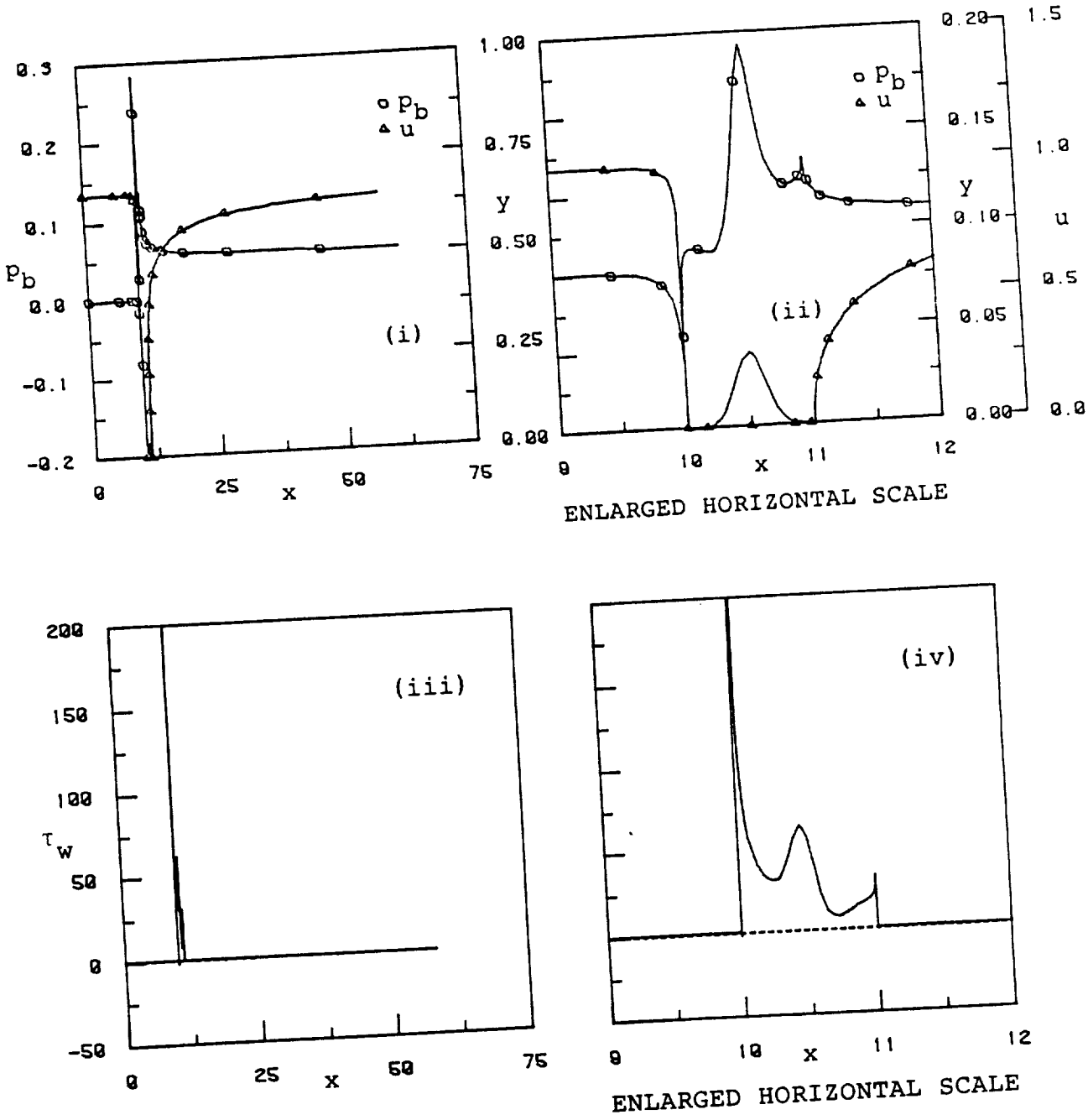

b. t/c = 0.075

FIG. 10 (CONT'D). WALL-PRESSURE, WAKE-CENTERLINE VELOCITY AND WALL-SHEAR PARAMETER DISTRIBUTIONS FOR A CASCADE OF EXPONENTIAL AIRFOILS, Re = 1500.

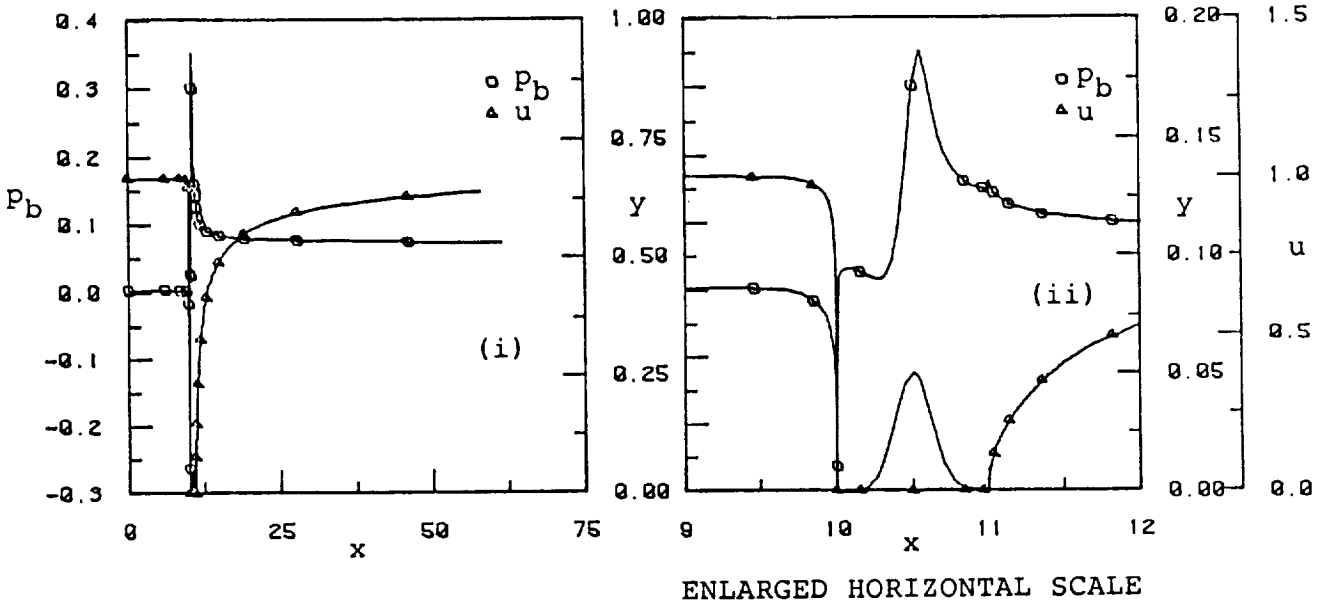

ENLARGED HORIZONTAL SCALE

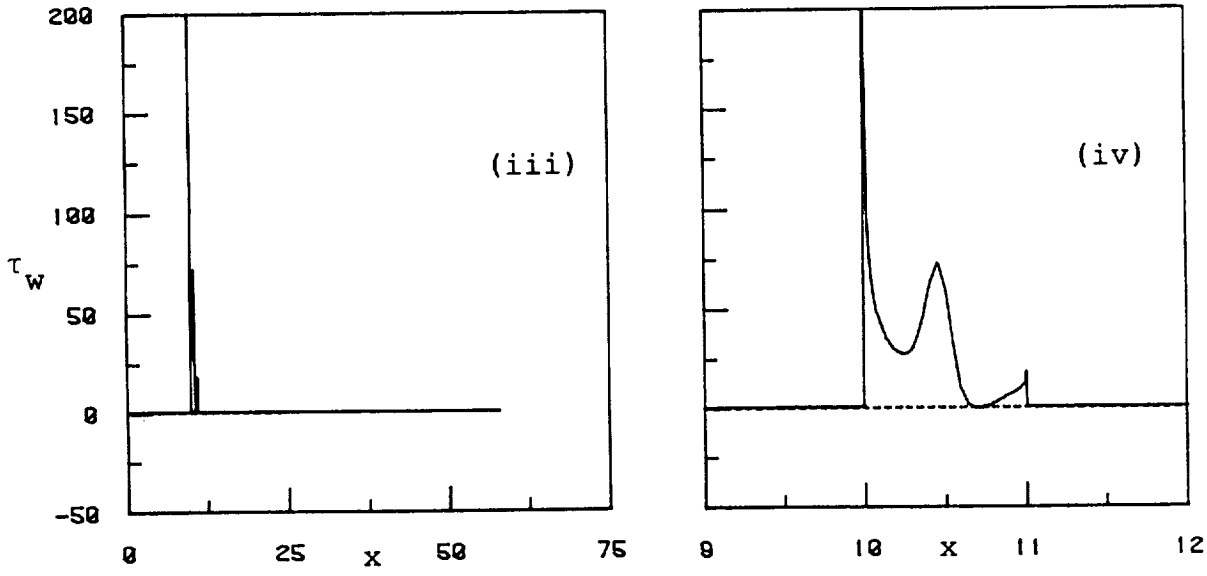

ENLARGED HORIZONTAL SCALE

c. t/c = 0.1

FIG. 10 (CONCLUDED). WALL-PRESSURE, WAKE-CENTERLINE VELOCITY AND WALL-SHEAR PARAMETER DISTRIBUTIONS FOR A CASCADE OF EXPONENTIAL AIRFOILS, Re = 1500.

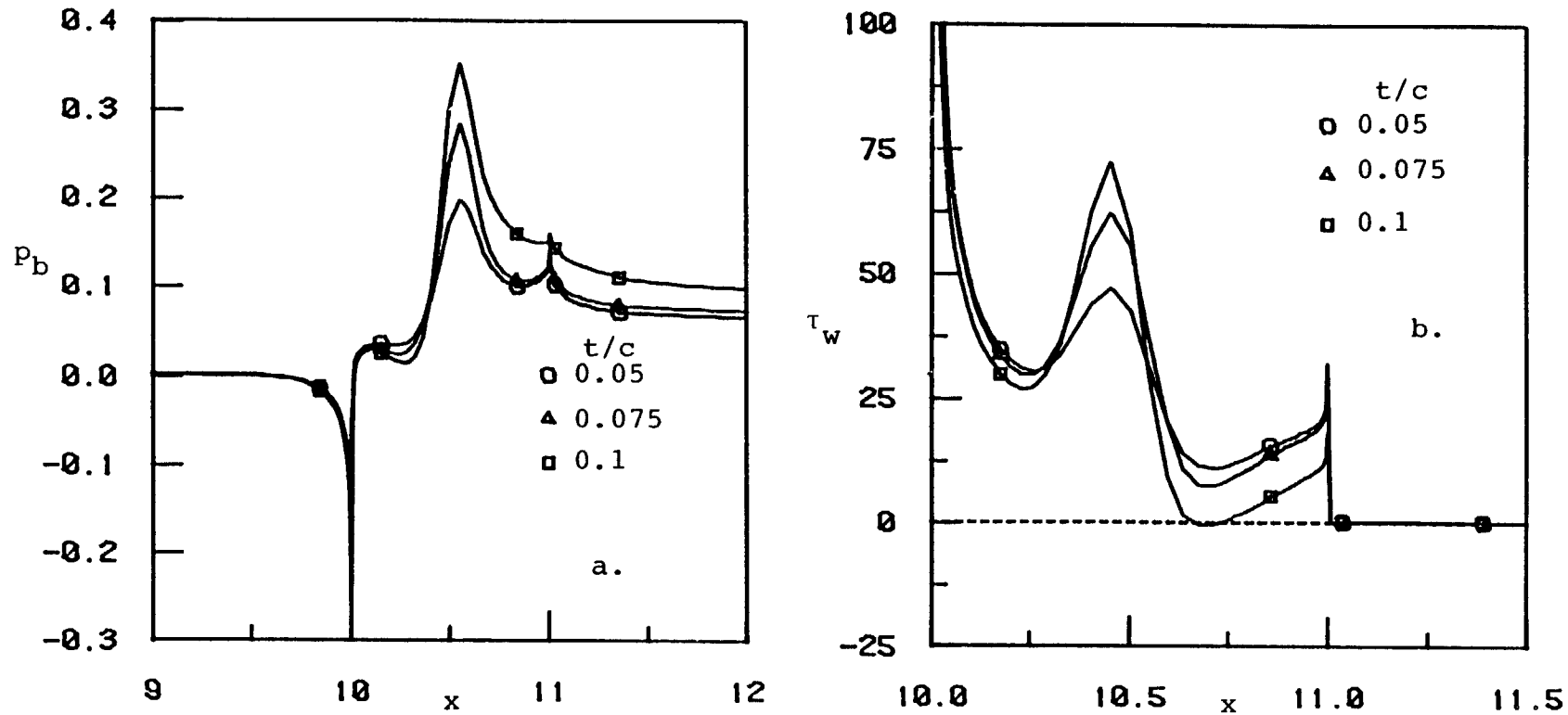

FIG. 11. COMPARISON OF WALL-PRESSURE AND WALL-SHEAR PARAMETER DISTRIBUTIONS FOR VARIOUS t/c FOR A CASCADE OF EXPONENTIAL AIRFOILS.

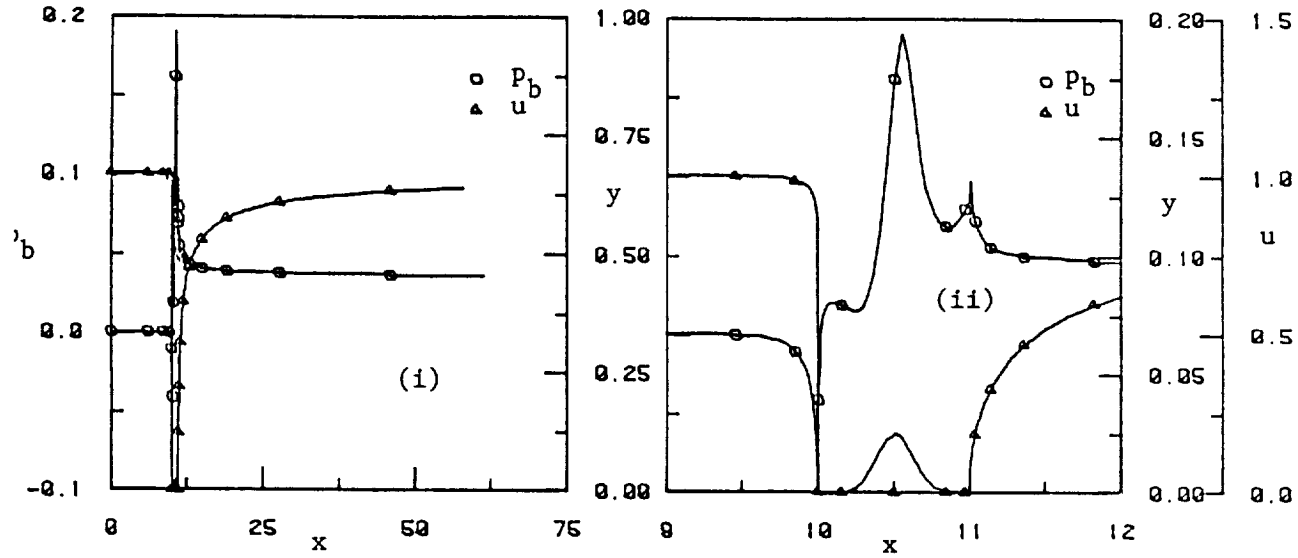

ENLARGED HORIZONTAL SCALE

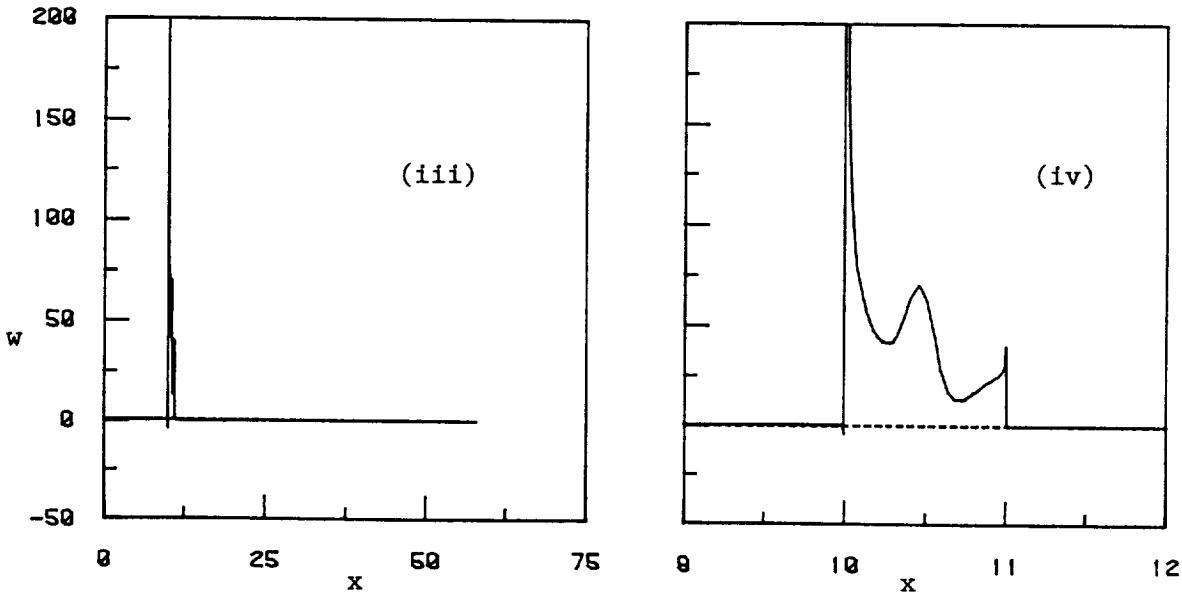

ENLARGED HORIZONTAL SCALE

a. Re = 3100

FIG. 12. WALL-PRESSURE, WAKE-CENTERLINE VELOCITY AND WALL-SHEAR PARAMETER DISTRIBUTIONS FOR A CASCADE OF EXPONENTIAL AIRFOILS, t/c = 0.05.

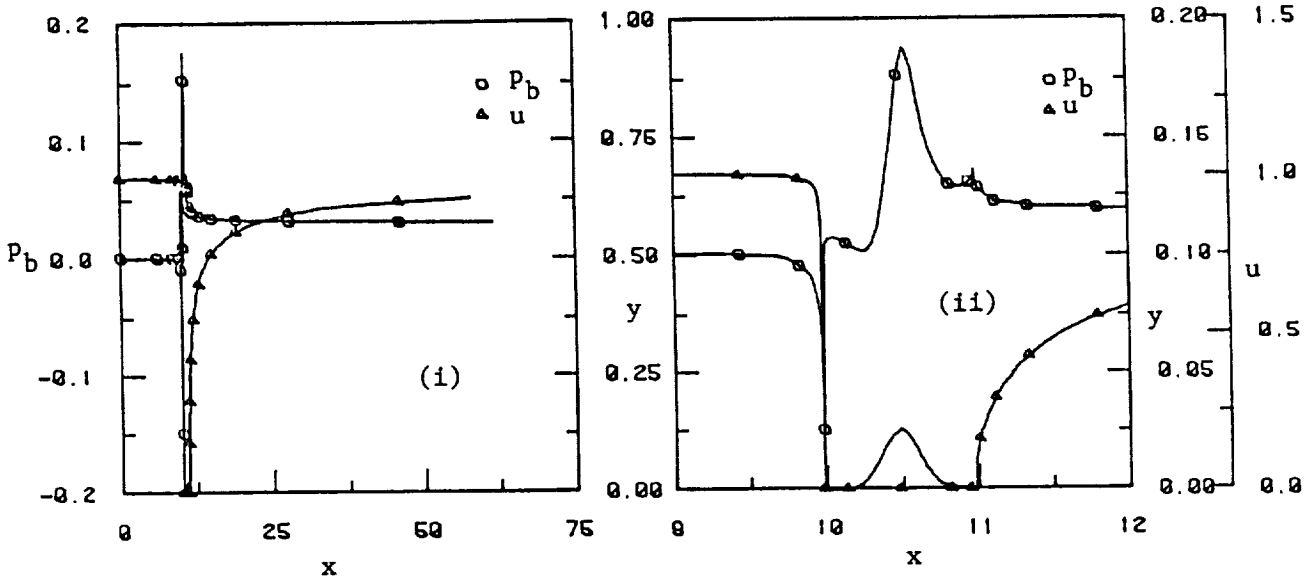

ENLARGED HORIZONTAL SCALE

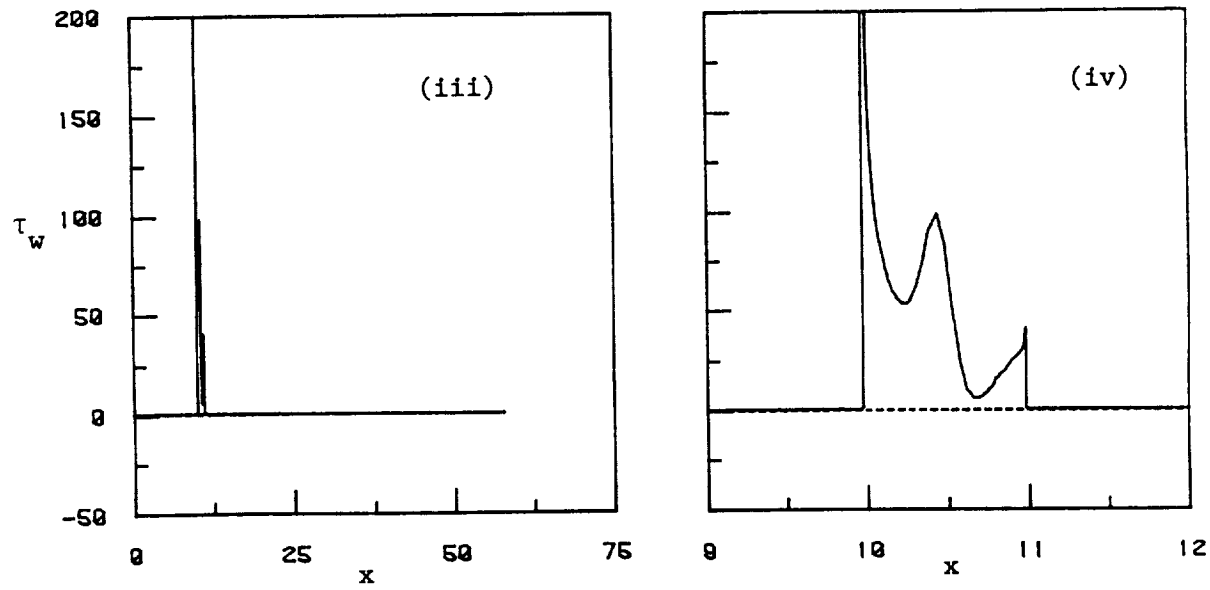

ENLARGED HORIZONTAL SCALE

b. Re = 6200

FIG. 12 (CONT'D). WALL-PRESSURE, WAKE-CENTERLINE VELOCITY AND WALL-SHEAR PARAMETER DISTRIBUTIONS FOR A CASCADE OF EXPONENTIAL AIRFOILS, t/c = 0.05.

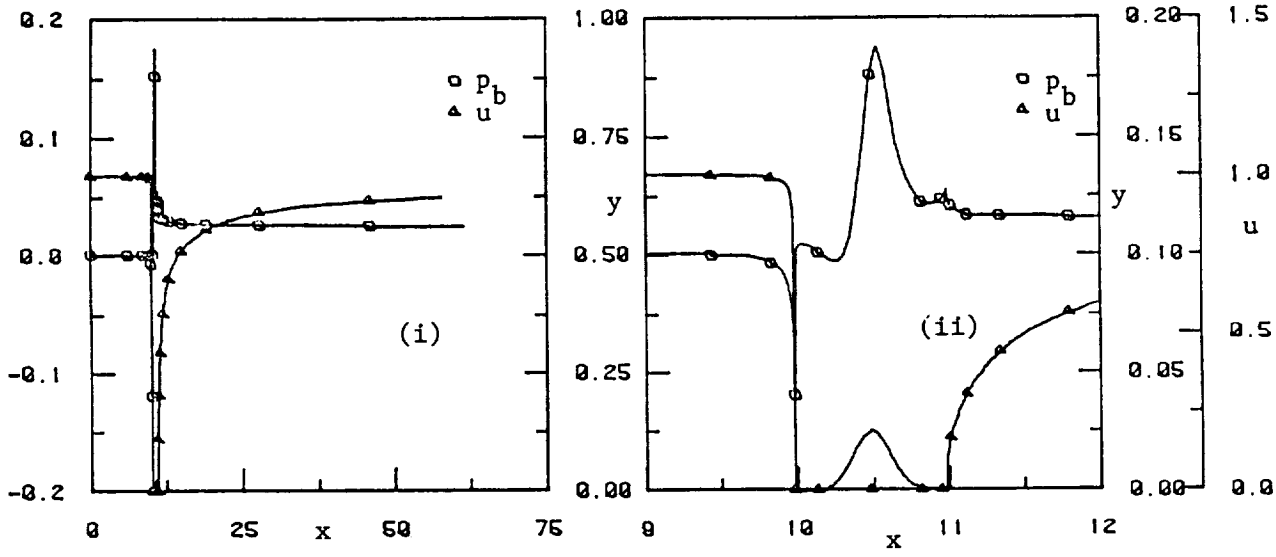

ENLARGED HORIZONTAL SCALE

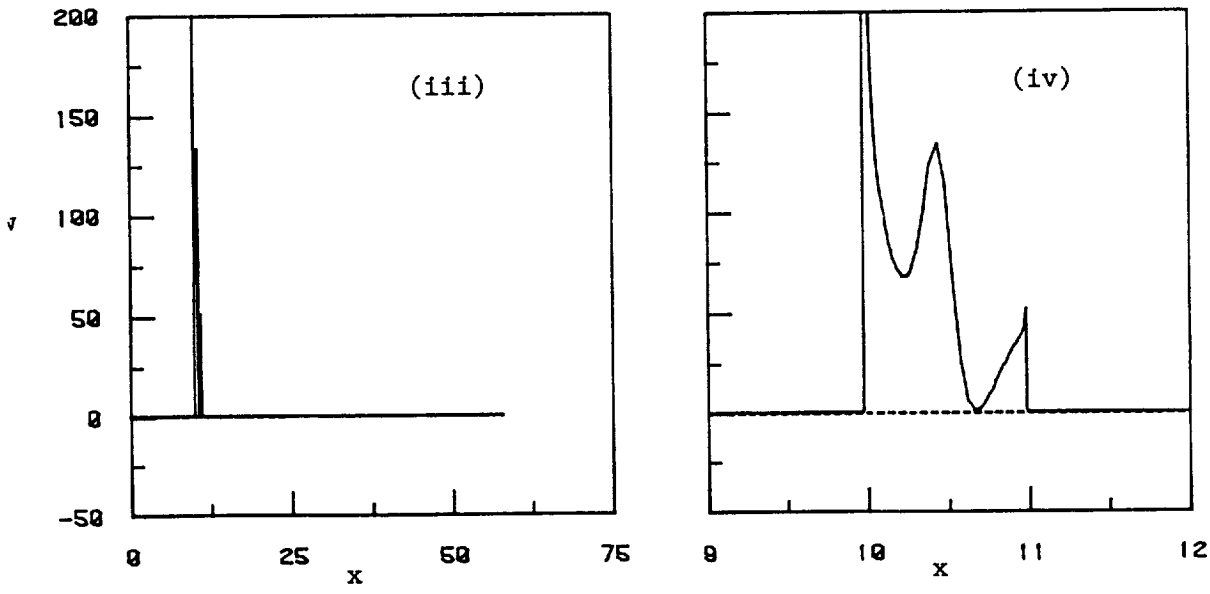

ENLARGED HORIZONTAL SCALE

c. Re = 11000

FIG. 12 (CONT'D). WALL-PRESSURE, WAKE-CENTERLINE VELOCITY AND WALL-SHEAR PARAMETER DISTRIBUTIONS FOR A CASCADE OF EXPONENTIAL AIRFOILS, t/c = 0.05.

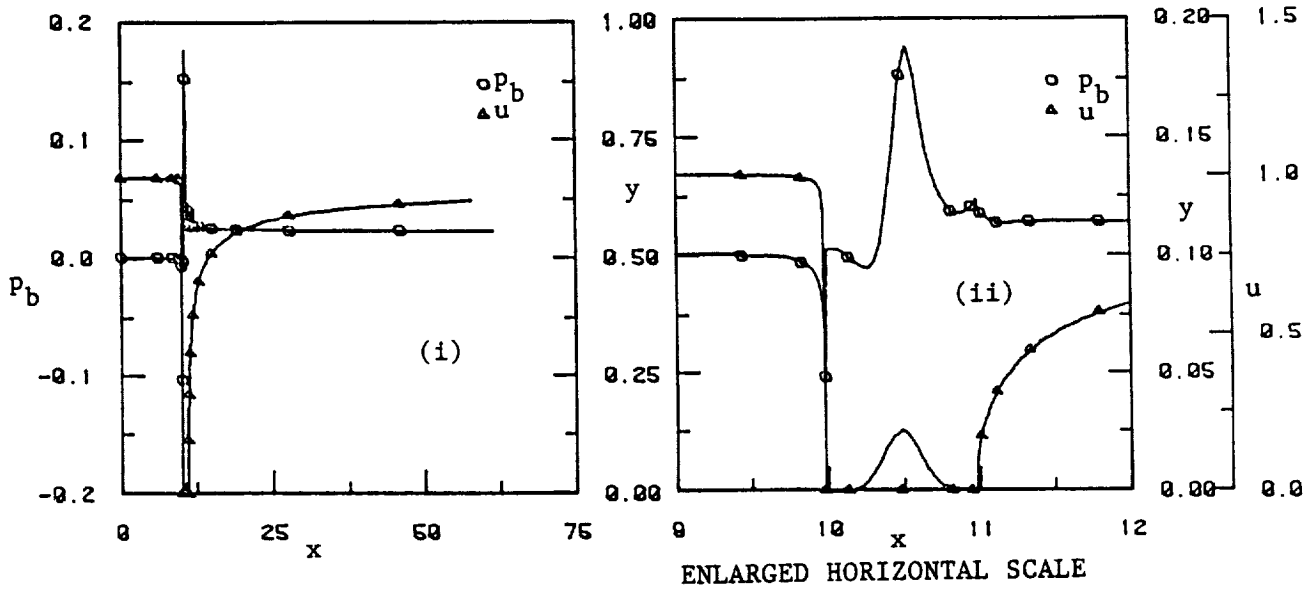

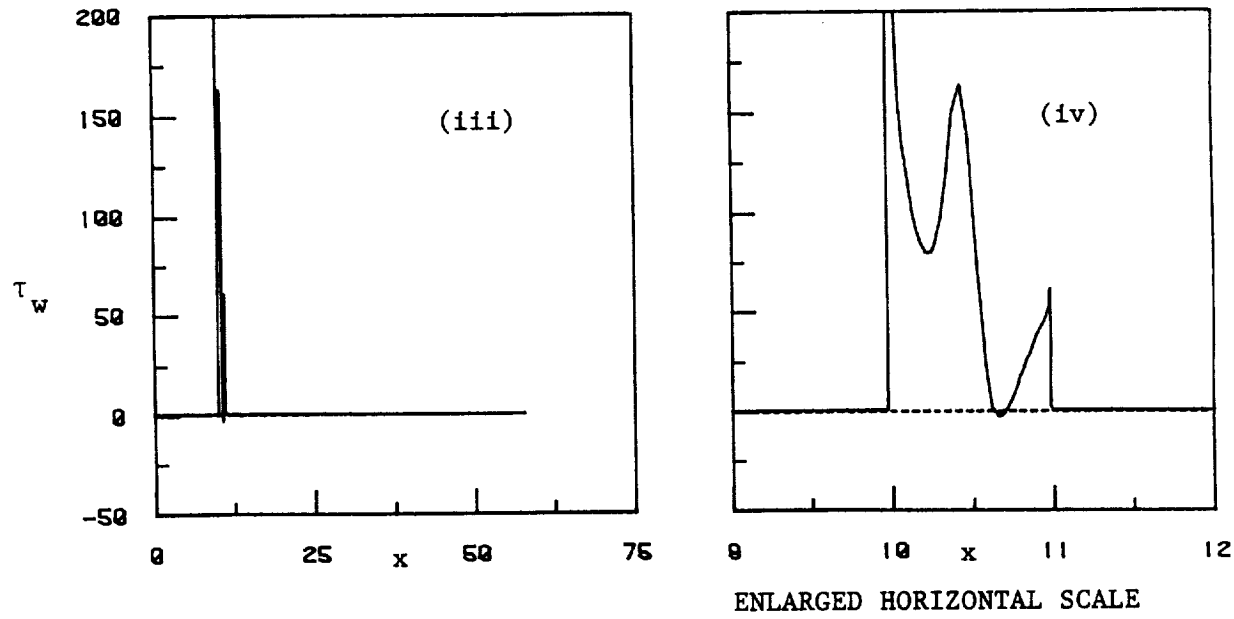

d. Re = 15000

FIG. 12 (CONCLUDED). WALL-PRESSURE, WAKE-CENTERLINE VELOCITY AND WALL-SHEAR PARAMETER DISTRIBUTIONS FOR A CASCADE OF EXPONENTIAL AIRFOILS, t/c = 0.05.

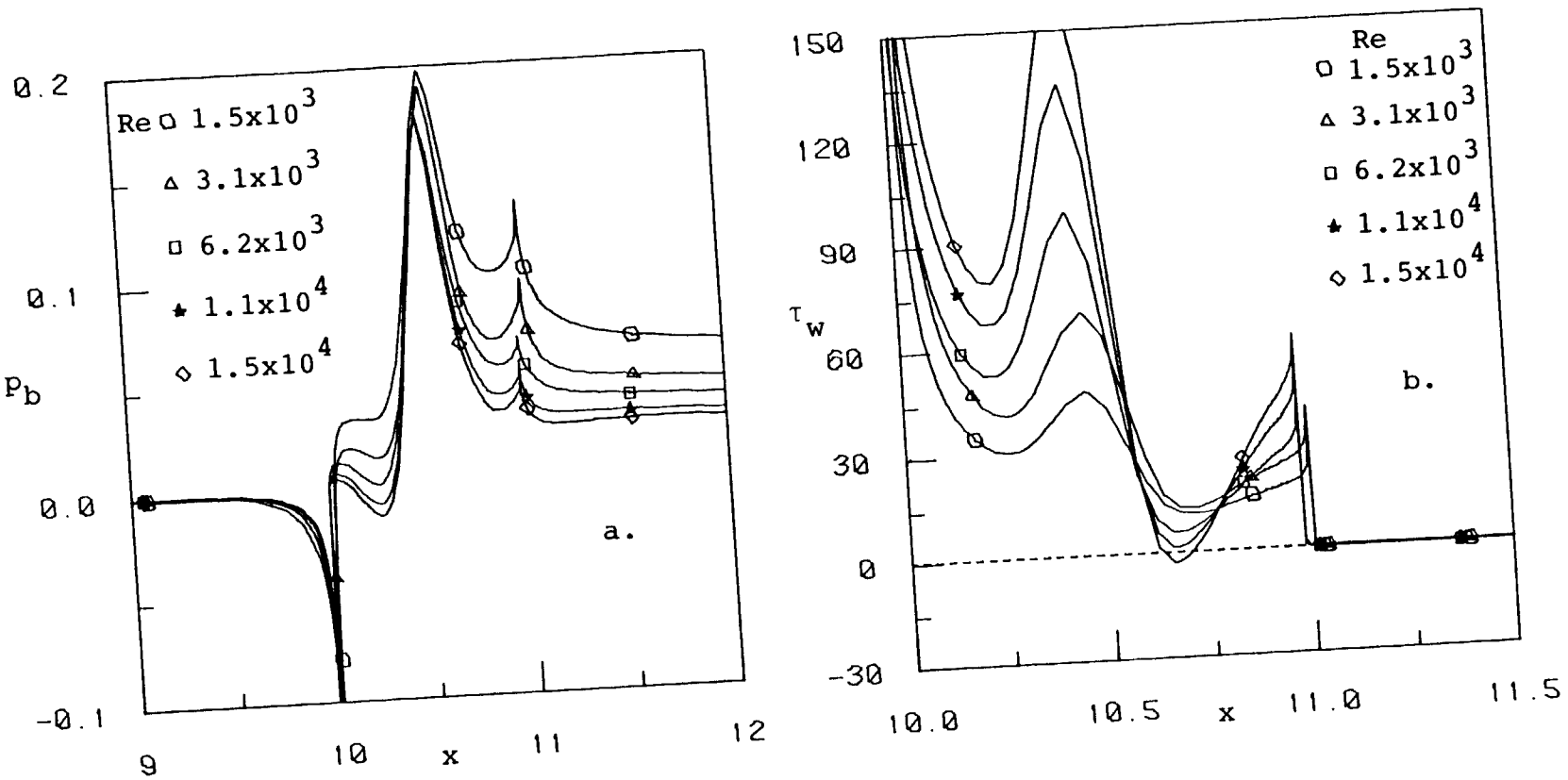

FIG. 13. COMPARISON OF WALL-PRESSURE AND WALL-SHEAR PARAMETER DISTRIBUTIONS FOR VARIOUS Re FOR A CASCADE OF EXPONENTIAL AIRFOILS.

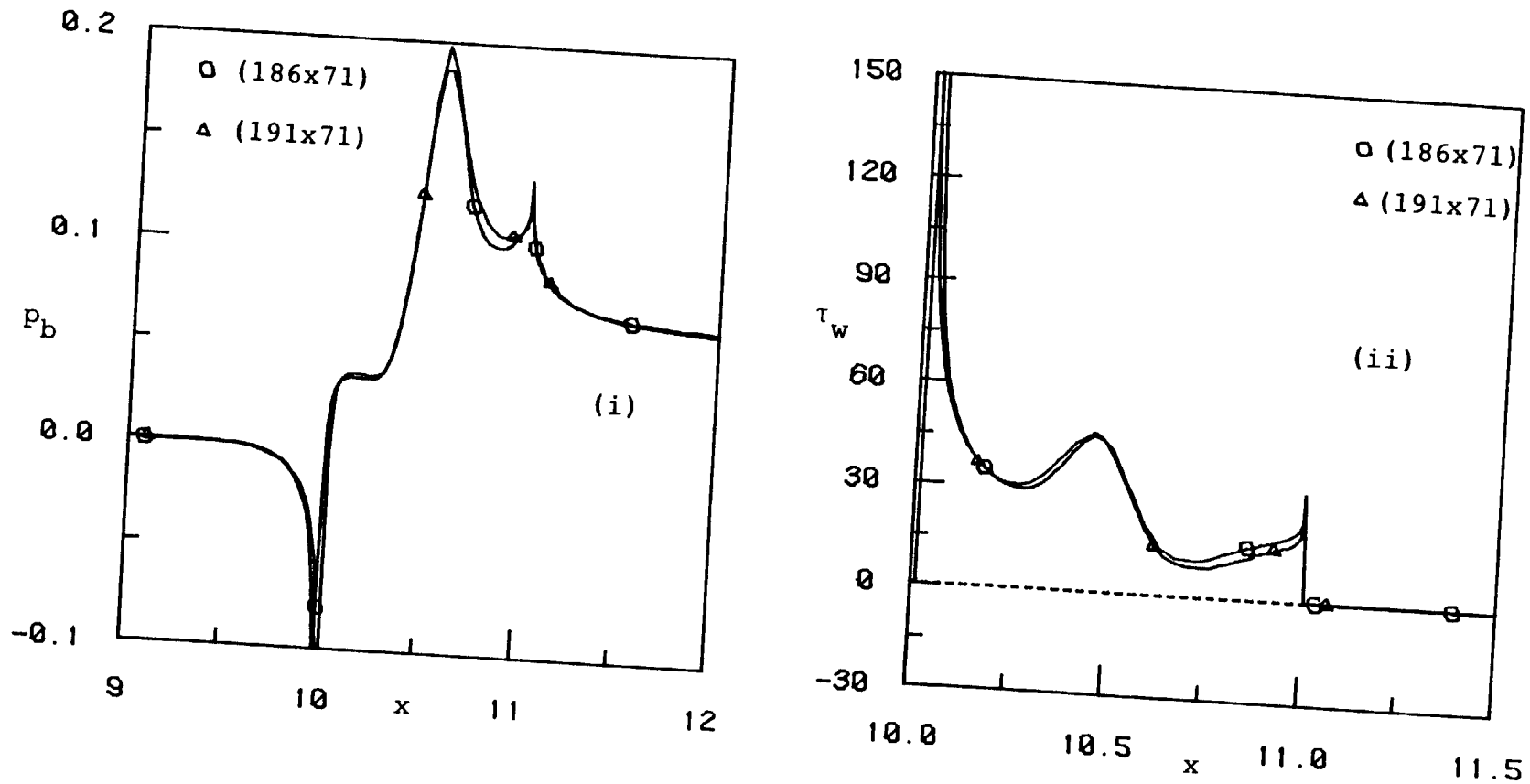

a. Re = 1500

FIG. 14. EFFECT OF GRID REFINEMENT FOR A CASCADE OF EXPONENTIAL AIRFOILS, t/c = 0.05.

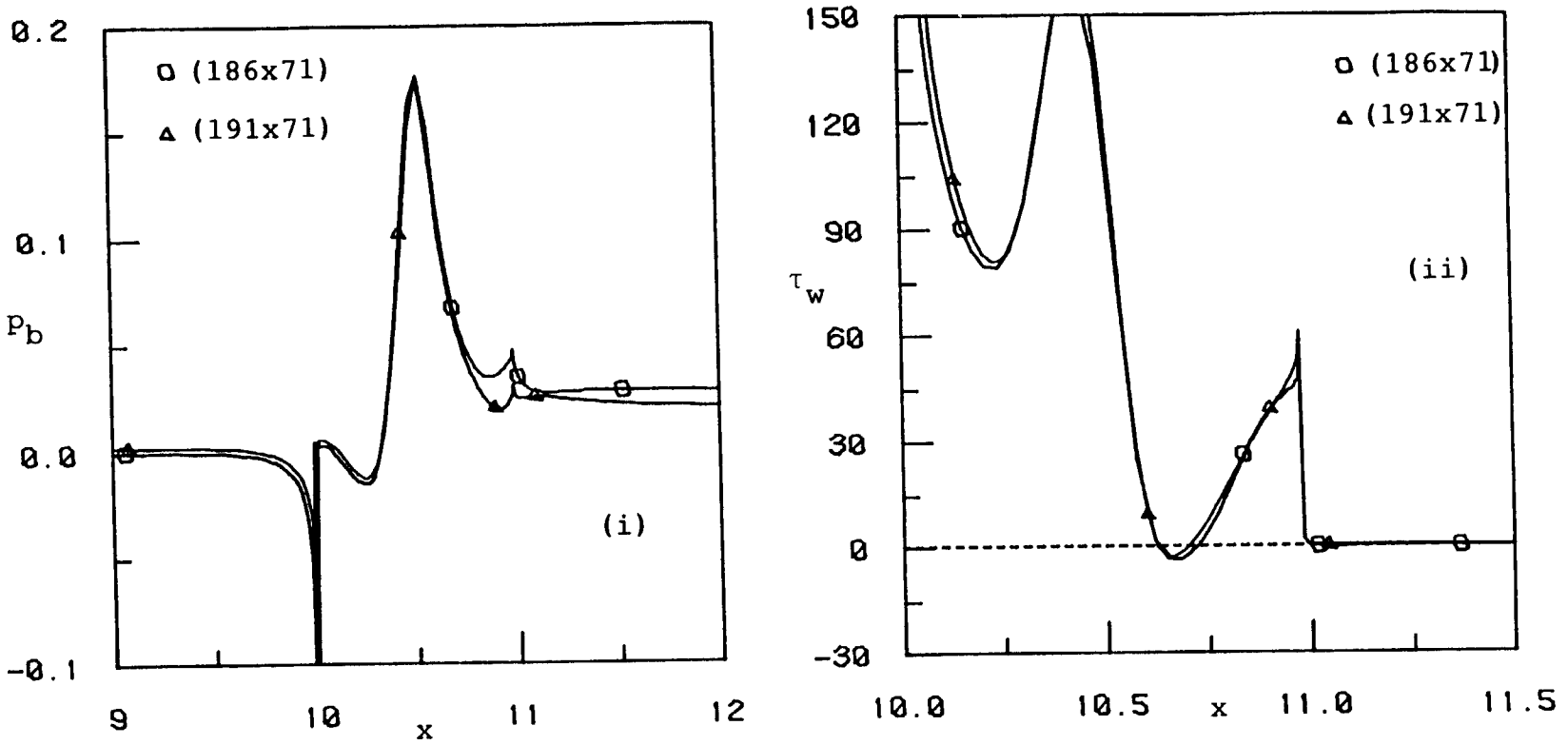

b. Re = 15000

FIG. 14 (CONCLUDED). EFFECT OF GRID REFINEMENT FOR A CASCADE OF EXPONENTIAL AIRFOILS, t/c = 0.05.

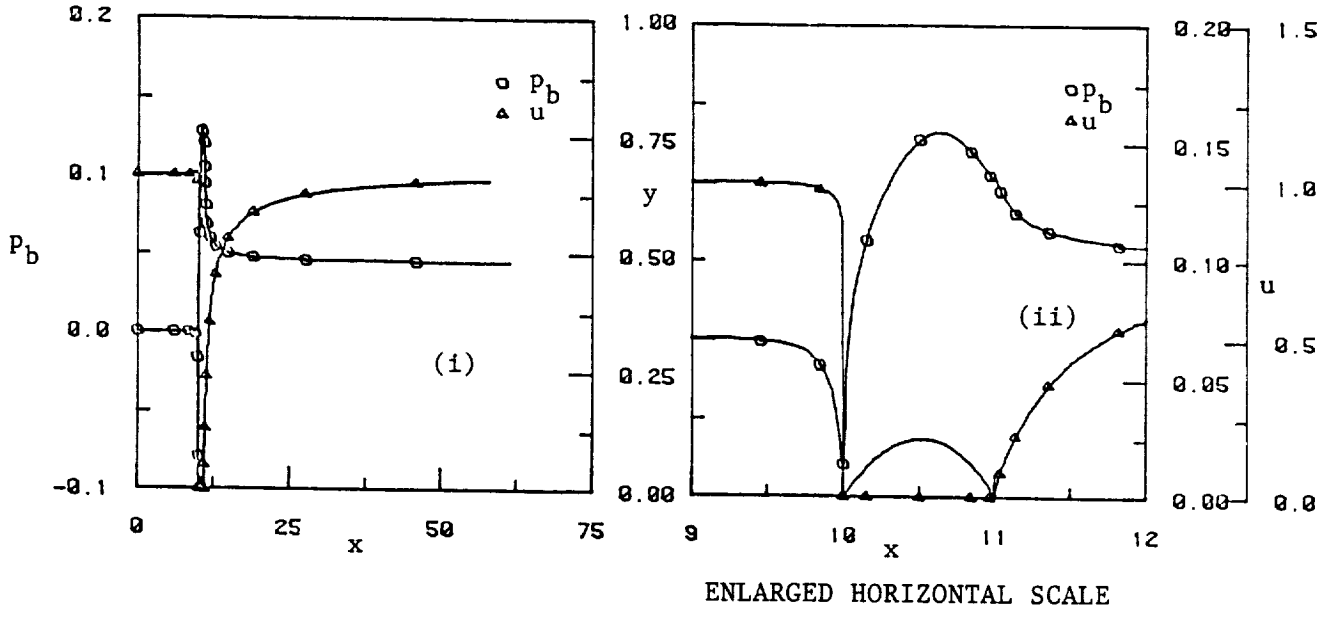

ENLARGED HORIZONTAL SCALE

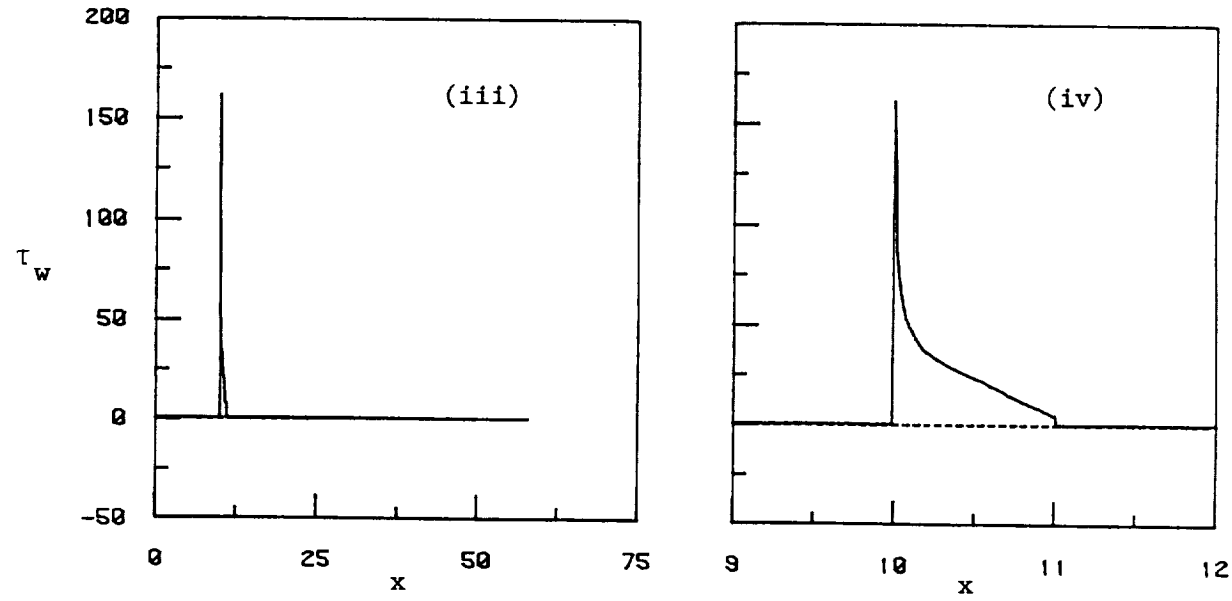

ENLARGED HORIZONTAL SCALE

a. t/c = 0.05

FIG. 15. WALL-PRESSURE, WAKE-CENTERLINE VELOCITY AND WALL-SHEAR PARAMETER DISTRIBUTIONS FOR A CASCADE OF PARABOLIC-ARC AIRFOILS, Re = 1500.

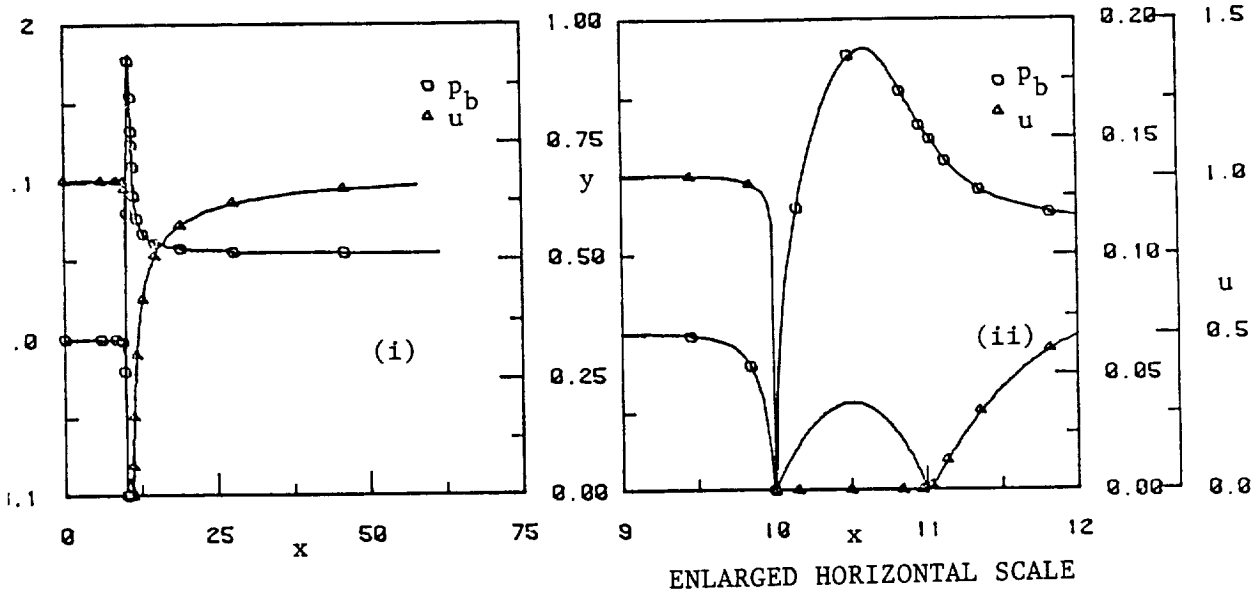

ENLARGED HORIZONTAL SCALE

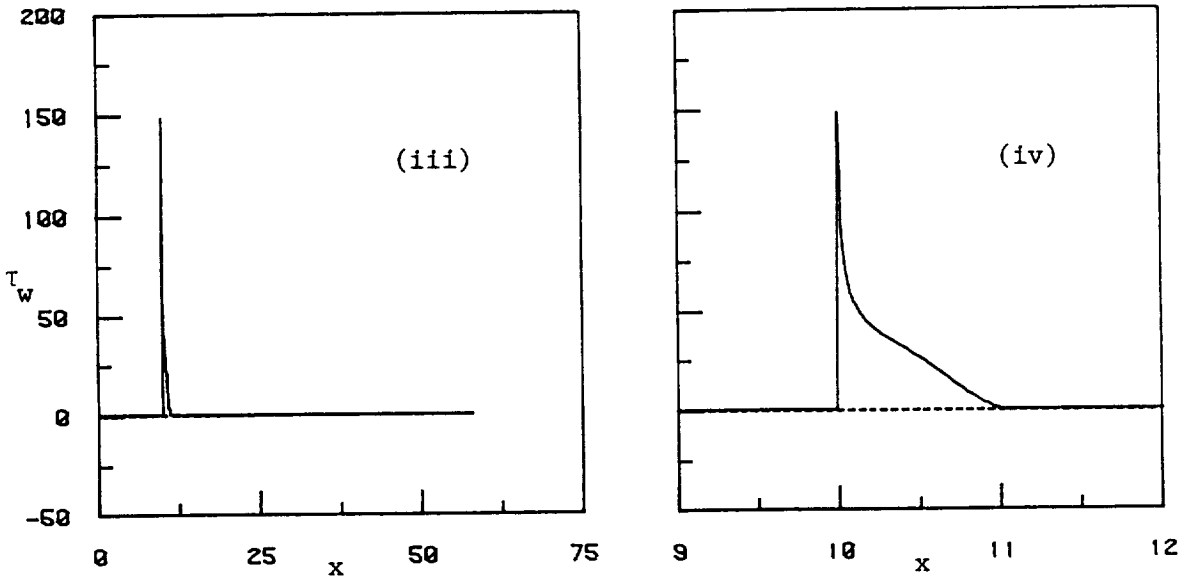

ENLARGED HORIZONTAL SCALE

b. t/c = 0.075

FIG. 15 (CONT'D). WALL-PRESSURE, WAKE-CENTERLINE VELOCITY AND WALL-SHEAR PARAMETER DISTRIBUTIONS FOR A CASCADE OF PARABOLIC-ARC AIRFOILS, Re = 1500.

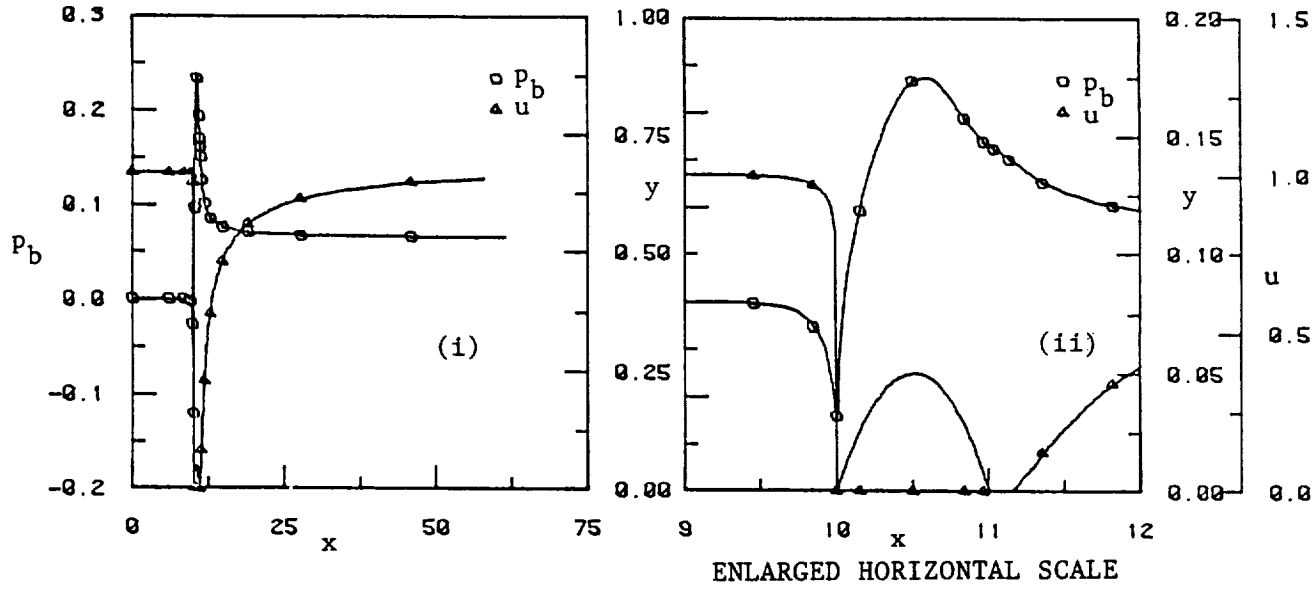

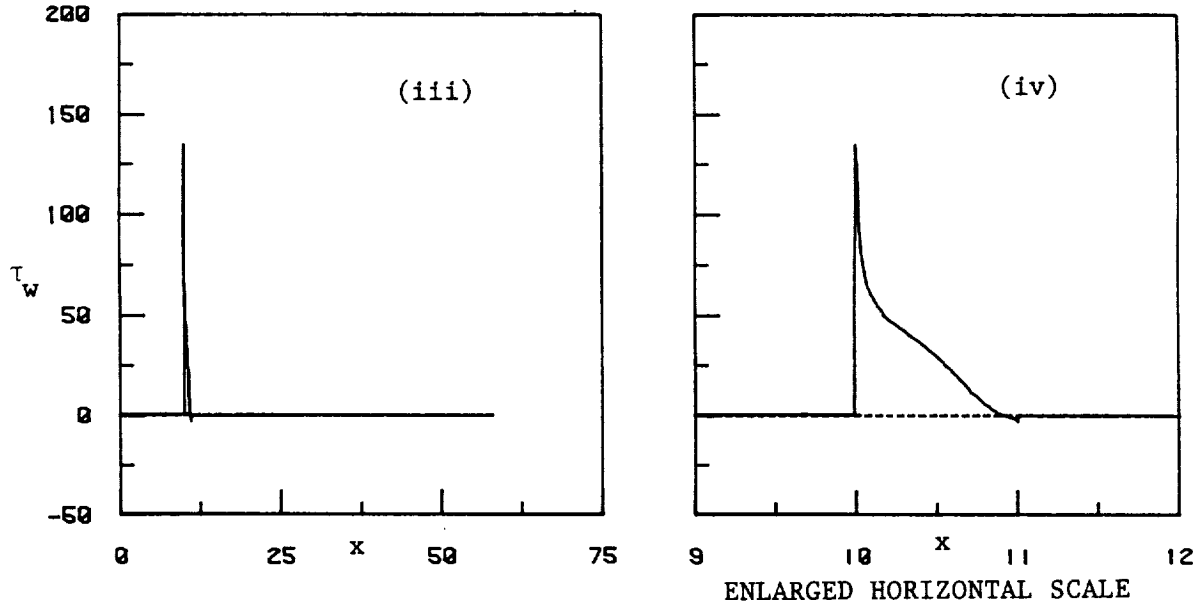

c. t/c = 0.1

FIG. 15 (CONCLUDED). WALL-PRESSURE, WAKE-CENTERLINE VELOCITY AND WALL-SHEAR PARAMETER DISTRIBUTIONS FOR A CASCADE OF PARABOLIC-ARC AIRFOILS, Re = 1500.

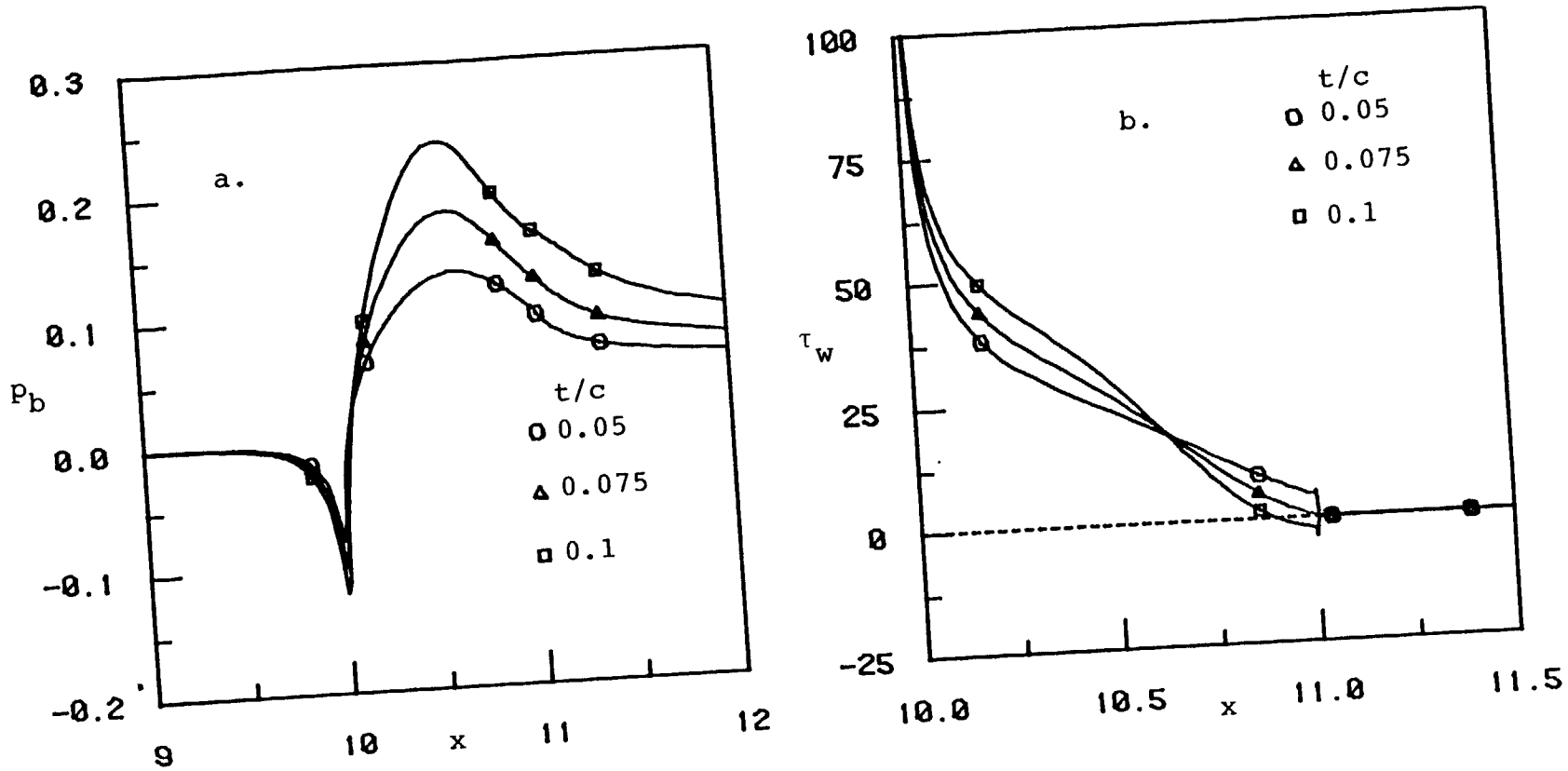

FIG. 16. COMPARISON OF WALL-PRESSURE AND WALL-SHEAR PARAMETER DISTRIBUTIONS FOR VARIOUS t/c FOR A CASCADE OF EXPONENTIAL AIRFOILS.

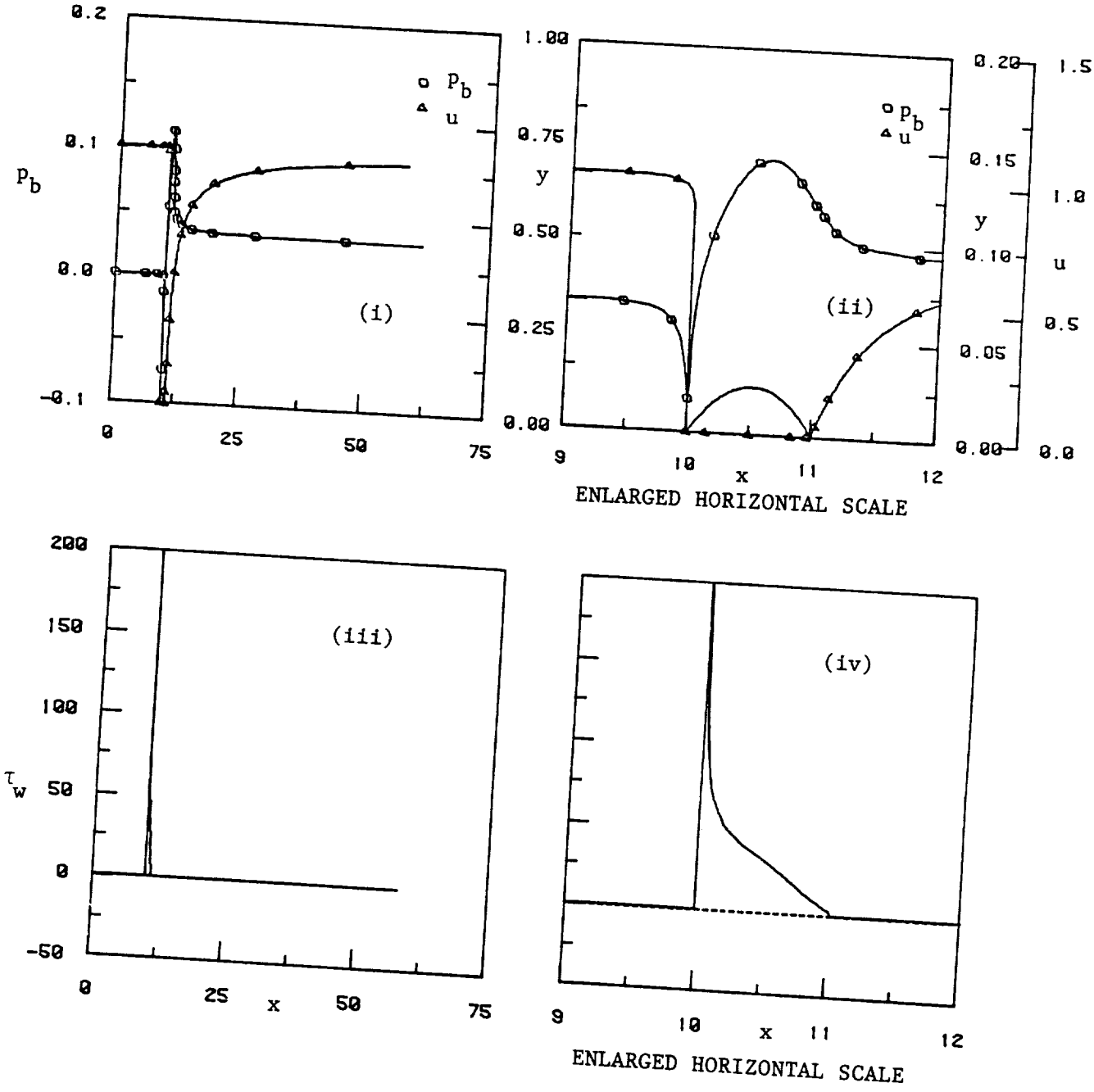

a. Re = 3100

FIG. 17. WALL-PRESSURE, WAKE-CENTERLINE VELOCITY AND WALL-SHEAR PARAMETER DISTRIBUTIONS FOR A CASCADE OF PARABOLIC-ARC AIRFOILS, t/c = 0.05.

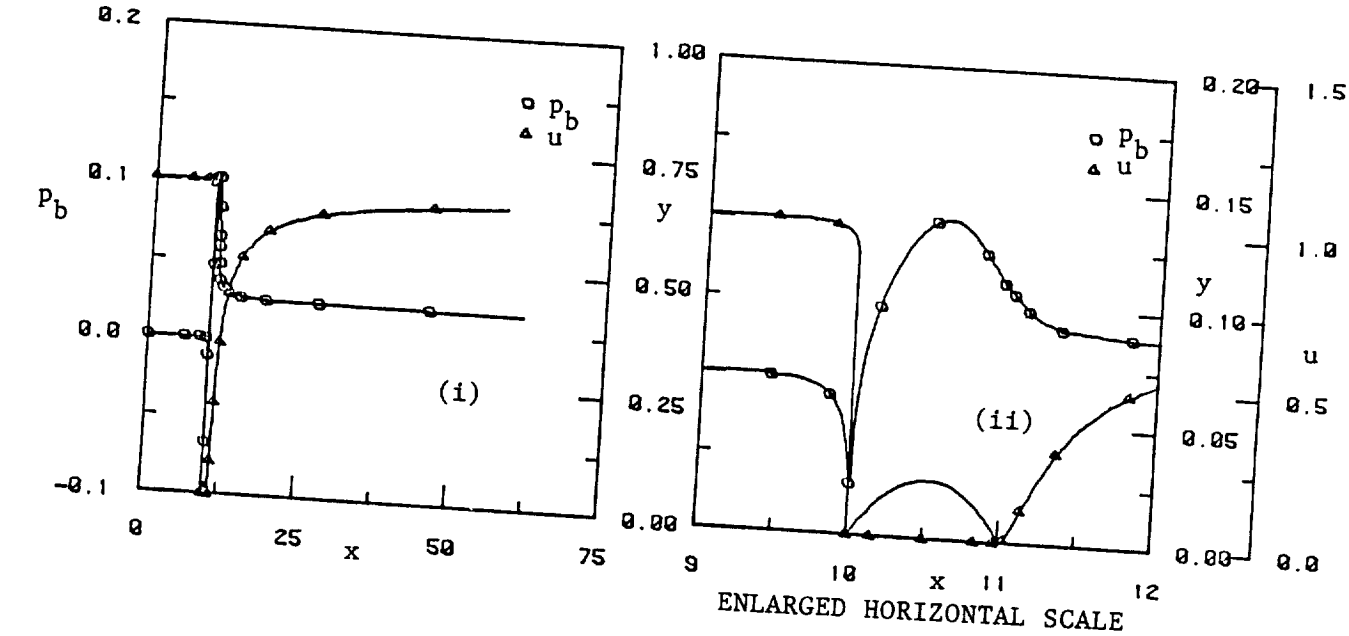

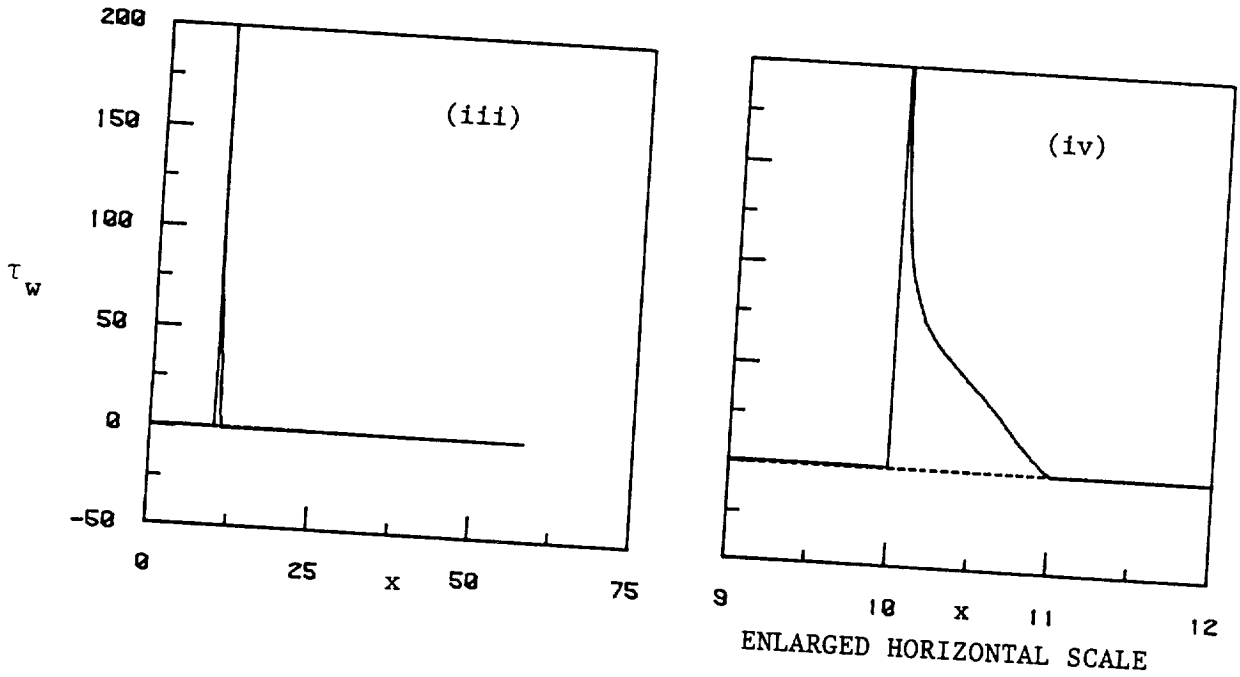

b. Re = 6200

FIG. 17 (CONT'D). WALL-PRESSURE, WAKE-CENTERLINE VELOCITY AND WALL-SHEAR PARAMETER DISTRIBUTIONS FOR A CASCADE OF PARABOLIC-ARC AIRFOILS, t/c = 0.05.

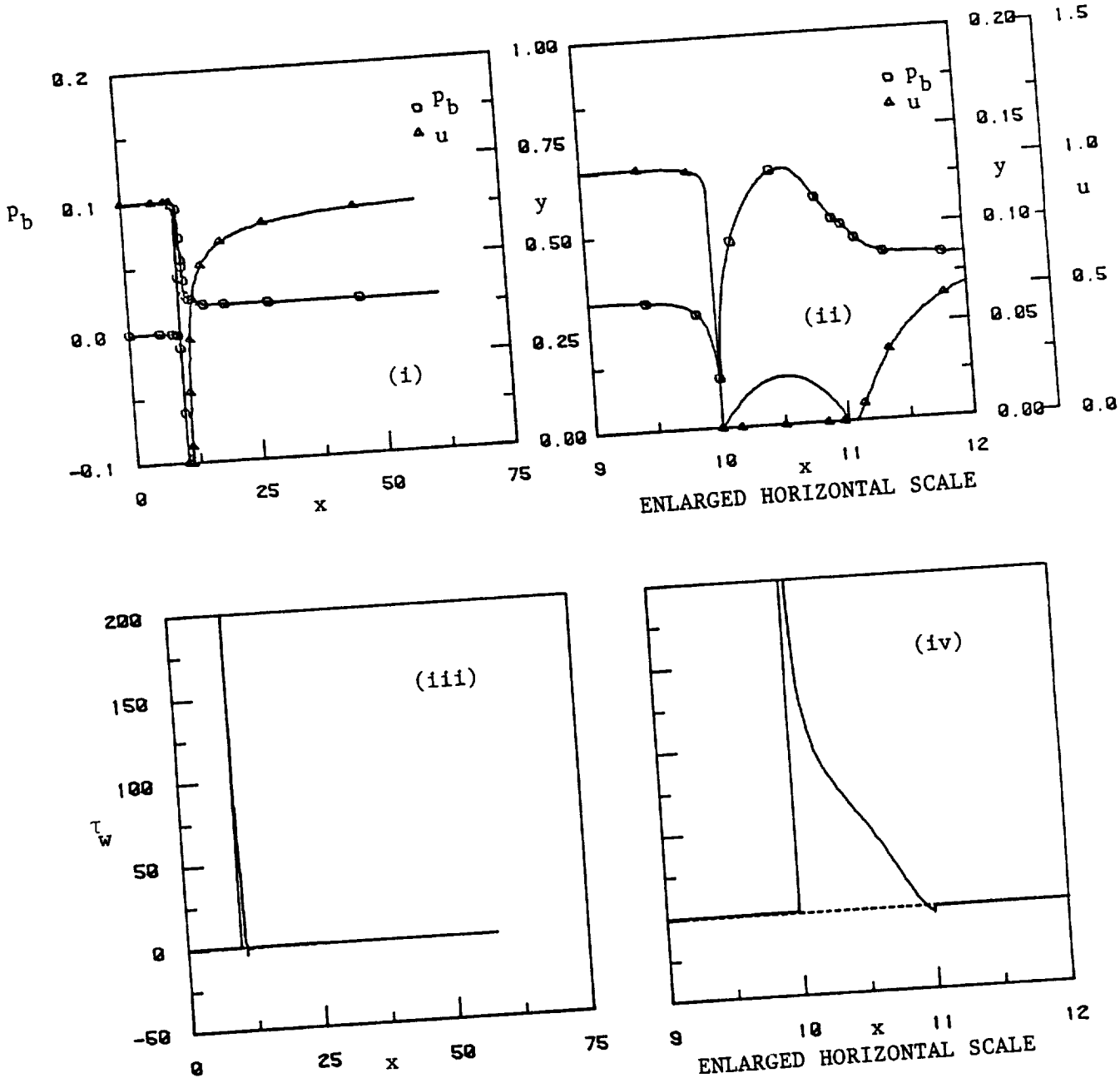

c. Re = 11000

FIG. 17 (CONT'D). WALL-PRESSURE, WAKE-CENTERLINE VELOCITY AND WALL-SHEAR PARAMETER DISTRIBUTIONS FOR A CASCADE OF PARABOLIC-ARC AIRFOILS, t/c = 0.05.

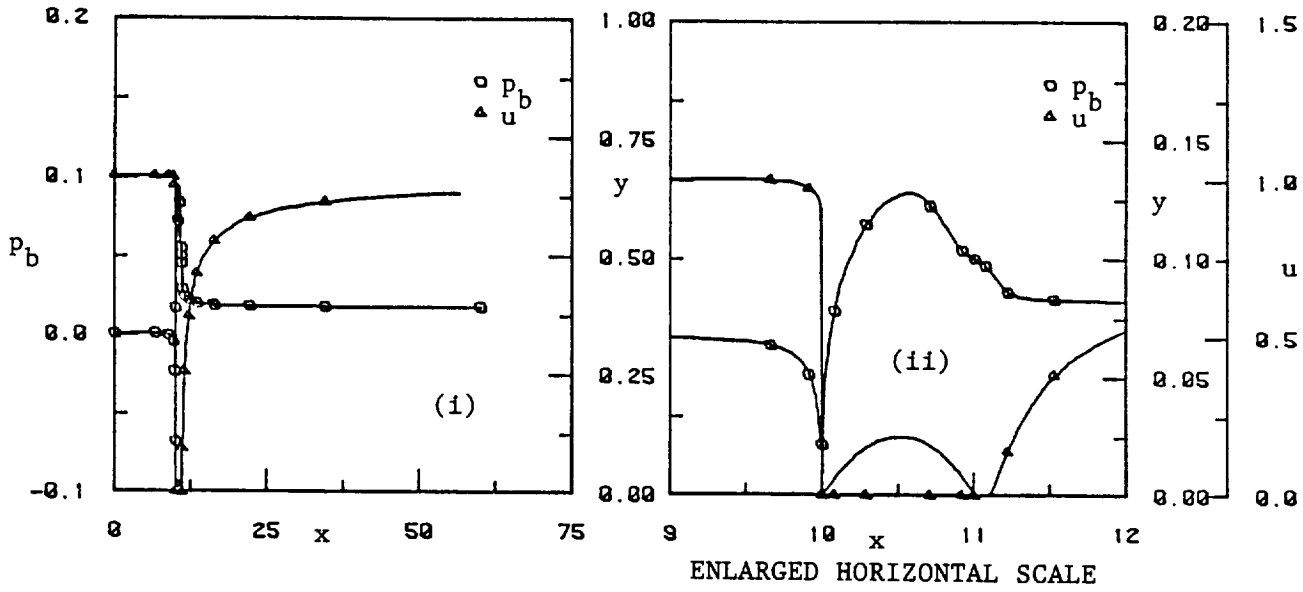

ENLARGED HORIZONTAL SCALE

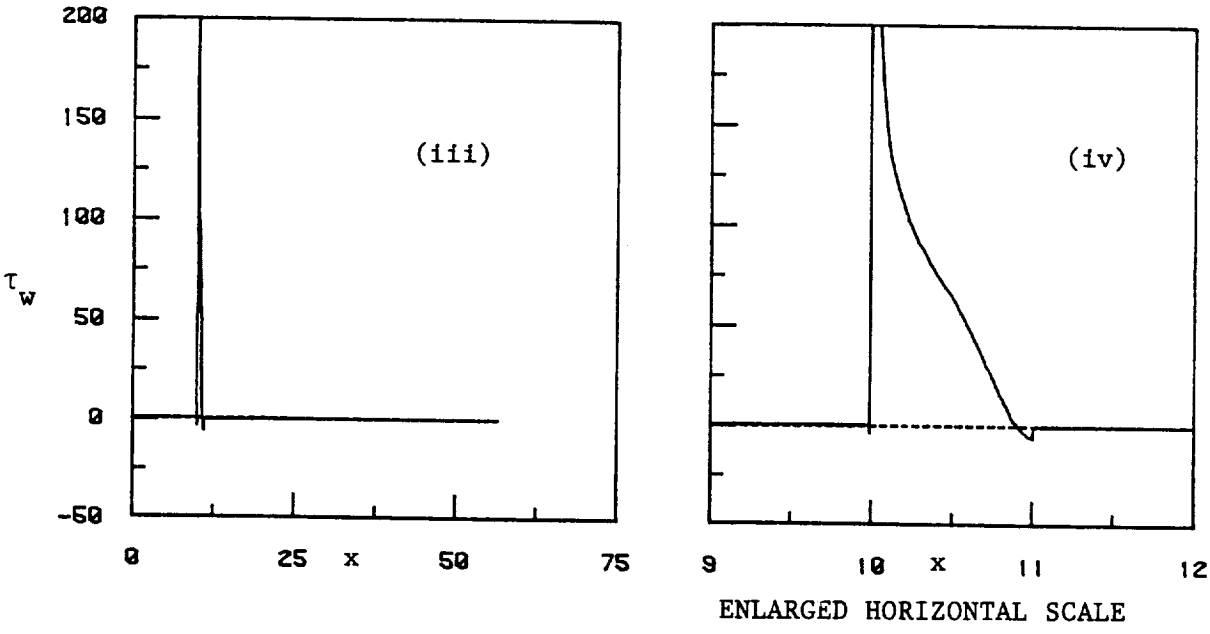

ENLARGED HORIZONTAL SCALE

d. Re = 15000

FIG. 17 (CONCLUDED). WALL-PRESSURE, WAKE-CENTERLINE VELOCITY AND WALL-SHEAR PARAMETER DISTRIBUTIONS FOR A CASCADE OF PARABOLIC-ARC AIRFOILS, t/c = 0.05.

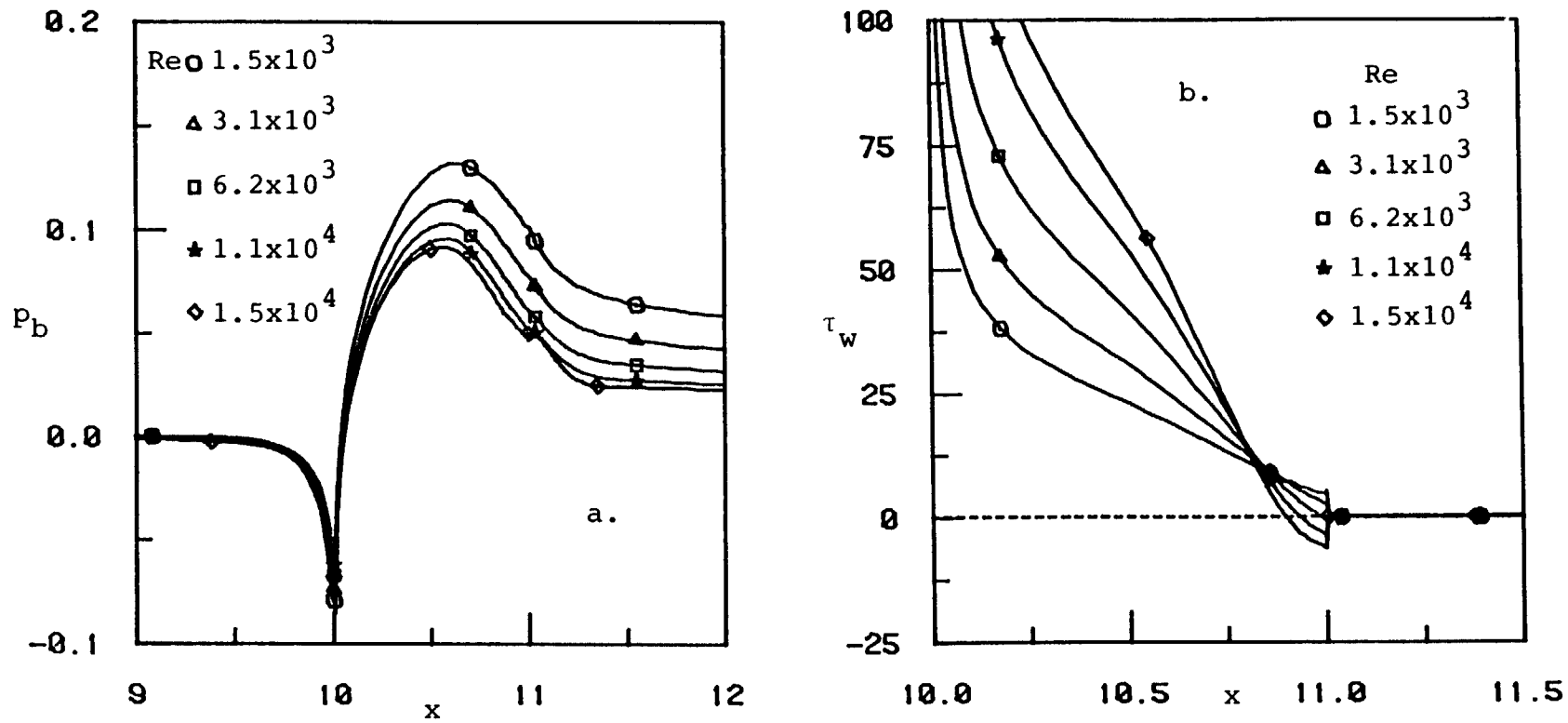

FIG. 18. COMPARISON OF WALL-PRESSURE AND WALL-SHEAR PARAMETER DISTRIBUTIONS FOR VARIOUS Re FOR A CASCADE OF PARABOLIC-ARC AIRFOILS.

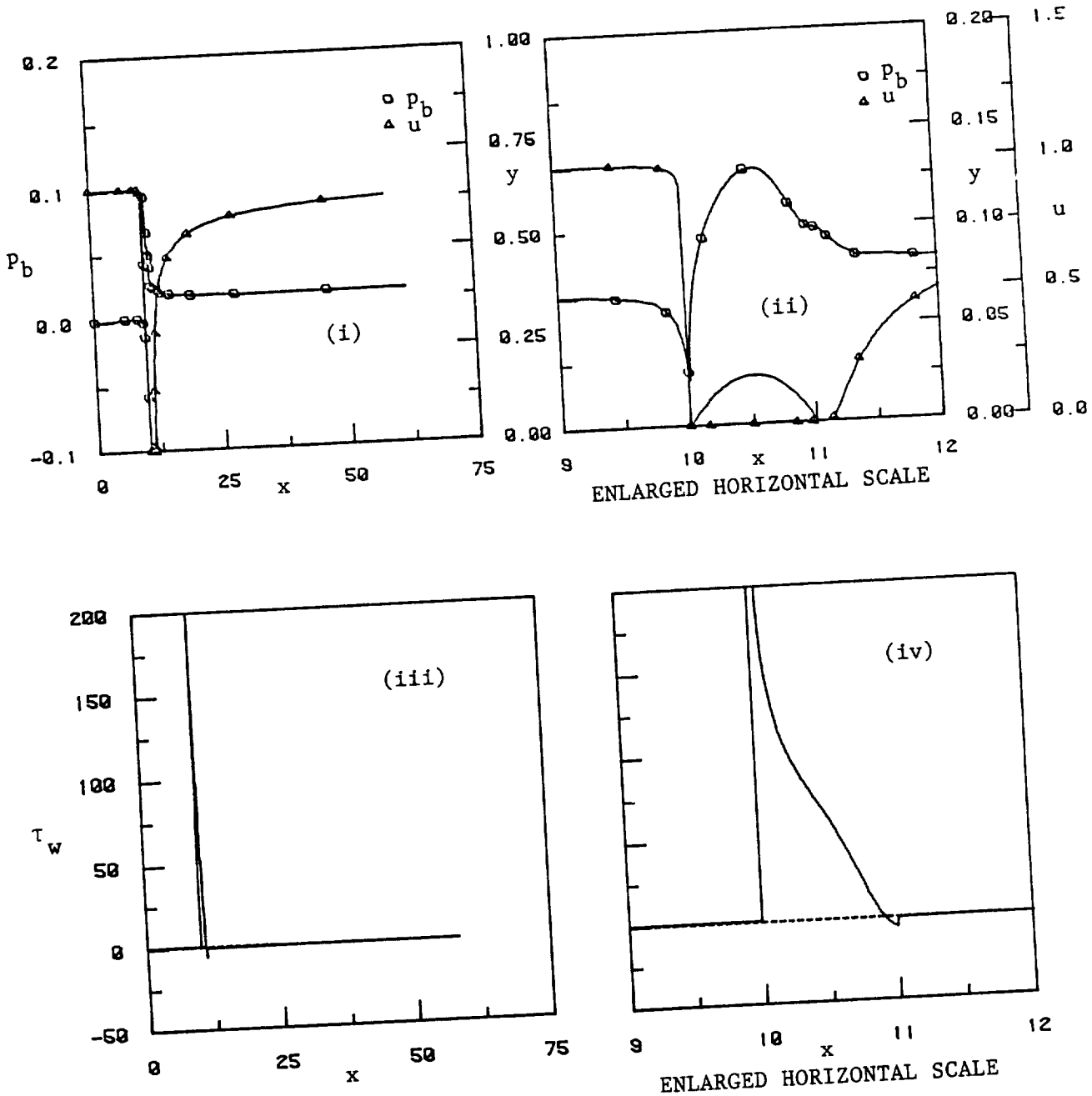

a. $M_\infty = 0.032$

FIG. 19. WALL-PRESSURE, WAKE-CENTERLINE VELOCITY AND WALL-SHEAR PARAMETER DISTRIBUTIONS FOR A CASCADE OF PARABOLIC-ARC AIRFOILS, t/c = 0.05, Re = 15000.

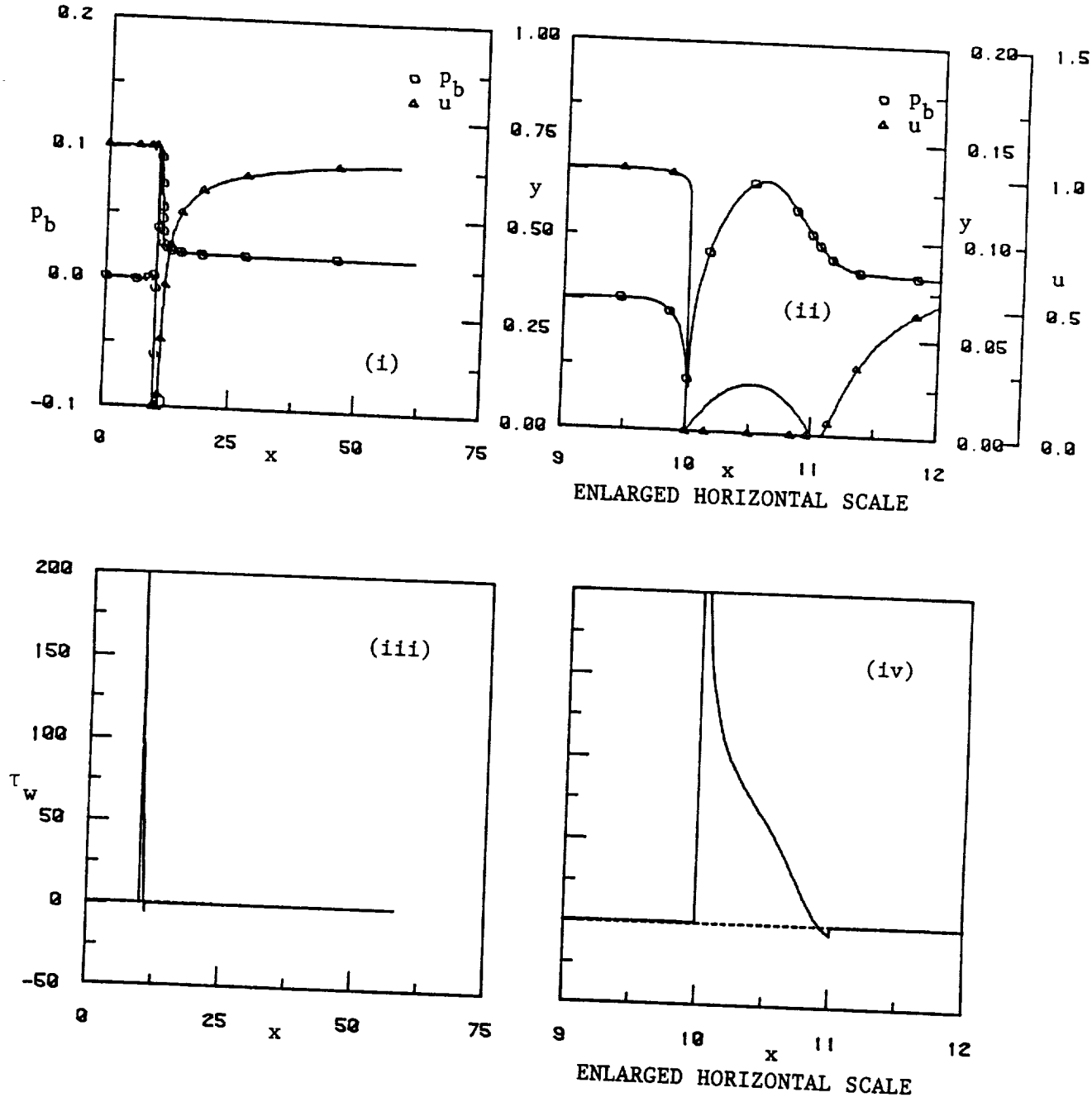

b. $M_\infty = 0.128$

FIG. 19 (CONT'D). WALL-PRESSURE, WAKE-CENTERLINE VELOCITY AND WALL-SHEAR PARAMETER DISTRIBUTIONS FOR A CASCADE OF PARABOLIC-ARC AIRFOILS, t/c = 0.05, Re = 15000.

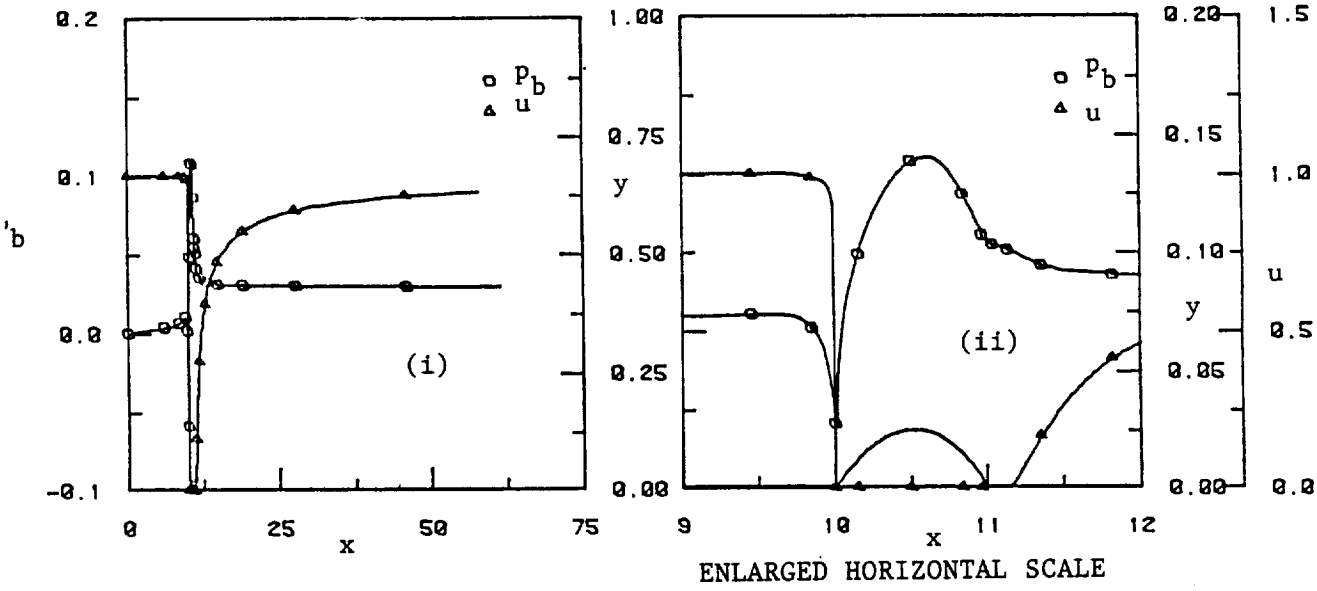

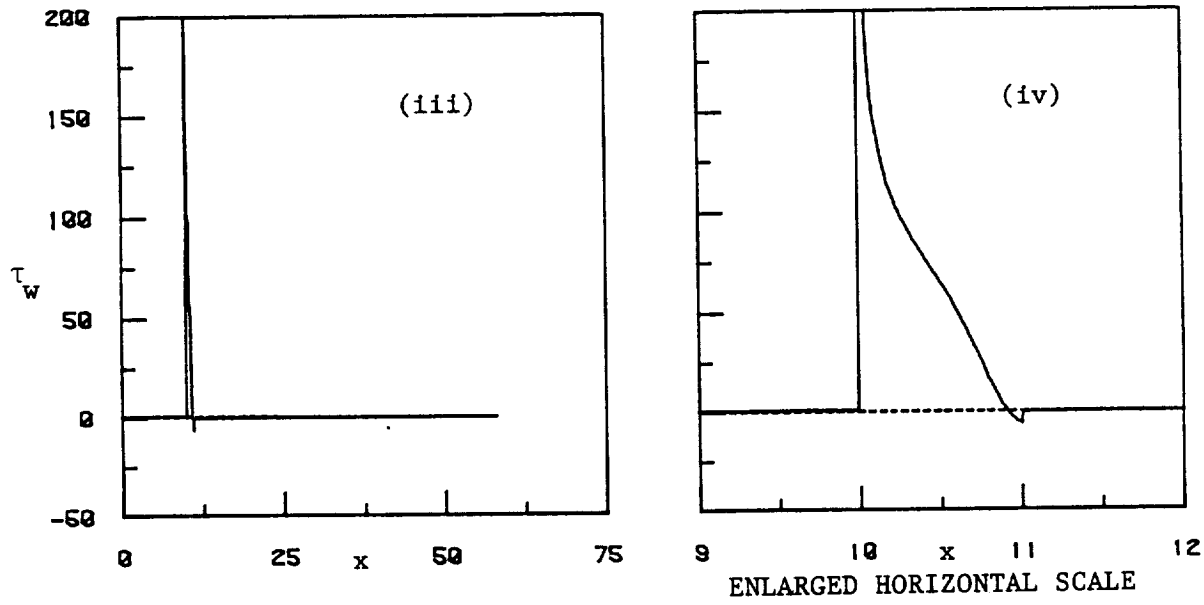

c. $M_\infty = 0.49$

FIG. 19 (CONCLUDED). WALL-PRESSURE, WAKE-CENTERLINE VELOCITY AND WALL-SHEAR PARAMETER DISTRIBUTIONS FOR A CASCADE OF PARABOLIC-ARC AIRFOILS, t/c = 0.05, Re = 15000.

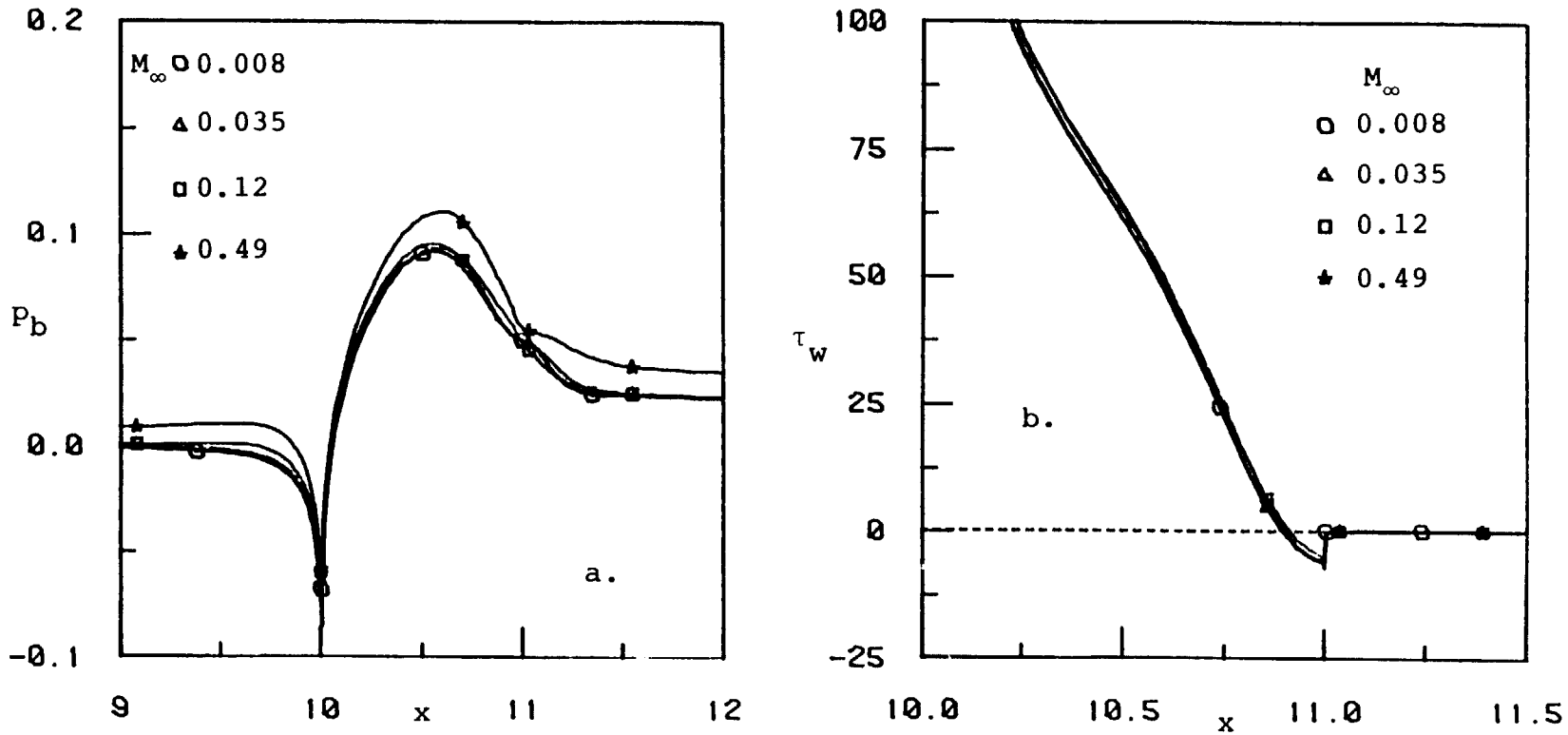

FIG. 20. COMPARISON OF WALL-PRESSURE AND WALL-SHEAR PARAMETER DISTRIBUTIONS FOR VARIOUS M_∞ FOR A CASCADE OF PARABOLIC-ARC AIRFOILS.

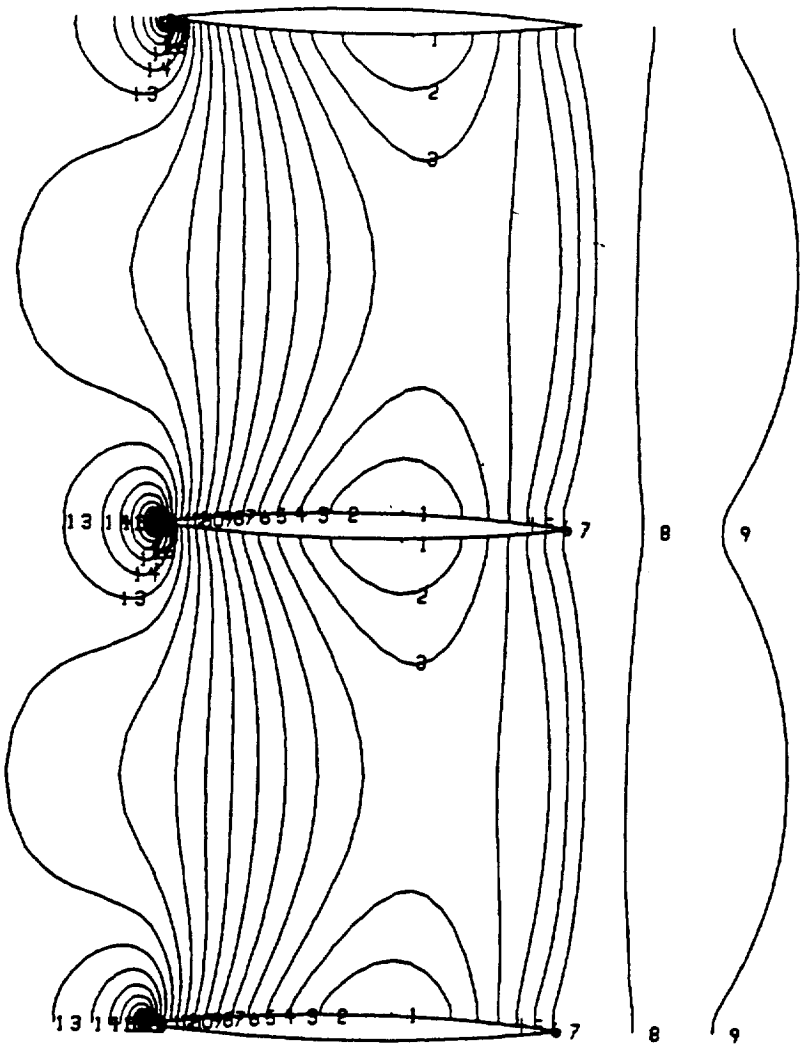

NO.	VALUE
1	0.29226E 01
2	0.29313E 01
3	0.29400E 01
4	0.29487E 01
5	0.29574E 01
6	0.29662E 01
7	0.29749E 01
8	0.29836E 01
9	0.29923E 01
10	0.30011E 01
11	0.30098E 01
12	0.30185E 01
13	0.30272E 01
14	0.30359E 01
15	0.30447E 01
16	0.30534E 01
17	0.30621E 01
18	0.30708E 01
19	0.30796E 01
20	0.30883E 01
21	0.30970E 01

FIG. 21. STATIC PRESSURE CONTOURS FOR A CASCADE OF PARABOLIC-ARC AIRFOILS, Re = 15000, M_∞ = 0.49.

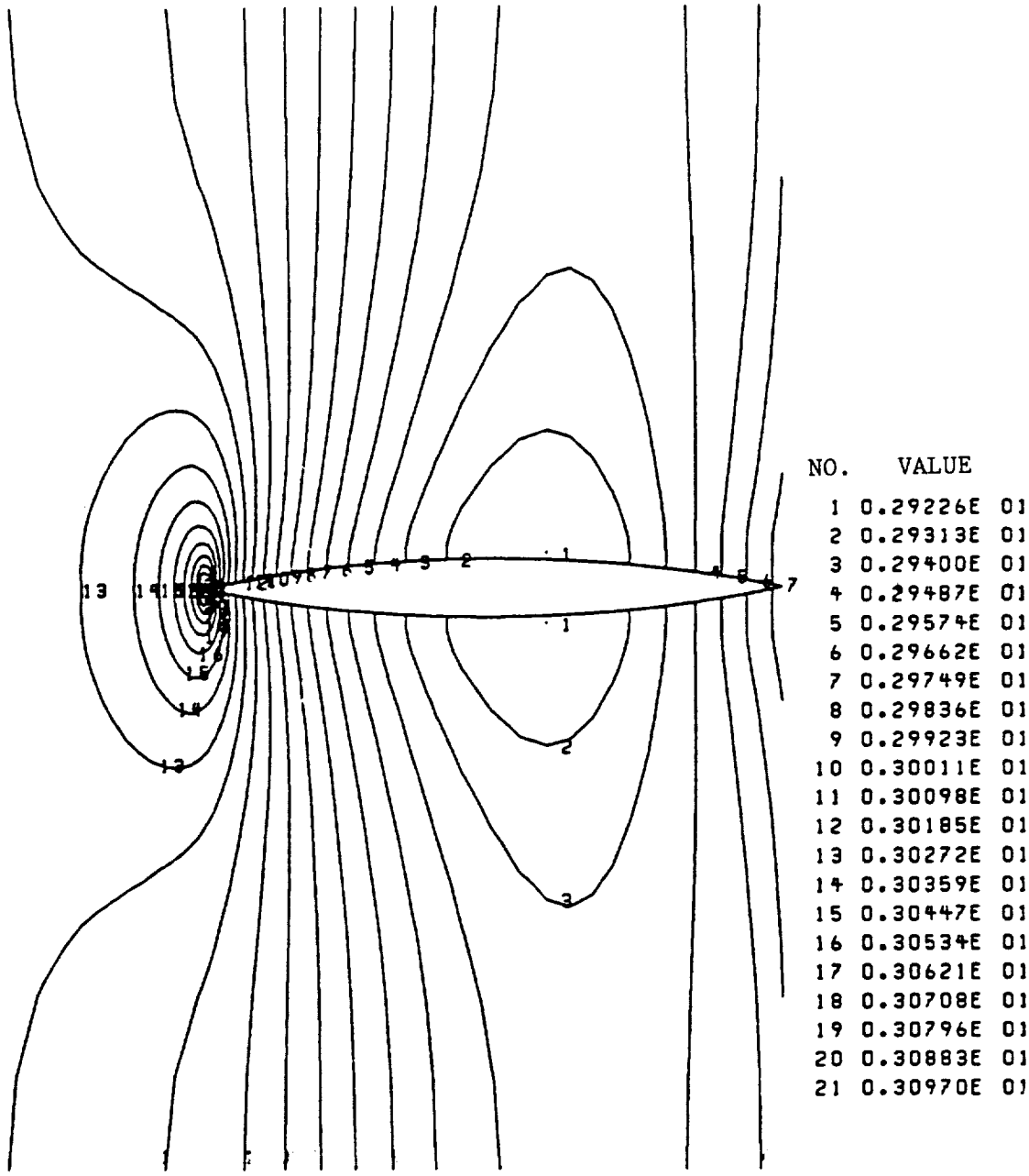

FIG. 21b. ENLARGED VIEW NEAR LEADING EDGE REGION.

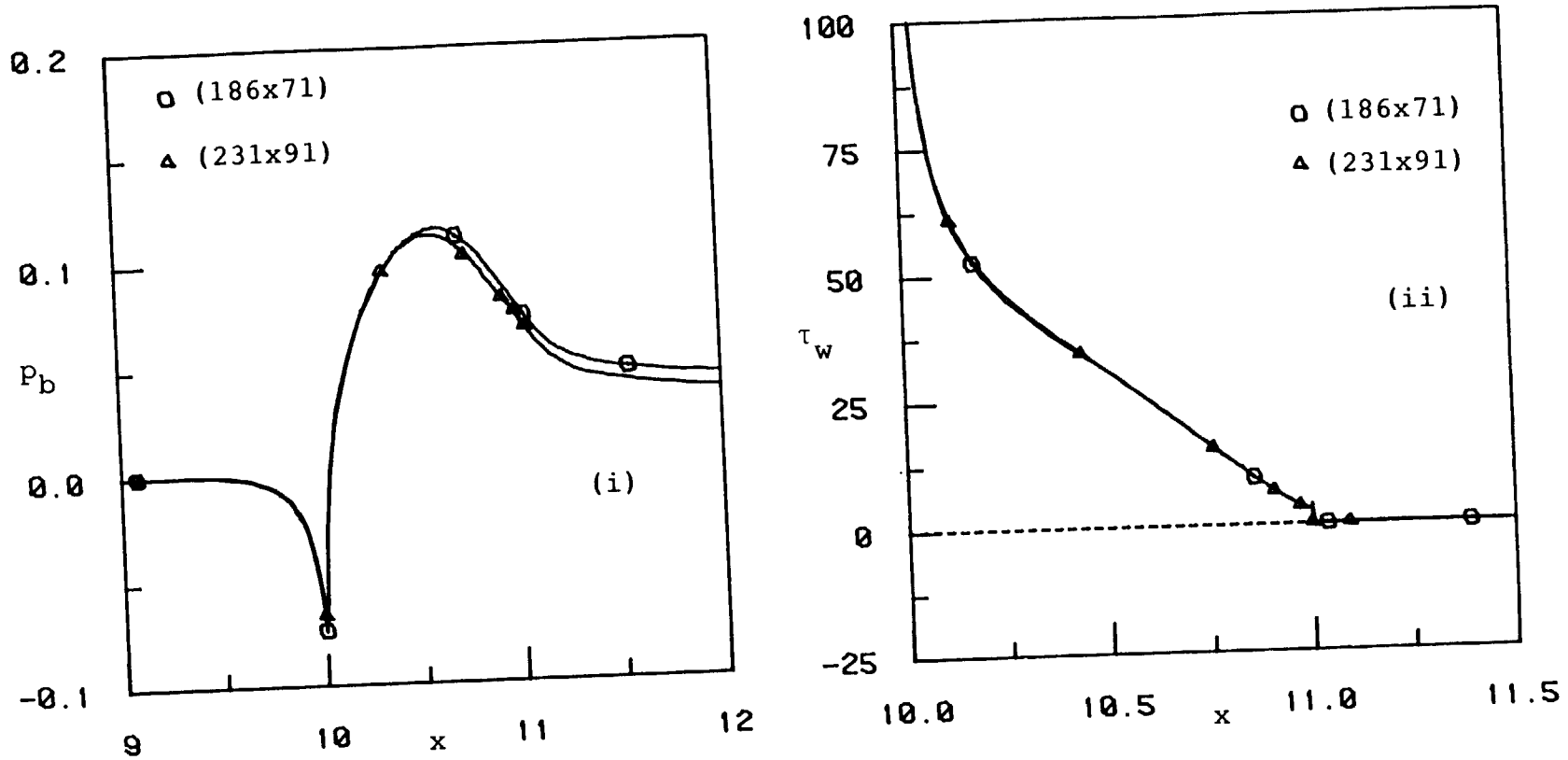

a. Re = 3100

FIG. 22. EFFECT OF GRID REFINEMENT FOR A CASCADE OF PARABOLIC-ARC AIRFOILS, t/c = 0.05.

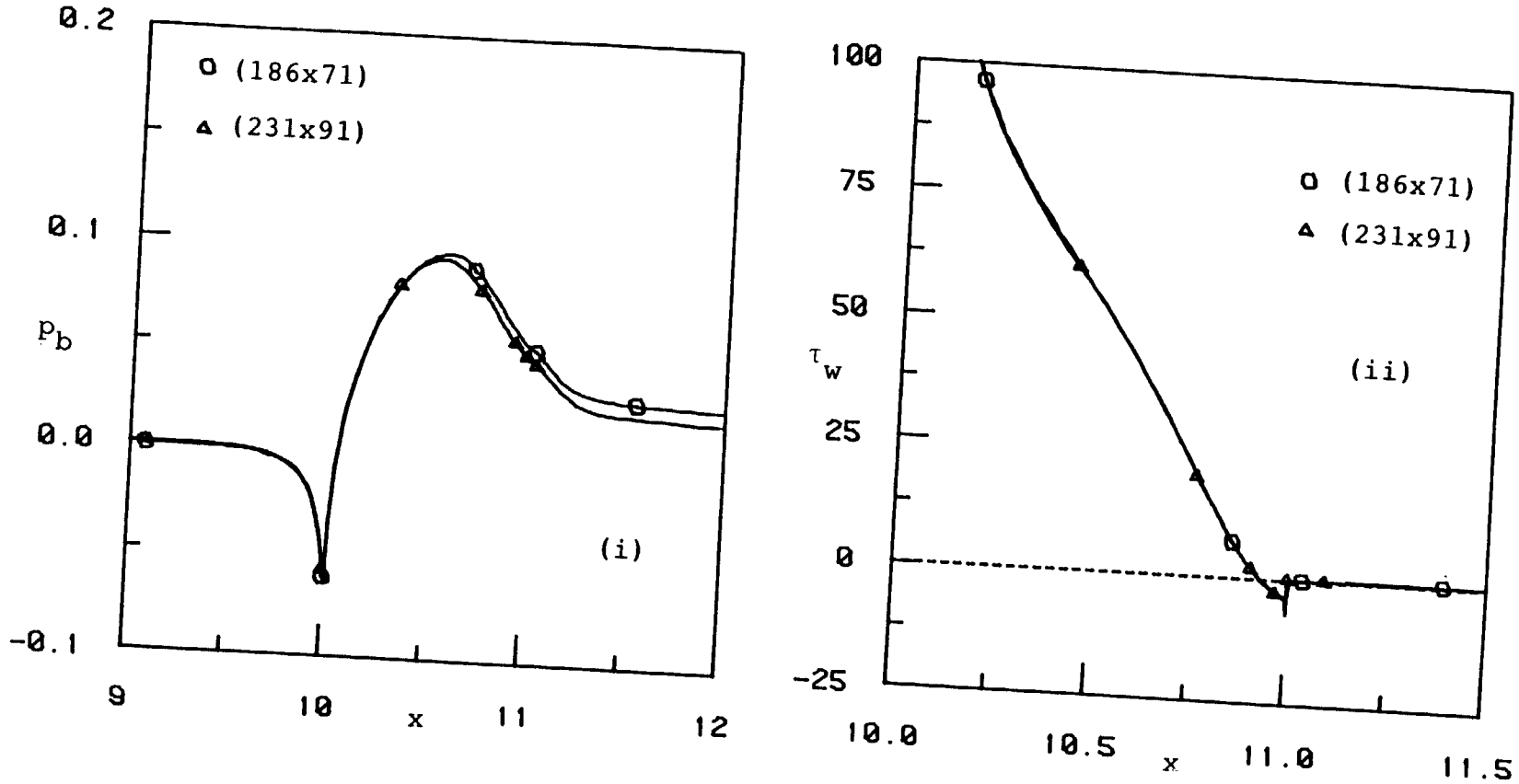

b. Re = 11000

FIG. 22 (CONCLUDED). EFFECT OF GRID REFINEMENT FOR A CASCADE OF PARABOLIC-ARC AIRFOILS, t/c = 0.05.

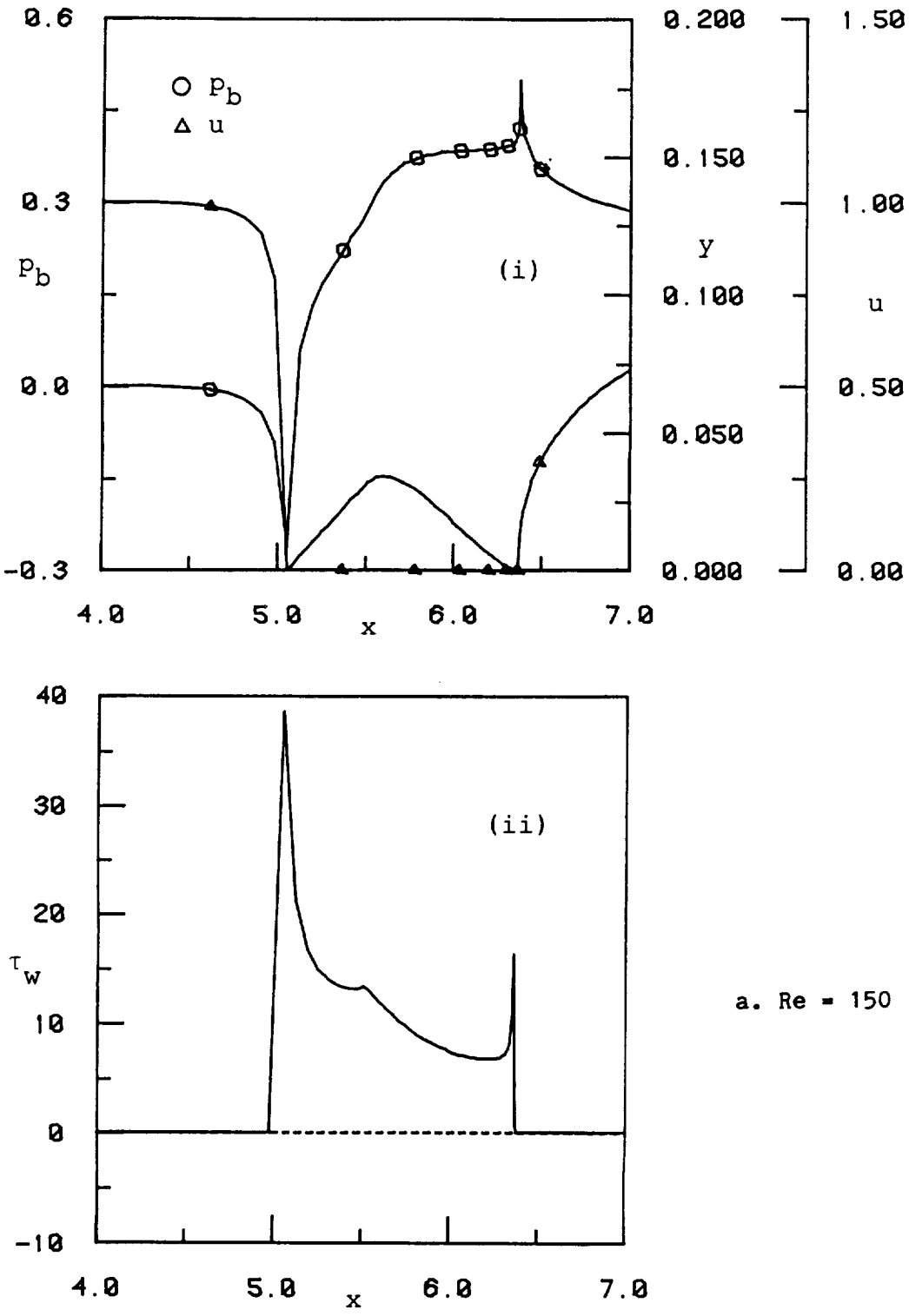

a. Re = 150

FIG. 23. WALL-PRESSURE, WAKE-CENTERLINE VELOCITY AND WALL-SHEAR PARAMETER DISTRIBUTIONS FOR A CASCADE OF JOUKOWSKI AIRFOILS (MODIFIED LEADING EDGE).

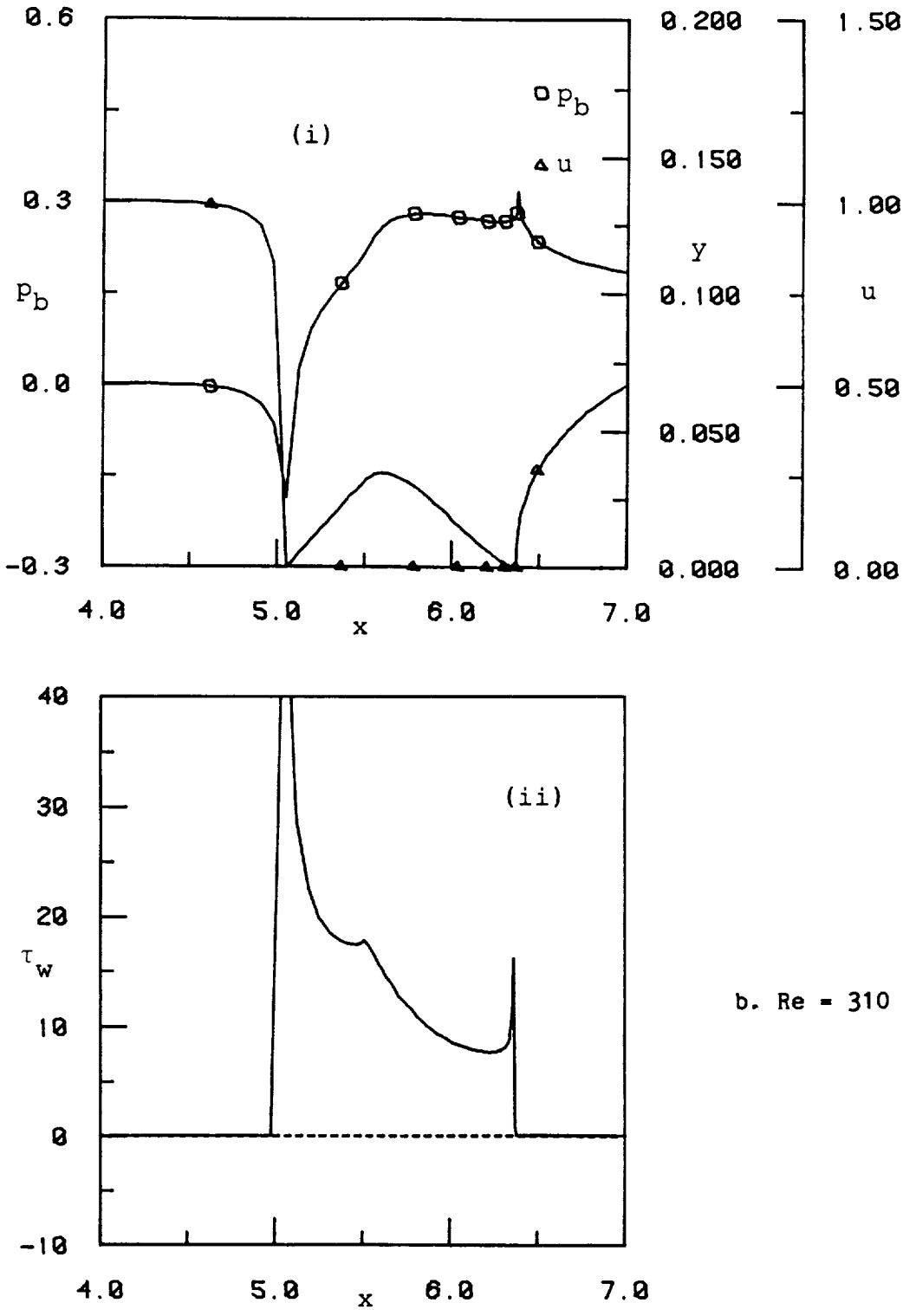

b. Re = 310

FIG. 23 (CONCLUDED). WALL-PRESSURE, WAKE-CENTERLINE VELOCITY AND WALL-SHEAR PARAMETER DISTRIBUTIONS FOR A CASCADE OF JOUKOWSKI AIRFOILS (MODIFIED LEADING EDGE).

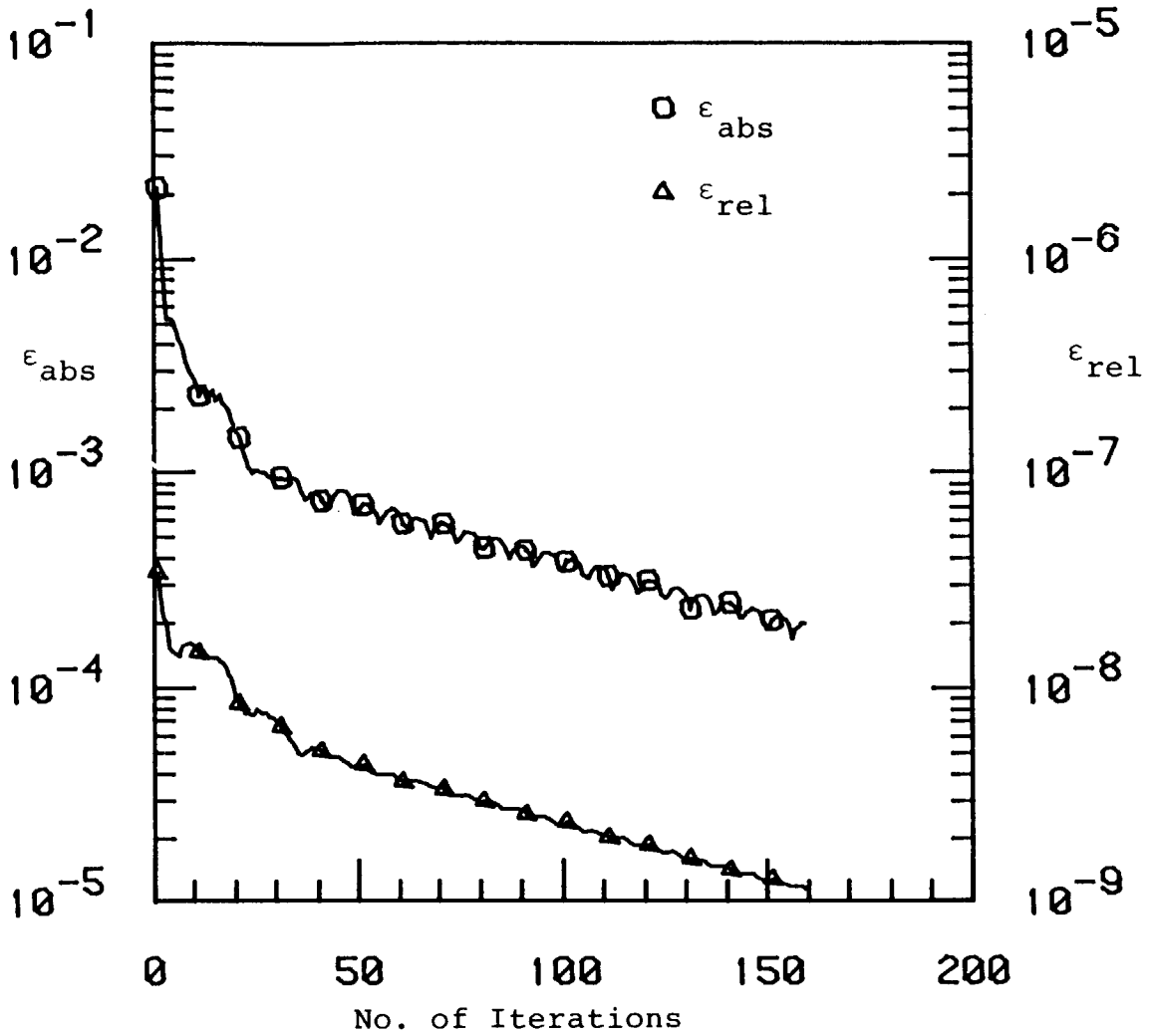

FIG. 24. CONVERGENCE HISTORY FOR A CASCADE OF PARABOLIC-ARC AIRFOILS, t/c = 0.05, Re = 6300.

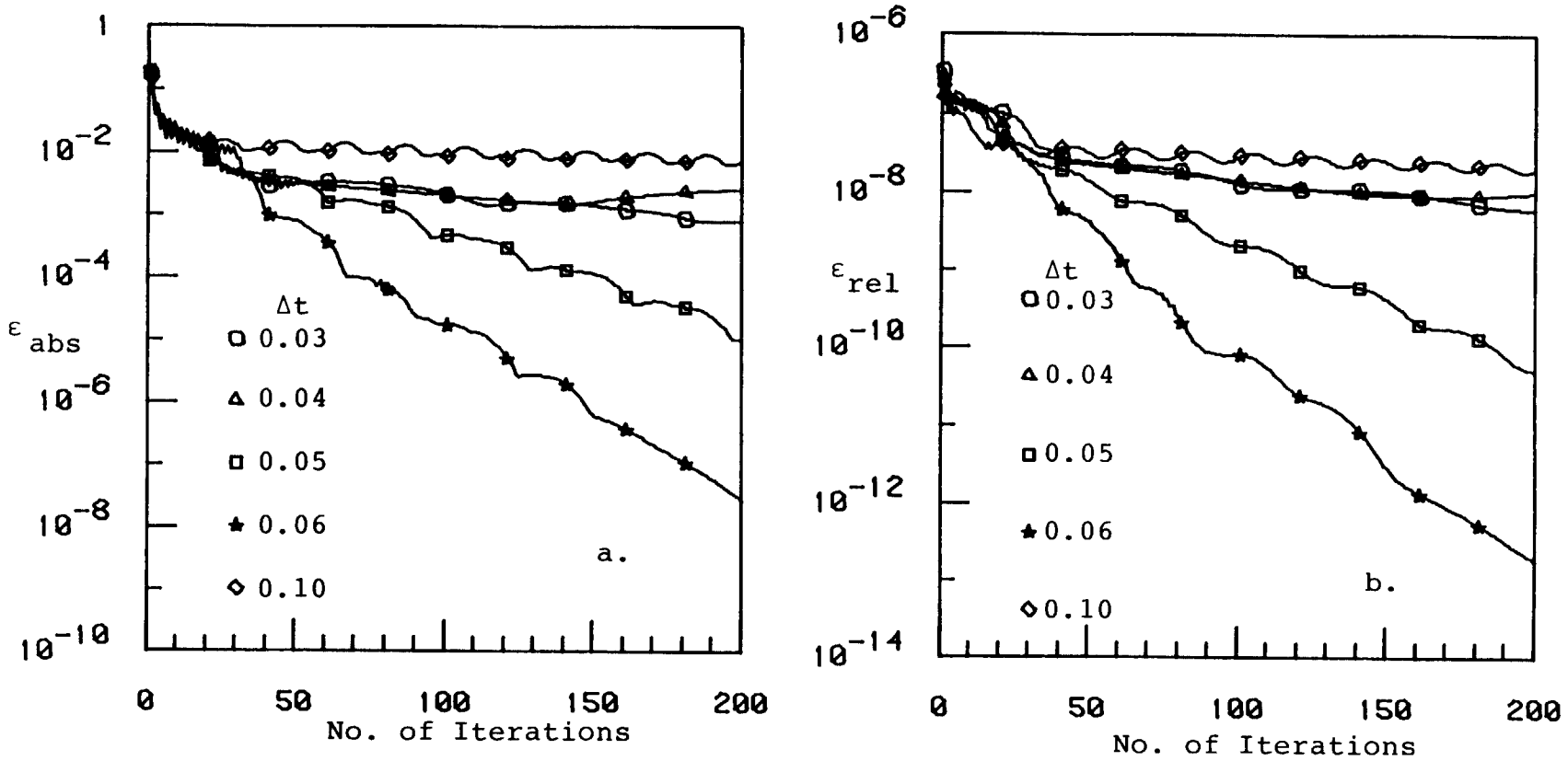

FIG. 25. EFFECT OF Δt ON CONVERGENCE FOR A FINITE FLAT-PLATE CASCADE WITH Δx = CONSTANT.

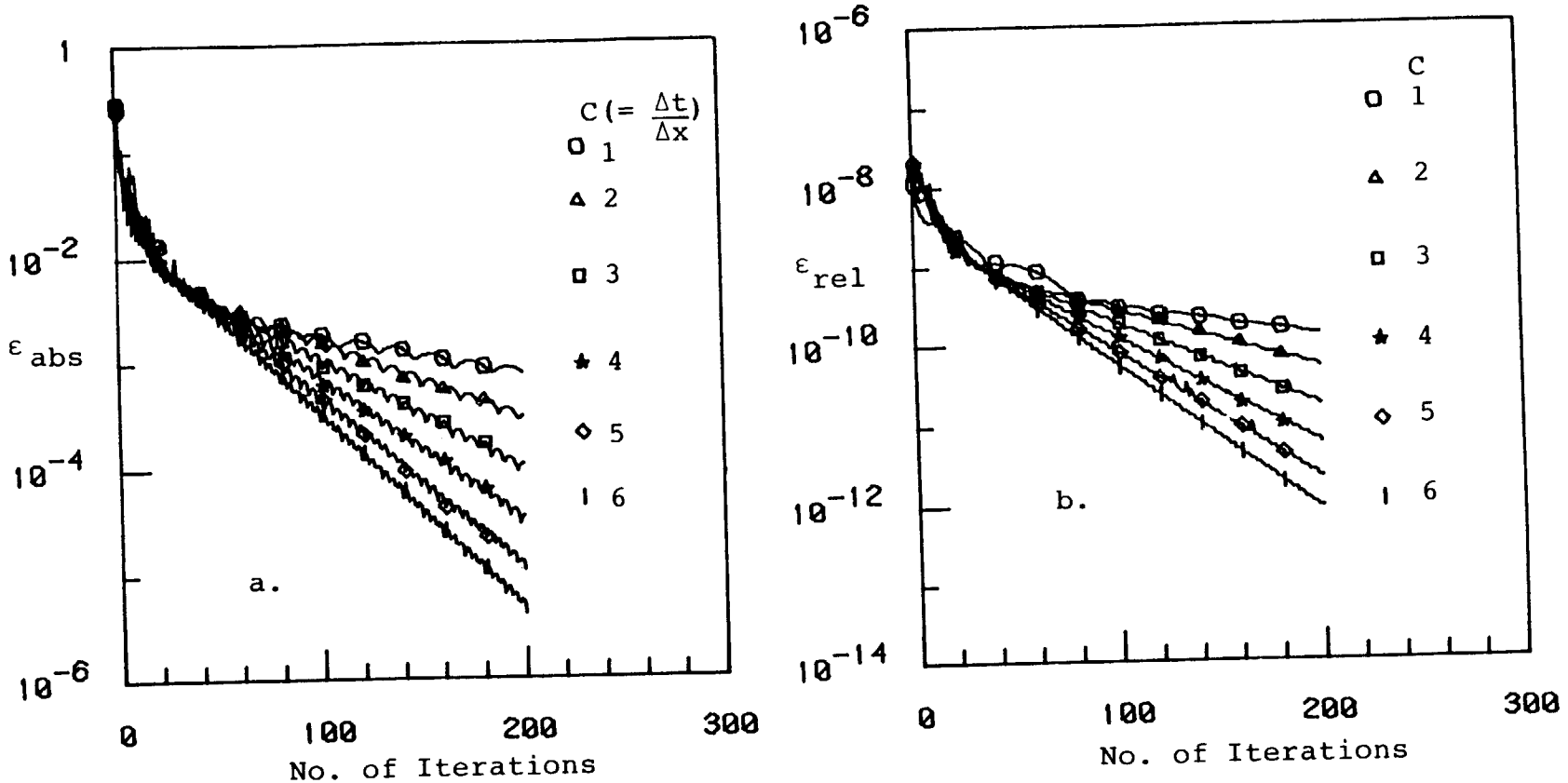

FIG. 26. EFFECT OF Δt ON CONVERGENCE FOR A FINITE FLAT-PLATE CASCADE WITH VARIABLE Δx.

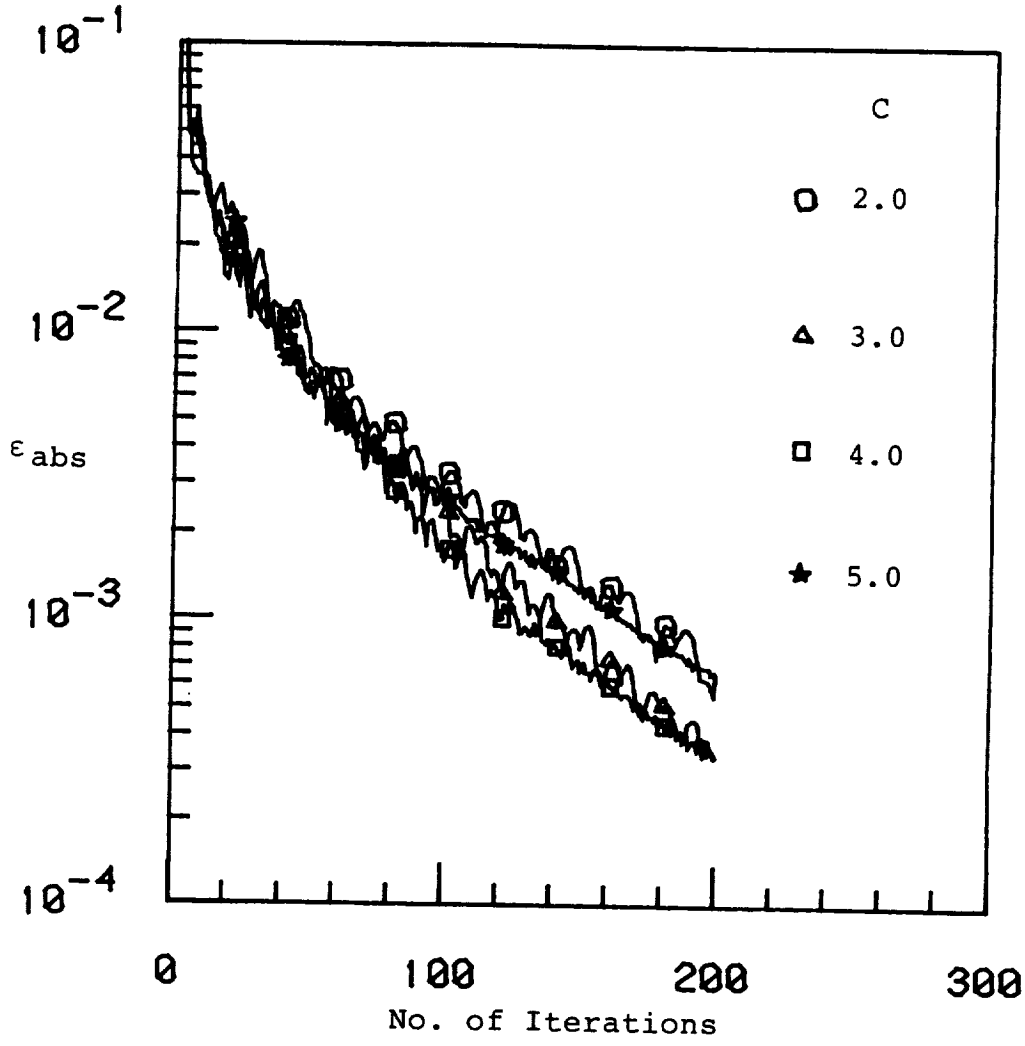

FIG. 27. EFFECT OF Δt ON CONVERGENCE FOR A CASCADE OF EXPONENTIAL AIRFOILS.

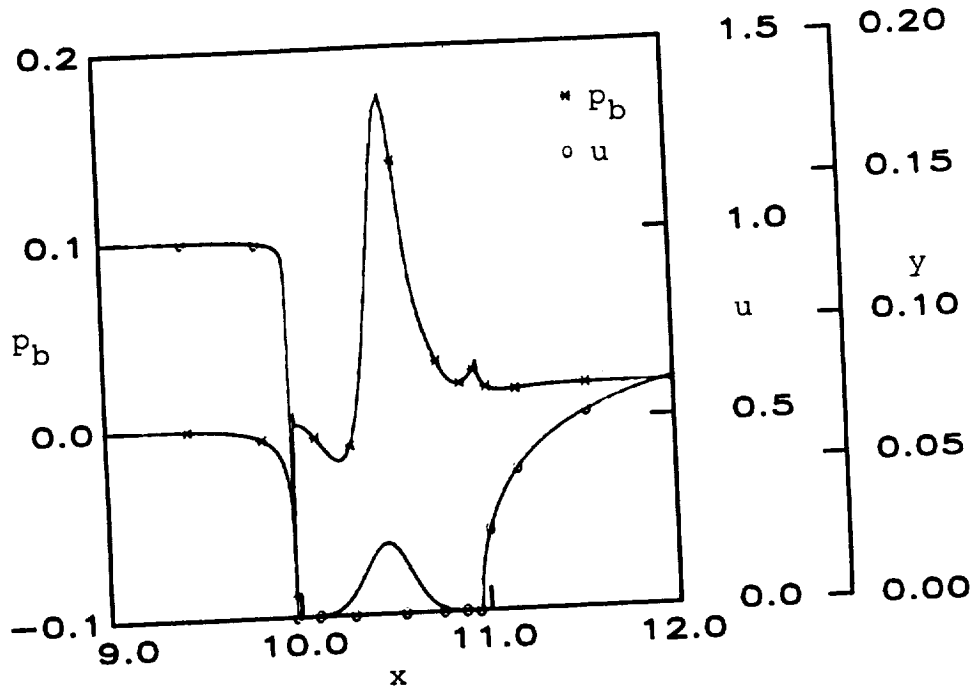

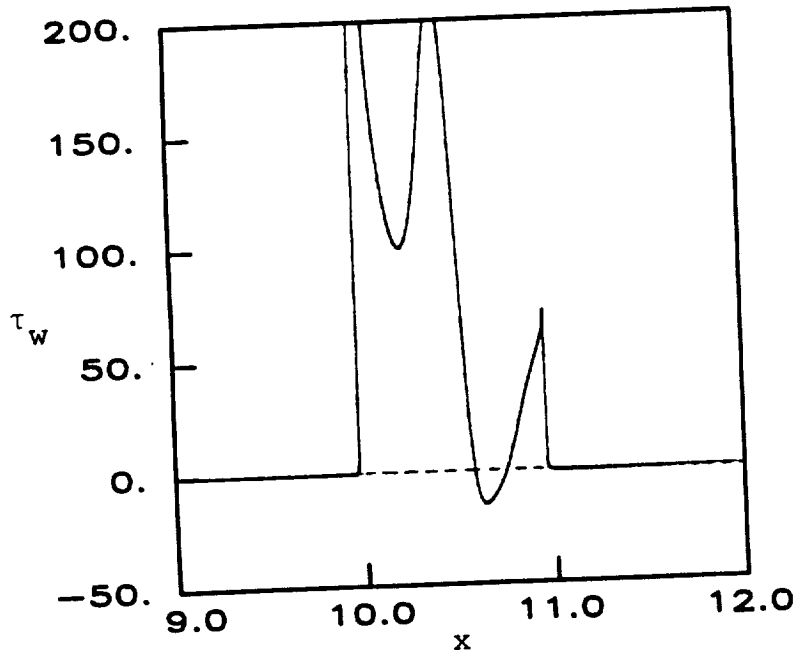

FIG. 28. WALL-PRESSURE, WAKE-CENTERLINE VELOCITY AND WALL-SHEAR PARAMETER DISTRIBUTIONS FOR A CASCADE OF EXPONENTIAL AIRFOILS, t/c = 0.05, Re = 25000.

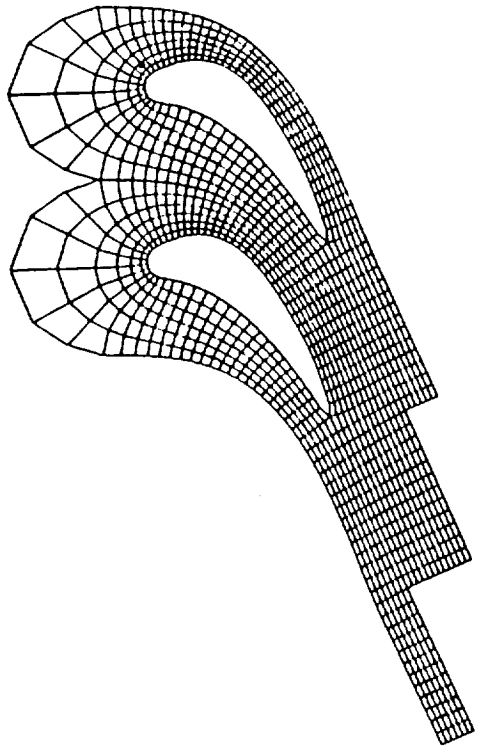

a. CONFORMAL C-GRID (AFTER REF. 41)

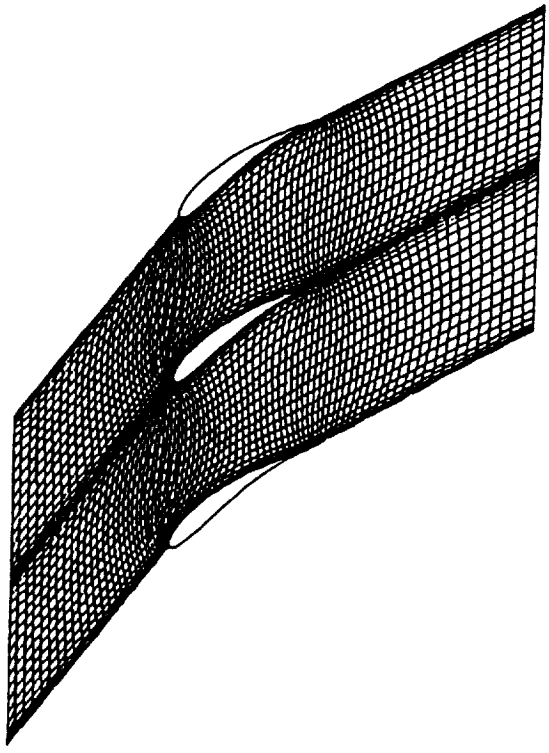

b. 'LINE-PERIODIC' H-GRID

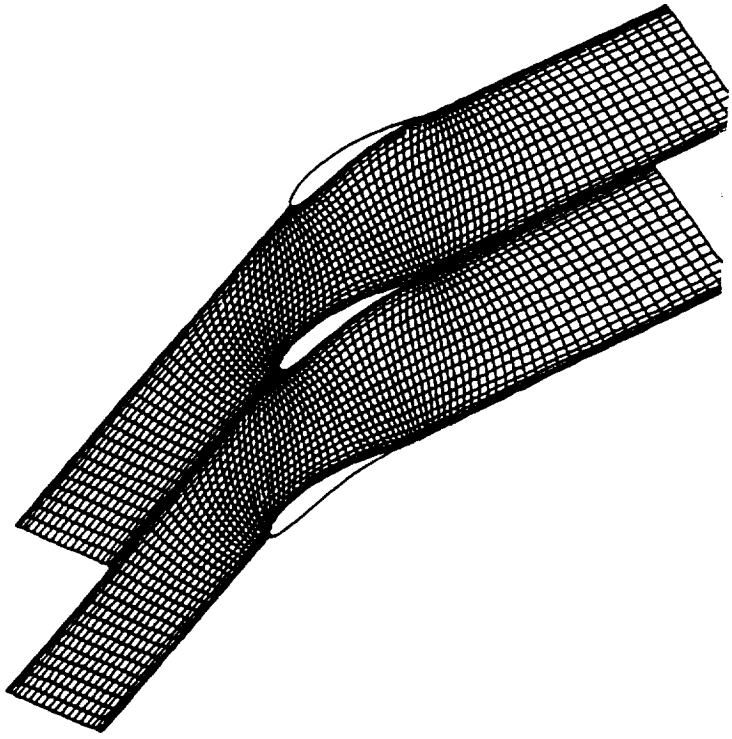

c. 'REGION-PERIODIC' H-GRID

FIG. 29. VARIOUS TYPES OF GRIDS FOR CASCADES.

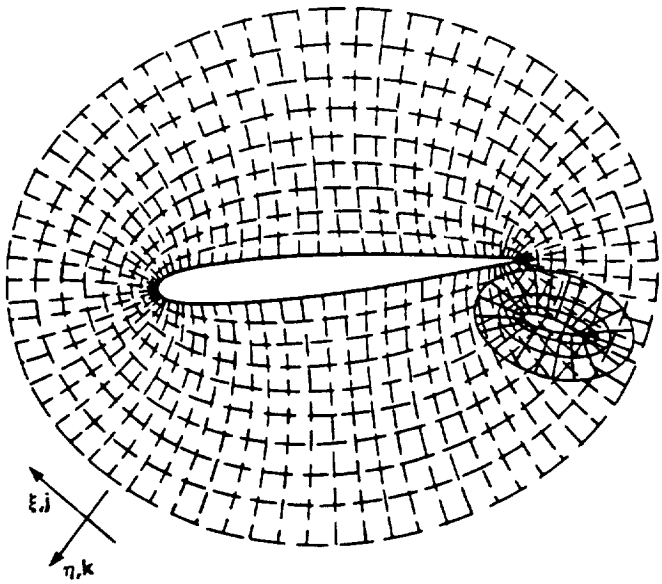

a. OVERSET GRID

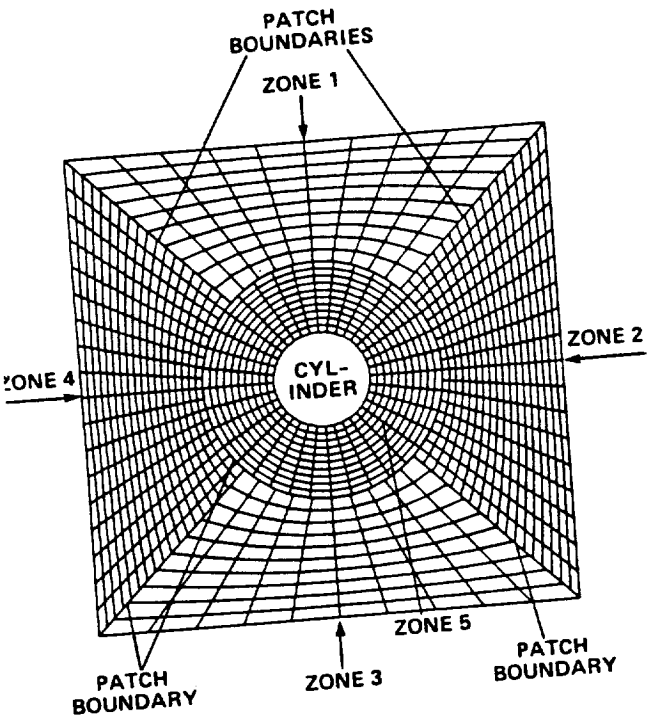

b. PATCHED-DISJOINT GRID

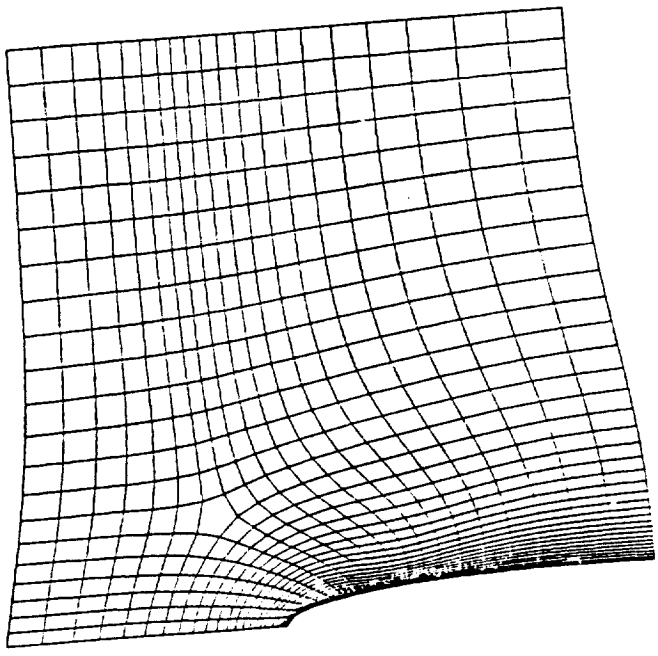

c. PATCHED-JOINT GRID

FIG. 30. TYPES OF MULTI-BLOCK STRUCTURED GRIDS.

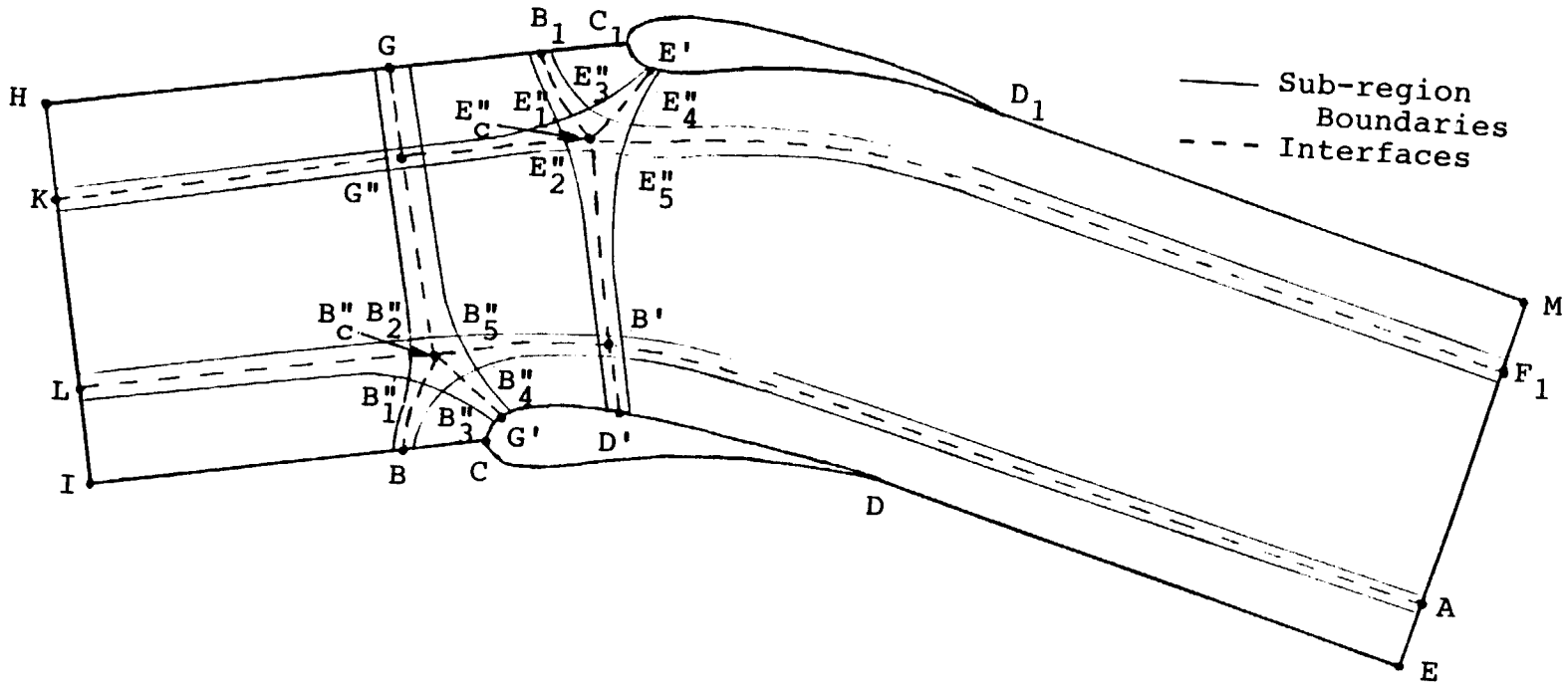

FIG. 31. DECOMPOSITION OF PHYSICAL REGION FOR STAGGERED CASCADE WITH ROUNDED LEADING-EDGE BLADES.

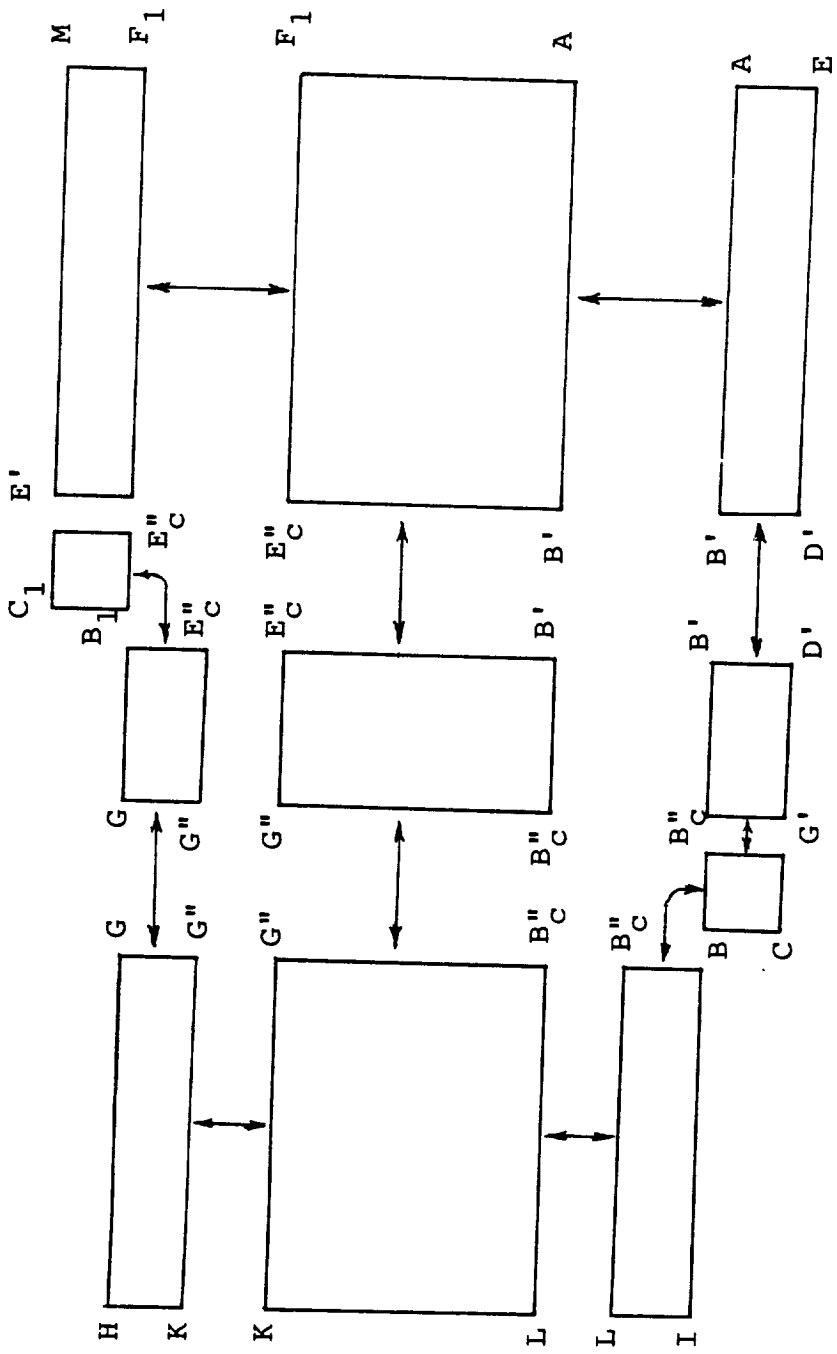

FIG. 32. COMPUTATIONAL BLOCKS FOR VARIOUS SUB-REGIONS OF A HYBRID GRID.

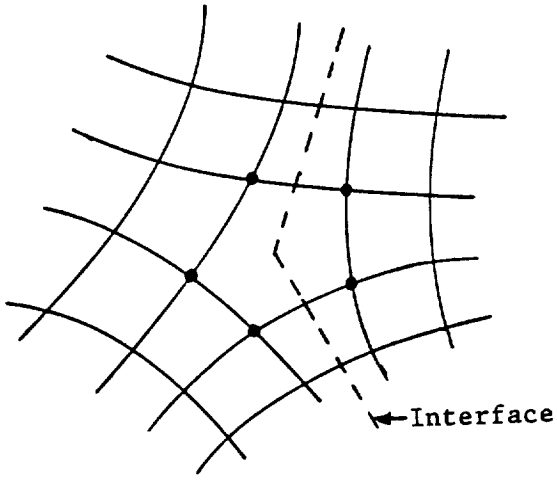

a. CELL WITH NON-STANDARD NUMBER OF FACES

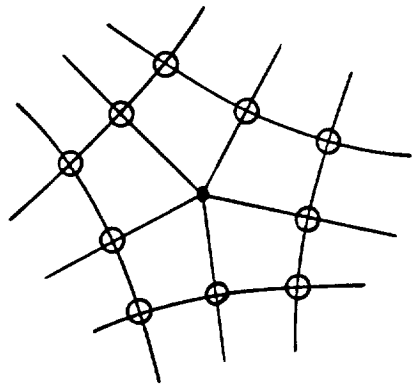

b. POINT WITH NON-STANDARD NUMBER OF NEIGHBOURS

FIG. 33. TYPES OF SPECIAL CELLS AND POINTS.

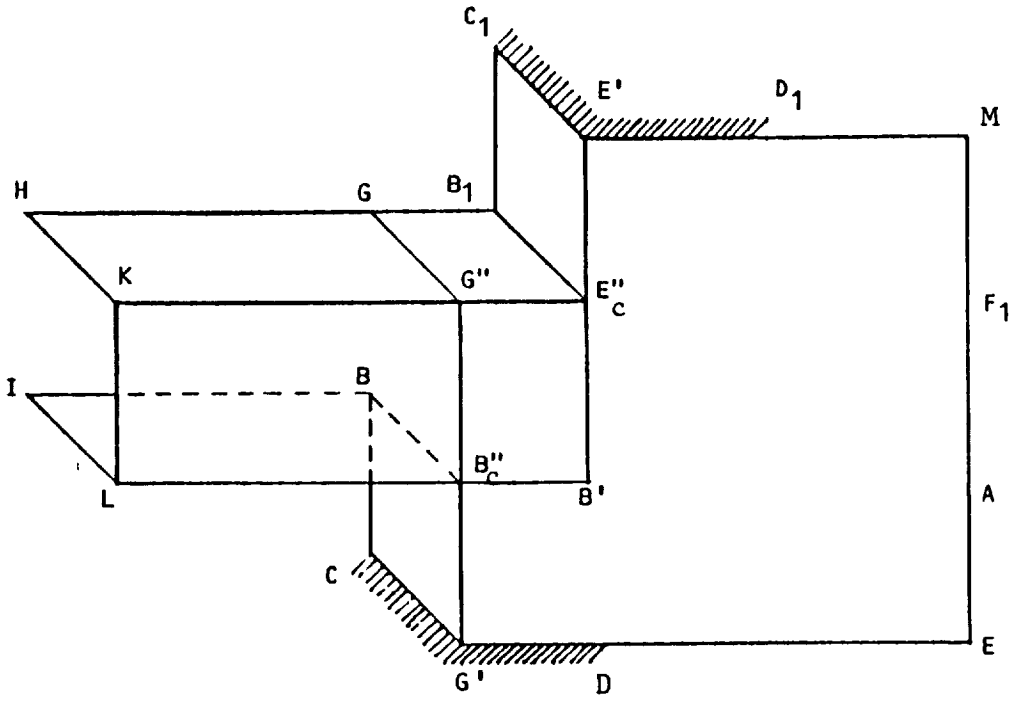

FIG. 34. 3-D VIEW OF THE COMPUTATIONAL DOMAIN.

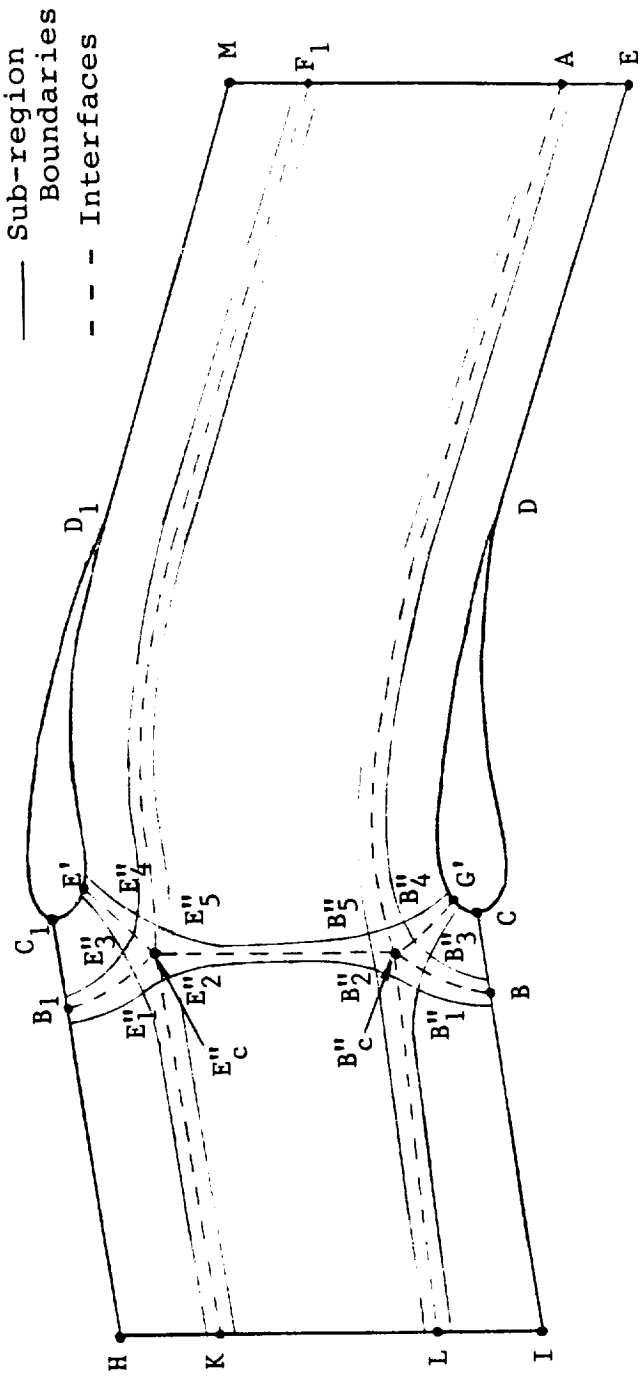

FIG. 35. DECOMPOSITION OF PHYSICAL REGION FOR AN UNSTAGGERED CASCADE WITH ROUNDED LEADING-EDGE BLADES.

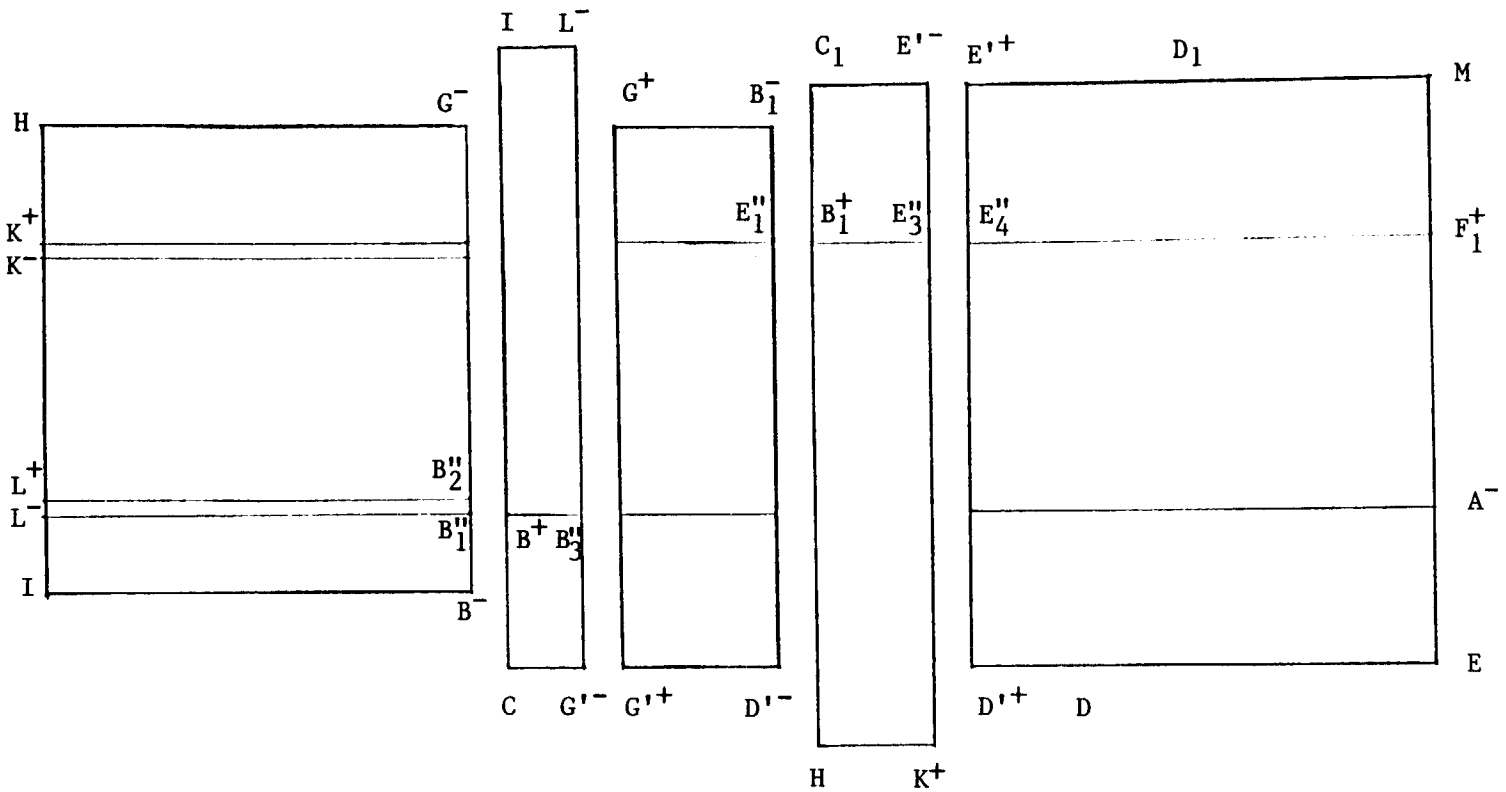

a. η-IMPLICIT SWEEP

FIG. 36. COMPUTATIONAL DOMAINS FOR THE TWO SWEEPS OF ADI SCHEME FOR A C-H HYBRID GRID.

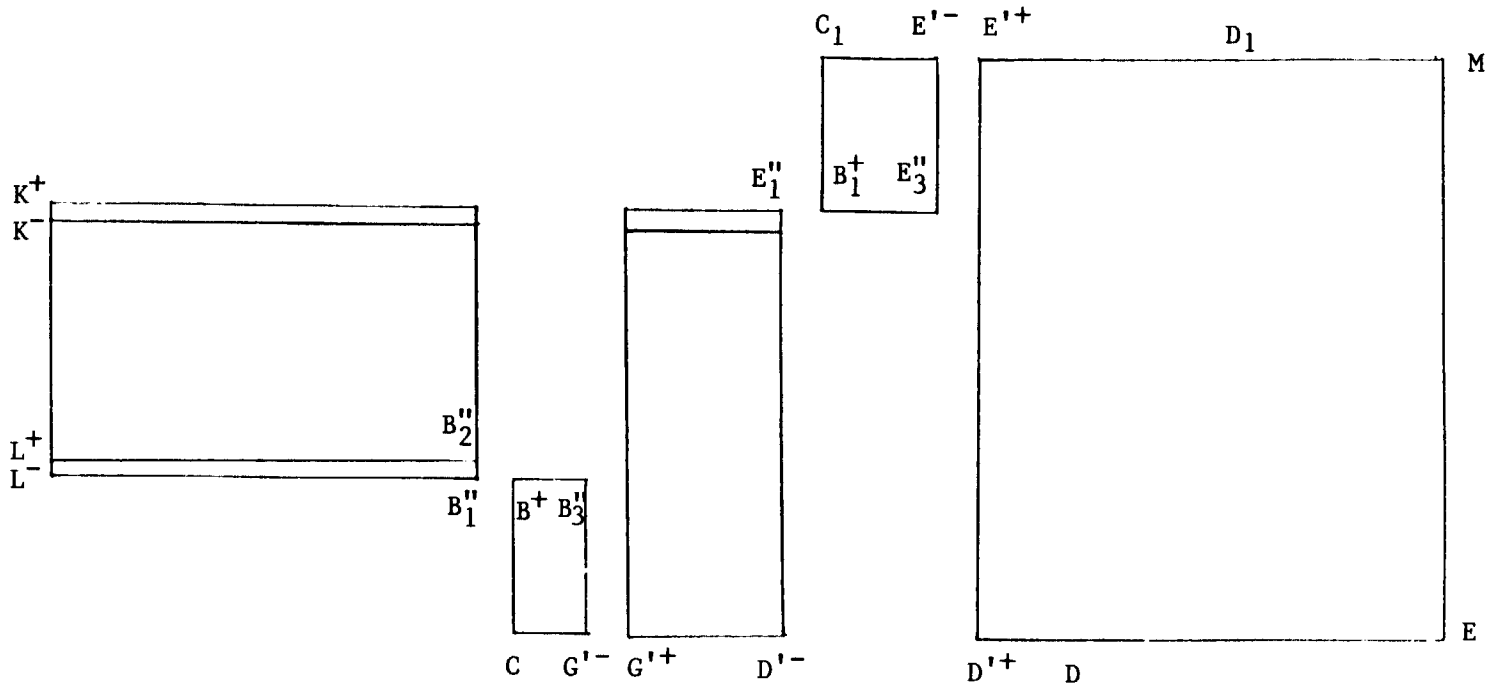

b. ξ-IMPLICIT SWEEP

FIG. 36 (CONCLUDED). COMPUTATIONAL DOMAINS FOR THE TWO SWEEPS OF ADI SCHEME FOR A C-H HYBRID GRID.

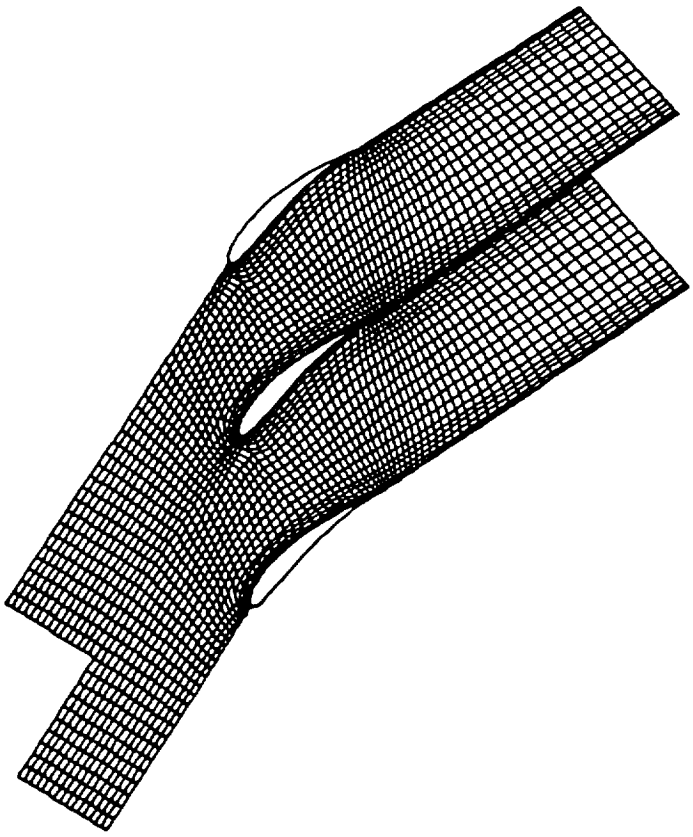

a. STAGGERED CASCADE (GOSTELOW'S CASCADE)

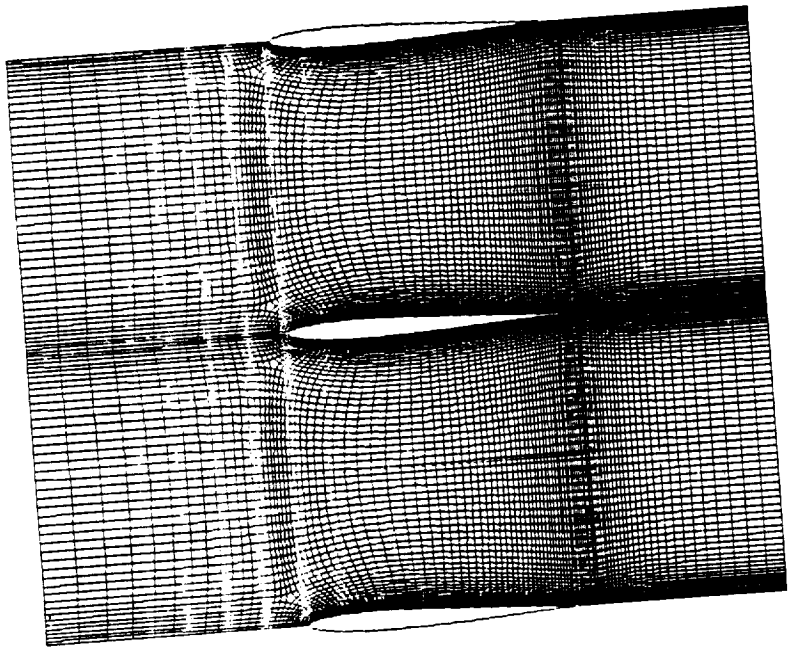

b. UNSTAGGERED CASCADE OF JOUKOWSKI AIRFOILS

FIG. 37. TYPICAL C-H HYBRID GRIDS.

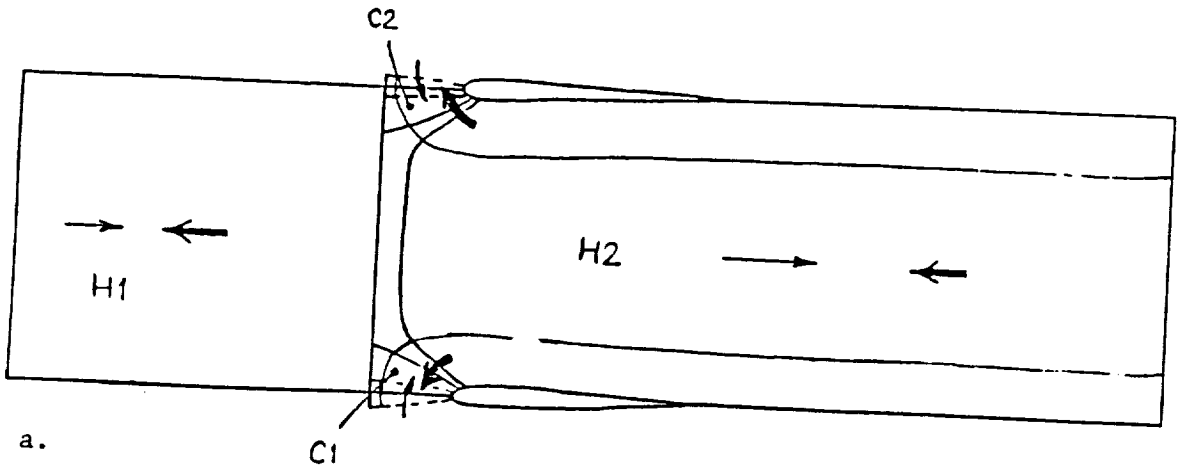

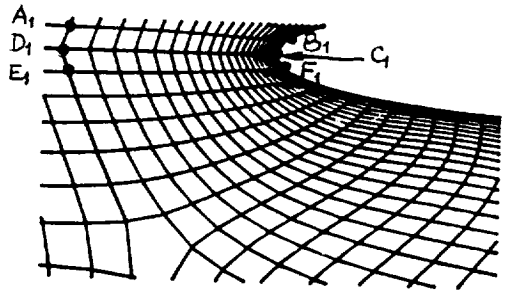

a. TWO-STEPS OF THE SOLUTION PROCEDURE

b.

b. ENLARGED VIEW OF LE REGIONS

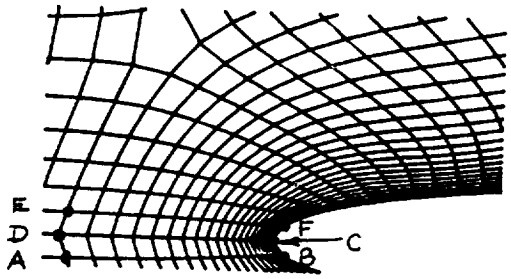

FIG. 38. MARCHING DIRECTIONS FOR SEMI-ELLIPTIC FLOW-SOLUTION PROCEDURE ON C-H HYBRID GRID.

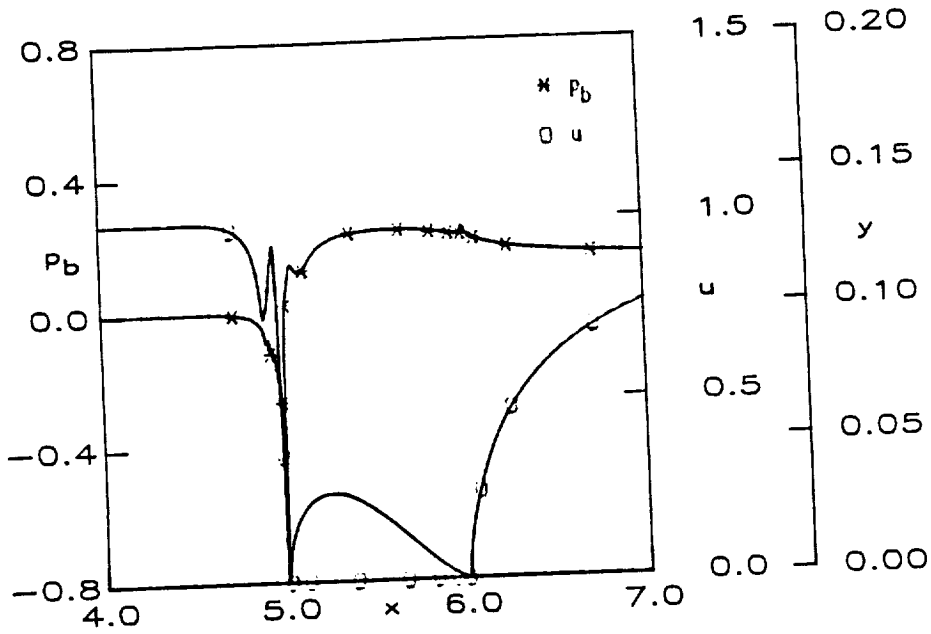

a. SURFACE PRESSURE AND WAKE-CENTERLINE VELOCITY DISTRIBUTIONS

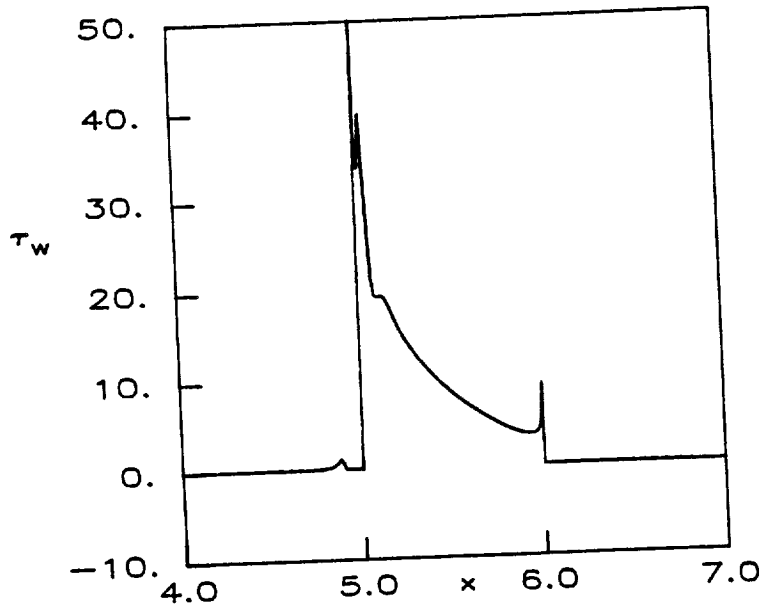

b. WALL-SHEAR PARAMETER DISTRIBUTION

FIG. 39. RESULTS FOR A CASCADE OF JOUKOWSKI AIRFOILS USING C-H HYBRID GRID, Re = 150.

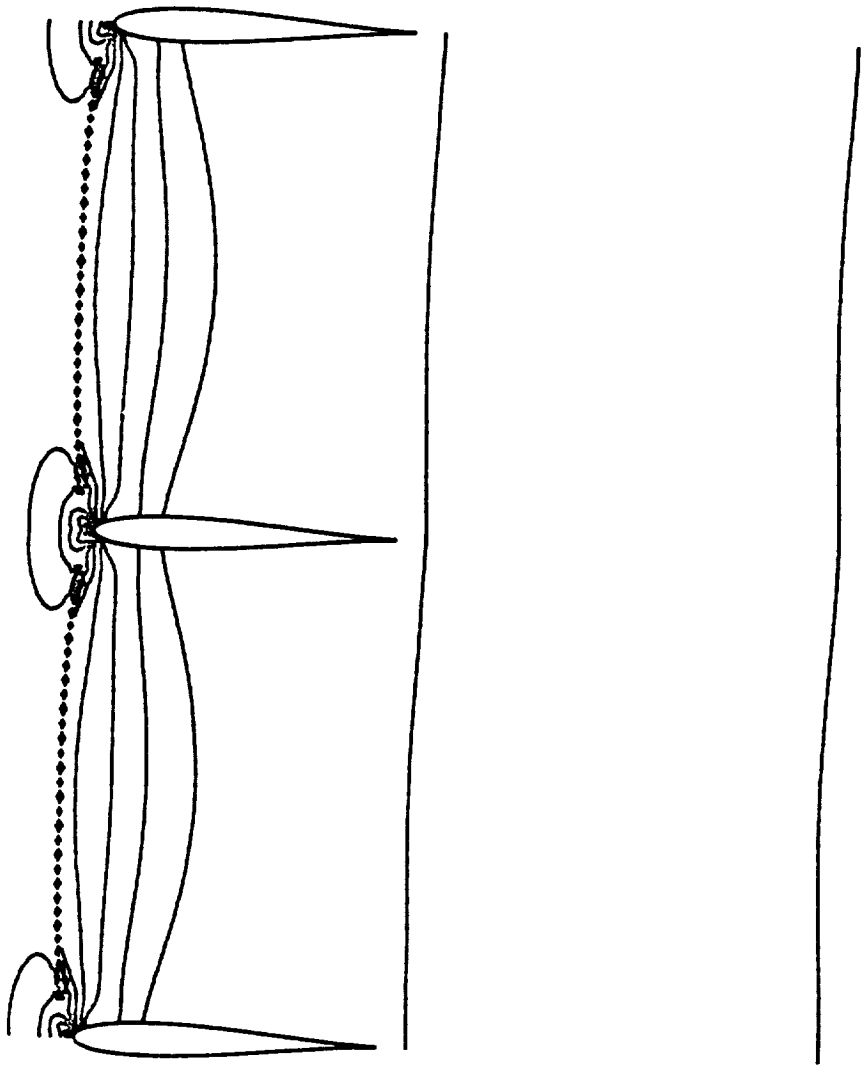

c. STATIC PRESSURE CONTOURS

FIG. 39 (CONT'D). RESULTS FOR A CASCADE OF JOUKOWSKI AIRFOILS USING C-H HYBRID GRID, Re = 150.

ORIGINAL PAGE IS
OF POOR QUALITY

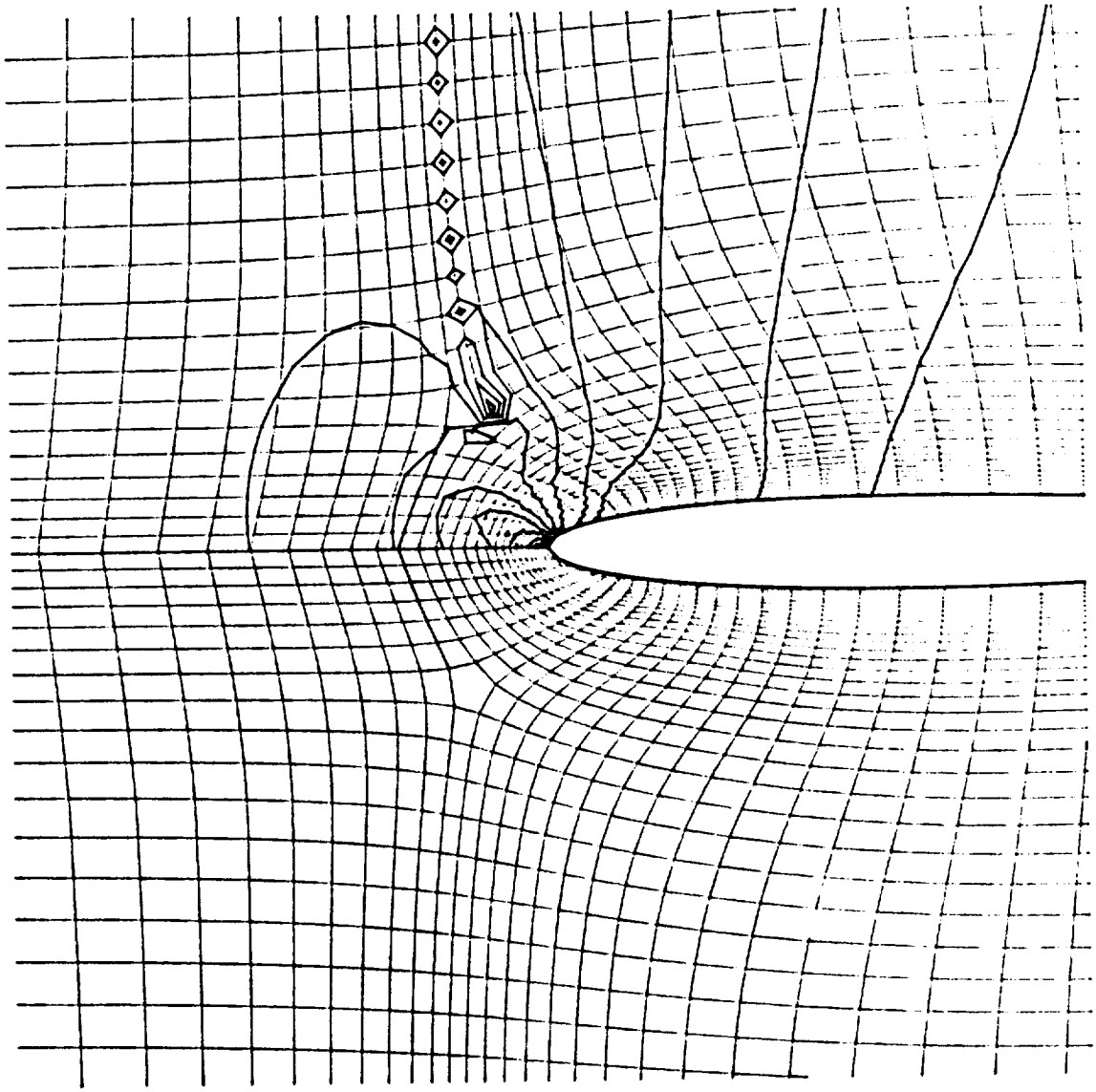

d. STATIC PRESSURE CONTOURS SUPERIMPOSED ON THE HYBRID GRID.

FIG. 39 (CONCLUDED). RESULTS FOR A CASCADE OF JOUKOWSKI AIRFOILS USING C-H HYBRID GRID, Re = 150.

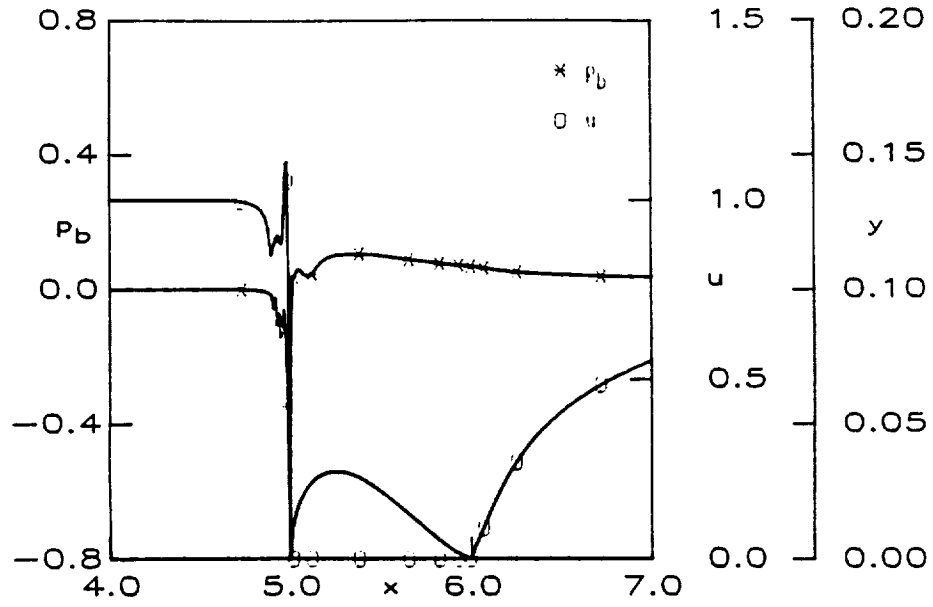

a. SURFACE PRESSURE AND WAKE-CENTERLINE VELOCITY DISTRIBUTIONS

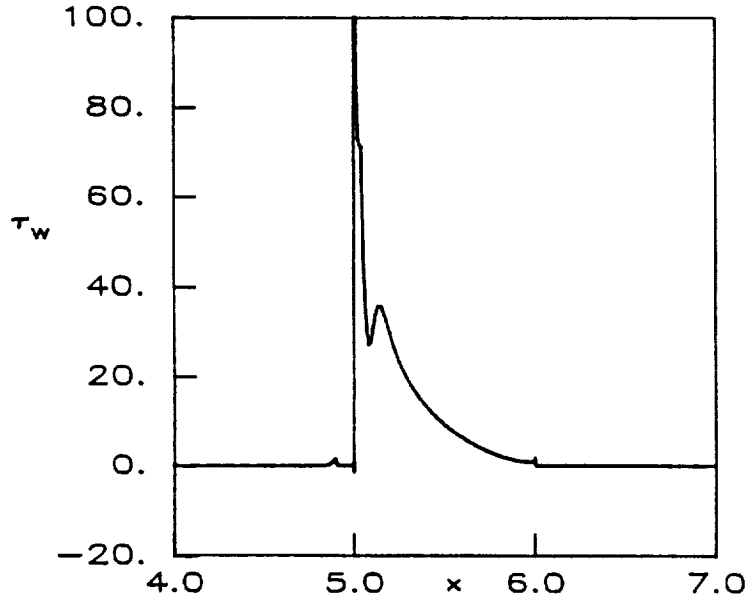

b. WALL-SHEAR PARAMETER DISTRIBUTION

FIG. 40. RESULTS FOR A CASCADE OF JOUKOWSKI AIRFOILS USING C-H HYBRID GRID, Re = 600.

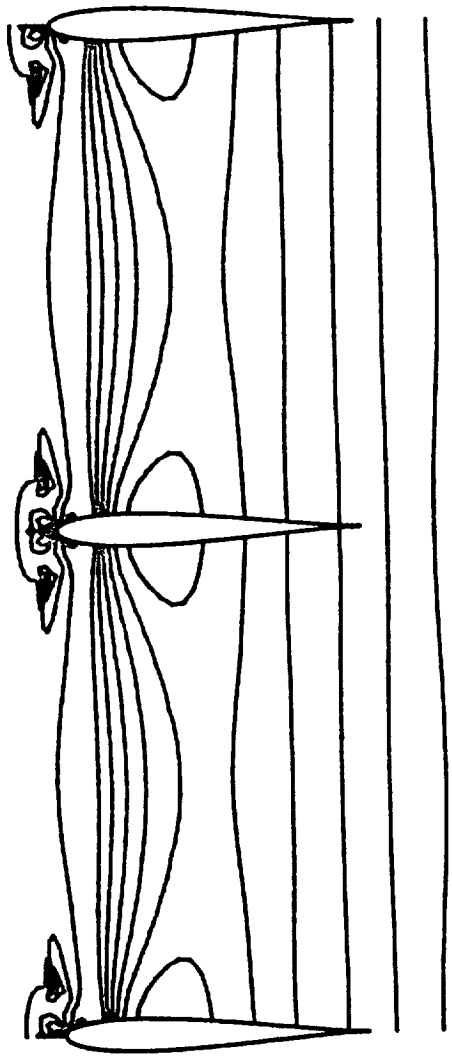

c. STATIC PRESSURE CONTOURS

FIG. 40 (CONT'D). RESULTS FOR A CASCADE OF JOUKOWSKI AIRFOILS USING C-H HYBRID GRID, Re = 600.

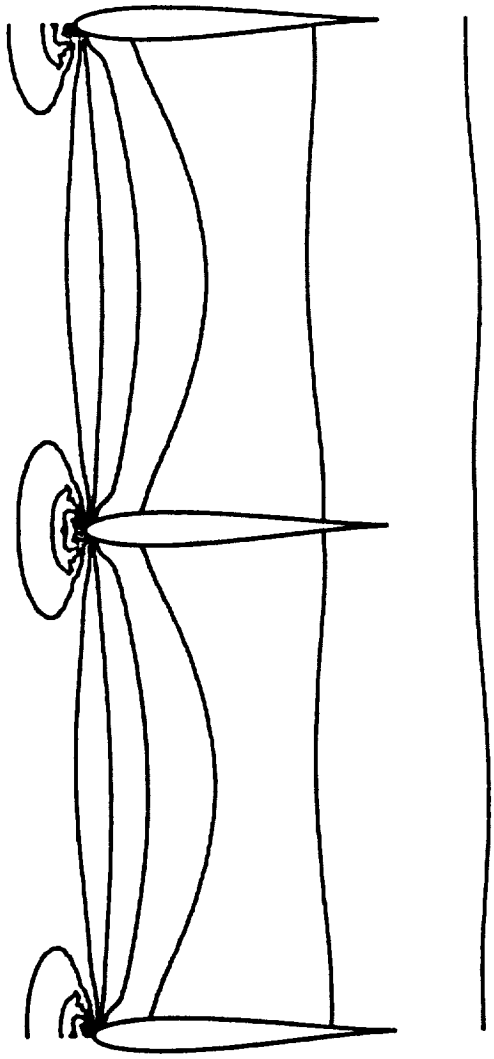

c. STATIC PRESSURE CONTOURS

FIG. 42 (CONT'D). RESULTS FOR A CASCADE OF JOUKOWSKI AIRFOILS USING C-H HYBRID GRID AND COMBINED SCL-CRCL FORM OF EQUATIONS, Re = 300.

ORIGINAL PAGE IS
OF POOR QUALITY

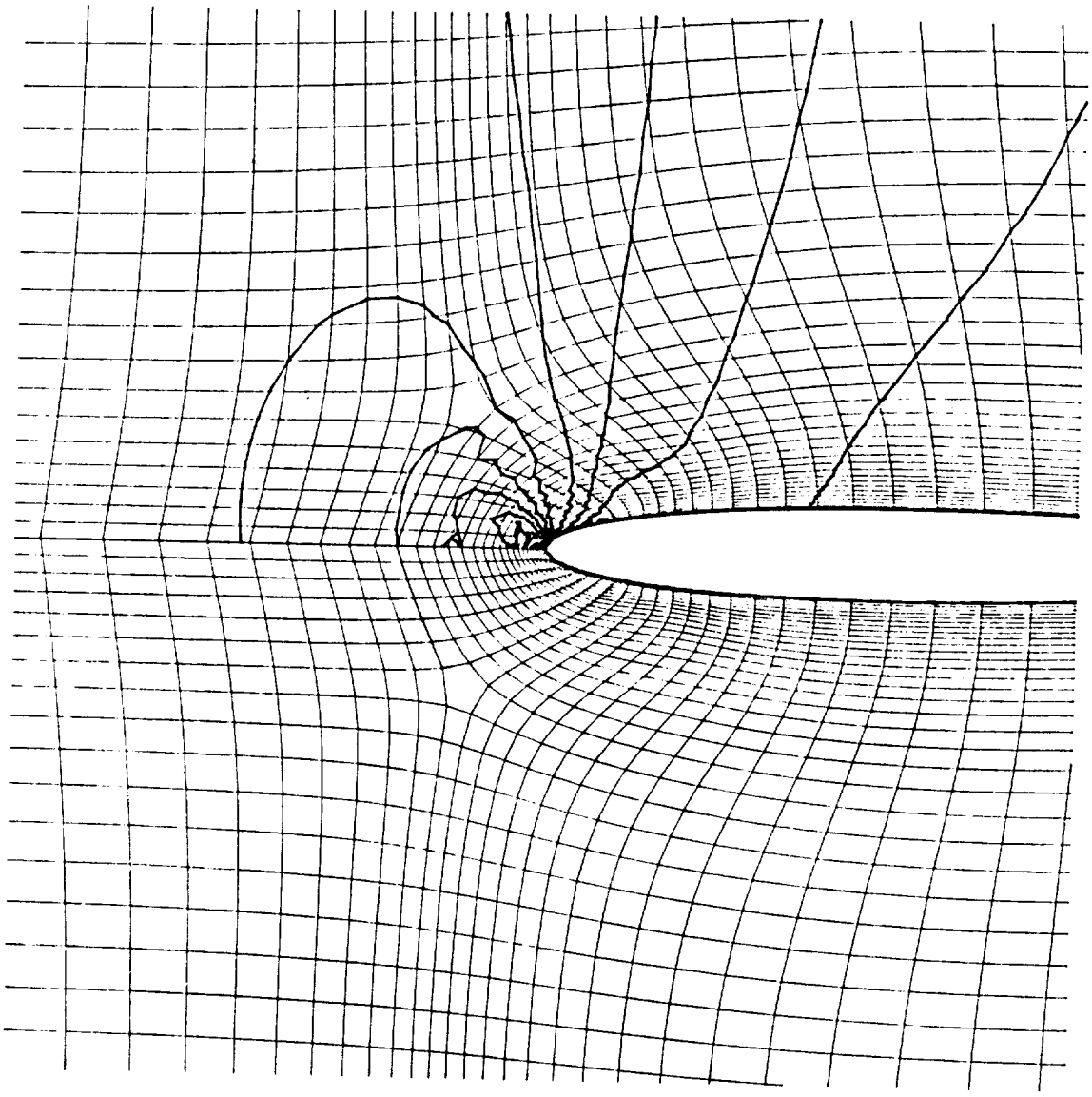

d. STATIC PRESSURE CONTOURS SUPERIMPOSED ON THE HYBRID GRID.

FIG. 42 (CONCLUDED). RESULTS FOR A CASCADE OF JOUKOWSKI AIRFOILS USING C-H HYBRID GRID AND COMBINED SCL-CRCL FORM OF EQUATIONS, Re = 300.

NASA
National Aeronautics and Space Administration

Report Documentation Page

1. Report No.	2. Government Accession No.	3. Recipient's Catalog No.
NASA CR-4180		

4. Title and Subtitle
Simulation of Two-Dimensional Viscous Flow Through Cascades Using a Semi-Elliptic Analysis and Hybrid C-H Grids

5. Report Date
October 1988

6. Performing Organization Code

7. Author(s)
R. Ramamurti, U. Ghia, and K.N. Ghia

8. Performing Organization Report No.
86-9-71 (E-4286)

10. Work Unit No.
505-62-21

9. Performing Organization Name and Address
University of Cincinnati
Dept. of Aerospace Engineering and Engineering Mechanics
and Dept. of Mechanical and Industrial Engineering
Cincinnati, Ohio 44221

11. Contract or Grant No.
NAG3-194

13. Type of Report and Period Covered
Contractor Report
Final

12. Sponsoring Agency Name and Address
National Aeronautics and Space Administration
Lewis Research Center
Cleveland, Ohio 44135-3191

14. Sponsoring Agency Code

15. Supplementary Notes
Project Manager, Peter M. Sockol, Internal Fluid Mechanics Division, NASA Lewis Research Center.

16. Abstract
A semi-elliptic formulation, termed the interacting parabolized Navier-Stokes (IPNS) formulation, is developed for the analysis of a class of subsonic viscous flows for which streamwise diffusion is negligible but which are significantly influenced by upstream interactions. The IPNS equations are obtained from the Navier-Stokes equations by dropping the streamwise viscous-diffusion terms but retaining upstream influence via the streamwise pressure-gradient. A two-step alternating-direction-explicit numerical scheme is developed to solve these equations. The quasi-linearization and discretization of the equations are carefully examined so that no artificial viscosity is added externally to the scheme. Also, solutions to compressible as well as nearly incompressible flows are obtained without any modification either in the analysis or in the solution procedure. The procedure is applied to constricted channels and cascade passages formed by airfoils of various shapes. These geometries are represented using numerically generated general curvilinear boundary-oriented coordinates forming an H-grid. Stagnation pressure, stagnation temperature and streamline slope are prescribed at inflow, while static pressure is prescribed at the outflow boundary. Results are obtained for various values of Reynolds number, thickness ratio and Mach number. The regular behavior of the solutions demonstrates that the technique is viable for flows with strong interactions, arising due to either boundary-layer separation or the presence of sharp leading/trailing edges. Mesh refinement studies are conducted to verify the accuracy of the results obtained. A new hybrid C-H grid, more appropriate for cascades of airfoils with rounded leading edges, is also developed. Appropriate decomposition of the physical domain leads to a multi-block computational domain bounded only by the physical-problem boundaries. This permits development of a composite solution procedure which, unlike most found in literature, is not a patching procedure. Satisfactory results are obtained for flows through cascades of Joukowski airfoils. The implementation of the IPNS formulation on the C-H grid exposes two small portions of the grid interfaces and these require special treatment. However, with a hybrid grid, the use of complete Navier-Stokes equations is recommended, so as also to avoid inconsistencies in the parabolization approximation due to changing orientation of the coordinates at a given location.

17. Key Words (Suggested by Author(s))
Parabolized Navier-Stokes; Cascades; Channels; Composite grids; Parabolized Navier-Stokes equations with upstream interaction via pressure; Alternating-direction explicit numerical method; General nonorthogonal grids; Composite procedure for hybrid grids; Cascades and channels; Compressible and incompressible flow; Separated flows

18. Distribution Statement
Unclassified - Unlimited
Subject Category 02

19. Security Classif. (of this report)	20. Security Classif. (of this page)	21. No of pages	22. Price*
Unclassified	Unclassified	196	A09

NASA FORM 1626 OCT 86

*For sale by the National Technical Information Service, Springfield, Virginia 22161

NASA-Langley, 1988

END